Fabrication additive de structures architecturées en alliages de titane conventionnel et superélastique pour cages intervertébrales

par

Anatolie TIMERCAN

THÈSE PAR ARTICLES PRÉSENTÉE À L'ÉCOLE DE TECHNOLOGIE
SUPÉRIEURE COMME EXIGENCE PARTIELLE À L'OBTENTION
DU DOCTORAT EN GÉNIE MÉCANIQUE
Ph. D.

MONTRÉAL, LE 28 MARS 2024

ÉCOLE DE TECHNOLOGIE SUPÉRIEURE
UNIVERSITÉ DU QUÉBEC

Anatolie Timercan, 2024

Cette licence Creative Commons signifie qu'il est permis de diffuser, d'imprimer ou de sauvegarder sur un autre support une partie ou la totalité de cette œuvre à condition de mentionner l'auteur, que ces utilisations soient faites à des fins non commerciales et que le contenu de l'œuvre n'ait pas été modifié.

PRÉSENTATION DU JURY

CETTE THÈSE A ÉTÉ ÉVALUÉE

PAR UN JURY COMPOSÉ DE :

M. Vladimir Brailovski, directeur de thèse
Département de génie mécanique à l'École de technologie supérieure

M. Patrick Terriault, codirecteur de thèse
Département de génie mécanique à l'École de technologie supérieure

M. François Duhaime, président du jury
Département de génie de la construction à l'École de technologie supérieure

M. Hakim Bouzid, membre du jury
Département de génie mécanique à l'École de technologie supérieure

M. Maxime Gauthier, examinateur externe
Conseil national de recherches Canada

ELLE A FAIT L'OBJET D'UNE SOUTENANCE DEVANT JURY ET PUBLIC

LE 13 MARS 2024

À L'ÉCOLE DE TECHNOLOGIE SUPÉRIEURE

REMERCIEMENTS

Tout d’abord je voudrais remercier mon directeur de recherche, le professeur Vladimir Brailovski. Merci de m’avoir pris sous votre aile et de m’avoir poussé à me dépasser. Vous avez inculqué en moi une éthique de travail qui restera avec moi jusqu’à la fin de ma carrière. Tant sur le plan professionnel que personnel, j’ai apprécié vos conseils judicieux et votre support. J’ai un énorme respect pour votre grande disponibilité et votre encadrement qui m’ont été indispensables dans la réalisation de ce travail.

J’aimerais également remercier mon co-directeur, le professeur Patrick Terriault, pour vos conseils et votre support tout au long du projet. Malgré les rencontres plus rares, je me compte chanceux d’avoir pu vous côtoyer et collaborer sur ce projet.

Je suis aussi reconnaissant à toute l’équipe du LAMSI : Morgan, Salah, Mykhailo, William, Étienne, Jean-René, Erika, Atefeh, Alena, Donatien, Aurore, Victor, Patrick, Julien, Linh-Aurore et Neda parmi tant d’autres. Mon passage à ce laboratoire m’a permis de créer des amitiés et des souvenirs que je chérirai à tout jamais. Je me sens privilégié d’avoir pu travailler et partager tout ce temps avec des gens aussi brillants et motivés. Vos conseils, votre support et les bons moments passés ensemble ont rendu ce travail plus qu’agréable. J’aimerais aussi remercier mes collègues à Moscou : Prof. Prokoshkin, Vadim, Sergey, Kristina, qui m’ont accueilli et fait sentir comme à la maison durant mon séjour.

Je tiens à souligner le support des techniciens de l’ÉTS : Radu Romanica, Mohammad Saadati, Serge Plamondon, Joel Grignon, Xavier Rimpault, Michel Drouin, Anthony Remington, Mario Corbin. Vous êtes les piliers qui soutiennent la recherche se déroulant à l’ÉTS. Sans votre aide et engagement, peu de travaux se réaliseraient.

Enfin, je veux remercier mes parents, Veaceslav et Iraida, et ma sœur, Diana, pour leur soutien infaillible et leur aide tout au long de mes études. À mes parents qui ont immigré au Canada en laissant tout derrière afin de nous offrir une meilleure vie et de nouvelles opportunités : tous mes accomplissements sont les Vôtres!

FABRICATION ADDITIVE DE STRUCTURES ARCHITECTURÉES EN ALLIAGES DE TITANE CONVENTIONNEL ET SUPERÉLASTIQUE POUR CAGES INTERVERTÉBRALES

Anatolie TIMERCAN

RÉSUMÉ

L'Organisation Mondiale de la Santé rapporte que les douleurs de dos, plus particulièrement du bas du dos, sont la principale cause d'invalidité au monde, affectant plus de 600 millions de personnes en 2020. La majorité des cas sont traités par physiothérapie et médication anti-inflammatoire, toutefois, certains patients peuvent avoir recours à l'intervention chirurgicale de fusion vertébrale. Les cages intervertébrales présentement utilisées pour ces chirurgies comportent des risques de complications majeures comme la perte de fixation, la migration et la défaillance de l'implant. La fabrication additive (FA), aussi appelée impression 3D, est une des technologies émergentes de production de composantes complexes. Dans le cadre de ce projet, la technique de fusion laser sur lit de poudre est employée pour fabriquer des structures architecturées à partir d'un alliage à mémoire de forme (AMF), le Ti-Ni, qui est une solution envisagée pour produire des cages légères et résistantes, possédant des propriétés fonctionnelles de superélasticité ainsi que la capacité d'ostéo-intégration qui ont le potentiel de réduire les complications.

En un premier lieu, un cahier de charges a été établi pour identifier les requis fonctionnels des cages intervertébrales et sélectionner de candidats de structures architecturées. Des structures en diamant à base de poutres et des structures gyroides surfaciques, avec une taille de pore de 750 µm et des niveaux de porosité de 60, 70 et 80%, ont été conçues et fabriquées à partir de l'alliage Ti-6Al-4V. Les structures produites ont été caractérisées en termes de géométrie, de propriétés mécaniques et de perméabilité fluidique. La rigidité des deux structures (1.9-4.8 GPa) est comparable à celle de l'os, tandis que leur résistance mécanique en compression (52-160 MPa) est supérieure à celle des vertèbres (3-6 MPa), réduisant ainsi les risques de détérioration osseuse ou défaillance de l'implant. La perméabilité aux fluides (5-57 x 10^{-9} m^2) et les rapports surface/volume (~3) des deux structures sont proches de ceux des vertèbres.

En second lieu, le comportement des structures cellulaires sous différents modes de chargement a été analysé. Les mêmes structures, mais avec des porosités de 50 à 80% ont été testées expérimentalement et simulées numériquement en traction/compression axiale et en torsion pour répliquer la flexion/extension, la compression et la rotation de la colonne vertébrale. Les simulations numériques surestiment le comportement expérimental d'environ 25%, probablement en raison de la présence de défauts de fabrication, notamment dans les structures plus poreuses. Les résultats expérimentaux et numériques ont démontré que les structures ont des propriétés mécaniques quasi-identiques en compression et en tension, mais plus élevées en torsion que prévu par les théories de limitation conventionnelles. Néanmoins, les propriétés sont adéquates pour satisfaire les exigences des cages intervertébrales.

Enfin, il fut possible de procéder à la FA de structures architecturées en AMF de Ti-50.26%atNi en utilisant tout d'abord un modèle numérique pour tester et étudier divers ensembles de paramètres d'impression. Une densité d'énergie volumétrique de 90 J/mm^3 et un taux de fabrication de 10 cm^3/h ont permis la production d'échantillons avec une densité de 99.94% et une température finale de transformation en austénite Af = 26.3°C. Des structures en diamant et gyroides avec un taux de porosité de 60% ont été fabriquées et testées en compression. Suite à un traitement thermique à 500°C pendant 30 minutes, les structures en diamant ont manifesté des déformations apparentes réversibles plus importantes que leurs équivalents gyroides (7% contre 6%) ainsi qu'une souplesse plus importante (E 2.9 contre 3.5 GPa), et des contraintes élastiques similaires (Sy ~48 MPa). Ceci indique que les structures en diamant sont un meilleur candidat pour une utilisation dans les cages intervertébrales. L'analyse par éléments finis a permis de comparer l'état de contraintes dans les deux structures et d'identifier les zones de concentration des contraintes. Comparées à l'alliage Ti-6Al-4V, les structures en Ti-Ni sont plus souples pour une porosité plus faible et ont des déformations réversibles plus importantes.

Mots-clés : Fabrication additive, Structures architecturées, Modélisation par éléments finis, Alliages à mémoire de forme

ADDITIVE MANUFACTURING OF LATTICE STRUCTURES USING CONVENTIONAL AND SUPERELASTIC TITANIUM ALLOYS FOR USE IN INTERVERTEBRAL CAGES

Anatolie TIMERCAN

ABSTRACT

The World Health Organization reports that back pain, especially lower back pain, is the leading cause of disability worldwide, affecting over 600 million people in 2020. While most cases are treated with physiotherapy and anti-inflammatory medication, some patients may opt for spinal fusion surgery. The intervertebral cages currently used in these surgeries pose significant risks of complications, such as loss of fixation, migration, and implant failure. Additive manufacturing (AM), also known as 3D printing, is an emerging technology for producing complex components. In this project, the laser powder bed fusion technique is used to manufacture lattice structures from a Ti-Ni shape memory alloy (SMA), which has the potential for producing lightweight and resistant cages with functional properties of superelasticity and osseointegration, possibly reducing complications.

First, the functional requirements of intervertebral cages were established and lattice structures candidates were selected. Strut-based diamond and sheet-based gyroid structures, with a pore size of 750 μm and porosity levels of 60%, 70%, and 80%, were designed and manufactured from Ti-6Al-4V alloy. The structures were characterized in terms of geometry, mechanical properties, and fluid permeability. The compressive stiffness of both structures (1.9-4.8 GPa) was comparable to that of bone, while their mechanical resistance (52-160 MPa) was greater than that of vertebrae (3-6 MPa), thus reducing the risks of bone deterioration and implant failure. Fluid permeability (5-57 x 10^{-9} m^2) and surface-to-volume ratios (~3) of both structures were close to those of vertebrae.

Secondly, a better understanding of the behavior of lattice structures under different loading modes was gained. The same two structures, but with porosities ranging from 50% to 80%, were tested experimentally and simulated numerically in axial tension/compression and in torsion to simulate flexion/extension, compression, and rotation of the spine. Numerical simulations overestimated the experimental behavior by about 25%, likely due to manufacturing defects, especially in most porous structures. Experimental and numerical results demonstrated that the structures had quasi-identical mechanical properties in compression and tension, but higher torsional properties than predicted by conventional limitation theories. Nevertheless, the lattice structures proved adequate and met the requirements of intervertebral cages.

Finally, lattice structures could be produced using AM of Ti-50.26%atNi SMA by using a numerical model to test and study various printing parameter sets. A volumetric energy density of 90 J/mm^3 and a build rate of 10 cm^3/h allowed the production of specimens with a density of 99.94% and an austenite finish temperature of Af = 26.3°C. Diamond and gyroid structures with a 60% porosity level were manufactured and compression tested. After heat treatment at 500°C for 30 minutes, diamond structures showed larger reversible deformations (7% vs 6%) and higher compliance (E 2.9 vs 3.4 GPa) and similar yield stresses (Sy ~48 MPa) compared to their gyroid equivalents. This indicates that diamond lattices are more suited for use in intervertebral cages. Finite element analysis allowed a comparison of stress distribution in both structures and the identification of stress concentration areas. Compared to the Ti-6Al-4V alloy, Ti-Ni structures were more compliant at lower porosity levels and exhibited larger reversible deformations.

Keywords: Additive manufacturing, Lattice structures, Numerical modeling, Shape memory alloys

TABLE DES MATIÈRES

Page

INTRODUCTION 1

CHAPITRE 1 REVUE DE LA LITTÉRATURE 5
1.1 Cages intervertébrales 5
  1.1.1 Colonne vertébrale 5
  1.1.2 Traitements disponibles 6
  1.1.3 Types de cages intervertébrales existantes 7
1.2 Alliages à mémoire de forme 11
  1.2.1 Effet mémoire de forme 16
  1.2.2 Effet superélastique 17
1.3 Fabrication additive 20
  1.3.1 Procédés courants de FA de métaux 21
  1.3.2 Fabrication additive d'alliages à mémoire de forme 22
1.4 Structures architecturées 24
  1.4.1 Propriétés des structures cellulaires 29
  1.4.2 Structures architecturées en AMF 32
  1.4.3 Méthodes de simulation de structures cellulaires 34
1.5 Résumé et rappel des objectifs 39

CHAPITRE 2 MECHANICAL PROPERTIES AND FLUID PERMEABILITY OF GYROID AND DIAMOND LATTICE STRUCTURES FOR INTERVERTEBRAL DEVICES: FUNCTIONAL REQUIREMENTS AND COMPARATIVE ANALYSIS 41
2.1 Avant-propos 41
2.2 Résumé 41
2.3 Abstract 42
2.4 Introduction 43
2.5 Functional requirements to intervertebral cages 46
2.6 Materials and methods 51
  2.6.1 Lattice selection 51
  2.6.2 Experimental testing 53
2.7 Results 57
2.8 Discussion 63
2.9 Conclusion 70
2.10 CRediT authorship contribution statement 71
2.11 Disclosure statement 71
2.12 Acknowledgements 71
2.13 Data availability statement 71

CHAPITRE 3 AXIAL TENSION/COMPRESSION AND TORSIONAL LOADING OF DIAMOND AND GYROID LATTICE STRUCTURES FOR BIOMEDICAL IMPLANTS: SIMULATION AND EXPERIMENT 73
3.1 Avant-propos......73
3.2 Résumé......73
3.3 Abstract......74
3.4 Introduction......75
3.5 Materials and methods......78
  3.5.1 Specimen design and manufacturing......78
  3.5.2 Numerical simulations......82
  3.5.3 Experimental testing......84
3.6 Results......85
  3.6.1 Geometric conformance......85
  3.6.2 Numerical simulations......87
  3.6.3 Experimental validation......91
3.7 Discussion......95
  3.7.1 Manufacturing of lattices......95
  3.7.2 Mechanical behavior of lattices......96
3.8 Conclusions......101
3.9 Acknowledgments......101
3.10 Funding......102
3.11 Data availability......102

CHAPITRE 4 PROCESS OPTIMIZATION OF LASER POWDER BED FUSION OF SUPERELASTIC TI-NI LATTICE STRUCTURES: AN EXPERIMENTAL AND NUMERICAL STUDY......103
4.1 Avant-propos......103
4.2 Résumé......103
4.3 Abstract......104
4.4 Introduction......105
4.5 Materials and methods......106
  4.5.1 Manufacturing parameter selection......106
  4.5.2 Manufacture, preparation, chemical and structural analyses of printed specimens......110
  4.5.3 Measurement of the transformation temperatures and mechanical testing......111
  4.5.4 Numerical simulations and experimental validation......113
4.6 Results......114
  4.6.1 Integrity and density of manufactured specimens......114
  4.6.2 Chemical composition......117
  4.6.3 Phase transition temperatures......118
  4.6.4 Crystalline phase analysis......120
  4.6.5 Numerical model and validation......122
4.7 Discussion......126
4.8 Conclusions......132

4.9 Acknowledgments ... 134
4.10 CRediT author contribution ... 134
4.11 Funding ... 134
4.12 Data availability ... 134
4.13 Annex A ... 135

CONCLUSION GÉNÉRALE ... 137

RECOMMANDATIONS ... 141

LISTE DE RÉFÉRENCES BIBLIOGRAPHIQUES ... 143

LISTE DES TABLEAUX

Page

Tableau 1.1 Survol des travaux portant sur la FA des cages intervertébrales 9

Tableau 1.2 Survol des travaux portant sur l'optimisation topologique des cellules unitaires 28

Tableau 1.3 Récapitulatif de divers articles traitant de structures architecturées en Ti6Al4V Tiré et adapté de Mahmoud et Elbestawi (2017).......................31

Tableau 2.1 Average dimensions of vertebrae at the cervical, thoracic and lumbar levels Tiré de Aharinejad et al. (1990), Panjabi et al. (1992) et Scoles et al. (1988) 46

Tableau 2.2 Selected diamond/gyroid lattice structure geometric parameters for a pore size of 750 µm and target porosities of 60, 70 and 80%...................53

Tableau 2.3 Scaling relations for modulus of elasticity, yield strength and permeability of the diamond and gyroid structures; Re1 and Re10 correspond to Reynolds numbers of 1 and 10..65

Tableau 2.4 Mechanical properties of biological tissues, commonly used spinal cage materials and manufactured lattice structures..67

Tableau 3.1 Parameters of the studied diamond and gyroid lattice structures having a target pore diameter of 750 µm..78

Tableau 3.2 Numerically predicted apparent mechanical properties: elasticity/shear moduli and yield stresses and volume fractions of the lattice structures undergoing plastic deformation (stresses exceed the bulk material yield stress of 900 MPa) at 5% of axial and 4% of torsional global strains 89

Tableau 3.3 Experimentally determined (apparent) mechanical properties of the diamond and gyroid structures under compression, tension and torsion...92

Tableau 3.4 Scaling relations of the diamond (D) and gyroid (G) lattice elasticity moduli (E and G) and yield stresses (S_y and S_{Sy}) for three loading modes and the corresponding R^2 correlation coefficients.........................93

Tableau 4.1 Material properties of Ti-Ni used for the LPBF process modeling and specimen densities prediction 108

Tableau 4.2 Printing parameters and predicted densities for 30 µm layer thickness and 70 µm hatch distance..109

Tableau 4.3 Mechanical properties of the as-built and heat-treated specimens in tension and idealized stress-strain parameters of the heat-treated specimens used for FEA simulations 123

Tableau 4.4 Density measurements using CT imaging and pycnometry 135

Tableau 4.5 Phase transition temperatures (°C) of the as-received powder (AR) and printed specimens (as-built and heat-treated) 135

LISTE DES FIGURES

Page

Figure 1.1 a) représentation schématique d'une colonne vertébrale; b) schéma d'un disque intervertébral Tiré de Friis, Arnold, et Goel (2017)................6

Figure 1.2 Techniques courantes de chirurgie de fusion vertébrale Tiré de Peck et al. (2018)..7

Figure 1.3 Types de cages intervertébrales A, BAK cage (Zimmer Spine). B, Ray Threaded Fusion Cage (Stryker Spine). C, LT-CAGE. D, INTER FIX device (Medtronic Sofamor Danek). E, Harms cage (DePuy Spine). F, PEEK cage (Medtronic Sofamor Danek). G, JAGUAR I/F CAGE (Brantigan Device; DePuy Spine). H, BOOMERANG. I, Bone Dowel. J, Femoral Ring (H–J Medtronic Sofamor Danek) Tiré de Williams, Gornet, et Burkus (2005)....................8

Figure 1.4 Cage intervertébrale en Ti-Ni poreux et en TiAlV conventionnel Tiré de M Assad et al. (2003b) 10

Figure 1.5 Cage intervertébrale poreuse en Ti-Ni fabriquée par synthèse de combustion Tiré de Aihara et al. (2019) 11

Figure 1.6 Schéma de modifications de la structure cristalline des alliages à mémoire de forme Tirée de Otsuka et Wayman (1999).........................12

Figure 1.7 Diagramme d'état de phase d'un AMF Tirée et adaptée de Brailovski et al. (2003) 13

Figure 1.8 Transformation des mailles élémentaires pour un AMF de l'austénite cubique face centrée à la martensite tétragonale centrée Tiré de Otsuka et Wayman (1999)..14

Figure 1.9 Exemple de macles formées pendant la transformation martensitique Tiré de reportage TV5...15

Figure 1.10 Représentation schématique de la transformation martensitique à l'échelle atomique Tirée et adaptée de Brailovski et al. (2003).............15

Figure 1.11 Graphiques contrainte-température et contrainte-déformation représentant l'effet de mémoire de forme Tirée et adaptée de Brailovski et al. (2003) 17

Figure 1.12 Graphiques contrainte-température et contrainte-déformation représentant l'effet superélastique Tirée et adaptée de Brailovski et al. (2003) 18

Figure 1.13 Variation des températures de transformation de phases des alliages Ti-Ni en fonction du taux de nickel en %at Tiré de Brailovski et al. (2003) 19

Figure 1.14 Comportement mécanique d'un alliage Ti-Ni en fonction de la température d'opération Tirée de Brailovski et al. (2003) 20

Figure 1.15 Techniques de FA. Gauche : fusion laser sur lit de poudre, centre : dépôt sous énergie et droite : consolidation de poudre par jet de liant Tiré du recueil SYS867 Brailovski (2017) 21

Figure 1.16 Spécimens en Ti-Ni imprimés avec divers paramètres de fabrication Tiré de Xue et al. (2022) 23

Figure 1.17 a) Comportement en traction de Ti-Ni imprimé par LPBF ne démontrant pas de superélasticité, b) Courbes contrainte-déformation de Ti-Ni imprimé avec le comportement superélastique en compression Tirés de a) H. Lu et al. (2022) et b) Moghaddam et al. (2019)................24

Figure 1.18 Exemple 2D de structure architecturée A) périodique; B) pseudopériodique; C) hétérogène et D) homogène Tiré et adapté de Y. Tang et Zhao (2016)................25

Figure 1.19 Structures à dominance de flexion (gauche) ou d’allongement (droite) Tiré de Deshpande et al. (2001)................26

Figure 1.20 Exemples de structures architecturées produites par FA Tiré et adapté de Al-Ketan et al. (2018) 27

Figure 1.21 Comportement contrainte-déformation typique des structures architecturées Tiré de Evans et al. (1998)................30

Figure 1.22 Comportement mécanique des structures imprimées avec a) haute puissance et vitesse (HP) et b) faible puissance et vitesse (LP) testées en compression à température ambiante. À noter les différentes fractions volumétriques (densité relative) Tiré de Sasan Dadbakhsh et al. (2015) ..33

Figure 1.23 a) structures architecturées testées en fatigue (A-Octahedron, B-Gyroide squeletal, C-Gyroide surfacique); b) contrainte maximale des structures en fonction du nombre de cycles Tiré et adapté de Speirs et al. (2017) 34

Figure 1.24 a) Structure architecturée avec 40960 éléments (hétérogène) et b) structure solide avec 512 éléments (homogène) Tiré de Ptochos et Labeas (2012)................36

Figure 1.25 Cellule cubique centrée renforcée en Z (BCCZ) simulée par : a) éléments poutre variables; b) éléments solides tétraédriques Tiré et adapté de Ravari et al. (2014)..37

Figure 1.26 a) Comparaison de résultats des simulations avec les tests expérimentaux et b) analyse de la distribution des contraintes Tiré de Abou-Ali et al. (2020) 38

Figure 2.1 Default unit cell disposition of the a) diamond lattice (Miller indices are added, for convenience), b) gyroid lattice. Unit cell as generated in this study and the control parameters c) diamond lattice and d) gyroid lattice. Specimens for compression testing: e) CAD, f) diamond lattice and g) gyroid lattice..50

Figure 2.2 Specimen distribution on the build plate 54

Figure 2.3 Specimen strut thickness measurements in ~70% porosity structures using the sphere method in VGStudio MAX software: a) diamond and b) gyroid structures 55

Figure 2.4 Permeability test setup: a) mixer tank/pump assembly, b) specimen holder, c) differential pressure transducer, d) flowmeter and e) laptop with LabView for data treatment. Not shown on the image are the power supply, pump controller and data acquisition card 57

Figure 2.5 Deviation maps between the designed and manufactured 70% diamond and gyroid structures following a best-fit: the detailed views show the design in a green outline and the scanned structure in solid white...........58

Figure 2.6 Comparison of the designed (d) and manufactured (m) diamond and gyroid structures: a) porosity, b) diamond strut thickness, c) gyroid sheet thickness, d) diamond pore diameter, and e) gyroid pore diameter..59

Figure 2.7 Stress-strain diagrams: a) diamond and b) gyroid structures.....................60

Figure 2.8 Compression testing of ~70% porosity structures: a) diamond and b) gyroid sample shape evolution during compression at various compression strain values. Areas where densification is observed are circled in red 61

Figure 2.9 Apparent mechanical characteristics of the manufactured structures: a) yield strength and b) modulus of elasticity..61

Figure 2.10 Flow and pressure drop experimental measurements, where D signifies diamond and G gyroid structures of different porosities; black rectangle delimits the extrapolated range where Reynolds number varies between 1 and 10 62

Figure 2.11 Permeability results from the extrapolated data are shown as the regions of the Darcy regime (Re1 and Re10 correspond to Reynolds numbers of 1 and 10); diamond (D) structures are presented in blue and gyroid (G) structures in grey 63

Figure 2.12 Surface roughness and sintered particles' impact on pore diameter measurement of the diamond lattice. The scanned structure in white and pore evaluation is color-coded 64

Figure 2.13 Yield strength vs modulus of elasticity comparison of the manufactured structures and bone tissues 66

Figure 2.14 (a) Strength-to-stiffness, (b) surface-to-volume ratios of the manufactured structures and (c) their comparison with bone tissues in the Sy/E - S/V space 68

Figure 3.1 Specimen designs and overall dimensions: Type 1 used for mechanical testing and Type 2 used for porosity verifications. Areas in blue indicate porous parts of the specimens 80

Figure 3.2 Central parts of the diamond (a,b), and gyroid (c,d) structures with a porosity of 50% (a,c) and 80% (b,d) 80

Figure 3.3 Specimens on the build plate after (a) manufacturing and (b) removal from machine; (c) specimens separation from the build plate 82

Figure 3.4 Scanning strategy for the diamond (a,b), and gyroid (c,d) structures with a porosity of 50% (a,c) and 80% (b,d). The blue outline indicates the structure cross-section, green lines indicate infill scanning, red and black lines are upskin and downskin areas, respectively, and contouring is shown in pink 82

Figure 3.5 Mesh details for the diamond and gyroid structures (a) and boundary conditions applied on the 80%-porosity diamond structure in compression (b) and torsion (c) 84

Figure 3.6 A mechanical testing setup with a digital image correlation apparatus 85

Figure 3.7 (a) Porosity levels of the designed and manufactured structures; (b) Surface deviation distributions of the 50% and 80% porous diamond (D) and gyroid (G) structures 86

Figure 3.8 Manufacturing-induced defects in the most porous (~80%) diamond (a) and gyroid (b) structures and comparison to the idealised CAD outlined in yellow 87

Figure 3.9 Numerically predicted apparent mechanical properties: elasticity/shear moduli and yield stresses 89

Figure 3.10 Simulated stress distributions in the diamond (a, b) and gyroid (c, d) structures at ~50% (a, c) and ~80% (b, d) porosity levels under global strains of 5% compression, 5% tension and 4% torsion 90

Figure 3.11 Stress-strain diagrams of all the experimental tests of the 50, 60, 70 and 80% porosity diamond and gyroid structures under compression, tension and torsion 92

Figure 3.12 Comparison of the experimental and FEA stress-strain diagrams (bold lines-experiment, dotted-calculations) 94

Figure 3.13 Experimental (EXP) and numerical (FEA) moduli of elasticity (E) and yield stresses (Sy) as functions of porosity for diamond (D) and gyroid (G) structures in compression, tension and torsion 94

Figure 3.14 Comparison of the numerical and experimental 70% diamond and gyroid structures under 4% tension strain......95

Figure 3.15 Examples of specimen failure of the 80% porous diamond and gyroid structures in compression, tension and torsion. Failure regions are encircled in red......98

Figure 3.16 Comparison of the numerically-obtained apparent elastic moduli (E and G) and yield stresses (Sy and Ssy) of the diamond and gyroid lattices for compression (vertical axis), tension (horizontal axis), and torsion (diagonal) to the range of properties of bone structures, presented as shaded zones in each diagram. Properties of the vertebrae and the femur for the three loading modes are shown as tangible examples of the potential application requirements......100

Figure 4.1 (a) Ti-Ni powder particle size distribution and (b) particle morphology observed by SEM 107

Figure 4.2 Processing map of the predicted material density as a function of VED and BR for 30 μm layer thickness and 70 μm hatch distance; zone encompassed by VED=70-100 J/mm^3 and BR=3-10 cm^3/h corresponds to the highest expected printed density......109

Figure 4.3 Idealized (a) DSC and (b) tensile diagrams of Ti-Ni SMA and corresponding temperature, stress and strain characteristics 113

Figure 4.4 Ti-Ni substrate featuring cylindrical specimens (10 and 5 mm diameter), tensile specimens and lattice structures 114

Figure 4.5 CT-scan analysis of the 5 mm diameter specimens printed with the 11 sets of parameters shown as a cross-section image and the sideview of the specimen porosity (red) and cracks (yellow). Images are arranged according to the specimen position on the processing map......115

Figure 4.6 (a) Measured relative density compared to the model prediction for each parameter set as related to the (b) processing map.........................117

Figure 4.7 Nickel content in the manufactured specimens as (a) a function of the VED and (b) in the BR-VED design space. Specimen 3 is considered an outlier; arrow indicates nickel content in the as-received powder......118

Figure 4.8 DSC results of the as-received powder and printed specimens: (a) as-built and (b) heat-treated..119

Figure 4.9 Af temperature of the specimens in the (a) as-built and (b) heat-treated conditions in the VED-BR coordinates; arrow indicates Af temperature of the as-received powder 120

Figure 4.10 X-ray diffractograms of the powder and printed specimens in the (a) as-built condition and (b) after heat treatment; peaks of austenite (red), martensite (blue) and R-phase (green) are identified...................121

Figure 4.11 Microstructure of the specimen printed using Parameter set 7: (a,b) optical microscopy and (c, d) EBSD in the as-built (a, c) and heat-treated (b, d) conditions 122

Figure 4.12 Tension stress-strain diagrams of the bulk specimens (Parameter set 7) in the as-built (AB) and heat-treated (HT) conditions with (a) incremental loading and (b) idealized material behavior law for the FEA simulations (dashed curve) based on an averaged stress-strain diagram in the heat-treated state (solid curve).......................................123

Figure 4.13 (a) Simulated stress-strain curves of the gyroid and diamond lattices, and stress distribution in the (b) gyroid and (c) diamond structures at their apparent yield strain and at 6% apparent strain with the material volume fraction in the plastic, superelastic and elastic stress states 124

Figure 4.14 Compression behavior of the as-built and heat-treated 60% porous (a) gyroid and (b) diamond lattices. (c) Apparent stress and (d) recovered strain values are plotted against the applied strain of all the tested structures with arrows indicating the effect of the heat treatment on the structures’ properties 125

Figure 4.15 Comparison of experimental and simulated stress-strain behavior of 60% porous (a) gyroid and (b) diamond lattices 126

Figure 4.16 Geometrical comparison between the designed and manufactured (a) gyroid and (b) diamond lattices. The red outline corresponds to the CAD and the colored outline corresponds to the printed surface, color-coded to the distance between the printed and CAD surfaces 126

Figure 4.17 (a) Color-coded measured densities superimposed on the model predictions map, (b) typical pore shape for high and low VED specimens and (c) pore size distribution for Specimens 1, 7 and 11 128

Figure 4.18 Af temperature in relation to the nickel content as presented in the literature and detailed view of the powder and the heat-treated specimens from the present work Tiré et adapté de Bassani et al. (2023), Brailovski et al. (2003), Chekotu, Goodall, Kinahan, et Brabazon (2022), W. Chen et al. (2021), H. Lu et al. (2022), H. Lu et al. (2023), Mahmoudi et al. (2018), Shen, Li, Guo, Guo, et Fang (2022) et Wen et al. (2021) 130

Figure 4.19 Comparison of the (a) experimental stress-strain diagrams of 60% porous Ti64 and Ti-Ni gyroid and diamond lattices and (b) Sy/E ratios of the studied lattices structures and data adapted from a previous study Tiré et adapté de Timercan et al. (2023)....................132

LISTE DES ABRÉVIATIONS, SIGLES ET ACRONYMES

AB	Tel que fabriqué (As-built)
AM	Additive manufacturing
AMF	Alliage à mémoire de forme
ASTM	American Society for Testing and Materials
BD	Direction de fabrication (Build direction)
BJ	Consolidation de poudre par jet de liant (Binder jetting)
BR	Taux de fabrication (Build rate)
CAD	Computer assisted design
CAO	Conception assistée par ordinateur
CT	Tomodensitométrie (Computed tomography)
DED	Ajout de matière par dépôt d'énergie (Directed energy deposition)
DEV	Densité d'énergie volumétrique
DSC	Calorimétrie différentielle à balayage (Differential scanning calorimetry)
EBSD	Diffraction d'électrons rétrodiffusés (Electron backscatter diffraction)
EBM	Fusion par faisceau d'électrons (Electron beam melting)
EPMA	Microsonde de Castaing (Electron probe microanalysis)
FA	Fabrication additive
FDA	Agence fédérale américaine des produits alimentaires et médicamenteux (Food and drug administration)
FEA	Analyse par éléments finis (Finite element analysis)
FLLP	Fusion laser sur lit de poudre
LPBF	Laser powder bed fusion

PEEK	Polyétheréthercétone (Polyether Ether Ketone)
SMA	Shape memory alloy
SE	Superélasticité (Superelasticity)
SEM	Microscope à balayage électronique (Scanning electron microscope)
SME	Effet à mémoire de forme (Shape memory effect)
STL	Format de fichier stéréolithographique (Stereolithography)
TPMS	Surfaces minimales triplement périodiques (Triply periodic minimal surfaces)
VED	Volumetric energy density
XRD	Diffraction à rayons X (X-Ray diffraction)

LISTE DES SYMBOLES ET UNITÉS DE MESURE

A_s	Température de début de la transformation austénitique	°C
A_f	Température de fin de la transformation austénitique	°C
E	Module d'élasticité (Young)	GPa
S_y/σ_y	Limite d'élasticité, résistance en traction	MPa
M_s	Température de début de la transformation martensitique	°C
M_f	Température de fin de la transformation martensitique	°C
R_s	Température de début de la transformation en phase R	°C
R_f	Température de fin de la transformation en phase R	°C
B	Coefficient de Clausius-Claypeyron	MPa/K
σ	Contrainte mécanique	MPa
T	Température	K
ΔS	Variation d'entropie	J/K
V_o	Volume initial du cristal	m^3
$\Delta\varepsilon$	Variation de la déformation	mm/mm
DEV	Densité d'énergie volumétrique	J/mm^3
P	Puissance du laser	W
v	Vitesse de balayage du laser	mm/s
h	Distance entre les parcours	mm
t	Épaisseur des couches	mm
ρ	Masse volumique	g/cm^3
ρ_r	Densité relative	%
φ	Porosité	%

S	Surface	mm^2
V	Volume	mm^3
k	Perméabilité fluidique absolue	m^2
Q	Débit du fluide à travers l’échantillon	m^3/s
μ	Viscosité dynamique du fluide	Pa·s
A	Aire de section de l’échantillon	m^2
Δp	Différence de pression en aval et en amont de l’échantillon	Pa
L	Longueur de l’échantillon	m
R_e	Nombre de Reynolds	

INTRODUCTION

Au cours du dernier siècle, une croissance du nombre de personnes ayant des problèmes de dos a été identifiée, causée par un mode de vie sédentaire et l'augmentation de l'espérance de vie. En effet, l'Organisation Mondiale de la Santé rapporte que les douleurs de dos, plus particulièrement du bas du dos, sont la principale cause d'invalidité au monde, affectant plus de 600 millions de personnes en 2020, chiffre qui est prévu de monter à 840 millions d'ici 2050. L'instabilité de la colonne et la dégénérescence des disques intervertébraux peuvent causer des douleurs dues à la compression de la moelle épinière. Pour soulager des cas extrêmes de ces maladies, la fusion vertébrale est utilisée, où deux vertèbres adjacentes sont fusionnées à l'aide d'une greffe osseuse et de structures spécialisées comme les tiges de stabilisation et les cages intervertébrales. Ces dispositifs sont nécessaires pour assurer un espace intervertébral adéquat pour la croissance osseuse durant la période de guérison ainsi que pour stabiliser la colonne et éviter la compression de la moelle épinière. Certaines complications majeures de la fusion vertébrale ont été associées avec les cages : la perte de fixation, la migration, la subsidence et la défaillance en fatigue de l'implant (Michel Assad et al., 2003a). Une des solutions envisageables pour ces problèmes est l'utilisation de nouveaux matériaux comme les alliages à mémoire de forme (AMF) et l'intégration de structures architecturées dans le design des cages afin d'avoir une meilleure fusion avec les vertèbres.

Les AMF sont des matériaux pouvant avoir un comportement superélastique ou de mémoire de forme dépendamment des conditions d'utilisation (température et chargement). Sous l'effet d'un stimulus externe comme un changement de température ou l'application d'une contrainte, ces matériaux réagissent par des changements de forme qui sont réversibles. L'effet de mémoire de forme a été découvert en 1951 par Chang et Read dans un alliage d'or-cadmium. Toutefois ce sont les travaux de Buehler, Gilfrich, et Wiley (1963) portés sur un alliage de nickel-titane qui ont popularisé ces matériaux. Les applications des AMF sont limitées. Ils sont utilisés dans les actuateurs, les antennes, les systèmes de déploiement, les connecteurs d'assemblage, les implants dentaires et intra osseux, les instruments chirurgicaux, etc. Un contrôle important des techniques de mise en forme de ces alliages est nécessaire pour éviter la modification de la composition chimique du matériau puisque les propriétés fonctionnelles en sont directement dépendantes (Mwangi et al., 2019). Ceci sous-entend des coûts élevés du matériau. De plus, les AMF sont difficilement usinables à cause de leur grande ductilité (Weinert & Petzoldt, 2004) qui, couplée aux faibles rendements des techniques conventionnelles de mise en forme par soustraction, a pour effet une augmentation des coûts des produits finis et une utilisation limitée de ces matériaux.

Parmi les options disponibles pour la fabrication de cages intervertébrales, mentionnons les techniques émergentes de fabrication additive (FA), aussi connue sous le nom d'impression 3D. Il existe une vaste gamme de technologies de FA de métaux, permettant la production de composants de géométries complexes avec des ratios de mise au mille significativement plus avantageux que les techniques d'usinage conventionnelles. La fabrication additive des matériaux à mémoire de forme porte le nom d'impression 4D (Kuang et al., 2018; Lee, An, & Chua, 2017; J. Ma et al., 2017; Mitchell, Lafont, Hołyńska, & Semprimoschnig, 2018; Momeni, M.Mehdi Hassani.N, Liu, & Ni, 2017), la quatrième dimension se référant au changement de la forme en fonction du temps, après que le composant imprimé est soumis à un changement de température ou de contrainte. Il y a présentement un grand intérêt pour la FA d'AMF (Elahinia et al., 2016; Scherbakov & Shishkovsky, 2018). L'avantage principal de la FA est la possibilité de créer des structures complexes, comme les structures architecturées par exemple, qui sont très difficilement, voire impossible, à fabriquer par des moyens conventionnels. L'utilisation de structures cellulaires dans les cages intervertébrales donne la possibilité de fabriquer des pièces légères ayant des propriétés mécaniques élevées, mais aussi un comportement biomimétique grâce à la superélasticité des alliages à mémoire de forme. De plus, ces structures permettent l'ostéo-intégration qui facilite la fixation du dispositif aux os et favorise ainsi la fusion vertébrale.

0.1 Problématique

Les cages intervertébrales présentement utilisées pour les chirurgies de fusion vertébrale comportent des risques de complications majeures. Une des solutions potentielles est l’utilisation de dispositifs en AMF, intégrant des structures architecturées possédant le comportement mécanique biomimétique et favorisant l’ostéo-intégration. La sélection des structures appropriées, leurs propriétés mécaniques ainsi que la fabrication additive d’AMF sont des défis qui nécessitent d’être résolus.

0.2 Hypothèse de travail

L’utilisation de structures architecturées en AMF dans les cages intervertébrales entraine de meilleures performances en termes de transfert de charges et d’intégration osseuse. Les propriétés superélastiques des AMF à l’échelle microscopique et le comportement des structures architecturées à l’échelle macroscopique se complémentent de façon synergique pour diminuer les risques de défaillance de cages.

0.3 Objectifs de recherche

L'objectif principal du projet est de créer et de caractériser le comportement mécanique de structures architecturées en AMF produites par fabrication additive, en vue d’une éventuelle utilisation dans les cages intervertébrales. En premier lieu, l’alliage de titane conventionnel Ti-6Al-4V sera utilisé pour caractériser les structures cellulaires et servir en tant que cas de référence (benchmark). L’AMF choisi pour cette étude est un alliage de Ti-Ni. Les objectifs spécifiques sont :

- établir les requis de fonctionnement des cages intervertébrales
- concevoir et modéliser numériquement les structures architecturées;
- valider le choix des structures à l’aide de l’alliage classique Ti6Al4V;
- identifier les paramètres optimaux de fabrication du Ti-Ni et caractériser les propriétés mécaniques et la microstructure;
- fabriquer et tester expérimentalement les structures architecturées en Ti-Ni.

Il est à noter qu’aucune cage intervertébrale ne sera fabriquée ou testée dans le cadre de ce travail, et seulement les structures architecturées seront analysées.

CHAPITRE 1

REVUE DE LA LITTÉRATURE

Ce chapitre présente tout d'abord une mise en contexte sur les problématiques de douleur de dos et les traitements présentement disponibles ainsi que leurs limitations. Ensuite, la revue de la littérature fera un survol des principes théoriques et des avancements récents dans les domaines des alliages à mémoire de forme, de la fabrication additive et des structures architecturées. Cette revue servira de base pour le développement et le déroulement des travaux proposés dans ce projet.

1.1 Cages intervertébrales

1.1.1 Colonne vertébrale

La colonne vertébrale joue un rôle vital de support et de protection du corps et elle est composée de trois types d'éléments : les vertèbres, les disques intervertébraux et la moelle épinière. La colonne est divisée en trois sections principales comptant 5 à 12 vertèbres comme illustré à la Figure 1.1a. Chaque section possède une courbure naturelle intitulée lordose (niveau cervical et lombaire) ou cyphose (niveau thoracique et sacré) qui permettent une plus grande flexibilité et mouvement. Les disques intervertébraux servent à amortir les chocs et à augmenter la mobilité de la colonne. Ceux-ci sont composés de deux zones : le nucleus mou au centre qui absorbe les chocs et l'annulus rigide en périphérie qui sert à contenir le nucleus (Figure 1.1b). Lorsqu'il existe des problèmes de stabilité de la colonne telle que la scoliose ou l'hyperlordose ou bien si le patient souffre de discopathie dégénérative, les disques sont déformés (hernie discale) résultant en inflammation et douleur. Dans des cas plus graves, le nucleus peut être expulsé de l'espace intradiscal, appliquant une pression sur la moelle épinière et causant des engourdissements et douleurs extrêmes. 95% des hernies discales se produisent dans la partie lombaire (L4-L5 ou L5-S1), car les charges transmises dans la section lombaire sont plus importantes et généralement au niveau postérolatéral, car le ligament longitudinal postérieur est plus fort que celui antérieur (Moore, Dalley, & Agur, 2013).

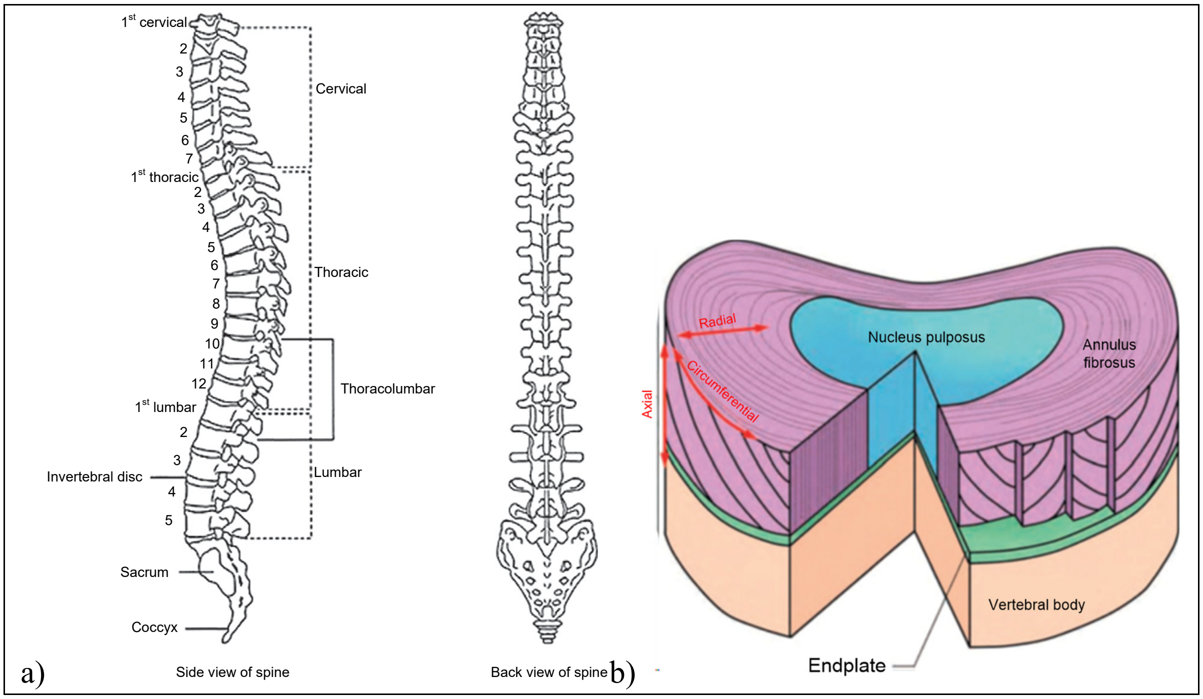
1st cervical
2
3
4
5
6
7
1st thoracic
2
3
4
5
6
7
8
9
10
11
12
1st lumbar
2
3
4
5
Invertebral disc
Sacrum
Coccyx
Cervical
Thoracic
Thoracolumbar
Lumbar
a)
Side view of spine
Back view of spine
b)
Radial
Circumferential
Axial
Nucleus pulposus
Annulus fibrosus
Vertebral body
Endplate

Figure 1.1 a) représentation schématique d’une colonne vertébrale;
b) schéma d’un disque intervertébral
Tiré de Friis, Arnold, et Goel (2017)

1.1.2 Traitements disponibles

Les traitements prioritaires pour ce type de maladies sont la physiothérapie et l’exercice physique, toutefois, dans certains cas, il est nécessaire d’avoir recours à une intervention chirurgicale appelée fusion vertébrale. Cette opération implique la résection d’une partie, ou de la totalité, du disque dégénéré et son remplacement par une greffe osseuse ainsi que l’utilisation des dispositifs de fixation, comme les cages intervertébrales et les tiges de stabilisation. Avec le temps, une croissance osseuse a lieu dans l’espace intradiscal occupé par la cage et la greffe, résultant en une fusion des deux vertèbres. Plusieurs techniques de fusion vertébrale existent pour chaque niveau de la colonne vertébrale. Au niveau lombaire, les approches les plus courantes sont la fusion intervertébrale lombaire antérieure (ALIF), postérieure (PLIF), transforaminale (TLIF) et transpsoas ou latérale (LLIF, DLIF ou XLIF). La différence entre ces techniques réside dans le type de cage généralement utilisé, le niveau d'invasion ainsi que la complexité de la chirurgie (Figure 1.2).

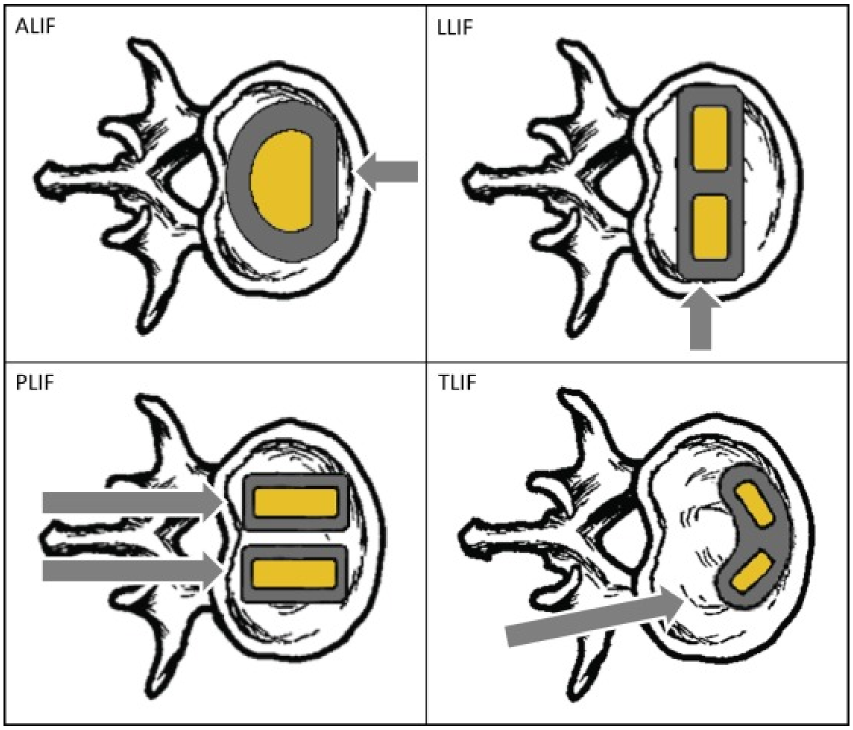

Figure 1.2 Techniques courantes de chirurgie de fusion vertébrale
Tiré de Peck et al. (2018)

1.1.3 Types de cages intervertébrales existantes

Un grand nombre de fabricants de cages intervertébrales existe, offrant plusieurs types de dispositifs (Figure 1.3). Les cages peuvent être classifiées par leur matériau (généralement titane ou PEEK) ou par la forme (cylindrique filetée, rectangulaire crantée (box ou bullet shape), semi-circulaire (kidney shape)).

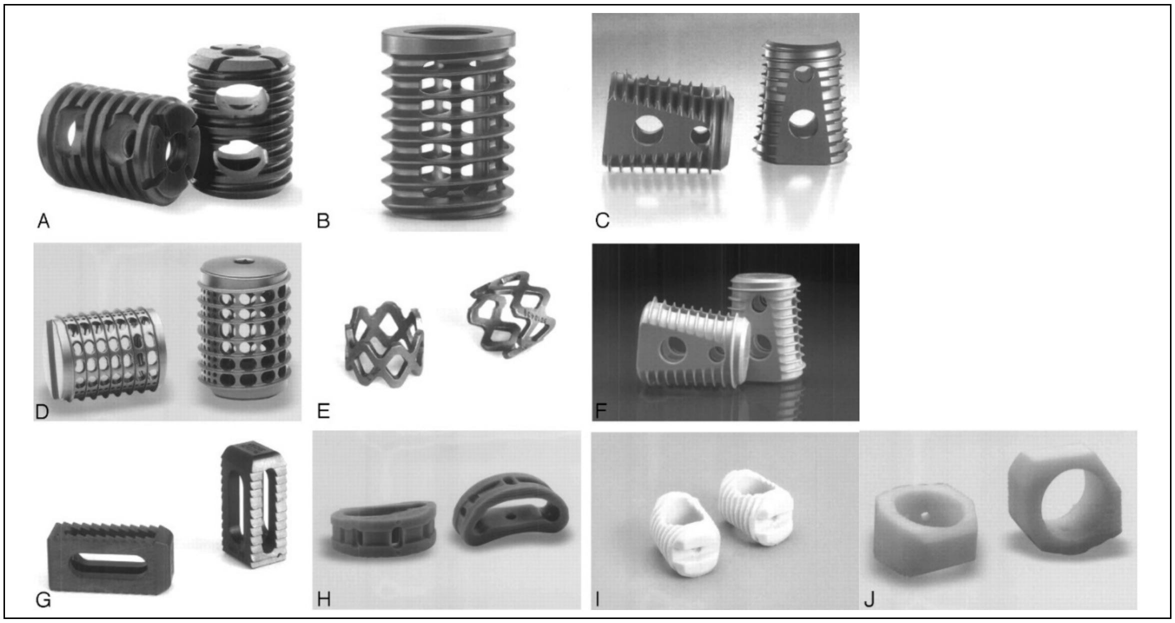

Figure 1.3 Types de cages intervertébrales A, BAK cage (Zimmer Spine). B, Ray Threaded Fusion Cage (Stryker Spine). C, LT-CAGE. D, INTER FIX device (Medtronic Sofamor Danek). E, Harms cage (DePuy Spine). F, PEEK cage (Medtronic Sofamor Danek). G, JAGUAR I/F CAGE (Brantigan Device; DePuy Spine). H, BOOMERANG. I, Bone Dowel. J, Femoral Ring (H–J Medtronic Sofamor Danek)
Tiré de Williams, Gornet, et Burkus (2005)

Ces types de cages, que l'on peut dénommer conventionnelles, ont fait objet de plusieurs études rétrospectives afin d'en évaluer les performances et les risques de complications. Les problèmes principaux liés à l'utilisation des cages sont la migration de la cage définie comme un déplacement dans le plan horizontal, la subsidence définie comme un enfoncement ou affaissement dans la vertèbre ou la rétropulsion qui est une migration dans le canal rachidien. Ces complications ont des taux d'occurrence variant entre 1.9% (Park et al., 2019) et 30% (Abbushi, Čabraja, Thomale, Woiciechowsky, & Kroppenstedt, 2009). La grande variation est due à un nombre important de variables comme le type et matériau des cages, la technique chirurgicale employée et les aptitudes du chirurgien parmi tant d'autres. Malgré cela, les causes présumées principales de ces problématiques sont une rigidité trop importante des cages en titane et une adhésion inadéquate des cages en PEEK. Néanmoins, dans le but de réduire au maximum les lacunes des cages conventionnelles, un certain nombre de travaux de recherche portant sur la fabrication additive de cages a été réalisé dans les derniers 10 ans (Tableau 1.1). La majorité de ces recherches utilisent l'alliage de titane grade 5 et exploitent l'aspect de personnalisation de la cage ou l'intégration de structures architecturées pour améliorer la fixation de la cage. Les résultats démontrent que ces cages offrent de meilleurs taux de fixation (Chung, Lee, Kwon, & Kang, 2017), une chirurgie simplifiée (Mobbs et al., 2019; Siu, Rogers, Lin, Thompson, & Owbridge, 2018; Spetzger, Frasca, & König, 2016) ainsi que des propriétés mécaniques adéquates (La Rosa, Clienti, & Mineo, 2018).

Tableau 1.1 Survol des travaux portant sur la FA des cages intervertébrales

Étude	Type de cage	Forme	Matériau	Technique de FA
Chung et al. (2017)		Rectangulaire (bullet) poreuse	Ti6Al4V	Electron beam melting (EBM)
La Rosa et al. (2018)		Rectangulaire modifiée poreuse	Ti6Al4V	EBM
Mobbs et al. (2019)		Personnalisée	Ti6Al4V	Direct metal laser sintering (DMLS)
Siu et al. (2018)		Personnalisée	Ti6Al4V	EBM
Spetzger et al. (2016)		Personnalisée poreuse	Ti6Al4V	Direct metal printing (DMP)

Il existe également des études sur l'utilisation de cages intervertébrales poreuses fabriquées par synthèse par combustion à partir d'un alliage à mémoire de forme, le Ti-Ni sous forme de mousse (Figure 1.4). En effet, M Assad et al. (2003b); Michel Assad et al. (2003a) ont investigué les propriétés d'ostéo-intégration, de résistance à la corrosion et le taux de libération du nickel, un élément nocif pour la santé, de telles cages implantées dans des moutons. La porosité a permis une ostéo-intégration et une fixation de l'os supérieure à une cage cylindrique conventionnelle. De plus, le taux de nickel dans le sang et dans les organes était équivalent dans les moutons de contrôle et dans les moutons avec les cages en Ti-Ni. L'analyse de la surface de la cage en AMF n'a pas identifié de traces de corrosion, indiquant une résistance adéquate.

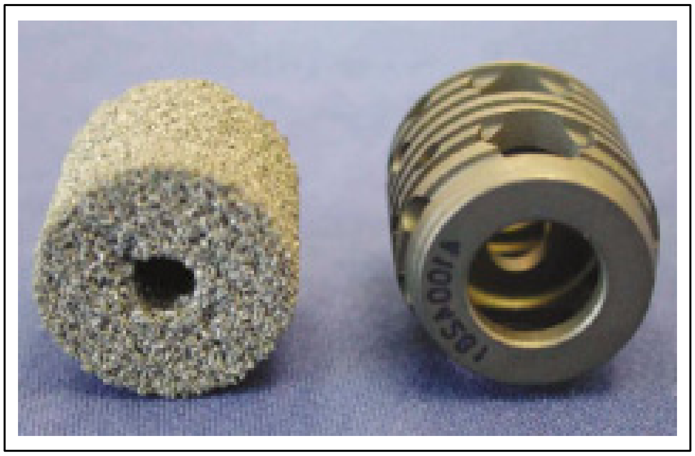

Figure 1.4 Cage intervertébrale en Ti-Ni poreux et
en TiAlV conventionnel
Tiré de M Assad et al. (2003b)

Aihara, Zider, Fanton, et Duerig (2019) ont aussi utilisé la synthèse par combustion pour produire des cages intervertébrales poreuses en Ti-Ni (Figure 1.5). Un module d'élasticité semblable à celui de l'os a été atteint (1 GPa), promettant un partage équivalent de la charge entre l'os et l'implant. L'implantation de cette cage dans un mouton a démontré l'ostéo-intégration à travers la cage en moins de 4 mois. Une analyse du taux de nickel dans le sang n'a pas indiqué d'augmentation ou diminution significative 6 mois après l'implantation de la cage.

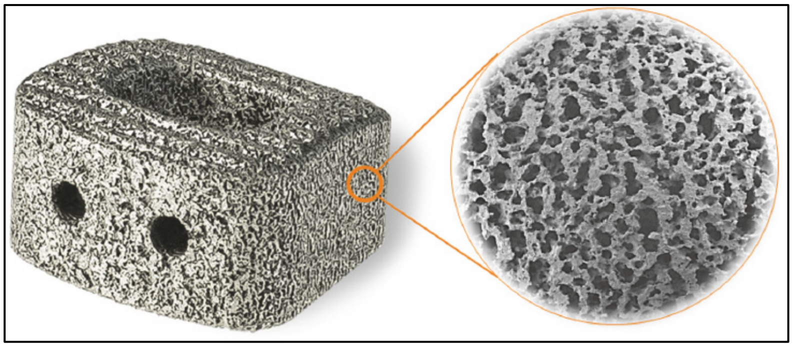

Figure 1.5 Cage intervertébrale poreuse en Ti-Ni fabriquée
par synthèse de combustion
Tiré de Aihara et al. (2019)

1.2 Alliages à mémoire de forme

Comme indiqué précédemment, les AMF font partie d'une catégorie de matériaux possédant des propriétés nommées fonctionnelles, qui incluent l'effet de mémoire de forme (shape memory effect (SME)) et la superélasticité (SE). Ces propriétés proviennent de la transformation martensitique, qui est un changement de la microstructure du matériau suite à une variation de la température ou à l'application d'une contrainte mécanique. Les AMF ont généralement deux phases stables : la martensite à basse température et l'austénite à haute température. Lorsque le matériau est chauffé ou refroidi, il y a changement d'une phase vers l'autre. Si le matériau est chauffé suite à l'application de certaines déformations plastiques, il passe de la martensite à l'austénite, lui permettant de retrouver sa forme initiale (Figure 1.6).

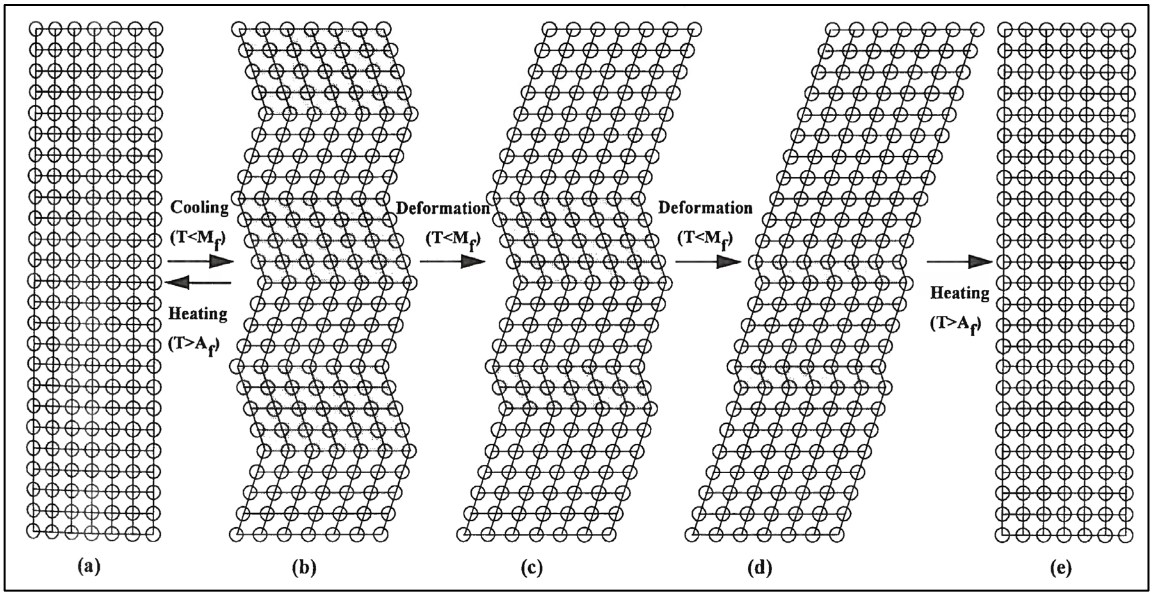

Figure 1.6 Schéma de modifications de la structure cristalline des alliages à mémoire de forme
Tirée de Otsuka et Wayman (1999)

Comme il peut être déduit, les températures de transformation entre ces deux phases sont critiques pour le comportement du matériau. L’équation de Clausius-Clapeyron sert à relier la température et la pression pour déterminer les courbes de changement de phase d’un matériau. Elle peut être adaptée pour les AMF, permettant de déterminer la température de changement de phase en relation avec la contrainte appliquée sur le matériau (Brailovski, Prokoshkin, Terriault, & Trochu, 2003).

$$\beta = \frac{d\sigma}{dT} = \frac{\Delta S}{V_o * \Delta \varepsilon} \tag{1.1}$$

Le facteur β représente le coefficient de Clausius-Claypeyron, σ la contrainte mécanique, T la température, ΔS la variation d’entropie, V_o le volume initial du cristal et $\Delta\varepsilon$ la variation de la déformation. En utilisant cette équation, les températures de changement de phase peuvent être tracées sur un graphique contrainte-température comme illustré à la Figure 1.7.

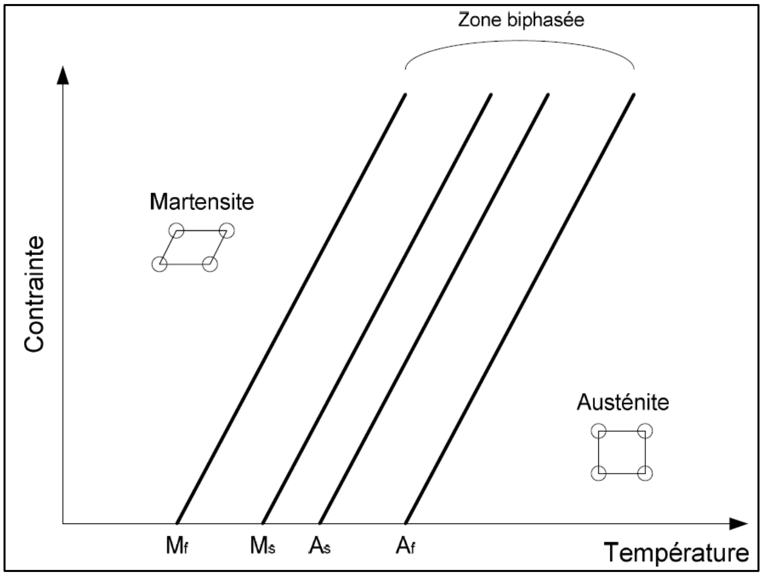

Figure 1.7 Diagramme d’état de phase d’un AMF
Tirée et adaptée de Brailovski et al. (2003)

Cette représentation sert à définir les températures de début et de fin de la transformation martensitique lors du refroidissement (Ms et Mf) ainsi que les températures de début et fin de la transformation austénitique lors du chauffage (As et Af) et ce, en fonction de la contrainte appliquée. À noter qu’en bas de la température Mf, le matériau a une structure martensitique et en haut de la température Af, la structure est austénitique. De plus, il peut être remarqué qu’il peut y avoir un changement de phases à température constante en appliquant une contrainte sur le matériau.

Par définition, la transformation martensitique est dite displacive et sans diffusion. Cela veut dire que pendant la transformation de phase, les déplacements des atomes sont très faibles, plus petits que les distances interatomiques, ce qui permet aux atomes de garder leurs positions relatives dans le réseau. Le changement d’une phase à l’autre a lieu par le cisaillement de la structure cristalline. La Figure 1.8 montre la transformation des mailles élémentaires d’un certain AMF d’une structure austénitique cubique face centrée à de la martensite qui est tétragonale centrée. Ce changement est accompagné par un rétrécissement dans deux directions et une élongation dans la troisième.

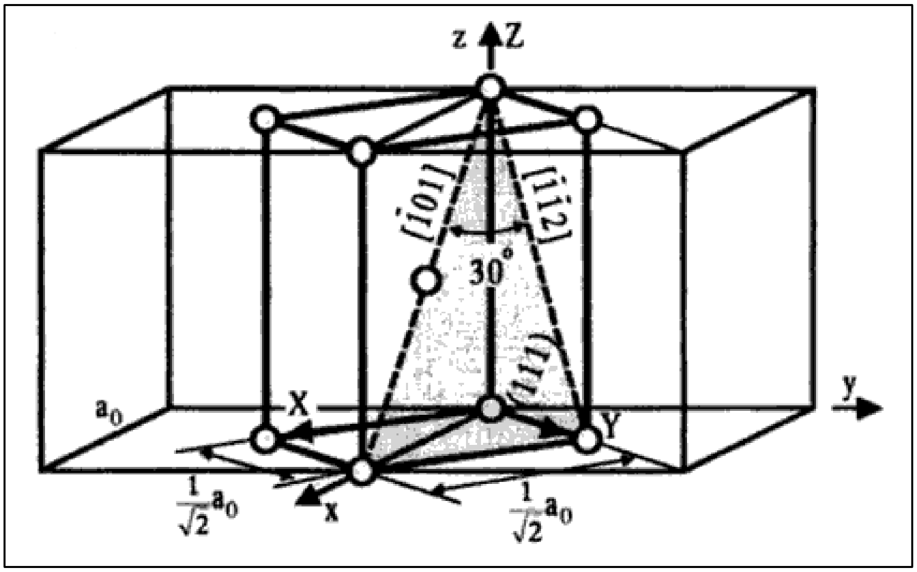

Figure 1.8 Transformation des mailles élémentaires pour un AMF de l’austénite cubique face centrée à la martensite tétragonale centrée
Tiré de Otsuka et Wayman (1999)

La transformation martensitique engendre alors une déformation homogène de la structure cristalline qui n’est pas toujours évidente à l’échelle macroscopique du matériau. Ceci s’explique par la formation de macles lors de la déformation du réseau pendant la transformation directe de l’austénite vers la martensite. Les macles offrent la possibilité à la phase martensitique de s’adapter dans l’espace disponible pour créer des plaquettes de martensite orientées de manière totalement aléatoire comme illustré à la Figure 1.9. C’est ce qu’on appelle de la martensite autoaccommodante. Lorsque le matériau est chauffé, il y a retour à la phase austénitique et les macles disparaissent. La Figure 1.10 permet d’illustrer les différentes transformations à l’échelle atomique.

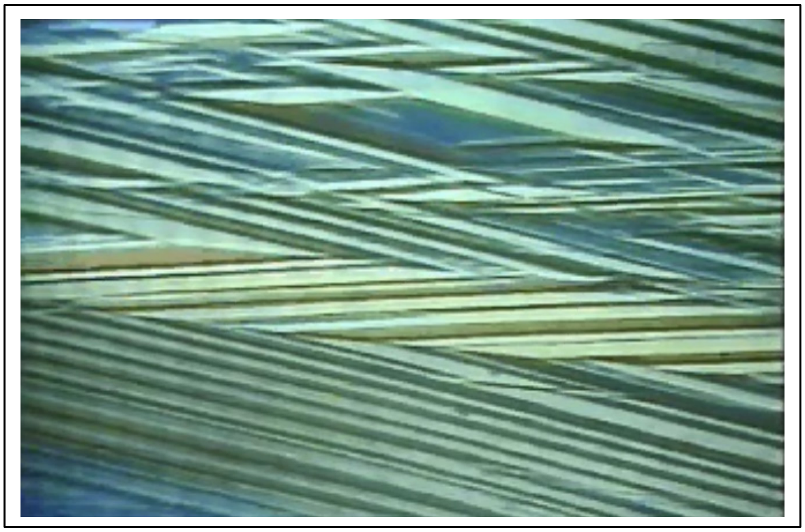

Figure 1.9 Exemple de macles formées pendant la transformation martensitique
Tiré de reportage TV5

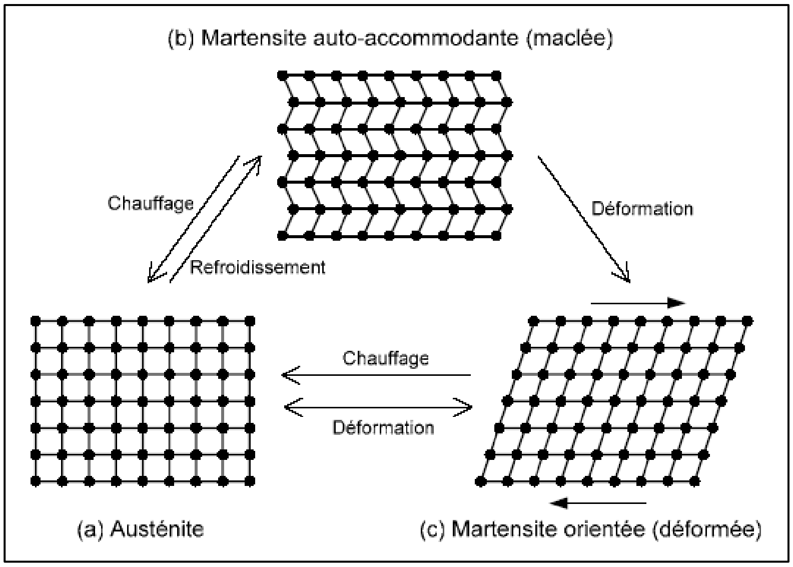
(b) Martensite auto-accommodante (maclée)
Chauffage
Refroidissement
Déformation
Chauffage
Déformation
(a) Austénite
(c) Martensite orientée (déformée)

Figure 1.10 Représentation schématique de la transformation martensitique à l'échelle atomique
Tirée et adaptée de Brailovski et al. (2003)

À partir d'un arrangement complètement austénitique, lors du refroidissement sans contrainte appliquée, il y a apparition de la martensite autoaccommodante (ou maclée) (Figure 1.10a → b). Généralement, il n'y a pas de déformation à l'échelle macroscopique grâce aux déplacements très petits impliqués. Cette transformation est totalement réversible, car, en chauffant la martensite autoaccommodante, celle-ci se transformera en phase austénitique (Figure 1.10b → a). Partant de la martensite maclée, en appliquant une contrainte sur le matériau, une déformation macroscopique est engendrée, causant une orientation préférentielle des aiguilles de martensite selon la direction de la contrainte (Figure 1.10b → c). C'est ce qu'on appelle de la martensite orientée (ou déformée). Si cette martensite orientée est chauffée à une température au-delà de Af, il y aura une transformation en phase austénitique, qui résulterait dans un retour du matériau à sa forme initiale (Figure 1.10c → a). L'application d'une contrainte mécanique assez importante sur la phase austénitique entraînera sa transformation en de la martensite déformée (Figure 1.10a → c).

Ayant effectué un survol des principes fondamentaux des transformations et de la déformation des AMF, il est maintenant possible d'explorer les propriétés fonctionnelles de mémoire de forme et de superélasticité.

1.2.1 Effet mémoire de forme

La Figure 1.11 permet de suivre le cycle thermomécanique (A-B-C-D-E) durant lequel l'effet de mémoire de forme simple sens peut être observé. Tel que mentionné à la section précédente, lorsque le matériau est refroidi d'une température T2 (état austénitique) à T1 (état martensitique) sous contrainte nulle, la structure se transforme de l'austénite en martensite maclée avec des plaquettes orientées de façon aléatoire (A→B). Lorsque le matériau est mis sous contrainte σ_1 (B→C), il y a une déformation macroscopique causée par les plaquettes de martensite qui s'orientent dans la direction d'application du chargement à contrainte constante (C→D). Lorsque la contrainte est relâchée, cette déformation ainsi que l'orientation de la martensite restent inchangées à l'exception d'un léger retour élastique (D→E). À ce stade, le matériau peut être chauffé à la température T2 supérieure à Af, permettant un retour à la phase austénitique et donc à la forme initiale du matériau (E→A). Ce processus peut alors être répété.

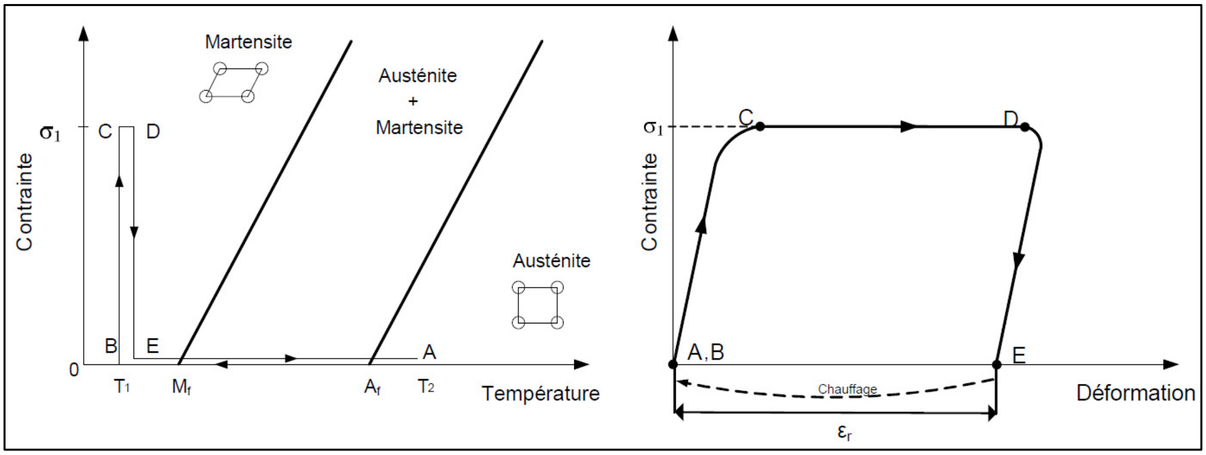

Figure 1.11 Graphiques contrainte-température et contrainte-déformation
représentant l'effet de mémoire de forme
Tirée et adaptée de Brailovski et al. (2003)

Afin d'imposer une géométrie particulière à un composant et observer l'effet de mémoire de forme avec cette géométrie donnée, il est nécessaire d'effectuer un traitement thermique dit d'entrainement. Il s'agit de déformer la pièce à la forme voulue et de la chauffer pendant un certain temps sous cette condition. Suite au refroidissement, la forme est imprégnée dans la mémoire du matériau comme forme de base. Le traitement thermique dépend de l'alliage utilisé en termes de température et durée de maintien.

1.2.2 Effet superélastique

De façon similaire, la Figure 1.12 illustre un cycle thermomécanique de l'effet superélastique. Cet effet est observable à une température constante sous l'application et le relâchement d'une contrainte mécanique. À partir d'une structure austénitique (A), une contrainte est imposée au matériau, résultant en la transformation martensitique en raison d'avoir passé par Ms et Mf (A→B→C). La phase résultante est de la martensite orientée comme mentionnée précédemment. Lorsque la contrainte est relâchée, le matériau traverse les points As et Af, retournant à la phase d'équilibre austénitique (C→D→E). Sur le graphique contrainte-déformation, il est possible de voir la transformation en martensite (B→C) et le retour en austénite (D→E) marqués par des plateaux appelés superélastiques.

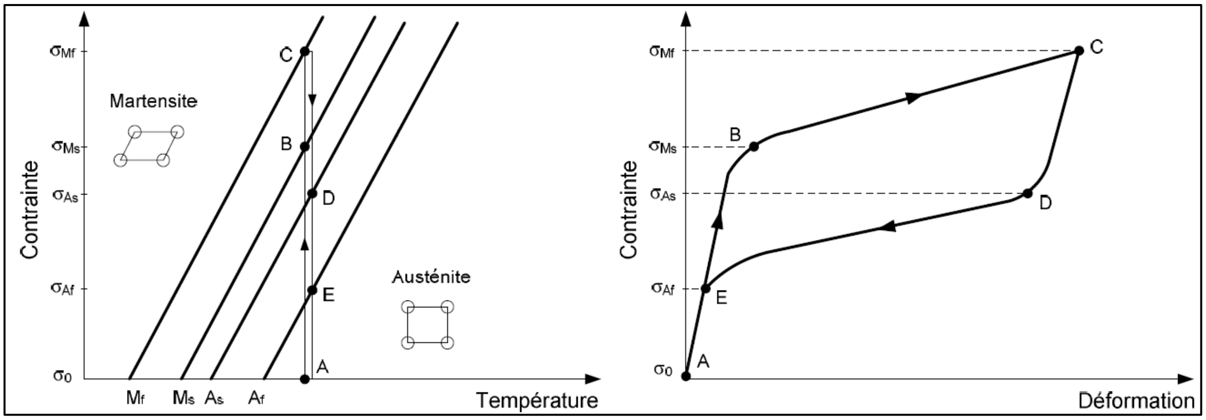
σMf
σMs
σAs
σAf
σ0
Contrainte
Martensite
Austénite
C
B
D
E
A
Mf
Ms
As
Af
Température
σMf
σMs
σAs
σAf
σ0
Contrainte
C
B
D
E
A
Déformation

Figure 1.12 Graphiques contrainte-température et contrainte-déformation représentant l’effet superélastique
Tirée et adaptée de Brailovski et al. (2003)

Comme indiqué précédemment, l’effet superélastique est observable lorsque la température d’utilisation du matériau est supérieure à la température de fin d’austénitisation Af. Afin d’avoir l’effet superélastique à température ambiante, il est nécessaire d’ajuster les températures de transformation. Dans certains cas, il est possible d’ajuster ces températures en modifiant la composition chimique de l’alliage. Comme illustré à la Figure 1.13, dans les alliages de Ti-Ni, une augmentation de 0.1% de la teneur en nickel a comme effet la diminution des températures de transformation d’environ 10 °C (Brailovski et al., 2003; Mitchell et al., 2018).

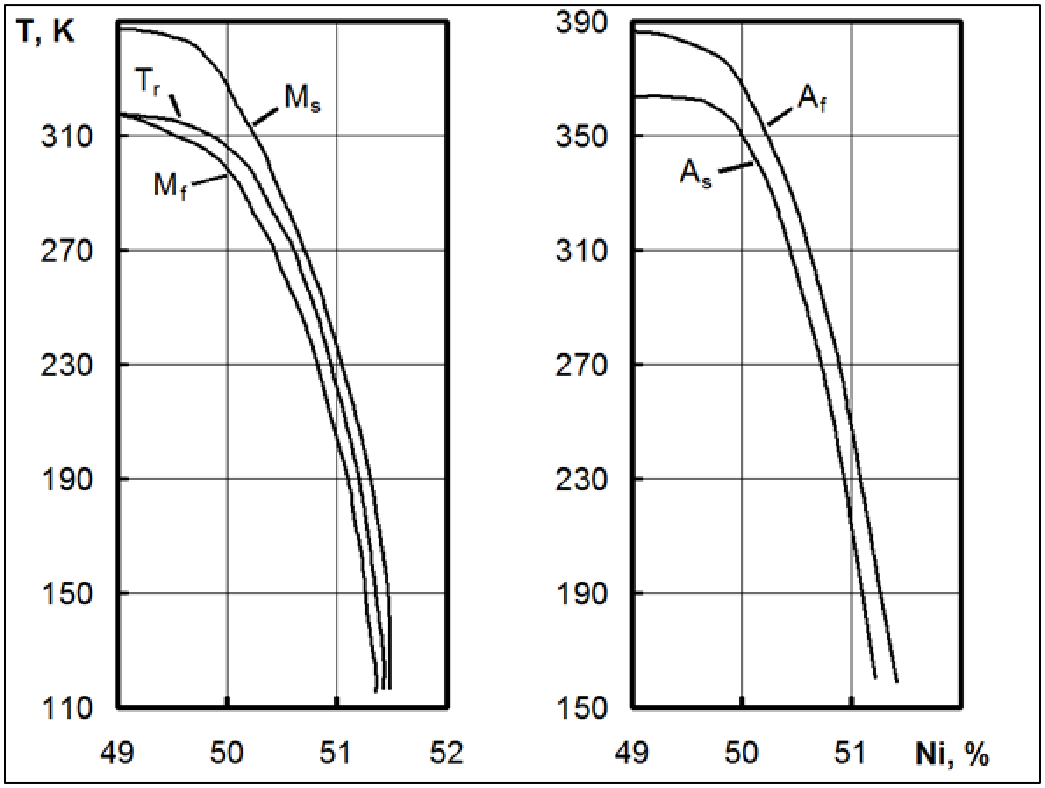

Figure 1.13 Variation des températures de transformation de phases des alliages Ti-Ni en fonction du taux de nickel en %at
Tiré de Brailovski et al. (2003)

La Figure 1.14 illustre les contraintes critiques en fonction de la température pouvant être appliquées à un alliage de nitinol afin d'avoir les effets de superélasticité et de mémoire de forme. En dépassant ces contraintes, il y a risque d'induire des déformations permanentes au matériau. Pour chaque plage de températures d'utilisation le comportement mécanique du matériau peut être observé. Dans la zone de martensite stable, c'est l'effet de mémoire de forme qui est prédominant. Dans la zone d'austénite stable, ce n'est qu'à partir de Af qu'il y a manifestation de la superélasticité pure. Entre As et Af il y a une combinaison de superélasticité et de mémoire de forme. À noter que plus l'écart entre la température de déformation et la Af est important, plus la contrainte critique pouvant être appliquée est importante. Ceci a une limite qui est la température M_s^σ à partir de laquelle il devient plus facile pour le réseau cristallin de glisser que de se transformer en martensite.

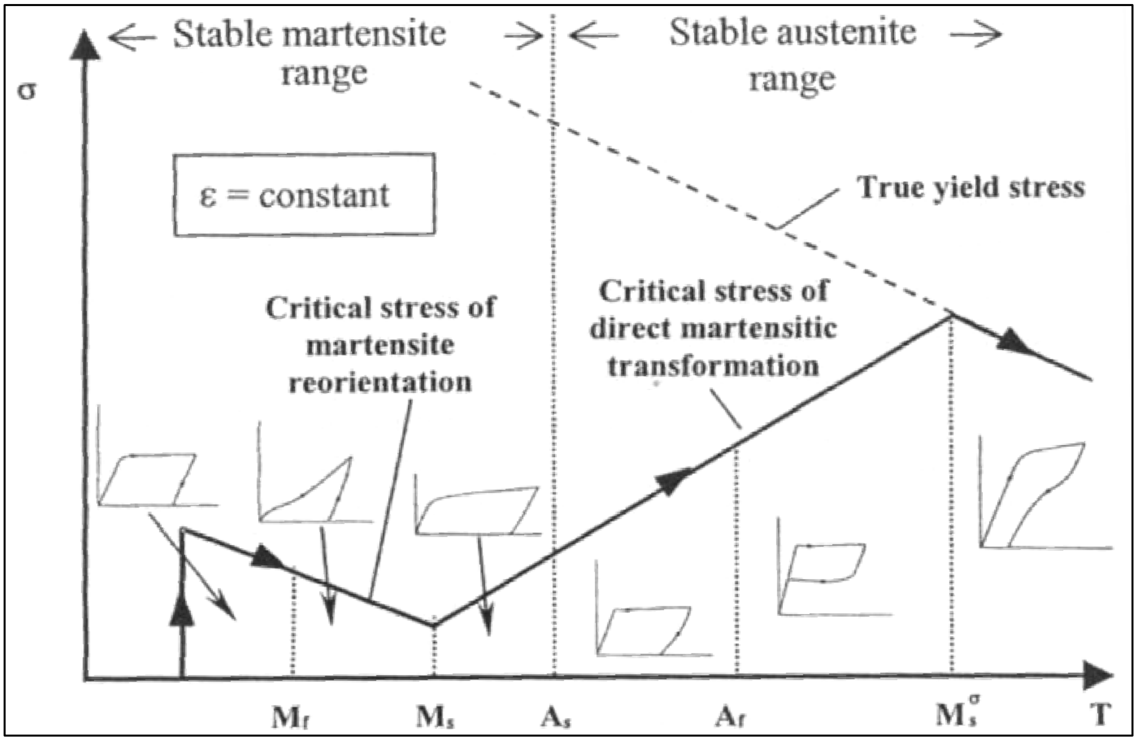

Figure 1.14 Comportement mécanique d'un alliage Ti-Ni en fonction de la température d'opération
Tirée de Brailovski et al. (2003)

1.3 Fabrication additive

La FA métallique est un ensemble des technologies ayant été développées dans les années 1980. Elle est relativement récente lorsque comparée aux techniques conventionnelles de fabrication de pièces qui sont pratiquées depuis des millénaires. C’est une méthode de production de composants en ajoutant la matière de façon itérative, couche par couche. Une multitude de techniques existent pouvant être applicables aux métaux. Avec l’expiration récente des brevets pour certaines technologies, on peut s’attendre à une croissance importante de la mise au marché de divers appareils utilisant des techniques différentes (Mitchell et al., 2018). L’avantage principal de la fabrication additive est la possibilité de fabriquer des structures très complexes, difficilement reproductibles par des moyens conventionnels de mise en forme. Puisque cette technologie fonctionne par ajout de matière sans outillage, l’autre avantage est une utilisation minimale de matériau.

1.3.1 Procédés courants de FA de métaux

Les procédés les plus répandus sont : la fusion sur lit de poudre que ce soit par faisceau d'électrons (electron beam melting EBM) ou par faisceau laser (laser powder bed fusion LPBF), l'ajout de matière par dépôt d'énergie (directed energy deposition DED) et la consolidation de poudre par jet de liant (binder jetting BJ) (Figure 1.15). Un critère que ces quatre technologies ont en commun est l'utilisation du matériau de base sous forme de poudre. La méthode de consolidation de cette poudre est toutefois différente : pour l'EBM et le LBPF la poudre est fusionnée localement sur le lit de poudre, le DED utilise un laser sous lequel la poudre est projetée et fusionnée et la technique de jet de liant utilise une tête d'imprimante pour projeter une colle qui lie les particules ensemble. Cette dernière technique nécessite plusieurs post-traitements pour se débarrasser du liant et arriver à un composant totalement dense.

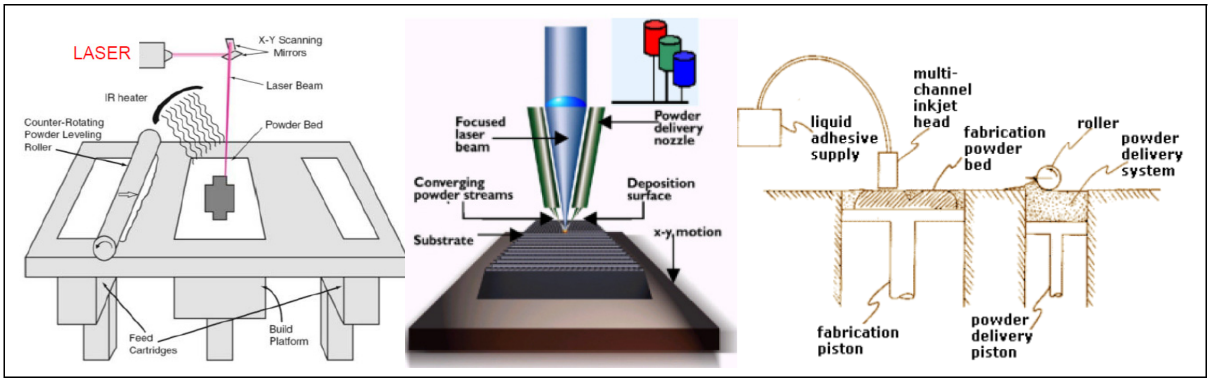
LASER
X-Y Scanning Mirrors
Laser Beam
IR heater
Counter-Rotating Powder Leveling Roller
Powder Bed
Feed Cartridges
Build Platform
Focused laser beam
Powder delivery nozzle
Converging powder streams
Deposition surface
Substrate
x-y motion
multi-channel inkjet head
liquid adhesive supply
fabrication powder bed
roller
powder delivery system
fabrication piston
powder delivery piston

Figure 1.15 Techniques de FA. Gauche : fusion laser sur lit de poudre, centre : dépôt sous énergie et droite : consolidation de poudre par jet de liant
Tiré du recueil SYS867 Brailovski (2017)

Chacune de ces technologies a ses avantages et ses limitations, toutefois la technologie LPBF est la plus adaptée pour la production de composants ayant des taux de porosités faibles, une précision relativement élevée et des propriétés mécaniques comparables aux méthodes conventionnelles de fabrication (Wong & Hernandez, 2012). Les systèmes LPBF sont généralement séparés en trois zones principales : la zone de distribution de poudre où la matière première est initialement chargée, la zone de fabrication où la plaque de fabrication est installée et le laser effectue son parcours, et la zone de récupération de poudre de surplus. Un système mécanique tel qu'un racleur ou un rouleau se déplace à travers les trois zones afin d'étaler les couches de poudre dans la zone de fabrication. Pour éviter l'oxydation de l'alliage lors de la fusion, l'environnement de fabrication est rempli d'un gaz inerte comme l'argon. Afin de fusionner la poudre, il y a divers paramètres qui doivent être contrôlés tels que la puissance du laser, sa vitesse de balayage, la distance entre les parcours du laser et l'épaisseur de la couche de poudre (Letenneur, Brailovski, Kreitcberg, Paserin, & Bailon-Poujol, 2017). La combinaison de ces paramètres donne la densité d'énergie volumétrique (DEV) transmise au lit de poudre. La formule suivante permet de calculer cette densité d'énergie en J/mm^3. P est la puissance (W), v est la vitesse de balayage (mm/s), h est la distance entre les parcours (mm) et t est l'épaisseur des couches (mm).

$$DEV = \frac{P}{v * h * t} \tag{1.2}$$

Chaque alliage requiert des paramètres différents en raison des différences des propriétés physiques comme la température de fusion, la conductivité et la dilatation thermique, l'absorptivité du laser, etc.

1.3.2 Fabrication additive d'alliages à mémoire de forme

La fabrication additive d'alliages à mémoire de forme est un sujet datant des années 2000, avec l'alliage principalement utilisé étant le Ti-Ni (Van Humbeeck, 2018). Toutefois, certains travaux portent sur d'autres alliages tel que le CuAlNi (Scherbakov & Shishkovsky, 2018) et le TiZrNb (Kreitcberg, Brailovski, & Prokoshkin, 2018). Comme mentionné précédemment diverses technologies de FA sont employées toutefois la plus utilisée est la fusion laser sur lit de poudre (Elahinia et al., 2016; Khoo et al., 2018).

Plusieurs tentatives de fabrication du Ti-Ni par fusion laser sur lit de poudre sont documentées dans la littérature, avec divers niveaux de réussite (Chekotu, Groarke, O'Toole, & Brabazon, 2019; Elahinia et al., 2016; Y. Zhang et al., 2021). Le défi principal dans ces efforts est la sélection de paramètres d'impression permettant la création de composants sans défauts tout en évitant une évaporation excessive du nickel de l'alliage (Bassani, Fiocchi, Tuissi, & Biffi, 2023; Biffi, Fiocchi, Valenza, Bassani, & Tuissi, 2020; Borisov, Starikov, Popovich, & Tihonovskaya, 2021; Chmielewska et al., 2021; Leon, Singamneni, Guraya, & Chen, 2023; Mahmoudi et al., 2018). Ce dernier point est particulièrement important car, tel qu'indiqué précédemment, les propriétés de mémoire de forme et de superélasticité du Ti-Ni dépendent fortement de la composition chimique du matériau (Brailovski et al., 2003). Comme illustré à la Figure 1.16, un problème majeur est la fissuration des spécimens lors de la fabrication, engendrée par les gradients thermiques importants (Mahmoudi et al., 2018; Xue et al., 2022; Zhao, Liang, Luo, Yang, & Wang, 2020). Pour y remédier, des pistes de solution incluent le chauffage de la plaque de fabrication et l'utilisation de supports de fabrication spécifiques (McCue et al., 2019; Qiu et al., 2020; Q. Zhang et al., 2020)

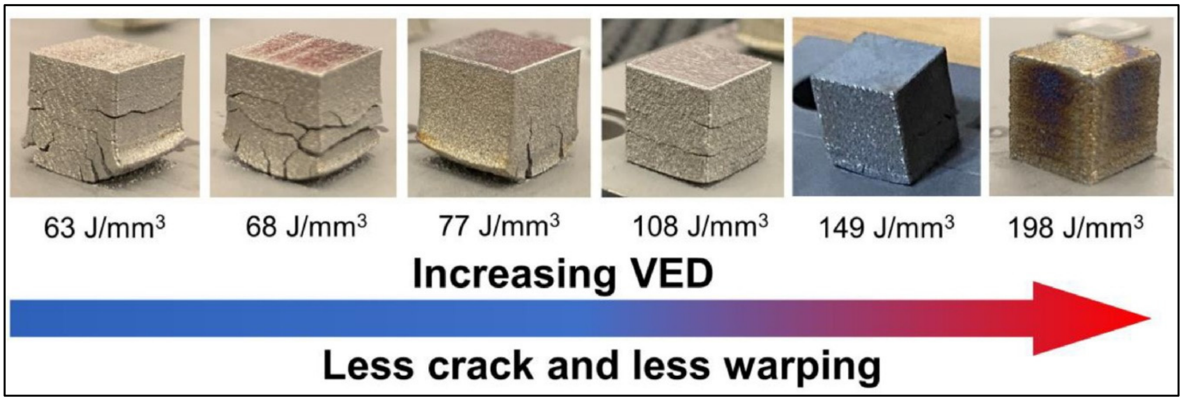

Figure 1.16 Spécimens en Ti-Ni imprimés avec divers paramètres de fabrication
Tiré de Xue et al. (2022)

Dans le cas où la fabrication du Ti-Ni est réussie sans défauts majeurs, les propriétés fonctionnelles peuvent ne pas correspondre aux attentes, comme était le cas de H. Lu et al. (2022) qui n'ont pas réussi à obtenir la superélasticité en raison de l'évaporation du nickel et des contraintes résiduelles élevées dans le matériau (Figure 1.17a). Néanmoins, certains travaux, comme ceux de Moghaddam et al. (2019) ont abouti en un comportement superélastique en compression tel qu'illustré à la Figure 1.17b. Pour ce faire, un alliage riche en nickel a été utilisé, et les conditions et paramètres de fabrication ont été optimisés.

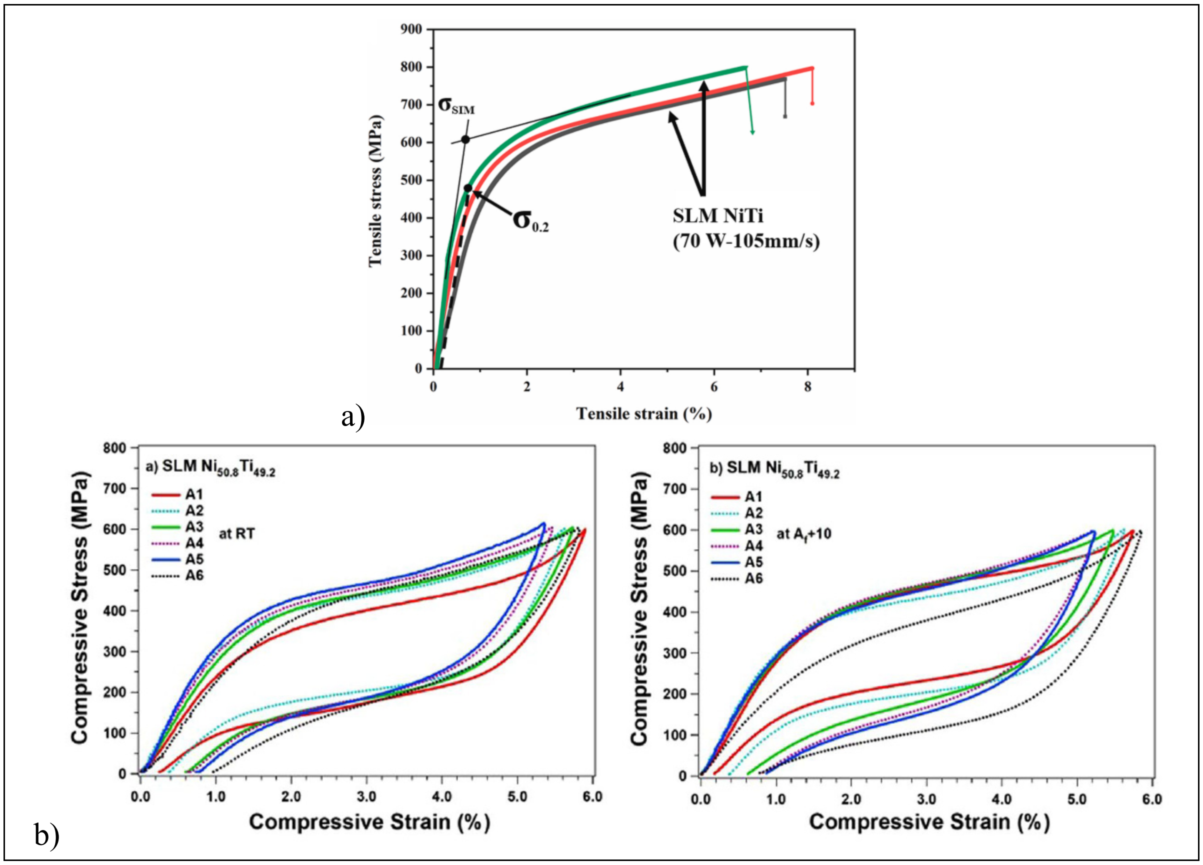

Figure 1.17 a) Comportement en traction de Ti-Ni imprimé par LPBF ne démontrant pas de superélasticité, b) Courbes contrainte-déformation de Ti-Ni imprimé avec le comportement superélastique en compression
Tirés de a) H. Lu et al. (2022) et b) Moghaddam et al. (2019)

1.4 Structures architecturées

Les structures architecturées, aussi appelées matériaux cellulaires poreux, sont essentiellement composées de matière solide sous forme de membrures ou feuilles interreliées et de vides sous forme de pores. Ces matériaux sont constitués de répétitions d'une maille élémentaire. L'avantage de telles structures est la résistance offerte par rapport à leur masse, ce ratio étant considérablement plus élevé pour les matériaux cellulaires que pour les matériaux totalement denses. Les structures cellulaires peuvent être organisées dans deux catégories principales : celles périodiques où une même maille est répétée et celles pseudopériodiques où la topologie des mailles est la même tandis que leur taille et leur orientation peut varier (Figure 1.18). Si l'épaisseur des membrures est constante, on considère la structure homogène sinon, elle est appelée hétérogène (Dong, Tang, & Zhao, 2017; Y. Tang & Zhao, 2016). Une précision doit être apportée concernant les termes hétérogène et homogène qui dans le cadre des simulations numériques veulent sous-entendre la présence ou non d'irrégularités, tels les concentrateurs de contrainte, dans la structure analysée. Dans ce contexte, tous les matériaux cellulaires sont hétérogènes et les matériaux totalement denses sont homogènes. Ces notions seront réitérées plus loin.

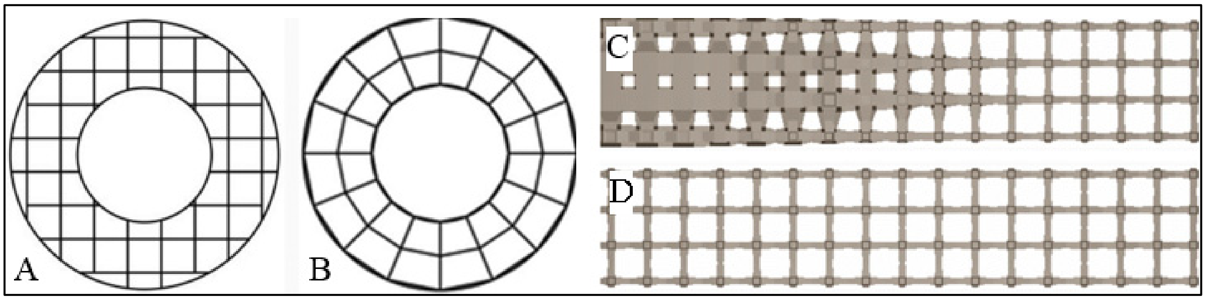

Figure 1.18 Exemple 2D de structure architecturée A) périodique; B) pseudopériodique; C) hétérogène et D) homogène
Tiré et adapté de Y. Tang et Zhao (2016)

Un autre moyen de classifier les structures architecturées est le mode de résistance des membrures qui peut être de deux types : par flexion ou par allongement. Ceci fait appel aux principes de rigidité structurelle comme illustré à la Figure 1.19. Les structures dites à dominance d'allongement sont beaucoup plus rigides et résistantes que les structures à dominance de flexion (Deshpande, Ashby, & Fleck, 2001). Toutefois, lorsqu'en compression, les structures à dominance d'allongement subissent le flambage des membrures, ce qui entraine une perte importante de la résistance tandis que celles à dominance de flexion conservent le même comportement.

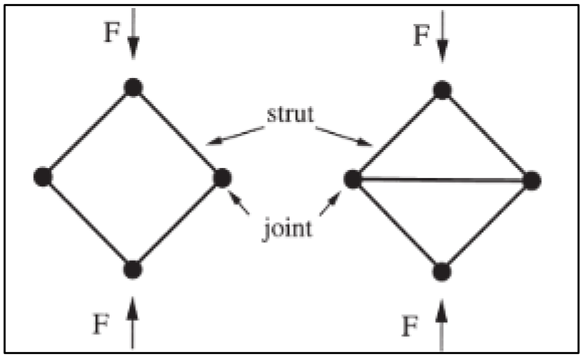

Figure 1.19 Structures à dominance de flexion (gauche) ou d'allongement (droite)
Tiré de Deshpande et al. (2001)

Puisque les mailles élémentaires ont une taille millimétrique ou microscopique, ceci permet de voir ces structures en tant que matériaux dont les propriétés mécaniques macroscopiques, telles que la résistance mécanique et le module d'élasticité, sont définies en fonction du matériau de base et de leur structure (Ashby, 2005). Les structures architecturées peuvent prendre toute sorte de formes, tailles, taux de porosité, épaisseur de membrures, orientations, etc. Les propriétés mécaniques au niveau macroscopique sont donc directement liées à ces paramètres. Toutefois, une tendance logique peut être déduite : plus le taux de porosité est important, plus la rigidité et la résistance mécanique de telles structures diminuent.

Puisque ces structures sont très difficiles, voire impossibles, à fabriquer par des techniques de fabrication traditionnelles, ce n'est que depuis le développement de la FA que les recherches dans ce domaine ont pris de l'envergure. En effet, comme illustré à la Figure 1.20, divers types de structures architecturées fabriquées par une variété de techniques de FA ont été explorées (Al-Ketan, Rowshan, & Abu Al-Rub, 2018; X.-Y. Zhang, Fang, & Zhou, 2017). Certains types de cellules sont basées sur des membrures linéaires tels que les modèles Kelvin et Octet-truss de la Figure 1.20, tandis que d'autres utilisent des équations surfaciques (triply periodic minimal surfaces - TPMS) pour en déterminer la forme comme est le cas des modèles « squelettaux » et « feuille » de la même figure. Un des avantages des formes surfaciques est la possibilité de représenter de grandes structures par des équations simples.

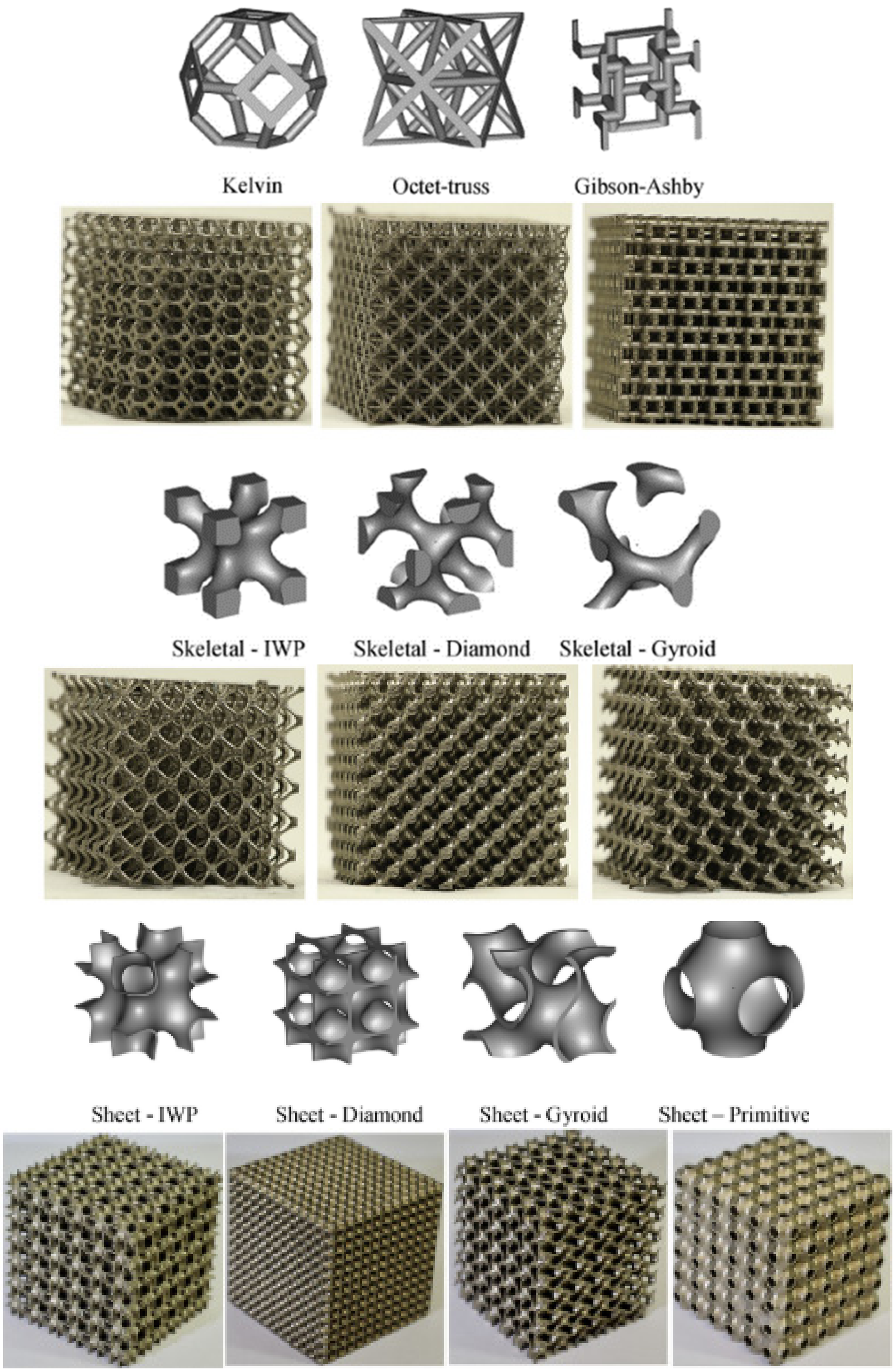
Kelvin
Octet-truss
Gibson-Ashby
Skeletal - IWP
Skeletal - Diamond
Skeletal - Gyroid
Sheet - IWP
Sheet - Diamond
Sheet - Gyroid
Sheet – Primitive

Figure 1.20 Exemples de structures architecturées produites par FA
Tiré et adapté de Al-Ketan et al. (2018)

Une tendance récente dans ce domaine s’impose. Il s’agit de l’optimisation topologique d’un volume unitaire afin d’en déterminer la meilleure distribution de matière pour un type de chargement imposé. L’optimisation topologique peut aussi permettre de maximiser les performances en termes de la souplesse, de la perméabilité et de la masse (Tableau 1.2).

Tableau 1.2 Survol des travaux portant sur l’optimisation topologique des cellules unitaires

Étude	Cellules optimisées	But d’optimisation
Coelho, Hollister, Flanagan, et Fernandes (2015)	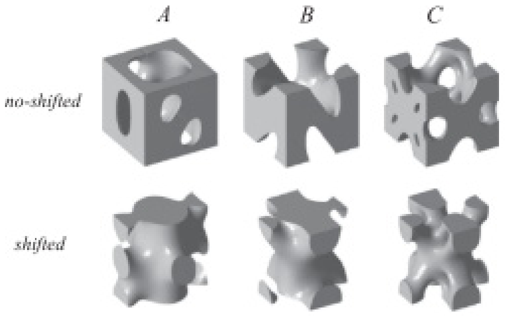	Avoir un bon compromis entre la rigidité et la perméabilité pour applications biomédicales
Almeida et Bártolo (2013)	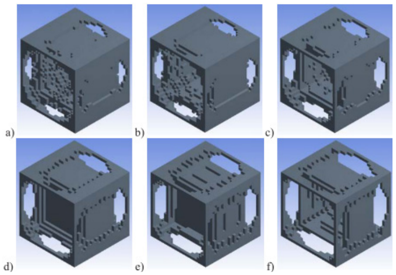	Maximiser les performances mécaniques pour divers taux de porosité et conditions limites
Challis, Roberts, Grotowski, Zhang, et Sercombe (2010)	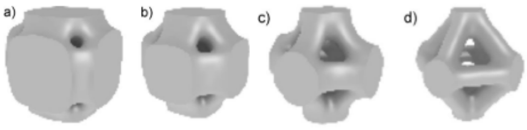	Maximiser la diffusivité pour une rigidité semblable à l’os
Lin, Kikuchi, et Hollister (2004)	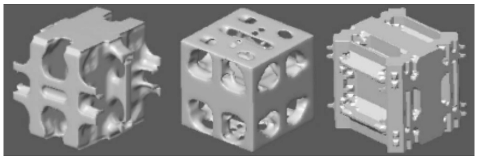	Répliquer les propriétés mécaniques des os trabéculaires

1.4.1 Propriétés des structures cellulaires

Lorna J Gibson et Ashby (1999) ont proposé des méthodes pour relier les propriétés mécaniques macroscopiques du matériau cellulaire à sa densité relative (ρ_r) par rapport à la densité du matériau totalement dense :

$$\rho_r = \frac{\rho *}{\rho_s} \tag{1.3}$$

où ρ*et ρ_s sont les densités du matériau cellulaire et du matériau totalement solide de la structure. La porosité φ, représentant la fraction de vide sur le volume total, peut être calculée par (1 - ρ_r). Le module d'élasticité apparent peut alors être calculé avec l'équation suivante :

$$E^* = E_s C_1 (1 - \varphi)^{n_1} \tag{1.4}$$

où E_s est le module d'élasticité de la phase solide et la constante C_1 et l'exposant n_1 dépendent de la géométrie de la maille élémentaire et de ses paramètres de fabrication. Des lois semblables peuvent être développées pour estimer les autres propriétés mécaniques du matériau cellulaire comme la limite d'écoulement S_y^* :

$$S_y{}^* = S_{y,s} C_2 (1 - \varphi)^{n_2} \tag{1.5}$$

où $S_{y,s}$ est la résistance à l'écoulement de la phase solide, et encore une fois, la constante C_2 et l'exposant n_2 dépendent de la géométrie et des caractéristiques de fabrication. Les paramètres critiques qui gèrent les propriétés mécaniques sont l'orientation des mailles et la taille des membrures de la structure. Ces deux paramètres influencent le taux de porosité ainsi que les facteurs C et n des équations ci-montrées.

Généralement, le comportement mécanique des structures architecturées peut être séparé en trois modes comme illustré à la Figure 1.21 : un premier régime linéaire élastique, un deuxième régime à contrainte constante causé par le flambage ou l'écrasement des membrures et un troisième régime de densification lorsque les membrures écrasées agissent comme le matériau dense (Evans, Hutchinson, & Ashby, 1998).

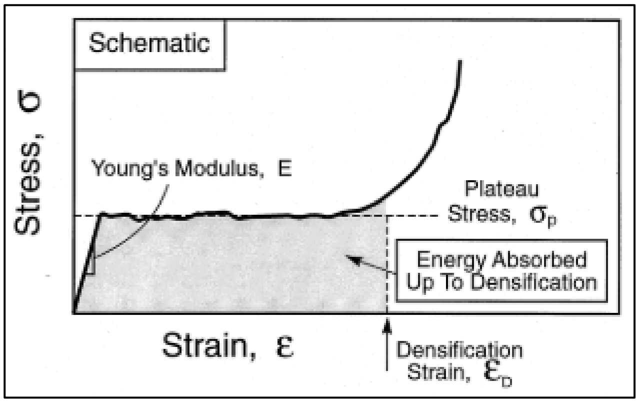

Figure 1.21 Comportement contrainte-déformation typique des structures architecturées
Tiré de Evans et al. (1998)

Des études expérimentales sur divers types de structures architecturées peuvent être utilisées pour classer les cellules unitaires en fonction de leurs propriétés mécaniques comme le module d'élasticité et la résistance à l'écoulement. Une des difficultés de cette comparaison est que d'une étude à l'autre la technologie de fabrication, le matériau, l'équipement utilisé, les taux de porosités et les méthodes de test sont trop variés. Le Tableau 1.3 ci-dessous combine les résultats de diverses études ayant traité de structures architecturées fabriquées à partir de Ti6Al4V (Mahmoud & Elbestawi, 2017). Malgré les taux de porosité ainsi que les tailles des membrures et des pores qui ne sont pas nécessairement comparables, dans la plage de porosité se chevauchant, il est possible de remarquer que le type de cellule ayant la meilleure limite d'écoulement est celle du gyroide. Effectivement, les structures TPMS ont suscité beaucoup d'intérêt dernièrement grâce à leurs propriétés mécaniques plus intéressantes comparé aux structures équivalentes à base de membrure (Al-Ketan et al., 2018; L.-Y. Chen, Liang, Liu, & Zhang, 2021; L. Zhang et al., 2018).

Tableau 1.3 Récapitulatif de divers articles traitant de structures architecturées en Ti6Al4V
Tiré et adapté de Mahmoud et Elbestawi (2017)

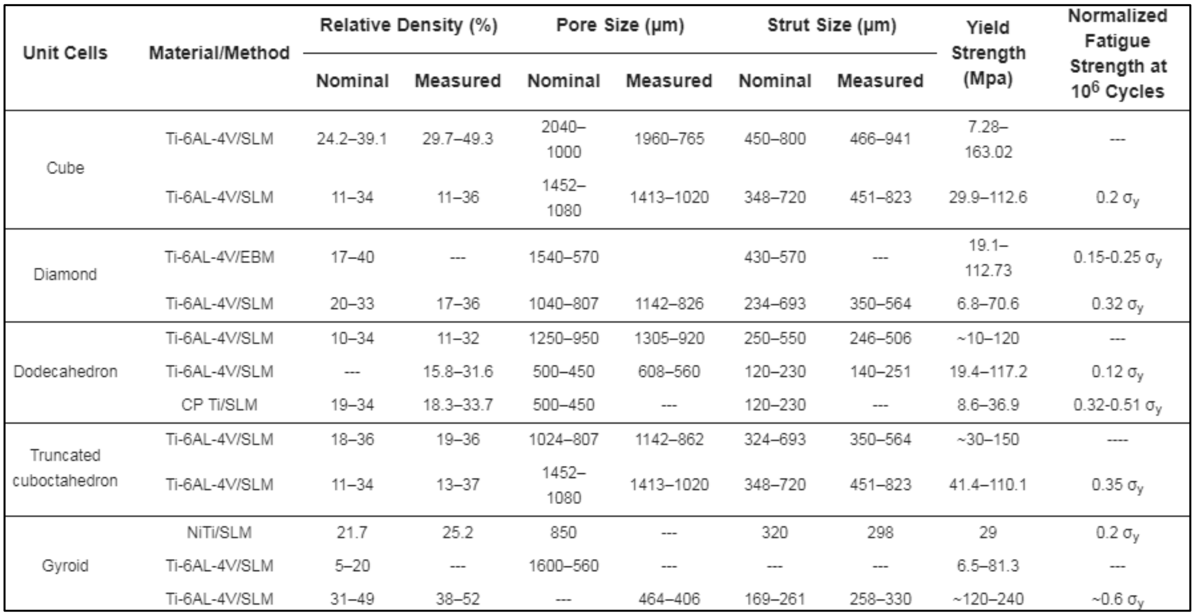

Unit Cells	Material/Method	Relative Density (%)		Pore Size (μm)		Strut Size (μm)		Yield Strength (Mpa)	Normalized Fatigue Strength at 10^6 Cycles
		Nominal	Measured	Nominal	Measured	Nominal	Measured		
Cube	Ti-6AL-4V/SLM	24.2–39.1	29.7–49.3	2040–1000	1960–765	450–800	466–941	7.28–163.02	---
	Ti-6AL-4V/SLM	11–34	11–36	1452–1080	1413–1020	348–720	451–823	29.9–112.6	0.2 σ_y
Diamond	Ti-6AL-4V/EBM	17–40	---	1540–570		430–570	---	19.1–112.73	0.15-0.25 σ_y
	Ti-6AL-4V/SLM	20–33	17–36	1040–807	1142–826	234–693	350–564	6.8–70.6	0.32 σ_y
Dodecahedron	Ti-6AL-4V/SLM	10–34	11–32	1250–950	1305–920	250–550	246–506	~10–120	---
	Ti-6AL-4V/SLM	---	15.8–31.6	500–450	608–560	120–230	140–251	19.4–117.2	0.12 σ_y
	CP Ti/SLM	19–34	18.3–33.7	500–450	---	120–230	---	8.6–36.9	0.32-0.51 σ_y
Truncated cuboctahedron	Ti-6AL-4V/SLM	18–36	19–36	1024–807	1142–862	324–693	350–564	~30–150	----
	Ti-6AL-4V/SLM	11–34	13–37	1452–1080	1413–1020	348–720	451–823	41.4–110.1	0.35 σ_y
Gyroid	NiTi/SLM	21.7	25.2	850	---	320	298	29	0.2 σ_y
	Ti-6AL-4V/SLM	5–20	---	1600–560	---	---	---	6.5–81.3	---
	Ti-6AL-4V/SLM	31–49	38–52	---	464–406	169–261	258–330	~120–240	~0.6 σ_y

Il est à noter que la majorité des tests mécaniques effectues sur les structures architecturées sont en compression (Abou-Ali, Al-Ketan, Lee, Rowshan, & Al-Rub, 2020; Al-Ketan, Lee, Rowshan, & Al-Rub, 2020; Bobbert et al., 2017; Issariyapat, Kariya, Alhazaa, Umeda, & Kondoh, 2021; C. Lu, Zhang, Wen, & Chen, 2021; S. Ma et al., 2020; Obadimu & Kourousis, 2021; Y. Wang et al., 2020). Ceci est dû à la simplicité de tests, ne nécessitant pas de montage spécifique pour permettre la traction, torsion ou cisaillement de l'échantillon. En effet, un grand nombre d'études sont disponibles traitant de la compression (Obadimu & Kourousis, 2021) et même des normes telles que la ISO13314 (2011) qui est publiée et l'ASTM WK76163 qui en rédaction.

Néanmoins, quelques travaux peuvent être identifiés, traitant des propriétés mécaniques des structures cellulaires en traction (Kelly et al., 2019; Yu et al., 2020) et torsion (Nelson, Kelly, & Gall, 2022; A Yánez, Cuadrado, Martel, Afonso, & Monopoli, 2018). Généralement, ces travaux indiquent que les structures cellulaires sont plus faibles en traction comparé à la compression, et en termes de torsion, la résistance est semblable à celle en compression.

Dans le domaine biomédical, un aspect important des structures architecturées est leur perméabilité fluidique qui assure une bonne circulation sanguine et un apport de nutriments aux cellules pour une meilleure ostéo-intégration dans l'implant. Les structures TPMS ont été identifiées comme des structures ayant des perméabilités similaires à celles des os trabéculaires (Soro, Attar, Wu, & Dargusch, 2019).

Comme indiqué plus tôt, la comparaison des structures architecturées devient compliquée dû au grand nombre de variables pouvant affecter les performances mécaniques de ces matériaux. Une des options permettant de faciliter cette comparaison est l'utilisation de rapports de propriétés comme le ratio résistance-rigidité (S_y/E) et le ratio surface-volume (S/V). Ces rapports seraient à maximiser afin d'avoir des structures plus résistantes ayant des surfaces plus importantes pour l'ostéo-intégration ou l'échange de chaleur.

1.4.2 Structures architecturées en AMF

Malgré les difficultés de fabrication additive des AMF, certains efforts ont été investis pour en produire des structures cellulaires. Bormann, de Wild, Beckmann, et Müller (2013) sont parmi les premiers à avoir fabriqué des structures architecturées en Ti-Ni par LPBF. Leur étude était limitée à une validation géométrique de la structure rhombo-dodecaèdrale imprimée et à la vérification d'un retour de forme après déformation et chauffage du spécimen. Sasan Dadbakhsh, Speirs, Kruth, et Van Humbeeck (2015) ont fabriqué des structures octaèdres et analysé l'influence des paramètres d'impression sur les propriétés fonctionnelles. Il a été démontré qu'une puissance et vitesse de laser élevées réduisaient les températures de transformation martensitique comparé à une puissance et vitesse de laser plus faibles, et ce, malgré des densités d'énergie volumétrique semblables. Ceci engendrait un comportement partiellement superélastique à température ambiante des structures à haute puissance et haute vitesse dû à la présence plus importante de la phase austénitique à température ambiante (Figure 1.22). Il est supposé que le taux de refroidissement plus élevé de la paramétrie haute puissance et vitesse engendraient une microstructure favorable pour l'austénite. Il est à noter que les niveaux de porosité des structures comparées ne sont pas les mêmes dû aux divergences géométriques des structures imprimées comparées au modèle CAO.

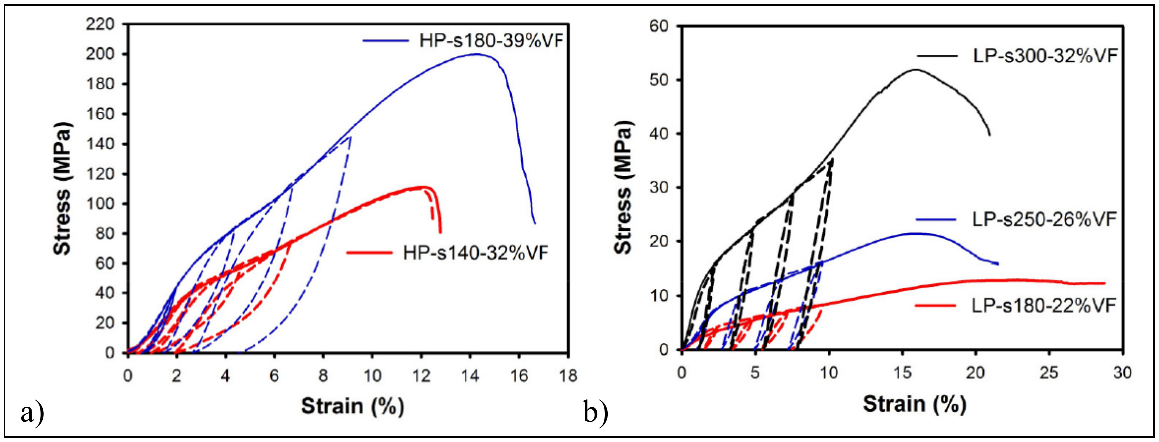

Figure 1.22 Comportement mécanique des structures imprimées avec a) haute puissance et vitesse (HP) et b) faible puissance et vitesse (LP) testées en compression à température ambiante. À noter les différentes fractions volumétriques (densité relative)
Tiré de Sasan Dadbakhsh et al. (2015)

Plus récemment, dans une tentative de créer des structures de faible rigidité, Bartolomeu, Costa, Alves, Miranda, et Silva (2020) ont fabriqué des structures cellulaires cubiques en Ti-Ni mais n'ont pas observé de réponse superélastique. Biffi, Bassani, Fiocchi, et Tuissi (2020) ont eu plus de succès, cependant, la superélasticité de leurs structures en diamant à base de poutres était seulement partielle. Cela était en partie dû à des températures de transformation martensitique élevées causées par les défis liés au contrôle de la composition chimique du matériau pendant l'impression.

Speirs, Van Hooreweder, Van Humbeeck, et Kruth (2017) ont testé les propriétés en fatigue en compression de trois types de structures fabriquées par LPBF en un alliage Ti-55.2%wt Ni à savoir : octaèdre, gyroide cellulaire (squeletal) et gyroide en feuille (surfacique) (Figure 1.23 gauche). Parmi les trois structures ayant un taux de porosité de 75%, la structure gyroide surfacique avait les meilleures performances en fatigue attribuables à un niveau plus faible de concentration de contraintes (Figure 1.23 droite).

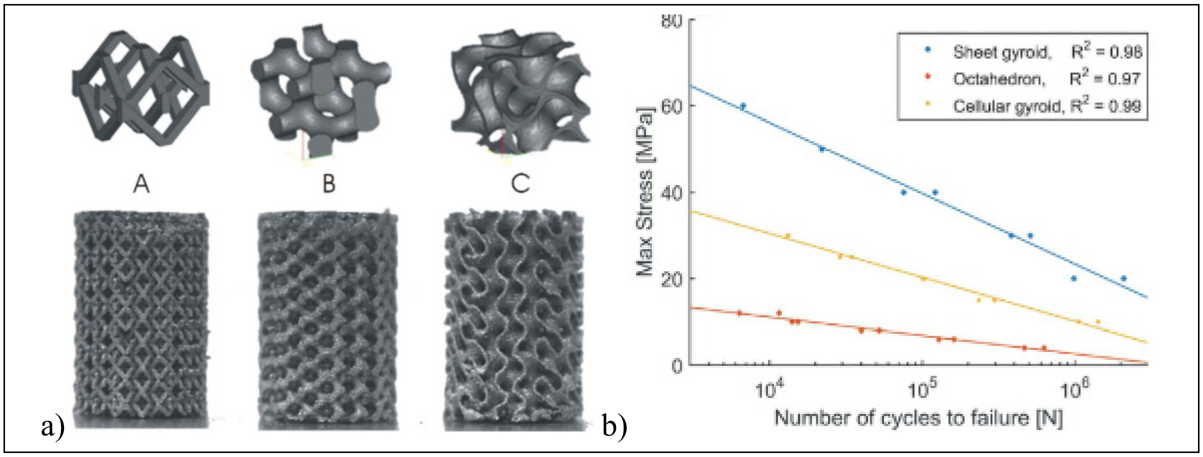

Figure 1.23 a) structures architecturées testées en fatigue (A-Octahedron, B-Gyroide squeletal, C-Gyroide surfacique); b) contrainte maximale des structures en fonction du nombre de cycles
Tiré et adapté de Speirs et al. (2017)

Gorgin Karaji et al. (2017) et Habijan et al. (2013) ont regardé les propriétés biofonctionnelles des structures cellulaires en Ti-Ni produits par LPBF. Malgré une certaine décharge d'ions de nickel, le niveau de ceux-ci était bien en deçà des limites cytotoxiques et les cultures cellulaires avaient subi des croissances indiquant que ces matériaux sont adéquats pour être utilisés dans les implants.

1.4.3 Méthodes de simulation de structures cellulaires

Étant donné la différence de taille entre les cellules unitaires et les composants dans lesquels elles sont employées, le nombre de cellules est souvent très important. Afin de simuler de telles géométries fidèlement, chaque cellule doit être subdivisée en un nombre suffisant d'éléments, nécessitant des ressources informatiques importantes. Dans certains cas où le nombre de cellules dépasse les milliers, même avoir recours à un centre de calcul haute performance n'est pas suffisant. C'est pourquoi des efforts sont en cours afin d'essayer de simplifier les méthodes de simulation de ces structures architecturées. Il existe deux méthodes principales de modélisation du comportement mécanique des telles structures. La première méthode est basée sur le principe d'homogénéisation où le matériau est modélisé comme un solide ayant des propriétés mécaniques équivalentes aux cellules poreuses. La deuxième méthode est une approche directe consistant de l'analyse de la structure entière avec l'utilisation d'éléments poutre ou d'éléments solides.

Il est important et possiblement évident d'indiquer que pour toutes les méthodes de simulation qui seront présentées, les conditions aux limites affectent grandement les résultats. Généralement, les déplacements de la base sont bloqués et la face opposée subit une compression ou tension appliquée en tant que déplacement des nœuds. Les autres faces peuvent être libres ou comporter des conditions de symétrie, si seulement une partie de la structure est simulée. Terriault et Brailovski (2017) sont arrivés à la conclusion qu'afin d'avoir un modèle numérique valide, les faces latérales doivent avoir des conditions limites correspondant au comportement global de la structure.

1.4.3.1 Méthode d'homogénéisation

Le fondement mathématique de l'homogénéisation a été développé dans les années 1970 sur des cas simples comme une barre cylindrique avec des cavités cylindriques (Cioranescu & Paulin, 1979). Dans le cas des structures architecturées, les modèles numériques sont utilisés et la démarche d'homogénéisation peut être séparée en deux étapes (Dumas, 2016). Premièrement, il s'agit d'effectuer des analyses sur une partie représentative de la structure périodique hétérogène (dans ce cas les cellules unitaires) afin d'en déterminer les propriétés équivalentes. Deuxièmement, ces propriétés peuvent être appliquées à une structure homogène qui est moins coûteuse à simuler (dans ce cas un matériau totalement dense) et le problème peut être résolu en substituant la structure hétérogène par la structure homogène. La Figure 1.24 illustre un exemple d'homogénéisation d'une structure cellulaire, permettant de réduire le nombre d'éléments de 40960 pour la structure architecturée à 512 pour le modèle solide. Il y a alors une réduction significative du temps de calcul et des ressources nécessaires pour la résolution.

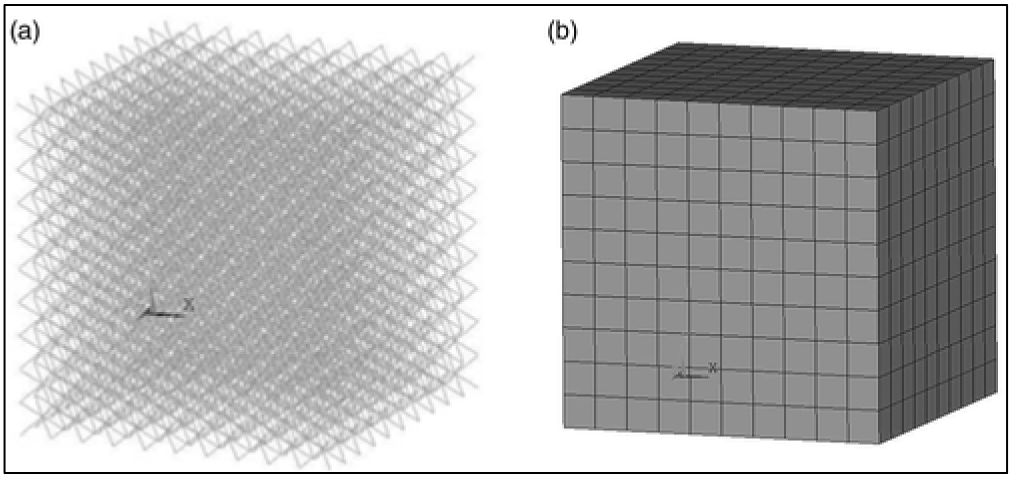

Figure 1.24 a) Structure architecturée avec 40960 éléments (hétérogène) et b) structure solide avec 512 éléments (homogène)
Tiré de Ptochos et Labeas (2012)

Une investigation par Coelho et al. (2015) sur trois structures cellulaires indique que si le nombre de cellules dans la structure est limité, des différences d'effet de taille sont identifiables entre le comportement prédit considérant un nombre limité de cellules (3-5) et celui prédit par la méthode homogénéisée qui considère un nombre infini de cellules. De plus, les auteurs indiquent que des différences non négligeables entre les prédictions numériques et les tests expérimentaux sont causées par les défauts de fabrication comme les déviations entre la surface nominale et celle fabriquée ainsi que les microporosités. Ceci indique que la qualité de la surface et autres défauts de fabrication doivent être considérés dans le développement des propriétés équivalentes.

1.4.3.2 Méthode des éléments finis

La deuxième méthode consiste à simuler la structure entière à l'aide d'éléments finis comme les éléments poutres ou les éléments solides. Ces méthodes sont plus difficiles à calculer, toutefois aboutissent à des résultats plus représentatifs et permettent un contrôle plus étroit des structures simulées. Une grande partie des travaux récents portant sur l'analyse par éléments finis des structures cellulaires utilisent l'approche directe.

Dans le cas des structures cellulaires à base de membrures, les simulations peuvent être effectuées avec deux types d'éléments : poutre et solide. Des études ont analysé les différences entre ces deux types d'élément, concluant que les deux sont adéquats, mais les modèles solides sont plus exacts que les modèles poutre malgré le temps de calcul plus important (Luxner, Stampfl, & Pettermann, 2005; Ravari, Kadkhodaei, Badrossamay, & Rezaei, 2014). Les éléments poutres sont limités par le fait qu'ils sont valables seulement pour des niveaux de porosité élevés (80-90%) et que les jonctions entre les membrures peuvent être problématiques lorsqu'un grand nombre de membrures se rejoignent. Un des avantages de l'approche de simulation directe est que les déviations géométriques engendrées par la fabrication peuvent être incluses dans l'analyse comme illustré à la Figure 1.25.

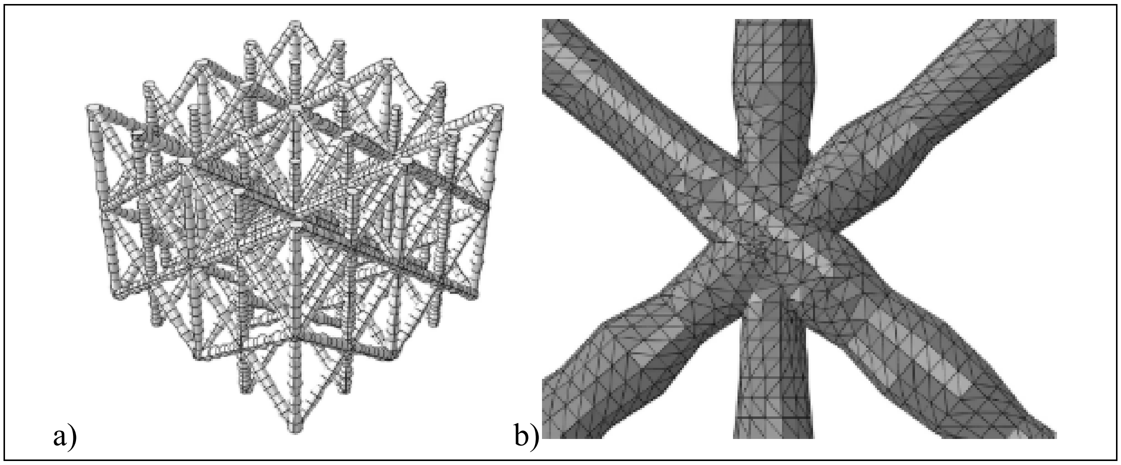

Figure 1.25 Cellule cubique centrée renforcée en Z (BCCZ) simulée par :
a) éléments poutre variables; b) éléments solides tétraédriques
Tiré et adapté de Ravari et al. (2014)

Dans le cas des structures TPMS, il est nécessaire d'utiliser des éléments solides. Les travaux récents peuvent être séparés en études analysant la distribution des contraintes dans la structure de façon qualitative (Soro, Saintier, Merzeau, Veidt, & Dargusch, 2021; Yu et al., 2020) et en études utilisant la simulation afin de calculer les propriétés apparentes des structures architecturées et les comparer aux résultats expérimentaux comme illustré à la Figure 1.26 (Abou-Ali et al., 2020; Ali & Sen, 2017; C. Lu et al., 2021; S. Ma et al., 2020; Y. Wang et al., 2020; Zhou, Zhao, Ma, Zhang, & Fu, 2020). Ces dernières présentent souvent des différences entre la modélisation et l’expérimental qui sont expliquées par la présence de défauts de fabrication comme les déviations géométriques, les porosités et un fini de surface inadéquat des composantes testées expérimentalement (C. Lu et al., 2021; S. Ma et al., 2020; Y. Wang et al., 2020; Zhou et al., 2020).

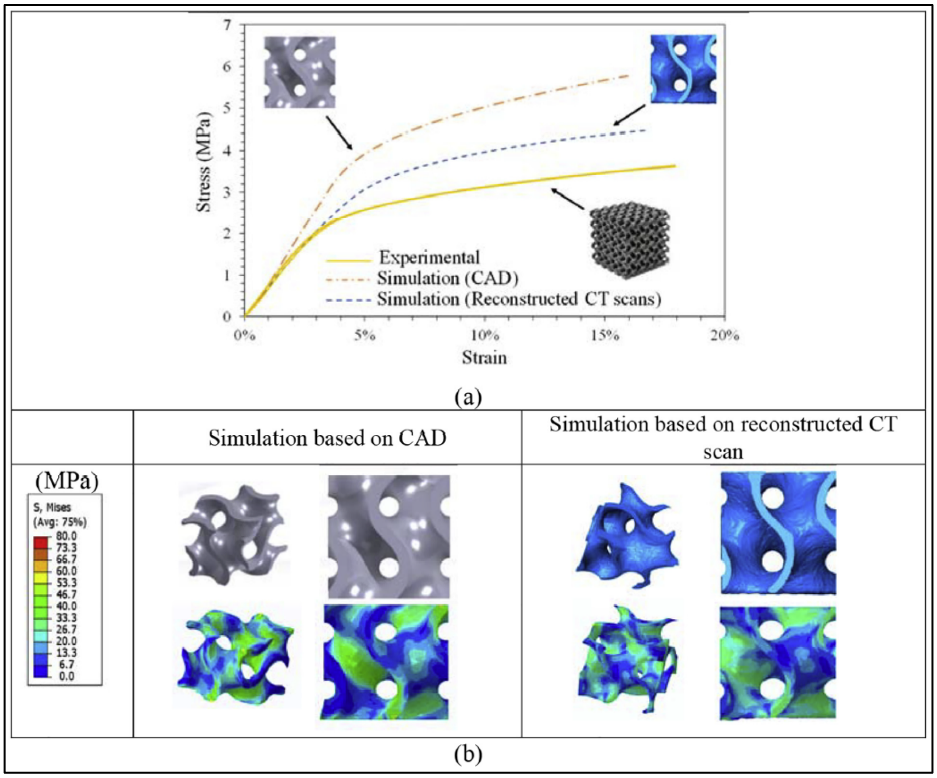

Figure 1.26 a) Comparaison de résultats des simulations avec les tests expérimentaux et b) analyse de la distribution des contraintes
Tiré de Abou-Ali et al. (2020)

Certains travaux existent également portant sur la simulation de structures architecturées en AMF (Maitrejean, Terriault, Devis Capilla, & Brailovski, 2014; Ravari et al., 2016). L’utilisation de lois de comportement du matériau spécifiques est nécessaire pour prendre en compte la transformation martensitique et l’effet de superélasticité ou mémoire de forme. Néanmoins, dans le cas de Ravari et al. (2016), la modélisation de la structure avec des défauts de fabrication a permis de répliquer le comportement expérimental. L’analyse numérique de Maitrejean et al. (2014) a mis en évidence l’avantage des structures architecturées ordonnées comparé aux structures stochastiques en termes d'utilisation des propriétés superélastiques, surtout à des niveaux de porosité élevés.

1.5 Résumé et rappel des objectifs

Ce survol de la littérature permet de conclure que la fabrication additive de cages intervertébrales est un sujet en développement avec des efforts identifiés portant sur l'intégration de structures architecturées dans ces dispositifs. Les principes de fonctionnement des alliages à mémoire de forme ont été présentés, les techniques courantes de fabrication additive ainsi que les avancées dans la FA des AMF ont été abordées. Finalement, des notions de base des structures architecturées, des études comparatives de leurs propriétés mécaniques ainsi que des méthodes de leur simulation ont été exposées. Un manque de travaux combinant la fabrication additive, les alliages à mémoire de forme, les structures architecturées et leur simulation pour la création de cages intervertébrales a été noté.

Cette étude vise à établir une démarche complète partant de la sélection des structures architecturées, allant jusqu'à leur fabrication en AMF et leur validation numérique et expérimentale pour application dans les cages intervertébrales. En premier lieu, l'alliage de titane conventionnel Ti-6Al-4V sera utilisé pour caractériser les structures cellulaires et servir en tant que cas de référence (benchmark). Cet alliage classique de titane est sélectionné pour la phase initiale des travaux, car c'est un matériau couramment utilisé, pour lequel les paramètres de fabrication sont connus et la matière première est facilement disponible. L'AMF choisi dans le cadre de cette étude est un alliage de Ti-Ni.

Pour y arriver, les objectifs spécifiques sont :
- établir les requis de fonctionnement des cages intervertébrales;
- concevoir et modéliser numériquement les structures architecturées;
- valider le choix des structures à l'aide de l'alliage classique Ti6Al4V;

- identifier les paramètres optimaux de fabrication du Ti-Ni et caractériser les propriétés mécaniques et la microstructure;
- fabriquer et tester expérimentalement les structures architecturées en Ti-Ni.

Les travaux effectués dans le cadre de cette thèse sont séparés en trois chapitres, les deux premiers utilisent l'alliage de titane classique et le troisième utilise l'alliage de Ti-Ni. Le chapitre 2 porte sur les requis fonctionnels des cages intervertébrales, la sélection des structures architecturées et leur caractérisation en termes des propriétés fluidiques et mécaniques en compression. Le chapitre 3 traite de la modélisation numérique de ces structures et la validation expérimentale pour les modes de chargement en tension, en compression et en torsion. Le chapitre 4 sert à l'optimisation des paramètres de fabrication de l'alliage de Ti-Ni ainsi qu'à la fabrication des structures avec cet alliage pour comparaison avec les structures équivalentes en l'alliage de titane de référence.

Les retombées de ce projet seront le développement des paramètres de fabrication d'un AMF ainsi que la caractérisation de structures cellulaires qui peuvent être utilisées dans le domaine biomédical pour l'application des cages intervertébrales. De plus, le développement d'un modèle numérique de simulation de structures architecturées permettra l'exploration de diverses configurations des propriétés de matériau et des formes de structures cellulaires.

CHAPITRE 2

MECHANICAL PROPERTIES AND FLUID PERMEABILITY OF GYROID AND DIAMOND LATTICE STRUCTURES FOR INTERVERTEBRAL DEVICES: FUNCTIONAL REQUIREMENTS AND COMPARATIVE ANALYSIS

Anatolie Timercan [1], Vadim Sheremetyev [2], Vladimir Brailovski [1]

[1] Department of of Mechanical Engineering, École de Technologie Supérieure, 1100 Notre-Dame West, Montreal, Quebec, Canada H3C 1K3
[2] Metal Forming Department, National University of Science and Technology MISiS, Leninskiy Prospekt 4, Moscow, Russia 119049

Article publié dans la revue « Science and Technology of Advanced Materials »,
le 21 avril 2021

2.1 Avant-propos

En premier lieu, il est important de définir les requis de fonctionnement des structures architecturées pour leur utilisation dans les cages intervertébrales, et ce, en termes de propriétés géométriques telle que le niveau de porosité et la taille des pores, en termes de propriétés mécaniques telle que la résistance élastique et le module d'élasticité, ainsi qu'en termes de perméabilité fluidique. Cet article porte sur la définition d'un cahier de charges pour les instruments intervertébraux, ainsi que la sélection de deux structures architecturées, leur fabrication, et leur caractérisation et comparaison avec les spécifications de fonctionnement. Comme indiqué auparavant, les travaux initiaux servent à établir une base de référence, donc l'alliage de Ti6Al4V traditionnel est utilisé ici en raison de son accessibilité et sa facilité de fabrication.

2.2 Résumé

Les dispositifs de fusion intervertébrale actuellement utilisés présentent de multiples risques de complications tels qu'un manque de fixation, la migration du dispositif et son affaissement dans les vertèbres. Une solution émergente à ces problèmes est l'utilisation de structures architecturées fabriquées par impression 3D qui sont souples et perméables aux fluides, favorisant ainsi l'ostéo-intégration et réduisant les risques de complications. Des structures en diamant à base de poutre et des structures gyroïdes à base de feuille, avec une taille de pore de 750 μm et des niveaux de porosité de 60, 70 et 80%, sont conçues et fabriquées à partir de l'alliage Ti-6Al-4V en utilisant la fusion laser sur lit de poudre. Les structures produites sont scannées par tomodensitométrie, testées en compression et soumises à une évaluation de la perméabilité aux fluides. La rigidité des deux structures (1.9-4.8 GPa) est comparable à celle de l'os, tandis que leur résistance mécanique (52-160 MPa) est supérieure à celle des vertèbres (3-6 MPa), réduisant ainsi les risques de détérioration osseuse ou défaillance de l'implant. La perméabilité aux fluides (5-57 x 10^{-9} m^2) et les rapports surface/volume (~3) des deux structures sont proches de ceux des vertèbres. Cette étude démontre que les deux types de structures architecturées peuvent être produits pour répondre aux spécifications fonctionnelles de l'application tout en étant limité par certaines contraintes physiques et liées à l'équipement. Les structures architecturées présentent ainsi des solutions potentielles pour la réduction des taux de complications des dispositifs vertébraux en offrant une meilleure fixation grâce à l'ostéo-intégration.

2.3 Abstract

Current intervertebral fusion devices present multiple complication risks such as a lack of fixation, device migration and subsidence. An emerging solution to these problems is the use of additively manufactured lattice structures that are mechanically compliant and permeable to fluids, thus promoting osseointegration and reducing complication risks. Strut-based diamond and sheet-based gyroid lattice configurations having a pore diameter of 750 μm and levels of porosity of 60, 70 and 80% are designed and manufactured from Ti-6Al-4V alloy using laser powder bed fusion. The resulting structures are CT-scanned, compression tested and subjected to fluid permeability evaluation. The stiffness of both structures (1.9-4.8 GPa) is comparable to that of bone, while their mechanical resistance (52-160 MPa) is greater than that of vertebrae (3-6 MPa), thus decreasing the risks of wither bone or implant failure. The fluid permeability (5-57 x 10^{-9} m^2) and surface-to-volume ratios (~3) of both lattice structures are close to those of vertebrae. This study shows that both types of lattice

structures can be produced to suit the application specifications within certain limits imposed by physical and equipment-related constraints, providing potential solutions for reducing the complication rate of spinal devices by offering a better fixation through osseointegration.

2.4 Introduction

According to Statistics Canada, spine health problems are amongst the most common sources of chronic pain in Canadians requiring intervertebral fusion surgery in extreme cases (Murphy, Gorber, Spence, & McIntosh, 2006). This procedure involves the fixation of two or more adjacent vertebrae using spinal instrumentation such as spinal rods and spinal cages. A number of different cage designs are commonly used by surgeons, depending on the surgery site, the illness severity, and the preferred surgical technique. Larger cages (threaded cylindrical and box-shaped) are employed in anterior and lateral intervertebral fusion approaches, while smaller cages (bullet- and kidney-shaped) are preferred for posterior and transforaminal intervertebral fusion (Peck et al., 2018; Peck et al., 2017). It must, however, be noted that the currently used commercial intervertebral cages present different complication risks, such as a lack of fixation, cage migration and subsidence (Y. Chen et al., 2013; Nemoto et al., 2014). The reported complication rates vary from 6 to 30%, depending on the cage type, the material, the size, and the surgical technique (Abbushi et al., 2009; Park et al., 2019).

Leading efforts to reduce the above problems concentrate on the employment of functional materials, such as superelastic alloys (Michel Assad et al., 2003a), and the development of porous (Chung et al., 2017; La Rosa et al., 2018) and patient-specific (Mobbs et al., 2019; Siu et al., 2018) spinal devices. Superelastic alloys have a lower modulus of elasticity than the traditionally used metallic implant materials. The plateau-like hysteretic behavior of these alloys, being closer to the mechanical behavior of bone, may reduce the risk of stress shielding (Head, Bauk, & Emerson, 1995). Porous structures are considered as good candidates for this application because of their lower stiffness than their bulk equivalents (Ashby, 2005; Zadpoor, 2019). Moreover, porous structures with open interconnected pores are permeable to fluids, which could improve their union with the surrounding tissues via osseointegration (Hara et al., 2016; Kienapfel, Sprey, Wilke, & Griss, 1999; Taniguchi et al., 2016; Zadpoor, 2019). Finally, patient-specific devices have the advantage of being based on patients' anatomy extracted from body scans, and thus promise a better fit and function due to their personalized geometries (Spetzger et al., 2016). An appropriate synergetic combination of all these attributes, spanning from the material behavior at the microscale to the structural arrangement at the mesoscale, and to the device geometry at the macroscale, could help to reach the ultimate objective of improving the clinical performances of spinal cages. This work focuses on the mesoscale aspect of spinal cages, i.e., on the design and performances of porous structures used for their manufacture.

Porous structures may be stochastic (foams) or ordered (cellular) structures. The foams used to be more common due to their production simplicity. However, with the advent of additive manufacturing, allowing the production of complex geometries, cellular structures have gained in interest and popularity (Mahmoud & Elbestawi, 2017). Cellular structures, also known as lattice structures, are defined by the 3D repetition of a given unit cell. As compared to their stochastic counterparts, the properties of lattice structures can more readily be controlled by tuning the lattice geometry, which makes them easier to model and simulate, and allows for a greater manufacturing repeatability.

Lattice structures can be classified in three main categories in terms of their geometry: strut-, skeletal- and sheet-based geometries (Al-Ketan et al., 2018). Strut-based structures are composed of linear rods with constant or variable cross-sections interconnected at the nodes. Among their advantages is the simplicity of creation. These lattice structures are, however, prone to stress concentrations at the nodes. Skeletal and sheet-based structures are built using triply periodic minimal surface equations based on sinusoidal functions. These lattice structures have smoother transitions, and, therefore, less pronounced stress riser effects. It is worth noting that at high porosity levels, manufacturing-induced defects can act as additional stress risers distributed over the entire structure for all the lattice categories, and their contribution can play a significant role when the strut thickness approaches the smallest feature resolution of the manufacturing system (Alejandro Yánez, Fiorucci, Cuadrado, Martel, & Monopoli, 2020).

Lattices may be characterized by a combination of three sets of attributes: geometric, mechanical and fluid-related, all the attributes that influence the service performance of lattices as implant materials. Geometric attributes include the strut/sheet thickness, the cell size, the pore diameter, the surface area, the total volume and the level of porosity. These parameters are co-dependent and directly affect the mechanical properties such as the strength and stiffness, as well as the fluid permeability. For example, the apparent modulus of elasticity and yield strength of lattice structures can be calculated as functions of porosity using scaling relations proposed by Gibson and Ashby (Eqs (2.1) and (2.2)):

$$E_{app} = E_b * C_1(1 - \varphi)^{n_1} \tag{2.1}$$

$$S_{y_{app}} = S_{y,b} * C_2(1 - \varphi)^{n_2} \tag{2.2}$$

where E_b and $S_{y,b}$ are the modulus of elasticity and the yield strength of the bulk material, and C and n are the empirically determined coefficients.

Similarly, fluid permeability can be related to porosity via the Kozeny-Carman equation (Eq (2.3)), which is used to approximate the absolute permeability of soil in the earth sciences (Xu & Yu, 2008):

$$k = \frac{\varphi^3}{c * (1 - \varphi)^2 * S^2} \tag{2.3}$$

where k is the absolute permeability, c is the Kozeny-Carman constant, and S is the specific surface area of the material.

In equations (2.1)-(2.3), the porosity φ is defined as the volume of voids divided by the total volume of the structure (Eq (2.4)):

$$\varphi\ (\%) = \frac{V_{void}}{V_{total}} * 100 = \left(1 - \frac{V_{material}}{V_{total}}\right) * 100 \tag{2.4}$$

In order to evaluate the performances of various lattice configurations and allow choosing the most appropriate one for a selected application (spinal cages, in our case), it is necessary to define the functional requirements and the range of acceptable properties for this application.

2.5 Functional requirements to intervertebral cages

The human spine is complex and does not accommodate a one-size-fits-all approach. It can be divided into three main regions, namely, the cervical, thoracic and lumbar zones, which progressively support a greater load, and are therefore increasingly larger (Singer, Edmondston, Day, Breidahl, & Price, 1995). Morphological analyses of the vertebrae at all levels have been carried out, and their average dimensions identified, as shown in Tableau 2.1. One of the limitations of the related studies is that they are based on an analysis of spines of deceased persons, and consequently, are biased toward older population (Aharinejad, Bertagnoli, Wicke, Firbas, & Schneider, 1990; Panjabi et al., 1992; Scoles, Linton, Latimer, Levy, & Digiovanni, 1988).

Tableau 2.1 Average dimensions of vertebrae at the cervical, thoracic and lumbar levels
Tiré de Aharinejad et al. (1990), Panjabi et al. (1992) et Scoles et al. (1988)

	Transverse diameter [mm]	Sagittal diameter [mm]	Endplate rim thickness [mm]	Vertebral height [mm]
Cervical	12-29	12-24	1-6	10-30
Thoracic	12-44	12-39	1-9	12-45
Lumbar	43-50	29-35	2-12	26-27

The load supported by the vertebrae and the intervertebral discs varies, depending on the activity performed and the body position. The load acts as a combination of compression, bending and torsion. The resistance of the vertebrae and disks is most easily tested in compression. It was found that the vertebral compression failure load is in the 2-6 kN range, or around 3-6 MPa, when distributed over the cross-section (Singer et al., 1995). For comparison, trabecular bone has a yield strength of 0.2-10.5 MPa (Lindahl, 1976), while that of cortical bone, of 42-176 MPa (Davis, 2003; Wolfram & Schwiedrzik, 2016). The modulus of elasticity of the vertebrae was measured to be 0.374 GPa (El Masri, Sapin de Brosses, Rhissassi, Skalli, & Mitton, 2012), which is situated much closer to the upper limit value of the apparent modulus of trabecular bone (0.043-0.165 GPa) (Nicholson et al., 1997) than to that of cortical bone (7-30 GPa) (Davis, 2003). Both mechanical attributes of human vertebrae, resistance and stiffness, are therefore defined mainly by those of trabecular bones, which is explained by a relatively small thickness of cortical bone in these structures (~300 μm) (Ritzel, Amling, Pösl, Hahn, & Delling, 1997).

From these values, the strength-to-stiffness ratio (Sy/E) for the vertebrae ranges from 8 to 16×10^{-3}; for trabecular bone, it ranges from 5 to 60×10^{-3}, and for cortical bone, it is $\sim 6 \times 10^{-3}$. It can be stated that the greater the Sy/E ratio of engineered lattice structures, the better they are suited for the application, providing the resistance of these structures exceeds that of surrounding tissues. Maximizing this ratio, while preventing mechanical failure, would allow maintaining the stiffness of a lattice structure as close as possible to that of the vertebrae, thus reducing the stress shielding effect which occurs when the implant stiffness is higher than that of bone in the site of implantation.

To stimulate osseointegration, lattice structures must respect certain criteria with regards to the porosity level, the pore size and permeability. In human bones, these parameters depend on their location, type of loading and bone quality (Lorna J Gibson, 2005). For example, the trabecular bone in the vertebrae has an apparent porosity ranging from 70 to 97% (Lindahl, 1976; Nicholson et al., 1997), which is significantly higher than the 30-70% porosity range recommended by the FDA for porous coated knee, hip and shoulder implants (Food and Drug Administration, 2007). Finally, to promote the ingrowth of bone instead of connective tissue, a pore size range of 100 to 1000 μm is recommended (Davis, 2003; Hara et al., 2016; Kienapfel et al., 1999; Taniguchi et al., 2016). As well, to select a better candidate for bone tissue scaffolds from different lattice structures, the surface-to-volume

(*S/V*) ratio can be used (Kienapfel et al., 1999; Taniguchi et al., 2016), since the greater this ratio, the greater the surface available to host the ingrowth tissue. This ratio in bones varies from 1 to 6 mm^{-1}, and in vertebrae, it varies from 2 to 3 mm^{-1} (Lerebours, Thomas, Clement, Buenzli, & Pivonka, 2015; Martin, 1984; Pivonka, Buenzli, Scheiner, Hellmich, & Dunstan, 2013).

Regarding the permeability of bones to fluids, which ensures an adequate nutrient supply to surrounding tissues, average values reported in the literature for vertebrae vary from 0.49 to 44.5 x 10^{-9} m^2, depending on the sample selection and preparation (Baroud, Falk, Crookshank, Sponagel, & Steffen, 2004; Nauman, Fong, & Keaveny, 1999; Syahrom, Kadir, Harun, & Öchsner, 2015). In these sources, the absolute permeability k is calculated using Darcy's law by measuring the pressure drop and fluid velocity through a bone sample (Eq (2.5)).

$$k = \frac{Q * \mu}{A * \frac{\Delta p}{L}} \tag{2.5}$$

where Q is the flow rate (m^3/s), μ is the dynamic viscosity (Pa·s), A is the bone sample cross-section (m^2), Δp is the pressure drop across the sample (Pa), and L is the sample length (m).

The objective of this study is to compare two competing lattice structure geometries, namely the strut-based diamond lattice and the sheet-based gyroid lattice, for use in spinal cages (Figure 2.1 a, b). These structures must satisfy the pre-established functional requirements for bone replacement and need to be compared in terms of their geometric, mechanical and fluid permeability attributes. The two types of cellular structures considered in this study resemble the two principal architypes of trabecular bone structure found in the skeleton, notably rod-like and plate-like structures (Lorna J Gibson, 2005). The diamond lattice is composed of struts connected at nodes that correspond to the carbon atom placement in a diamond. One of the advantages of the diamond lattice is its strut orientation, which is convenient for additive manufacturing since it does not require supports. This structure is one of the most studied in the literature, and can be generated using a number of commercial software applications, including *Magics* and *3matic* from the *Materialise* suite, *Workbench-Material Designer* by *Ansys* and *Optistruct* by *Altair Hyperworks*. On the other hand, the sheet-based gyroid lattice is a triply periodic minimal surface structure (TPMS) based on sinusoidal functions. To create these structures, some programming software, such as *Grasshopper* from *Rhino3D* and *MATLAB* by *MathWorks* could be used; software allowing the custom unit cell lattice replication, such as the *Structures Module* of *Magics* or *Simpleware* by *Synopsys*, could also be employed. The gyroid lattice structures were shown to have a greater surface area and mechanical resistance, but lower fluid permeability, than their strut-based equivalents with similar porosities and cell sizes (Al-Ketan et al., 2018; Du Plessis, Yadroitsava, Yadroitsev, le Roux, & Blaine, 2018; Speirs et al., 2017). It is worth noting that some recently-developed software tools such as MSLattice for example, allow the creation of structures with functionally-graded porosity, resulting in lattices with progressive morphology similar to that of bone (Al-Ketan et al., 2020; Han et al., 2018; Liu et al., 2018; Yang et al., 2020; X.-Y. Zhang, Yan, Fang, & Liu, 2020; Zhou et al., 2020). However, an adequate understanding of the behavior of lattice structures with constant porosity represents a necessary prerequisite for the effective practical application of these graded materials.

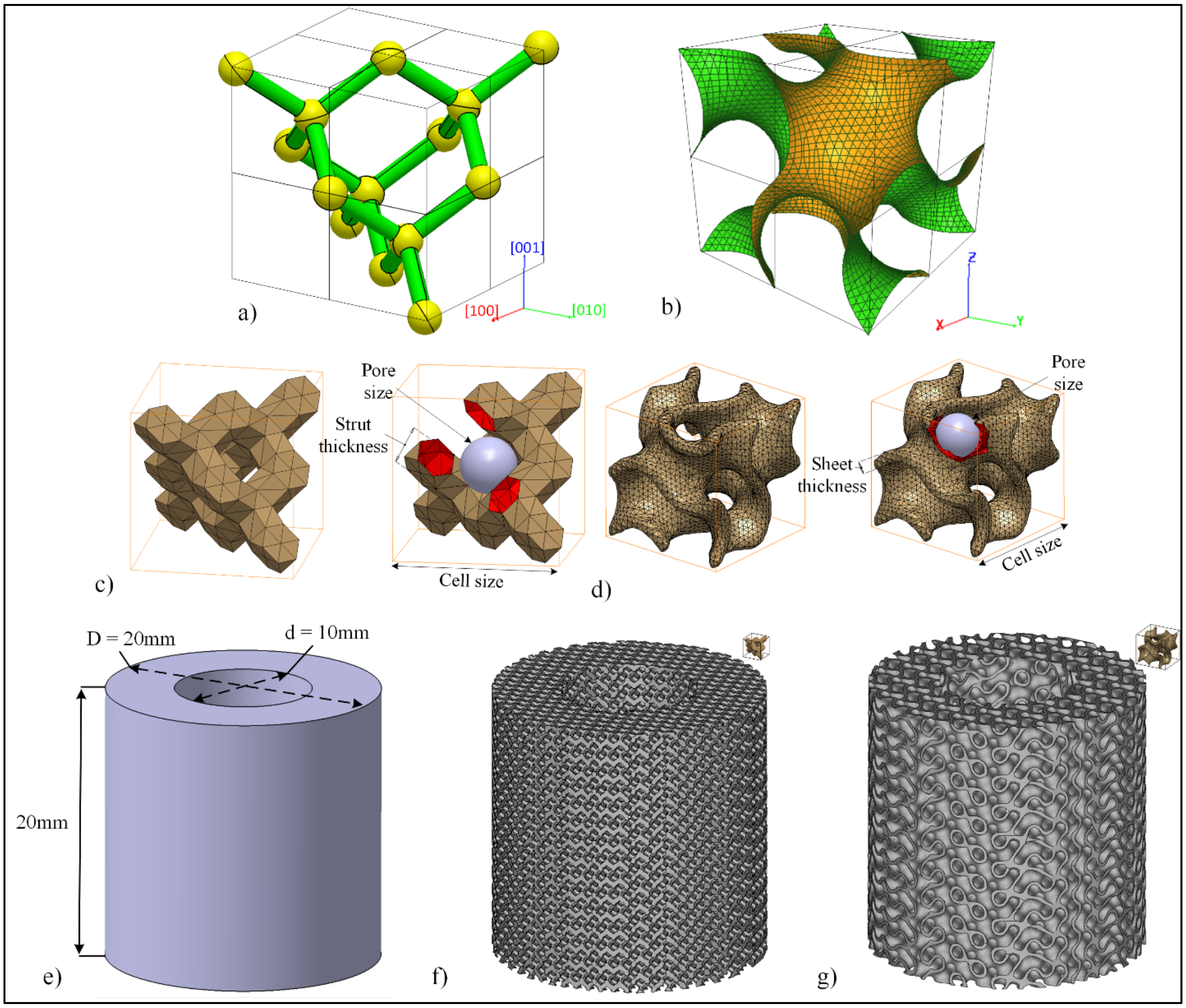
a)
[001]
[100]
[010]
b)
Z
X
Y
Pore size
Strut thickness
Cell size
c)
Sheet thickness
Pore size
Cell size
d)
D = 20mm
d = 10mm
20mm
e)
f)
g)

Figure 2.1 Default unit cell disposition of the a) diamond lattice (Miller indices are added, for convenience), b) gyroid lattice. Unit cell as generated in this study and the control parameters c) diamond lattice and d) gyroid lattice. Specimens for compression testing: e) CAD, f) diamond lattice and g) gyroid lattice

To the authors' knowledge, there are multiple studies analyzing different lattice structures on the basis of their geometry attributes and either mechanical or fluidic permeability characteristics. However, there is a lack of comprehensive studies that compare different lattice structures concurrently on the basis of all three characteristic sets, especially with a specific end-use in mind and in a significantly large range of porosity variations. Among the most recent studies, the following can be mentioned: Yu et al. (2020) studied all three attributes for different lattice geometries (primitive, gyroid, bcc) but with a single porosity level, S. Ma et al. (2020) and Bobbert et al. (2017) analysed the mechanical and the mass-transport properties of lattice structures with different levels of porosity but limited their studies to either gyroid (S. Ma et al., 2020) or sheet TPMS structures (Bobbert et al., 2017). To this end, the lattice geometry and parameters are selected in conformity with the established functional constraints. Then, the selected structures are designed and manufactured using the laser powder bed fusion additive manufacturing technology. Finally, their geometric, mechanical and fluid permeability properties are assessed using computed tomography, compression testing and permeability measurement techniques.

2.6 Materials and methods

2.6.1 Lattice selection

Both types of lattice structures can be defined by three parameters: cell size, strut/sheet thickness and pore size, two of which are independent and can be adjusted to control the porosity (Figure 2.1 c, d). In this work, diamond structures are generated with the help of a proprietary *MATLAB* algorithm (Dumas, Terriault, & Brailovski, 2017), which uses voxelization to create a triangular mesh of struts in the form of hexagonal prisms and connection nodes in the form of truncated tetrahedrons. To create the gyroid structures, the free-access mathematical modelling software *MathMod* is used to generate a zero-thickness mesh of the gyroid, which is then scaled and offset to the desired cell size and sheet thickness in the *CATIA V5* software environment.

Among the three main diamond cell orientations: [001], [011] and [111], the [001] is selected, since it displays a more constant cross-sectional area along the vertical direction, thus reducing the stress riser effect and improving the tensile fatigue resistance of the structure (Soul, Terriault, & Brailovski, 2018). Although some recent works study the impact of the gyroid orientation on its stiffness and strength (Barber, Kelly, Nelson, & Gall, 2021; Caiazzo, Alfieri, & Bujazha, 2021; Maskery & Ashcroft, 2020), they present conflicting results, therefore the gyroid structure orientation is kept by default, and is determined by the governing equation used for its generation (Eq (2.6)):

$$\cos(x) * \sin(y) + \cos(y) * \sin(z) + \cos(z) * \sin(x) = 0 \qquad (2.6)$$

For this study, diamond and gyroid lattice structures with a constant pore diameter of 750 µm and three target porosity levels of 60, 70 and 80% are designed using the lattice parameter sets shown in Tableau 2.2. The pore diameter of 750 µm, which is near the upper limit of the recommended 100-1000 µm range, is selected to favor osseointegration, while keeping pore dimensions large enough from a manufacturing constraints viewpoint (Hara et al., 2016). The porosity window of this study, 60-80%, is determined based on the geometric limitations of gyroid structures, which have inherently larger cell sizes and thinner sheets than diamond structures of the same porosity. For example, to keep a minimum of two contiguous cells along the intravertebral height of ~5 mm (Belytschko, Kulak, Schultz, & Galante, 1974; Pooni, Hukins, Harris, Hilton, & Davies, 1986), a unitary gyroid cell cannot be bigger than 2.5 mm (2500 µm), which results in a porosity of 60%. At an upper level of 80%, the minimal sheet thickness of ~100 µm of the gyroid structures is close to the manufacturing limits of most laser powder bed fusion (LPBF) additive manufacturing systems (Khorasani, Gibson, Veetil, & Ghasemi, 2020). The middle value of 70% is selected to provide a minimum of three data points for the generation of scaling relations. It is worth noting that the highest level of porosity in this study corresponds to 80%; higher porosity levels are achievable by increasing the cell size or by reducing the strut thickness, as shown in A Yánez et al. (2018). The porosity and the surface-to-volume ratio of both structures are calculated by extracting the total volume, the object volume and the object surface area using the mesh analysis (Tableau 2.2).

Tableau 2.2 Selected diamond/gyroid lattice structure geometric parameters for a pore size of 750 µm and target porosities of 60, 70 and 80%

	Strut [µm]	Cell [µm]	Porosity [%]	S/V [mm^{-1}]
Diamond	455	1485	62.2	2.66
	345	1336	71.0	2.82
	240	1193	80.9	2.81
Gyroid	305	2431	61.0	2.40
	210	2191	70.2	2.74
	125	1977	80.1	3.10

2.6.2 Experimental testing

The design of hollow cylinder compression testing specimens is based on the geometry of an average cervical disc, with an outer diameter of 20 mm and an inner diameter of 10 mm. Their height is set to 20 mm in order to respect the ISO13314 standard for compression testing of cellular materials (ISO13314, 2011), which requires a height-to-diameter ratio of ~1-2. The porous specimens are generated by Boolean intersection between an oversized lattice structure and the specimens' CAD (Figure 2.1 e, f, g). Similarly, full cylinder permeability testing specimens with an outer diameter of 10 mm and a height of 20 mm are also created.

Specimen manufacturing is carried out on a *TruPrint1000* LPBF system (*Trumpf*) with a laser spot size of 30 µm. The material used in this study is Ti64-ELI which has a tabulated modulus of elasticity of 114 GPa and a yield strength of 1120 MPa (Jetté, Brailovski, Dumas, Simoneau, & Terriault, 2018). The powder particle size distribution as provided by the manufacturer is 15-45 µm. The default printing parameters indicated by Trumpf are used: 155 W laser power, 1200 mm/s scanning speed, 110 µm hatching space and 20 µm layer thickness. Preliminary prints indicated a 70 µm manufacturing error, which is accounted for in the actual design of the cellular structures. Two specimens for mechanical testing and one specimen for permeability testing of the diamond and gyroid structures with target porosities of 60, 70 and 80% are manufactured, bringing a total number of specimens to 18 (Figure 2.2).

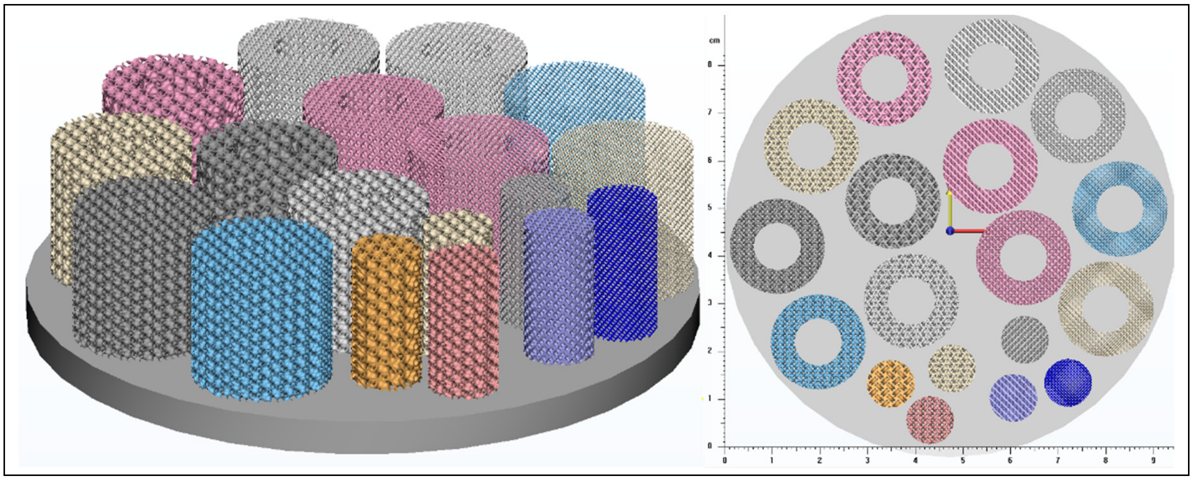

Figure 2.2 Specimen distribution on the build plate

Prior to part separation from the build plate, a dual stage heat treatment (DSHT) under vacuum (45 min at 1010 °C followed by 1 h at 850 °C) is performed following the recommendations of the equipment manufacturer. Specimens are cut by wire EDM and cleaned using high-pressure water.

The resulting structures are scanned using an *XTH225* micro computed tomography (μ-CT) system (*Nikon*) with a 190 kV tube voltage, 50 μA current and 10.8 μm resolution. The scans are reconstructed using *CT Pro 3D* software (*Nikon*) to generate TIFF image stacks. *VGStudio MAX 3.1* software (*Volume Graphics*) is used to convert the image stacks to volumes and compare these volumes to the respective CAD models. Analyses of the specimen geometry in terms of porosity, strut thickness and pore diameter are also carried out (Figure 2.3).

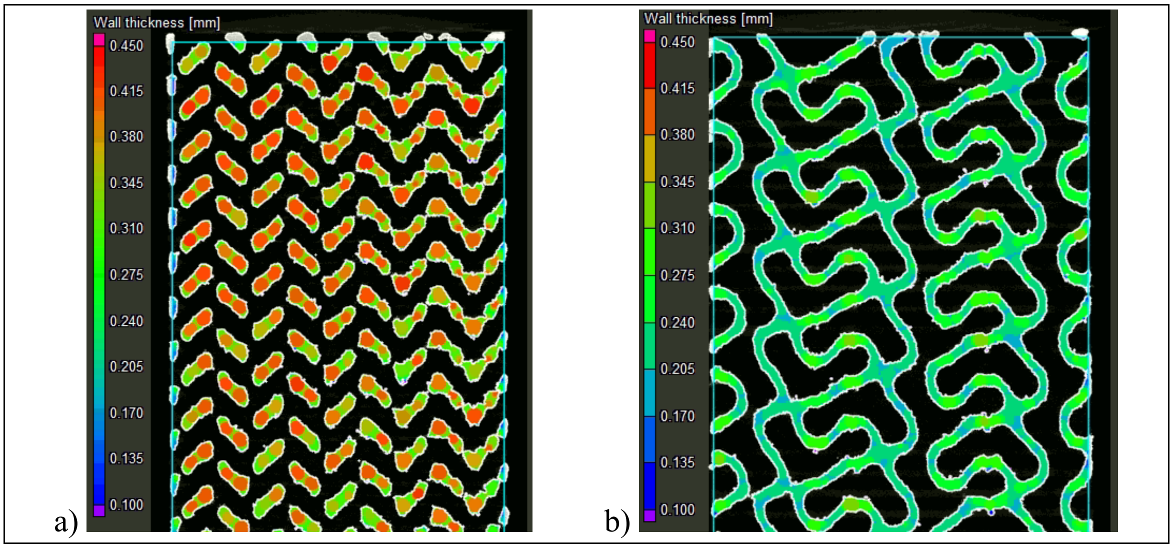

Figure 2.3 Specimen strut thickness measurements in ~70% porosity structures using the sphere method in VGStudio MAX software: a) diamond and b) gyroid structures

Next, an experimental porosity evaluation is conducted in conformity with the ASTM F2450-18 standard by calculating the volume of the matter in the total volume of the specimen measuring its mass (*Acculab L-series* scale, ±0.0001 g) and geometry (*Mitutoyo Absolute* caliper, ±0.01 mm) (ASTM, 2018). To that end, Eq (2.4) is used where the volume of material is calculated by dividing the specimen mass by its density (4.43 g/cm^3 for Ti-6Al-4V), and the total volume is calculated based on the specimen diameter and height.

Two previous porosity measurements are verified using Archimedes' technique (ASTM B963-18) (ASTM, 2017a). To this end, specimens are weighed three times: dry, impregnated with oil (*Mobil SHC 634*), and submerged in water while oil-impregnated (*Sartorius Secura 324-1s* scale, ±0.0001 g) (Eq (2.7)).

$$\varphi\,(\%) = \left(\frac{m_{oil} - m_{dry}}{(m_{oil} - m_{oil\,water}) * \rho_o} * 100\right) * \rho_w \tag{2.7}$$

where m_{dry} is the mass of the dry specimen (g), m_{oil} is the mass of the specimen impregnated with oil (g), $m_{oil\,water}$ is the mass of the oil-impregnated specimen submerged in water, ρ_o is the relative density of oil (0.87) and ρ_w is the water density (0.9977 g/cm^3); both at room temperature.

Next, one specimen of each structure is placed between parallel lubricated platens and tested in compression on an *Instron 150LX* materials testing system at a displacement rate of 5 mm/min until densification onset. The compression rate falls within a recommended range of 10^{-3}-10^{-2} s^{-1} (ISO13314, 2011). The acquired force-displacement data are converted to the stress-strain diagrams using the specimen cross-section and length, and the apparent modulus of elasticity and yield strength values are then extracted.

The structures' permeability is measured using an in-house manufactured setup (Figure 2.4). Distilled water is pumped through the specimen using a *Levitronix PTM-1* pump mixer assembly with a flow range of 0 to 17 L/min. The flow is measured using a *Leviflow LFS-20-Z* 0 to 20 L/min sensor with an accuracy of ±1%. Prior to testing, specimens undergo an ultrasonic bath cleaning to remove any loosely bonded particles inside the structure. To avoid bypass flow, the lateral walls of the permeability specimens are wrapped using PTFE tape. The differential pressure between the inlet and outlet ports is measured using an *Omega PX26* differential transducer with a capacity of ±1 bar and an accuracy of ±1%. An *Omega DPG4000-15-RM* high accuracy (±0.05%) digital pressure gauge is used to calibrate the differential transducer in the 0-0.4 bar measurement range.

A *National Instruments USB-6212* data acquisition card and the *LabView 2018* software are used to acquire and register data from the flowmeter and the pressure transducer. Measurements are carried out from 0.4 to 2 L/min in increments of 0.1 L/min under steady state conditions, and the results obtained are approximated by a power law. Next, the flow and pressure drop values are extrapolated for the Reynolds numbers ranging from 1 to 10 to fall within the definition of the Darcy regime (Bobbert et al., 2017; Hassanizadeh & Gray, 1987; Sobieski & Trykozko, 2014; Sukop, Huang, Alvarez, Variano, & Cunningham, 2013). To calculate the Reynolds number, equation (2.8) is used:

$$Re = \frac{\rho * v_f * l}{\mu} \tag{2.8}$$

where ρ is the fluid density (997 kg/m^3 for water), v_f is the fluid velocity (m/s) also equal to flow Q (m^3/s) divided by specimen cross-section A (m^2), l is the pore diameter (m) as measured from the CT-scan and μ is the dynamic viscosity of the fluid (0.001 Pa·s for water).

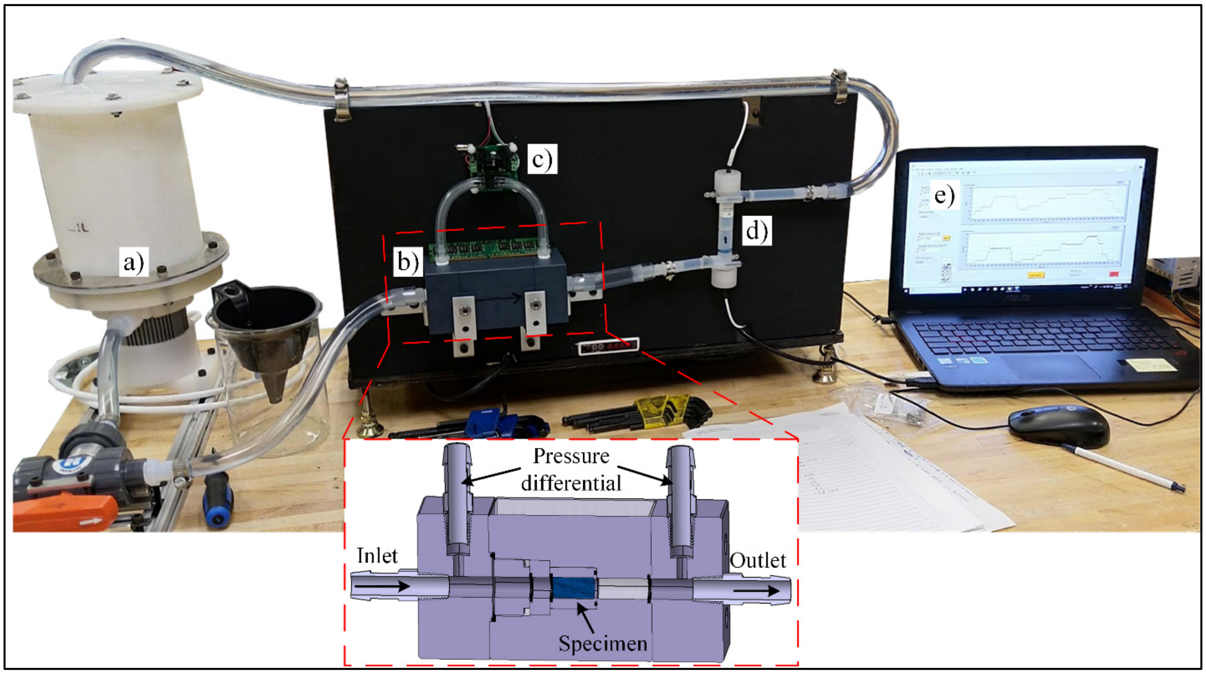

Figure 2.4 Permeability test setup: a) mixer tank/pump assembly, b) specimen holder, c) differential pressure transducer, d) flowmeter and e) laptop with LabView for data treatment. Not shown on the image are the power supply, pump controller and data acquisition card

2.7 Results

A visual comparison between the designed and manufactured geometries indicates a shrinkage in the build direction (Figure 2.5). All manufactured structures show deviations situated between ±100 and ±250 μm for 10-25% of their total surface; the remaining 75-90% of their surface falls within the ±100 μm range of deviations from the CAD geometry. No powder plugging can be observed inside the structures which would affect the mechanical or permeability measurements.

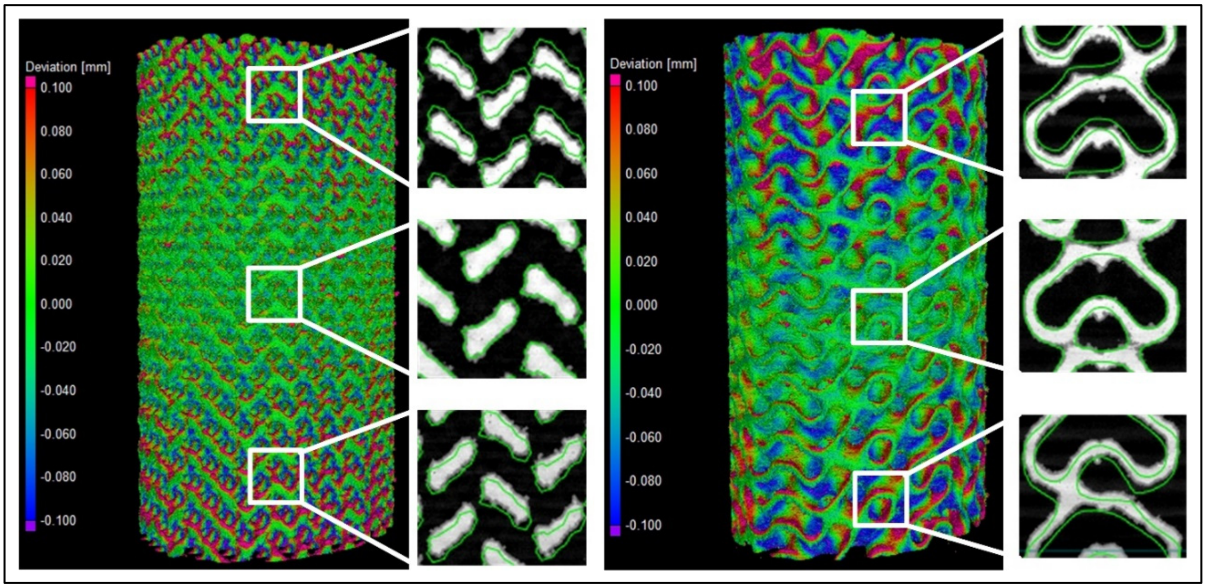

Figure 2.5 Deviation maps between the designed and manufactured 70% diamond and gyroid structures following a best-fit: the detailed views show the design in a green outline and the scanned structure in solid white

Figure 2.6 summarizes the results of the geometric comparison between the designed and manufactured structures. All the manufactured structures have a slightly lower porosity than the designed ones, no matter the measurement technique (Figure 2.6 a). The manufactured 60 and 70% porosity specimens are generally closer to the designed ones than the 80% specimens. The highest discrepancy among the three competing porosity measurement techniques (VG Studio, ASTM F2450 and Archimedes' ASTM B963) corresponds to 3.9% of porosity, and the results obtained using the ASTM F2450 approach are generally higher. These last porosity values will be used for all the following representations and comparisons.

Notwithstanding with the above, the strut thicknesses of the manufactured diamond structures are closer to the designed values than those of their gyroid equivalents (Figure 2.6 b, c). For all the structures, the pore diameters of the manufactured specimens are smaller than those of the designed ones, with the pores of the diamond structures being smaller than those of the gyroid structures (Figure 2.6 d, e). The 80% porosity gyroid structures seem to approach the limits of the manufacturing system, since their sheet thickness and pore diameter diverge the most from their designed equivalents.

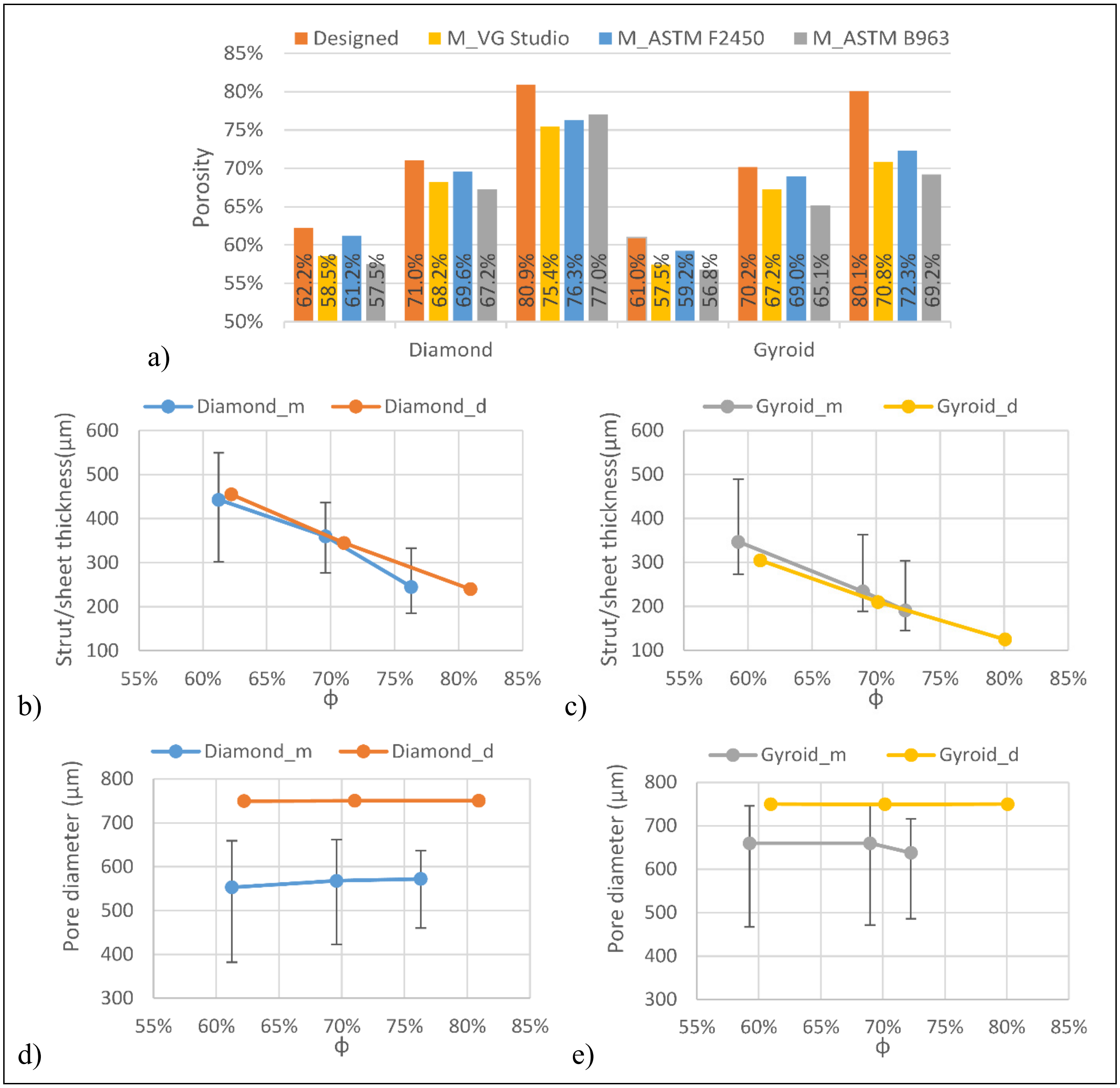

Figure 2.6 Comparison of the designed (d) and manufactured (m) diamond and gyroid structures: a) porosity, b) diamond strut thickness, c) gyroid sheet thickness, d) diamond pore diameter, and e) gyroid pore diameter

Considering the mechanical behavior (Figure 2.7 a, b), the diamond lattice structures (Figure 2.7 a) exhibit a more unstable behavior after reaching the peak stress than do their gyroid equivalents (Figure 2.7 b). That indicates a sudden collapse of certain struts in the diamond structures, as opposed to the gyroid lattices, in which the cell collapse is more gradual. A similar behavior was observed by Al-Ketan et al. (2018) and Zhou et al. (2020), where strut- and skeletal-based structures experienced larger stress variations following the first maximum compressive strength than the sheet-based structures.

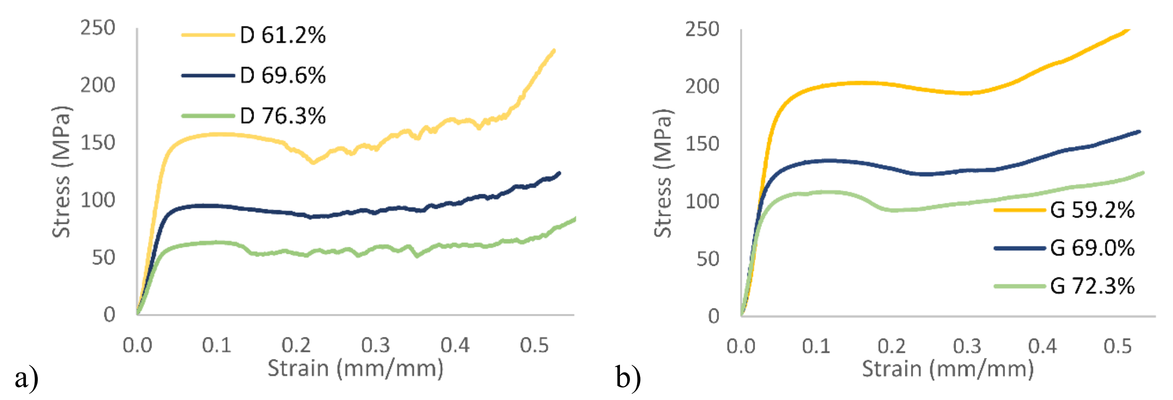

Figure 2.7 Stress-strain diagrams: a) diamond and b) gyroid structures

Figure 2.8 illustrates the deformation of the specimens during compression testing and the onset of densification in the structures, which occurs at a strain level of ~30%. From a mechanical properties' standpoint, it can be seen that the gyroid lattice is stiffer and stronger than its diamond counterpart for the same levels of porosity (Figure 2.9 a, b).

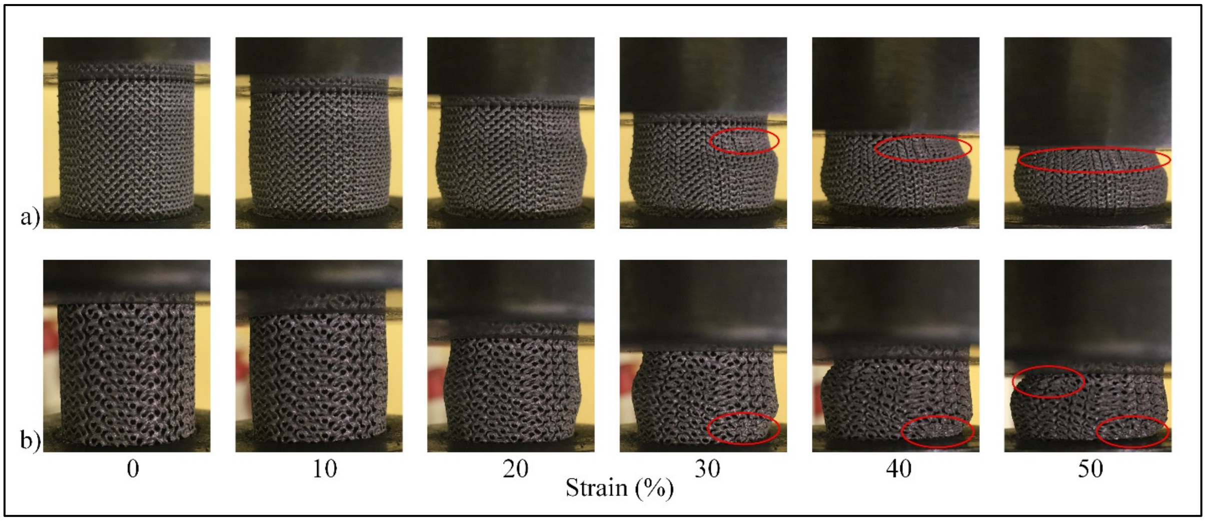

Figure 2.8 Compression testing of ~70% porosity structures: a) diamond and b) gyroid sample shape evolution during compression at various compression strain values. Areas where densification is observed are circled in red

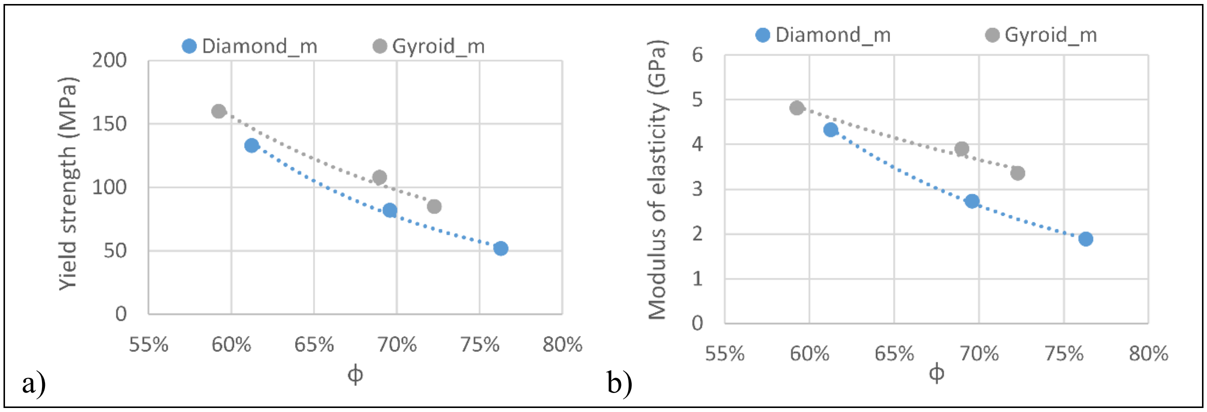

Figure 2.9 Apparent mechanical characteristics of the manufactured structures: a) yield strength and b) modulus of elasticity

Figure 2.10 shows the experimental flow and pressure drop measurements for all the studied lattice structures along with their respective fitted power law curves. All fitted equations had R^2 correlation factors over 99.97%. The Darcy regime corresponds to flow rates situated between 0.007 and 0.08 L/min, where the Reynolds number ranges from 1 to 10. These flow rate values are in the same range as those used for permeability testing of bone or engineered lattice structures in (Bobbert et al., 2017; Castro, Pires, Santos, Gouveia, & Fernandes, 2019; Nauman et al., 1999; Syahrom et al., 2015), and the fluid velocities (flow *Q*/area *A*) are in the same range as those used for fluid flow stimulation of bone cells (Estermann & Scheiner, 2018). The permeabilities of the manufactured structures corresponding to the Darcy regime region are plotted in Figure 2.11.

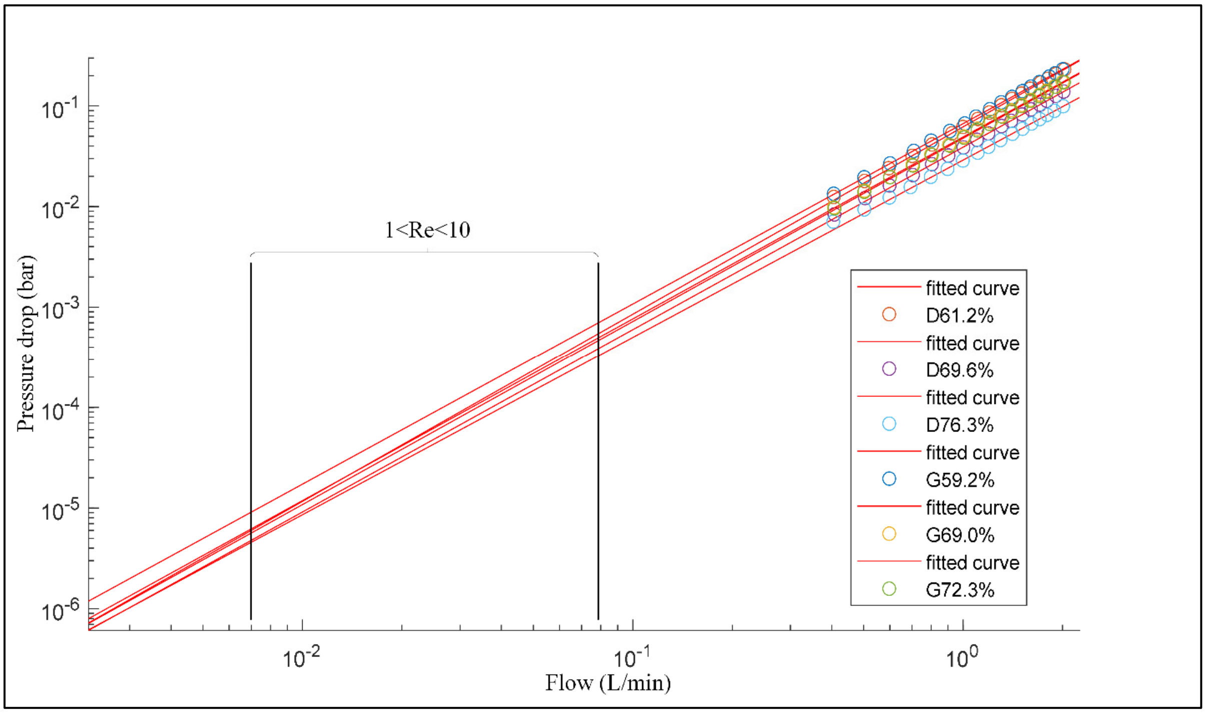

Figure 2.10 Flow and pressure drop experimental measurements, where D signifies diamond and G gyroid structures of different porosities; black rectangle delimits the extrapolated range where Reynolds number varies between 1 and 10

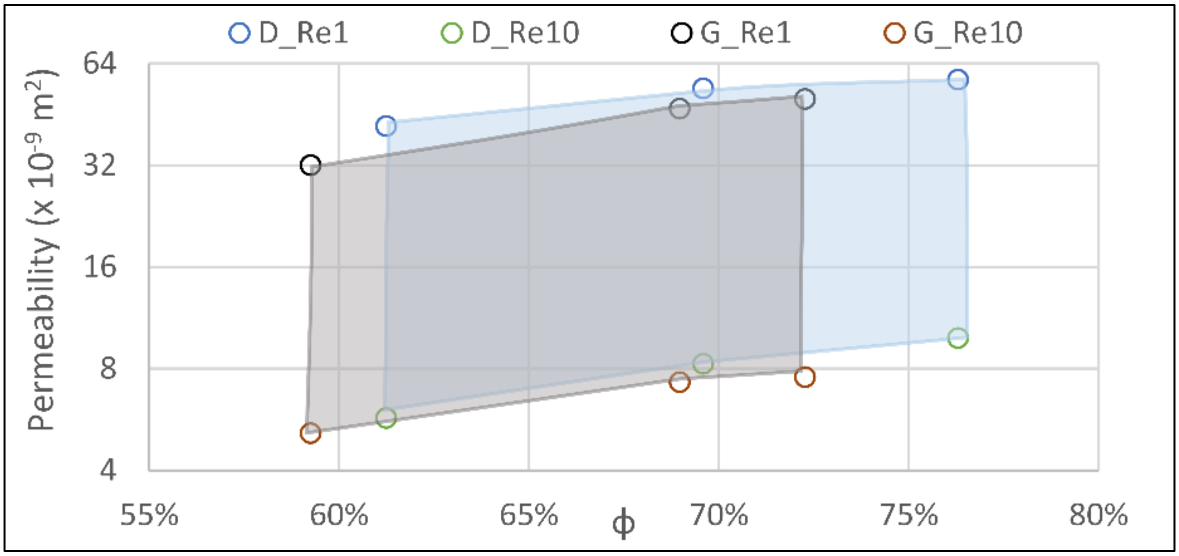

Figure 2.11 Permeability results from the extrapolated data are shown as the regions of the Darcy regime (Re1 and Re10 correspond to Reynolds numbers of 1 and 10); diamond (D) structures are presented in blue and gyroid (G) structures in grey

From the data obtained, the following scaling relations can be extracted for the yield strength, the modulus of elasticity and the permeability of both structures. These relations can help to predict the behavior of lattice structures having a constant pore size of 750 μm for varying levels of porosity. The modulus of elasticity and yield strength equations follow the Gibson and Ashby $X=C*(1-\varphi)^n$ scaling relation format (Tableau 2.3). The permeability equation fitting the Kozeny-Carman formulation yields negative R^2 values, meaning that a horizontal line is a better fit than the formulation, and therefore, the classical Gibson and Ashby formulation is used in this case also.

2.8 Discussion

Vertical shrinkage identified during the geometrical analysis of all the specimens of this study is explained by the use of a rubber blade in the powder recoating assembly of a Trumpf LPBF system. Contrary to less compliant metallic blades, rubber blades allow positive vertical deformations caused by thermal stresses, and result in lesser compressed, and therefore, more vertically shrunk structures. In the manufactured structures, the overall porosity is lower than designed, which can be partly attributed to the powder particles sintered to the surface. In order to get rid of the sintered particles and come closer to the desired porosity, a more thorough cleaning or etching may be warranted. This effect is also responsible for the smaller than designed pore diameters as seen in Figure 2.12. Another concern regarding weakly-bonded particles is the risk of their loosening after implantation which could pose health problems from ion release in other parts of the body. High concentrations of powder particles (>1x10^5 particles/mL) are known to affect cell viability indicating the need to minimise the quantity of surface-sintered particles (J. Tang et al., 2020).

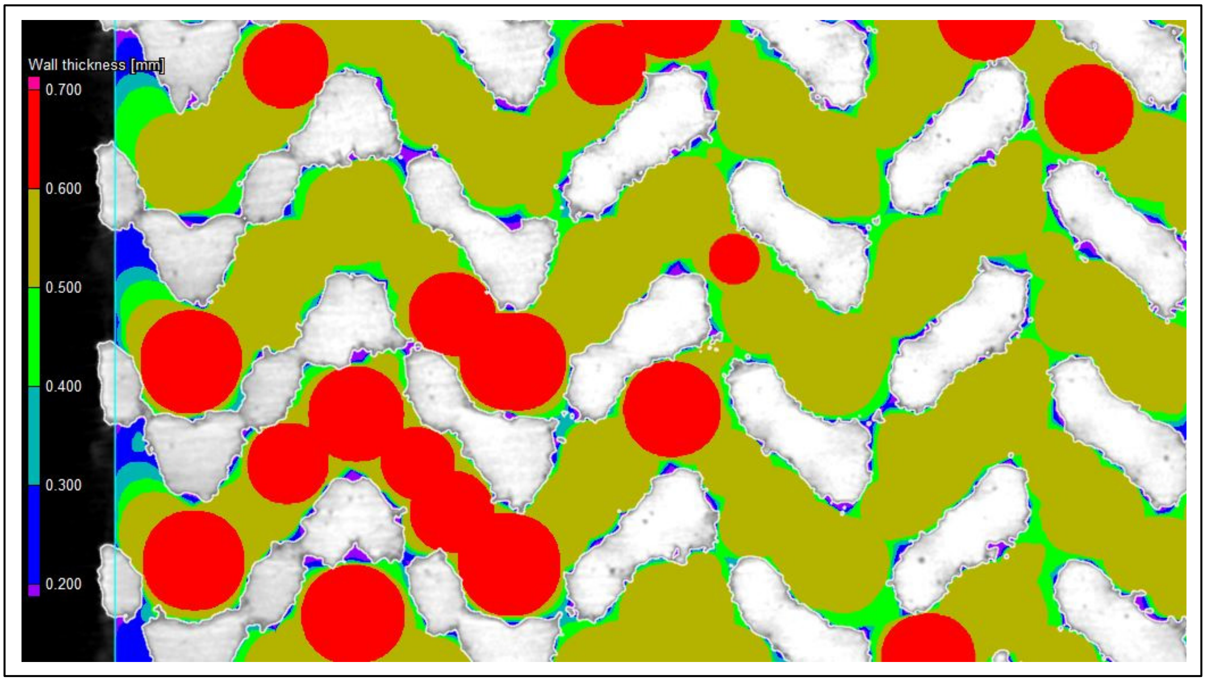

Figure 2.12 Surface roughness and sintered particles' impact on pore diameter measurement of the diamond lattice. The scanned structure in white and pore evaluation is color-coded

Among the three porosity measurement techniques used in this study, each has its own set of drawbacks. The porosity value resulting from CT-scans is highly dependent on the threshold value used. The porosity values measured using ASTM F2450 are affected by the diameter and height measurements, which, in their turn may be overestimated due to the as-built surface roughness. Lastly, the porosity obtained using Archimedes' technique (ASTM B963) depends on the quality of the oil impregnation and weighting procedures (all voids must be filled with oil and this oil must be kept inside the specimen during all the manipulations to improve precision of these measurements).

The deviations in terms of the strut/sheet thickness and pore diameter between the manufactured and designed specimens can be further explained by the fact that the preliminarily determined 70 µm laser compensation is only viable for the X-Y manufacturing plane and not in the Z build direction, where the melt pool depth and not the laser path, determines the process accuracy. To correct the build direction accuracy would require a tuning of the printing parameters such as the laser power and the scanning speed. Some studies have noted this effect and developed an optimization procedure to compensate for such a discrepancy (Bobbert et al., 2017). The gyroid lattice manufactured with the highest target porosity of 80% presents the largest deviations from the designed structure which can affect the testing results, notably the fluidic permeability. Nonetheless, a porosity range of ~60-75% and a pore diameter range of 550-660 µm of the manufactured structures fall within the recommended ranges for porous implants - 30-70% porosity and 100-1000 µm pore diameter range. It can be hypothesized that spinal cages integrating such porous structures would favor osseointegration, and therefore, enhance the implant fixation quality.

Tableau 2.3 Scaling relations for modulus of elasticity, yield strength and permeability of the diamond and gyroid structures; Re1 and Re10 correspond to Reynolds numbers of 1 and 10

Diamond	$E_{app} = E * 0.1977 * (1-\varphi)^{1.747}$	R^2.9965
	${S_y}_{app} = S_y * 0.7427 * (1-\varphi)^{1.937}$	R^2.9995
	Extrapolated $k_{Re1} = 23.56 * 10^{-9} * (1-\varphi)^{-0.5978}$ Extrapolated $k_{Re10} = 2.159 * 10^{-9} * (1-\varphi)^{-1.031}$	R^2.8671 R^2.9543
Gyroid	$E_{app} = E * 0.0938 * (1-\varphi)^{0.884}$	R^2.9826
	${S_y}_{app} = S_y * 0.5865 * (1-\varphi)^{1.569}$	R^2.9936
	Extrapolated $k_{Re1} = 10.94 * 10^{-9} * (1-\varphi)^{-1.166}$ Extrapolated $k_{Re10} = 2.041 * 10^{-9} * (1-\varphi)^{-1.002}$	R^2.9700 R^2.9477

The mechanical properties of the manufactured structures also correspond to the defined set of functional requirements (Tableau 2.4). The modulus of elasticity, ranging from 1.9 to 4.8 GPa, is situated between that of cortical bone (7-30 GPa) and that of trabecular bone (0.043-0.165 GPa). Next, the yield stress of the lattice structures (52-160 MPa) is in the same range as that of cortical bone (42-176 MPa), being from 5- to 15- times higher than that of trabecular bone (0.2-10.5 MPa) (Figure 2.13).

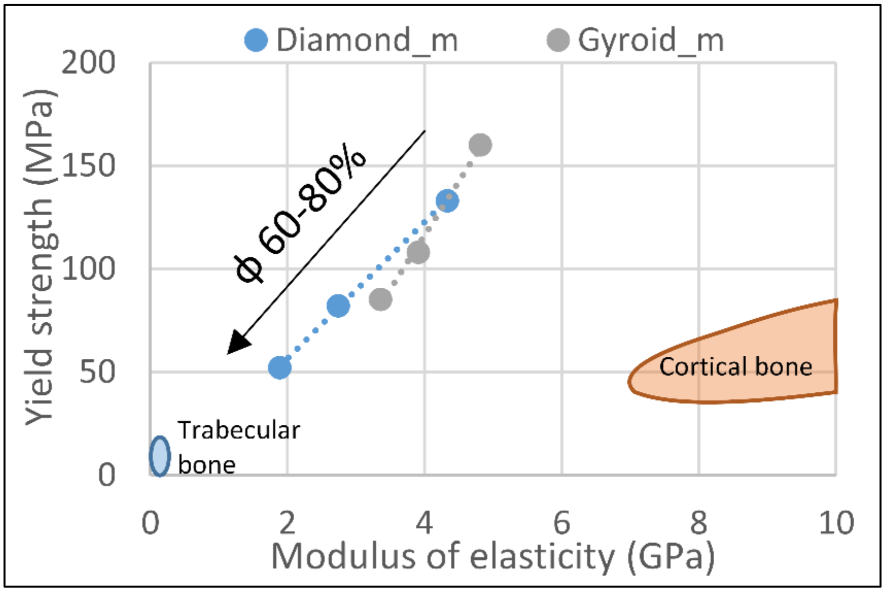

Figure 2.13 Yield strength vs modulus of elasticity comparison of the manufactured structures and bone tissues

At higher levels of porosity, the yield strength of the diamond structures is 52 MPa and that of the gyroid structures, 85 MPa, meaning that a porous spinal cage can cover only ~12% of the vertebral face contact area and still be as resistant as the vertebrae itself. This can allow the use of smaller spinal devices, requiring less invasive surgery and easier rehabilitation. However, such smaller devices would result in higher local stresses in surrounding vertebrae, increasing the risk of implant subsidence and bone failure. Therefore, the porous implant must be optimized to facilitate surgery, while reducing such risks of post-surgery complications.

Tableau 2.4 Mechanical properties of biological tissues, commonly used spinal cage materials and manufactured lattice structures

			Sy / failure stress* [MPa]	Young's Modulus E [GPa]	*Sy*/*E* [x 10^{-3}]	*S*/*V* [mm^{-1}]	Permeability [x 10^{-9} m^2]
Cortical bone			42 - 176	7 - 30	5.9 - 6	2 - 4	0.5 - 44.5
Trabecular bone			0.2 - 10.5	0.043 - 0.165	5 - 60	1 - 6	
Vertebrae			3 - 6*	0.374	8 - 16	2 - 3	
PEEK (MatWeb, 2019)			97.5	3.9	25	-	-
Ti-6Al-4V (Dumas et al., 2017)			1120	114	9.8	-	-
Ti64 Diamond lattice	φ [%]	61.2	133	4.3	30.7	3.43	5.71 - 41.7
		69.6	82	2.7	30.0	3.50	8.26 - 53.9
		76.3	52	1.9	27.6	3.52	9.84 - 57.2
Ti64 Gyroid lattice	φ [%]	59.2	160	4.8	33.3	3.04	5.15 - 32.0
		69.0	108	3.9	27.6	3.35	7.28 - 46.9
		72.3	85	3.4	25.3	3.66	7.55 - 50.1

Strength-to-stiffness ratios of 25-33 x 10^{-3} are achieved with the lattice structures of this study, which are much higher than those of bulk metals, having *Sy*/*E* ratios of ~10 x 10^{-3}, and are in the same range as PEEK at ~25 x 10^{-3} (Tableau 2.4). Compared to fully dense Ti-6Al-4V, this represents a 24-60-fold decrease in the modulus of elasticity, while only reducing the yield stress by a factor of 7-21, indicating that the porous structures greatly outperform their bulk equivalents currently used in spinal devices. The strength-to-stiffness ratios of the diamond lattices are slightly lower than those of the gyroid lattices at lower porosities, while at higher porosities, the situation is reversed (Figure 2.14 a). This effect originates from the stiffness of gyroid structures which is less influenced by porosity variations as compared to the diamond structures (Figure 2.9). Though it may seem counterintuitive, the *Sy/E* ratio of the gyroid lattice is more porosity-sensitive than that of its diamond equivalent. For example, when φ increases from 60 to 80%, the *Sy/E* ratio of the former decreases by ~24%, while the latter, only by ~10%. Since the *Sy/E* criterion should be maximized, the gyroid lattice is more suited for porosities lower than ~63%, and the diamond lattice, for porosities above this threshold. When compared to the *Sy/E* of bone tissues (Figure 2.14 c), the lattice structures exhibit higher ratios than cortical bone (~6 x 10^{-3}) and vertebrae (8-16 x 10^{-3}), but are situated in the same range as trabecular bone (5-60 x 10^{-3}).

The *S/V* ratios of all the manufactured structures are higher than the designed values (Tableau 2.2 and Figure 2.14 b), which is mainly due to sintering of powder particles to the part surface. At lower porosities, the gyroid lattices exhibit smaller *S/V* values than the diamond lattices, but overtake them at ~70% (Figure 2.14 b). Since a higher surface-to-volume ratio is better for the application, for porosities under 70%, diamond structures appear to be more advantageous, while above 70%, gyroid structures prevail. As with the *Sy/E* criterion, the *S/V* ratio of the diamond structures is less porosity-dependent (~3% increase when φ increases from 60 to 80%) than that of the gyroid structures (~15% increase). Finally, all the studied structures have *S/V* ratios in the range of 3-4 mm^{-1}, which corresponds to the mean *S/V* value of trabecular bones, and is significantly higher than that of vertebrae (Figure 2.14 c).

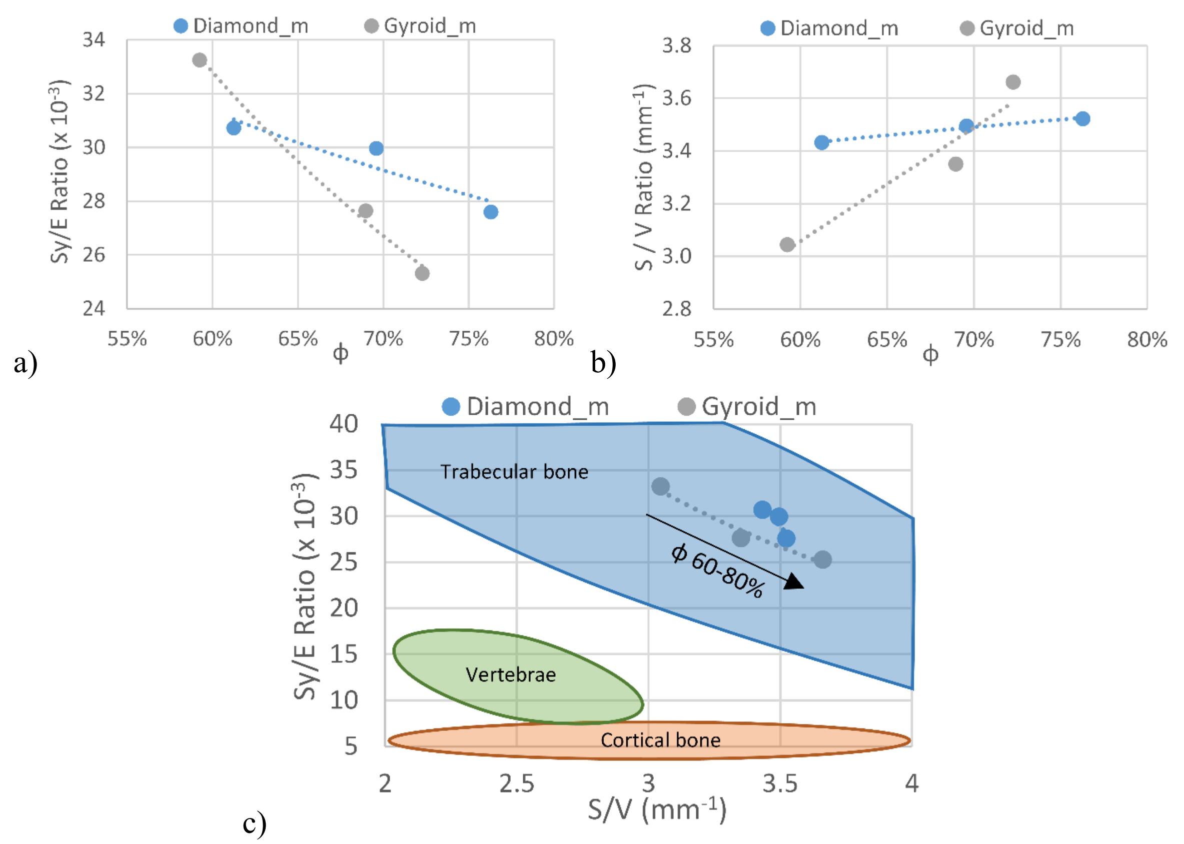

Figure 2.14 (a) Strength-to-stiffness, (b) surface-to-volume ratios of the manufactured structures and (c) their comparison with bone tissues in the Sy/E - S/V space

The permeability extrapolated to the Darcy regime range (Tableau 2.4) indicates that the diamond structures are more permeable across the range of porosities of this study, which is in agreement with previous research showing that strut-based lattices are more permeable than their sheet-based equivalents (Du Plessis et al., 2018). Nonetheless, all the obtained permeability values range from 5.15 to 57.2 x 10^{-9} m^2, thus covering the reported vertebrae permeability range of 0.49 to 44.5 x 10^{-9} m^2.

The difference in the *Sy/E* and *S/V* ratios between the two structures is fairly small as compared to the ranges covered by bone tissues. In addition, the two criteria indicate some ambiguity and do not allow selecting a better candidate between the two analyzed structures. While the permeability results indicate that the diamond structures are marginally better suited for spinal cages applications than the gyroid structures, the latter are stronger and contain a lesser amount of stress risers as demonstrated by their respective failure modes. In fact, given the small difference of *Sy/E* values between the two structures, the gyroid structures, which manifest higher mechanical resistance, appear to be more advantageous. In addition, according to the literature (Speirs et al., 2017), the less pronounced stress riser effect could bring an even more significant advantage of gyroid structures in terms of their fatigue resistance.

While a comparison between the present results and other studies could be beneficial, there is a large disparity between the current work and the literature in terms of lattice design, porosity level and pore size. This discrepancy results in a limited overlap between studies, rendering direct comparisons almost impossible. Notwithstanding that, the mechanical response of the ~60% porous gyroid structure studied in this work (*E*=4.8 GPa and *Sy*=160 MPa) is very close to that of the ~60% porous gyroid structures in Bobbert et al (Bobbert et al., 2017): *E*=4-6 GPa and *Sy*=150-200 MPa. Furthermore, the fluidic permeability of gyroid structures of this study (5-50 x 10^{-9} m^2) is of the same order of magnitude as its equivalents in Bobbert et al (Bobbert et al., 2017) (1-3 x 10^{-9} m^2), Ma et al (S. Ma et al., 2020) (0.25-5 x 10^{-9} m^2) and Castro et al (Castro et al., 2019) (25-120 x 10^{-9} m^2).

This study is aimed at filling the gap in terms of a concurrent assessment of the geometric, mechanical and fluid permeability properties of the diamond- and gyroid-based lattice structures with identical porosities and pore sizes, and their conformity with the functional requirements of spinal cages. Among the limitations of this study are a relatively limited range of analyzed porosities (60-80%) and the application of just the compression mechanical testing mode. In the continuation, in addition to the mandatory fatigue testing, the mechanical properties must be evaluated not only for compression, but also for bending and torsion, since these testing modes approximate the real loading conditions in the spine.

2.9 Conclusion

This experimental study covered the selection and comparison of two competing lattice structures for use in intervertebral cages. Their geometric, mechanical and fluid permeability properties were analyzed experimentally and compared to spinal implants functional requirements. Results reveal that the above-mentioned attributes of the diamond and gyroid lattices fall within the established requirements, providing potential solutions for reducing the complication rates of spinal devices by offering a better fixation through osseointegration. The diamond and gyroid lattice structures provide very similar results under this study's testing conditions. The major differences are in the failure mode, which consists of sudden buckling of certain struts in the diamond lattice, while the gyroid lattice exhibits a more progressive failure via the collapse of lattice walls. This would seem to indicate, as previously stipulated, that stresses are distributed more uniformly in the gyroid lattices than in their diamond equivalents, which promise greater fatigue resistance. The stiffness of both structures (1.9-4.8 GPa) is much lower than that of the dense material used for their manufacture (~100 GPa), while their mechanical resistance (52-160 MPa) is greater than that of vertebrae (3-6 MPa), thus decreasing the risks of bone and implant failure. The small differences between the *Sy/E* (25-33 x 10^{-3}) and *S/V* (3-4 mm^{-1}) ratios of both structures make it difficult to select a better-suited candidate for the application. The fluid permeability (5-57 x 10^{-9} m^2) and *S/V* ratios of both lattice structures are close to those of vertebrae, promising an adequate osseointegration. Further work should focus on the fatigue resistance of the gyroid and diamond lattice under different loading modes, including compression, tension and torsion.

2.10 CRediT authorship contribution statement

Anatolie Timercan: Conceptualization, Methodology, Software, Formal analysis, Investigation, Writing - Original Draft, Visualization **Vadim Sheremetyev**: Methodology, Investigation, Resources, Writing - Review & Editing, **Vladimir Brailovski**: Conceptualization, Resources, Writing - Original Draft, Visualization, Supervision, Project administration, Funding acquisition.

2.11 Disclosure statement

No potential competing interest was reported by the authors.

2.12 Acknowledgements

The authors would like to acknowledge CONMET LLC for their investment and contribution to the manufacture of specimens for this study. In addition, this study would not be possible without the financial support from the Fonds de Développement de l'École de Technologie Supérieure (FDÉTS) through A. Timercan's scholarship for ÉTS' bachelor's graduates, the Fonds de recherche du Québec - Nature et technologies (FRQNT) [grant number 272262], and V. Brailovski's Discovery grant from the Natural Sciences and Engineering Research Council of Canada (NSERC).

2.13 Data availability statement

The raw/processed data required to reproduce these findings cannot be shared at this time as the data also forms part of an ongoing study.

CHAPITRE 3

AXIAL TENSION/COMPRESSION AND TORSIONAL LOADING OF DIAMOND AND GYROID LATTICE STRUCTURES FOR BIOMEDICAL IMPLANTS: SIMULATION AND EXPERIMENT

Anatolie Timercan [1], Patrick Terriault [1] and Vladimir Brailovski [1]

[1] Department of Mechanical Engineering, École de Technologie Supérieure, 1100 Notre-Dame West, Montreal, Quebec, Canada H3C 1K3

Article publié dans la revue « Materials and Design », le 2 janvier 2023

3.1 Avant-propos

En se basant sur les résultats du premier article, cette deuxième publication sert à approfondir les connaissances des propriétés mécaniques des structures en diamant et gyroide en analysant le comportement de ces structures sous différents modes de chargement. Un concept d'échantillon pouvant être testé en compression, en tension et en torsion est développé, et des spécimens sont fabriqués à partir d'alliage de Ti64 et caractérisés géométriquement et mécaniquement. De plus, un modèle numérique par éléments finis est bâti pour simuler le comportement des structures architecturées. Ce modèle, une fois validé, peut servir à anticiper le comportement de telles structures fabriquées à partir d'alliages comme le Ti-Ni.

3.2 Résumé

Les structures architecturées sont de plus en plus utilisées dans le domaine biomédical, notamment dans les cages intervertébrales, nécessitant une meilleure compréhension de leur comportement sous différents modes de chargement qu'elles subissent lors de leur application. Des structures en diamant à base de poutres et des structures gyroides à base de feuille avec des niveaux de porosité variant de 50 à 80% et une taille de pore constante de 750 µm ont été conçues et fabriquées à partir de l'alliage Ti6Al4V. Les spécimens ont été testés expérimentalement et simulés numériquement en traction/compression axiale et en torsion pour simuler la flexion/extension, la compression et la rotation de la colonne vertébrale humaine. La porosité des structures fabriquées était à 5% près de la valeur ciblée (conçue). Les simulations numériques surestimaient la rigidité apparente et la résistance des structures testées expérimentalement d'environ 25% en moyenne, probablement en raison de la présence de défauts de fabrication, notamment dans les structures plus poreuses. Les résultats expérimentaux et numériques ont démontré que les structures ont des propriétés mécaniques quasi-identiques en compression et en tension. Cependant, une comparaison des propriétés en torsion et axiales a indiqué que les théories conventionnelles de résistance des matériaux telles que le critère de limitation de von Mises ne s'appliquent pas aux propriétés apparentes des structures architecturés. Les structures étudiées avaient une résistance adéquate pour être utilisées dans les cages intervertébrales, cependant leur rigidité était supérieure à celle des vertèbres, tout en se situant dans la plage de rigidité de l'os cortical.

3.3 Abstract

Lattice structures are increasingly used in biomedical implants, notably intervertebral cages, requiring a better understanding of their behavior for the different types of loading they undergo during application. Strut-based diamond and sheet-based gyroid structures with porosity levels ranging from 50 to 80% and an identical pore size of 750 µm were manufactured from Ti6Al4V alloy, tested experimentally and simulated numerically in axial tension/compression and in torsion to simulate flexion/extension, compression and rotation of the human spine. The manufactured structures were within 5% of the targeted porosity. However, numerical simulations overestimated the experimental apparent (effective) stiffness and strength of the structures by an average of 25%, likely due to the presence in them of manufacturing defects, especially in the higher porosity lattices. Experimental and numerical results showed that the structures have quasi-identical mechanical properties in compression and in tension. However, a comparison of the torsion and axial results indicated that conventional bulk material failure theories such as the von Mises limitation criterion do not apply to the apparent properties of lattice structures. Studied lattices exhibited adequate

resistance for use in intervertebral cages, however their stiffness was greater than those of the vertebrae, while situated in the stiffness range of cortical bone.

3.4 Introduction

Recent accessibility of high-end additive manufacturing (AM) systems and their increased use in industry have resulted in more widespread applications. Particularly of interest is the use of AM systems to produce complex geometries that cannot be obtained using traditional machining or forming methods. Biomedical applications are particularly well-suited to take advantage of the design freedom offered by AM through the use of biomimicking structures. Lattice structures have been successfully employed in biomedical implants to simultaneously reduce implant stiffness and promote tissue ingrowth, both leading to more stable fixation at the operation site (L.-Y. Chen et al., 2021; Mahmoud & Elbestawi, 2017; Murr, 2020; Zadpoor, 2019; X.-Y. Zhang et al., 2017). Titanium, one of the most used metals to manufacture biomedical implants, has an elastic modulus of ~110 GPa which is considerably higher than the elastic modulus of bone (7-30 GPa) (Timercan, Sheremetyev, & Brailovski, 2021). Through the use of lattices, the apparent (effective) modulus of elasticity of titanium structures can easily be reduced to that of the bone range (Murr, 2020; Zadpoor, 2019). Many types of lattice structures are under investigation for biomedical applications, ranging from stochastic to ordered and from homogeneous to graded, with unit cells varying from strut-based to network (skeletal)-based and sheet-based (Y. Tang & Zhao, 2016). There is growing interest in triply periodic minimal surface (TPMS) structures due to their increased mechanical properties as compared to their strut-based lattice equivalents (Al-Ketan et al., 2018; L.-Y. Chen et al., 2021; L. Zhang et al., 2018). To adequately design devices integrating lattice structures and ensure their resistance and longevity, it is necessary to understand the mechanical properties and behavior of these lattice structures under real-life loading conditions.

Most research regarding the mechanical properties of lattice structures focus on compression testing since it is the simplest to perform and does not require specialized testing setups

(Abou-Ali et al., 2020; Al-Ketan et al., 2020; Bobbert et al., 2017; Issariyapat et al., 2021; C. Lu et al., 2021; S. Ma et al., 2020; Obadimu & Kourousis, 2021; Y. Wang et al., 2020). However, under real-life conditions, these structures are also submitted to tensile, torsional, and combined loading cases for which the structures' mechanical response must be known. Some efforts have been deployed to characterize lattice structures under more than one loading mode. Yu et al. (2020), compared sheet-based TPMS and strut-based structures under tension and compression and found that the former structures yield higher strengths and stiffnesses than the latter. For all the structures, while the elastic moduli in tension and compression were found to be nearly identical, the compressive strength proved to be approximately 1.5 times higher than the tensile strength. Kelly et al. (2019) reported that the tensile stress-strain diagrams of sheet-based gyroid TPMS structures did not exhibit inflection points corresponding to the onset of plastic deformation contrary to compression for which plateau and densification regions could be observed. Furthermore, under monotonic testing conditions, the compressive strength of the TPMS structures was found to be 1.2-2.2 times greater than the tensile strength, this effect being more pronounced under fatigue testing conditions (4.5-11.5 times). The number of works that also investigate torsional loading of lattice structures is much smaller. Among them, A Yánez et al. (2018) conducted static compression and torsion tests on network-based gyroid structures, finding that the compressive and shear properties are very close in terms of the elastic moduli and ultimate strengths. Nelson et al. (2022) is the only identified study that contains results on the mechanical behavior of lattice structures under more than two simple testing modes: tension, compression, torsion and compressive shear. Their findings indicate that the TPMS structures are stronger and stiffer than their strut-based equivalents across all the loading modes. However, since this study is limited to experimental testing and the different loading modes used varying specimen designs, comparison between the stress-states for the same lattice type proved challenging. They concluded that a universal specimen design must be developed to allow adequate comparison of the mechanical behavior for different loading modes.

Numerical simulations using finite element analysis (FEA) constitute an alternative to costly experimental testing to characterize the behavior of components subjected to different loading conditions. When calibrated correctly, they have been proven to be a powerful tool. The simulation of lattice structures presents a great challenge due to their geometric complexity, requiring fine meshing, and therefore, large computational resources (Simoneau, Brailovski, & Terriault, 2016). The two most used approaches for FEA of lattice structures are direct simulations, where the entire structure is modeled, and analyses by homogenization, where solid elements with lattice-equivalent properties are used. The former method is more appropriate in cases where the local behavior of structures must be studied, while the latter is preferred for simulating the behavior of large components incorporating significant volumes of lattice structures (Dong et al., 2017). Combining the two approaches allows a multiscale modeling of such constructs. The most recent efforts on lattice FEA use direct simulations and can be separated into two levels of analysis, the first calculating the stress distributions inside lattice structures (Soro et al., 2021; Yu et al., 2020) and the second, calculating the apparent properties of these structures (Abou-Ali et al., 2020; Ali & Sen, 2017; C. Lu et al., 2021; S. Ma et al., 2020; Y. Wang et al., 2020; Zhou et al., 2020). Generally, the mechanical properties of lattice structures predicted by numerical simulations differ significantly from their experimental equivalents, with some models overestimating the actual properties (Abou-Ali et al., 2020; S. Ma et al., 2020), and others, underestimating them (C. Lu et al., 2021; Zhou et al., 2020). These differences are explained by the presence of manufacturing-induced geometric deviations, internal defects and surface roughness (C. Lu et al., 2021; S. Ma et al., 2020; Y. Wang et al., 2020; Zhou et al., 2020).

To sum-up the preceding, few studies have been carried out on the mechanical response of lattice structures under more than one loading mode, and to the authors’ knowledge, no studies have compared simulations and experiments of various lattice structures under different loading modes. This study aims to partially fill this gap by studying the monotonic axial tension/compression and torsional mechanical behavior of two lattice structures, strut-based diamonds and sheet-based TPMS gyroids, which could be considered representative, respectively, of rod- and plate-based trabecular bone structures (Lorna J Gibson, 2005). Both structure types were manufactured by laser powder bed fusion from Ti6Al4V alloy powder with a constant pore size of 750 µm and a porosity level ranging from 50 to 80%, with both characteristics selected in accordance with the recommendations for improved osseointegration (Food and Drug Administration, 2007; Hara et al., 2016; Kienapfel et al., 1999; Taniguchi et al., 2016). Numerical models were built for each type of the lattice structures, each level of porosity and each loading mode, and partially validated by comparing the numerical and experimental results. The mechanical properties for the three loading modes that simulate flexion/extension, compression and rotation of the human spine were assessed and compared to the properties of bony tissues and the functional requirements of intervertebral cages.

3.5 Materials and methods

3.5.1 Specimen design and manufacturing

A proprietary *MATLAB (MathWorks, Massachusetts, USA)* algorithm was used to create the diamond structures using hexagonal prisms as struts to facilitate meshing (Dumas et al., 2017). A more detailed explanation of the parameter selection and structures design can be found in the previously published study (Timercan et al., 2021). Gyroid structures were generated using *nTopology (nTopology, New York, USA)* software. Tableau 3.1 summarizes the selected geometric parameters of both structures and the expected porosity levels.

Tableau 3.1 Parameters of the studied diamond and gyroid lattice structures having a target pore diameter of 750 µm

	Strut/sheet thickness [µm]	Cell size [µm]	Designed porosity [%]
Diamond	586	1663	50.1
	455	1485	59.9
	345	1336	69.8
	240	1193	80.4
Gyroid	430	2754	50.6
	305	2431	61.4
	210	2191	70.5
	125	1977	81.3

The specimens used in this study were designed to allow their compression, tension and torsion testing and their design was loosely based on that of standard cylindrical dog-bone test specimens (Figure 3.1 – Type 1). All the specimens featured a central gauge part with constant porosity and cross-section, solid end pieces that interfaced with the materials testing machine, and transition zones connecting the two. The transition zones with decreasing porosity and increasing cross-section allowed a gradual connection between the studied lattice structure and the fully dense end pieces (Figure 3.2). Moreover, to allow sound torsional testing, the central part of the specimens was designed as a hollow cylinder with an outer diameter of 10 mm and inner diameter of 2 mm. The height of the region of interest was set to 10 mm. These dimensions ensured that at least one complete unit cell filled the specimen wall thickness for all selected structures. In addition, the selected geometry was the result of a compromise between the compression testing requirements (height = 1-2 x diameters), torsion testing requirements (height = 6-8 diameters) and manufacturing considerations, such as the minimum feature thickness and total specimen height (ASTM, 2021; ISO13314, 2011). Although not without any drawbacks, the universal specimen design presents a good compromise between the requirements for compression, tension and torsion testing and must allow adequate comparison between lattice response to the three loading modes. Finally, solid end pieces featured two flat parallel surfaces and transversal holes which, when used in conjunction with pins and adapters for the MTS machine, allowed the application of tensile and torsional loads, in addition to compression. For more precise and detailed experimental verification of manufactured porosities using the ASTM F2450-18 standard (ASTM, 2018), a second type of specimens in the shape of plain cylinders with a 10 mm diameter and 20 mm height was also designed (Figure 3.1 – Type 2).

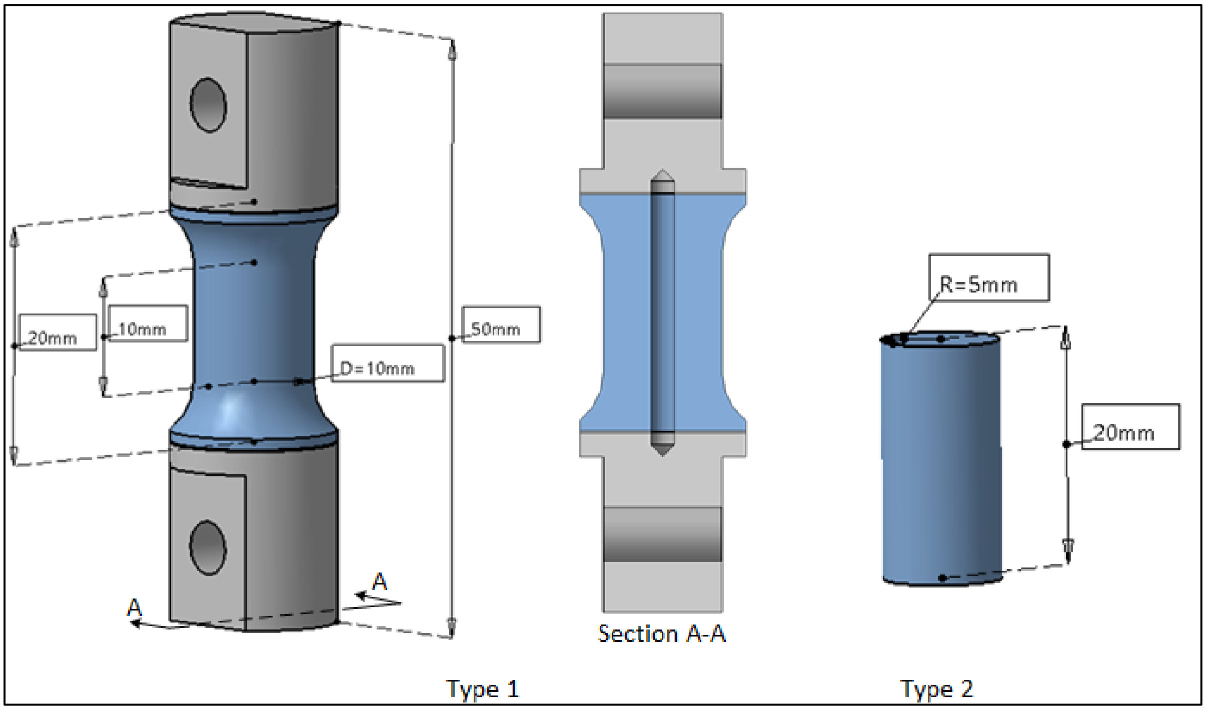
20mm
10mm
D=10mm
50mm
A
A
Section A-A
R=5mm
20mm
Type 1
Type 2

Figure 3.1 Specimen designs and overall dimensions: Type 1 used for mechanical testing and Type 2 used for porosity verifications. Areas in blue indicate porous parts of the specimens

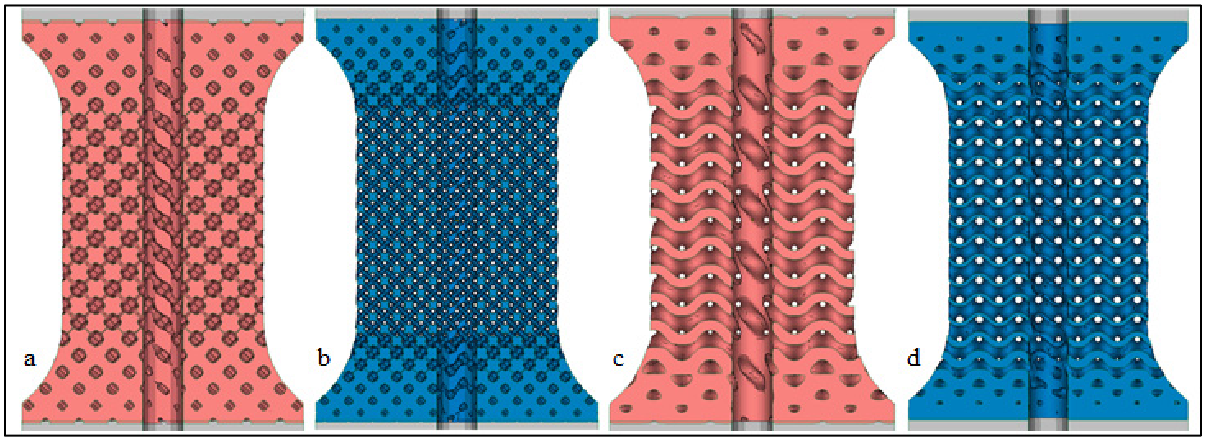

Figure 3.2 Central parts of the diamond (a,b), and gyroid (c,d) structures with a porosity of 50% (a,c) and 80% (b,d)

A total of 120 Type 1 specimens (15 per porosity level) and 16 Type 2 specimens (2 per porosity level) were manufactured using an *EOS M280 (Krailing,Germany)* laser powder bed fusion system (Figure 3.3). Ti6Al4V alloy powder (particle size distribution d_{10}=24 µm,

d_{50}=44 µm and d_{90}=61 µm) from *GE Additive (Boisbriand, Canada)* was used and the default *EOS* printing parameters for 30 µm layer Ti64 were employed. The scanning strategy for the part infill was stripe hatching with a 67° rotation between succeeding layers, laser power 280W, scanning speed 1200 mm/s and hatching distance 140 µm; contours were scanned with a 150W laser power and a 1250 mm/s scanning speed. It is important to note that for the most porous gyroid structure (~80%), contour printing parameters were primarily applied, since the walls thickness was too small for the infill scanning strategy (Figure 3.4). To ensure that manufactured specimens respected the design requirements as closely as possible, the AM system-specific laser beam offset was determined for the two types of structures (35 µm for diamond and 20 µm for gyroid). After printing, a stress relief heat treatment of 800°C for 4 hours under inert atmosphere was carried out. The specimens were then separated from the build plate by means of bandsaw cutting. Supports were removed and functional surfaces machined to ensure adequate fit with the testing apparatus. All the specimens were cleaned in an ultrasound bath for 30 minutes to remove any remaining loose powder and cutting oil. One sample of both the diamond and gyroid specimens (Type 1) of each porosity level were scanned using a *Nikon XTH225 (Tokyo, Japan)* computed tomography (CT) system to verify their geometric conformity, structural integrity and the absence of debris inside the lattice. The scans were carried out with a 192 kV tube voltage, 55 µA current and 12 µm resolution. *CT Pro 3D (Nikon, Tokyo, Japan)* software was used to reconstruct the scans and generate TIFF image stacks that were then imported into *VGStudio MAX 3.1 (Volume Graphics, Heidelberg, Germany)* software and converted into volumes for analysis. The porosity validation plain cylindrical specimens (Type 2) were weighed (*Sartorius Secura 324-1s* scale, ±0.0001 g) and their diameter and height measured (*Mitutoyo* micrometer ±0.001 mm). Porosity was calculated according to Equation (3.1). The material volume was obtained by dividing the specimen mass by the material density (4.43 g/cm^3 for Ti6Al4V) and the total volume was calculated using the diameter and height of the specimens.

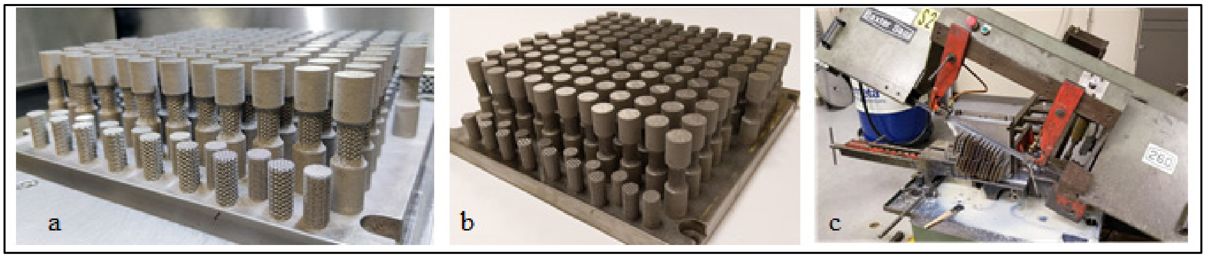

Figure 3.3 Specimens on the build plate after (a) manufacturing and (b) removal from machine; (c) specimens separation from the build plate

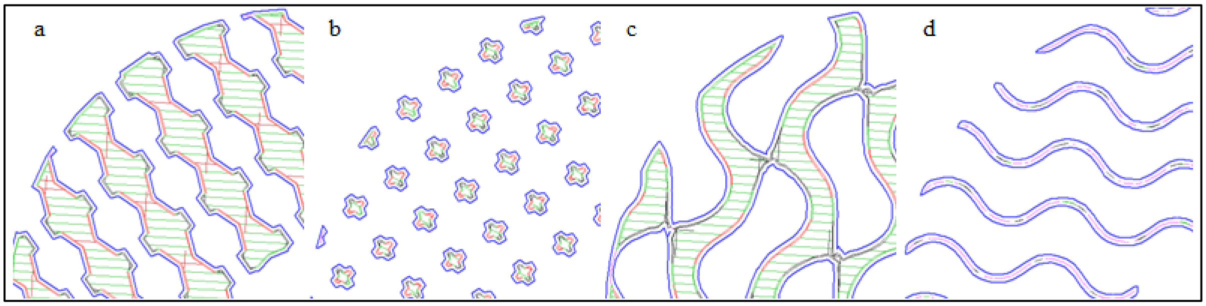

Figure 3.4 Scanning strategy for the diamond (a,b), and gyroid (c,d) structures with a porosity of 50% (a,c) and 80% (b,d). The blue outline indicates the structure cross-section, green lines indicate infill scanning, red and black lines are upskin and downskin areas, respectively, and contouring is shown in pink

$$\varphi\ (\%) = \frac{V_{void}}{V_{total}} * 100 = \left(1 - \frac{V_{material}}{V_{total}}\right) * 100 \tag{3.1}$$

3.5.2 Numerical simulations

Concurrently, finite element analyses were carried out on the central constant-porosity portions of the specimens using a workstation with two 14 core Intel Xeon E5-2660 CPUs and 256GB of RAM. STLs of the central sections with a height of 10 mm were imported into Ansys Workbench 2021R1 where compression, tension and torsion loading modes were simulated with large deformation analyses. The FEA mesh was created using the layered tetrahedrons method with a layer height of 0.1 mm and an element size of 0.1 mm (Figure 3.5 a). The number of elements varied from ~1.5 million for the most porous structures to ~3.5 million for the least porous structures. The material properties of Ti6Al4V alloy were applied to the structures using the bilinear kinematic hardening model (E = 110 GPa, E_T = 833 MPa, ν = 0.33, S_y = 900 MPa (Brika, Letenneur, Dion, & Brailovski, 2020)). Mesh convergence analysis was carried out on the equivalent von Mises stress of the 80% porosity gyroid structure, since this structure has the thinnest walls and requires the smallest elements to provide adequate geometric conformance. The element size selected with a convergence criterion of 5% also respected the best practice, which recommends at least 2 elements in the wall thickness of the thinnest feature.

For compression and tension testing, the boundary conditions consisted of displacements directly applied to the structure nodes. The displacements of all bottom surface nodes were set to zero in the axial direction, as were the transverse displacements of the central part of the bottom surface nodes (Figure 3.5 b). The top nodes' axial displacements were applied using automatic stepping up to 5% apparent strain, with an average of 20 steps to resolve. For torsional testing, the bottom displacements were set to zero in all directions and the rotation was applied using automatic stepping up to 4% apparent shear strain as remote displacements of the top surface nodes using rigid behavior (Figure 3.5 c). The reaction force and reaction moment probes were applied to the blocked displacements and then converted to compression/tensile and shear stresses using, respectively, the specimens' cross-section areas and the polar moments of inertia. The resulting stress-strain data were used to calculate the structures' apparent modulus of elasticity and yield stress. In addition to calculating the stress-strain data, the simulations were also used to calculate the material volume fractions under different states of stress. To this end, a script was written using the Ansys parametric design language (APDL) commands tool and was used to select the elements in different stress states (elastic, plastic) and extract their relative volumes.

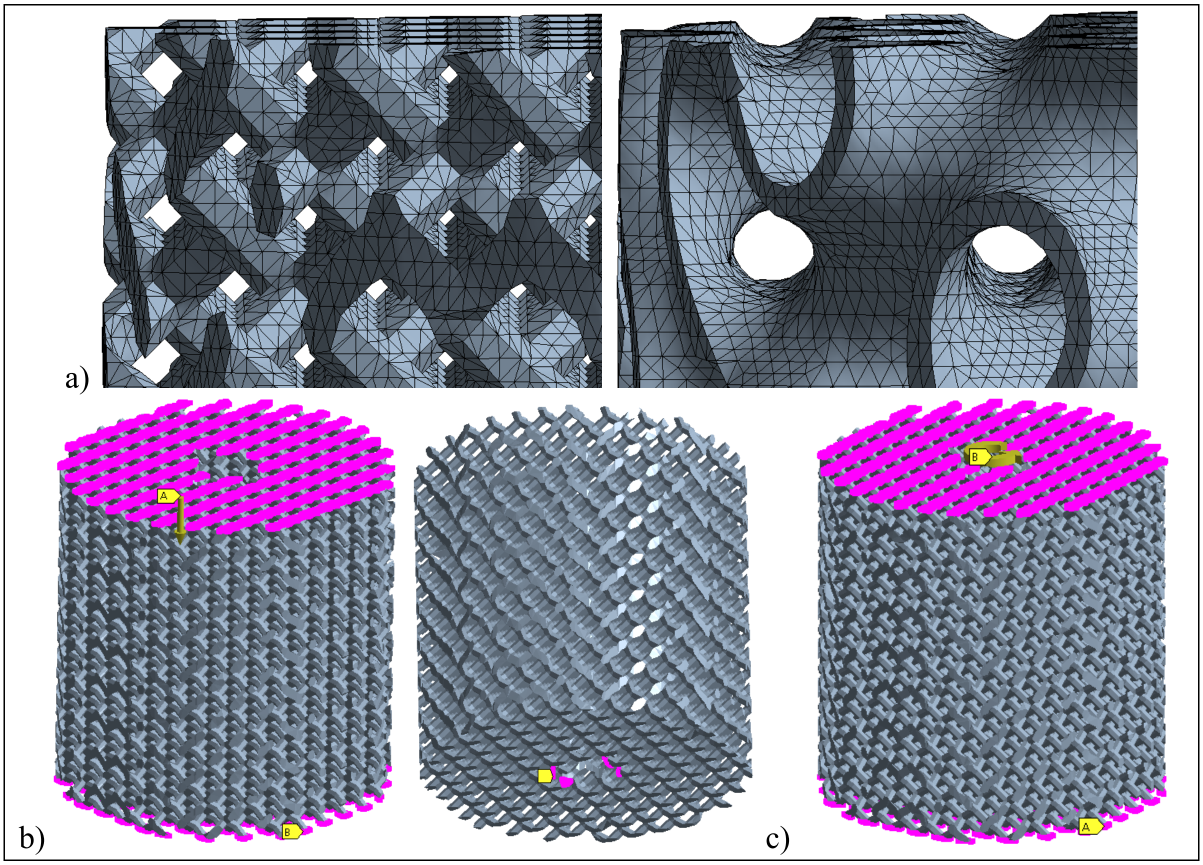

Figure 3.5 Mesh details for the diamond and gyroid structures (a) and boundary conditions applied on the 80%-porosity diamond structure in compression (b) and torsion (c)

3.5.3 Experimental testing

Mechanical testing was carried out on an 858 MiniBionix II MTS system using a 15 kN-150 Nm axial-torsional load cell. Three specimens of each type of structure were tested for each loading mode: compression, tension and torsion, for a total of 9 tests for each structure and porosity level. Separate specimens were used for each test. Loading was applied by increasing the axial increments by 0.5 mm at a rate of 0.01 mm/s and the torsional increments by 5° at a rate of 0.115°/s, until structure failure. For torsional testing, the axial control was set to “floating mode” to prevent additional loading of the structure caused by axial expansion or contraction. Axial forces and displacements, torsional torques and angles were acquired at a rate of 40 Hz. A digital image correlation (DIC) system *Aramis 5M (GOM mbH, Braunschweig, Germany)* was used as a digital extensometer to measure displacements and strains of two points in the central constant porosity part of the specimens at a rate of 1 Hz (Figure 3.6). The data obtained were synchronized and post-treated in *MATLAB*, and then converted to a stress-strain format to extract the modulus of elasticity, yield and peak stresses apparent values. The modulus of elasticity was obtained during the unloading phase of the tests by fitting a linear equation to the largest portion of data, while maintaining a correlation of ~99%. This approach was favored in order to minimize the effects of the pin clearance in the apparatus assembly on the specimen stiffness which was observed during the initial loading phase.

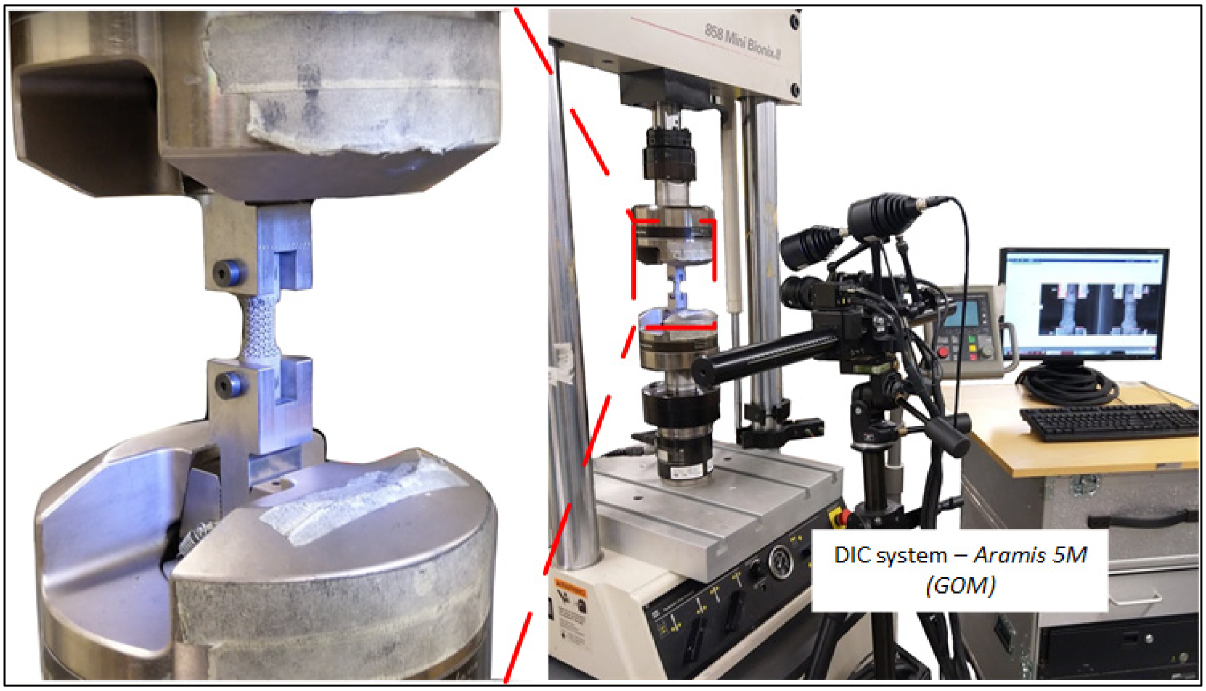

Figure 3.6 A mechanical testing setup with a digital image correlation apparatus

3.6 Results

3.6.1 Geometric conformance

The porosity of the plain cylindrical specimens obtained by weight measurements was generally within 2% of the target, except for the highest porosity levels where the deviation reached up to 5% (Figure 3.7 a). For all porosity levels, the porosity values obtained from the

CT analyses were systematically lower (1-2%) than the ones measured using the specimen mass and volume. The geometric conformity analysis indicated that for all the specimens, at least 90% of the total structure surface was within ~80 µm of deviation from the CAD, which is acceptable, given the printing resolution of 80 µm. The deviation distributions between the actual and CAD surfaces were not symmetrical with respect to zero, as illustrated in Figure 3.7 b. Although the mean deviations for all structures were close to zero, the peaks of the deviation distributions ranged from -13 µm to +5 µm, and only structures with the highest (~80%) porosity had positive deviation peaks (Figure 3.7 b). At higher porosities, where the strut/sheet thickness was of the same order of magnitude as the laser beam diameter, manufacturing-induced defects such as pores, geometrical discontinuities and structural distortions were observed (Figure 3.8). The gyroid structures exhibited more defects than their diamond equivalents, as expected from their thinner features: 125 µm walls for the former vs 240 µm struts for the latter.

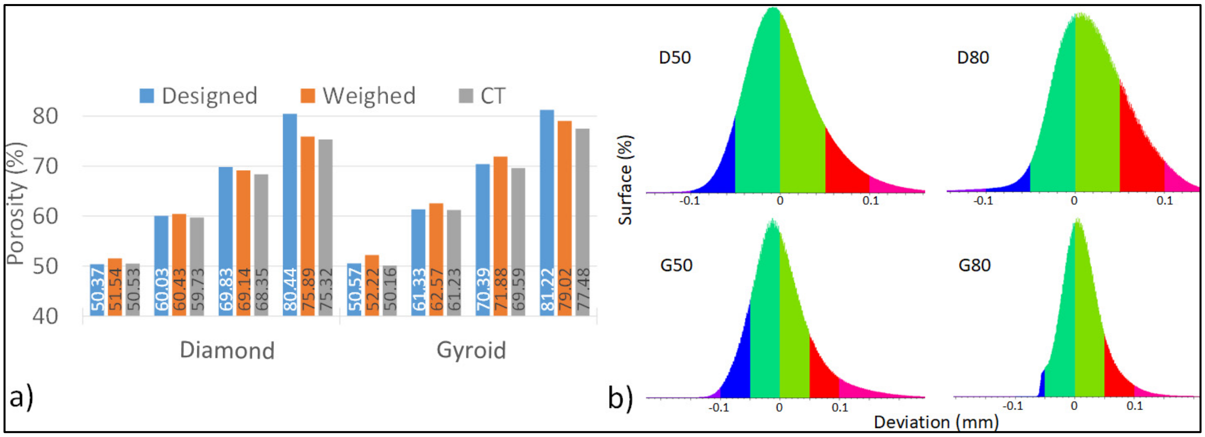

Figure 3.7 (a) Porosity levels of the designed and manufactured structures; (b) Surface deviation distributions of the 50% and 80% porous diamond (D) and gyroid (G) structures

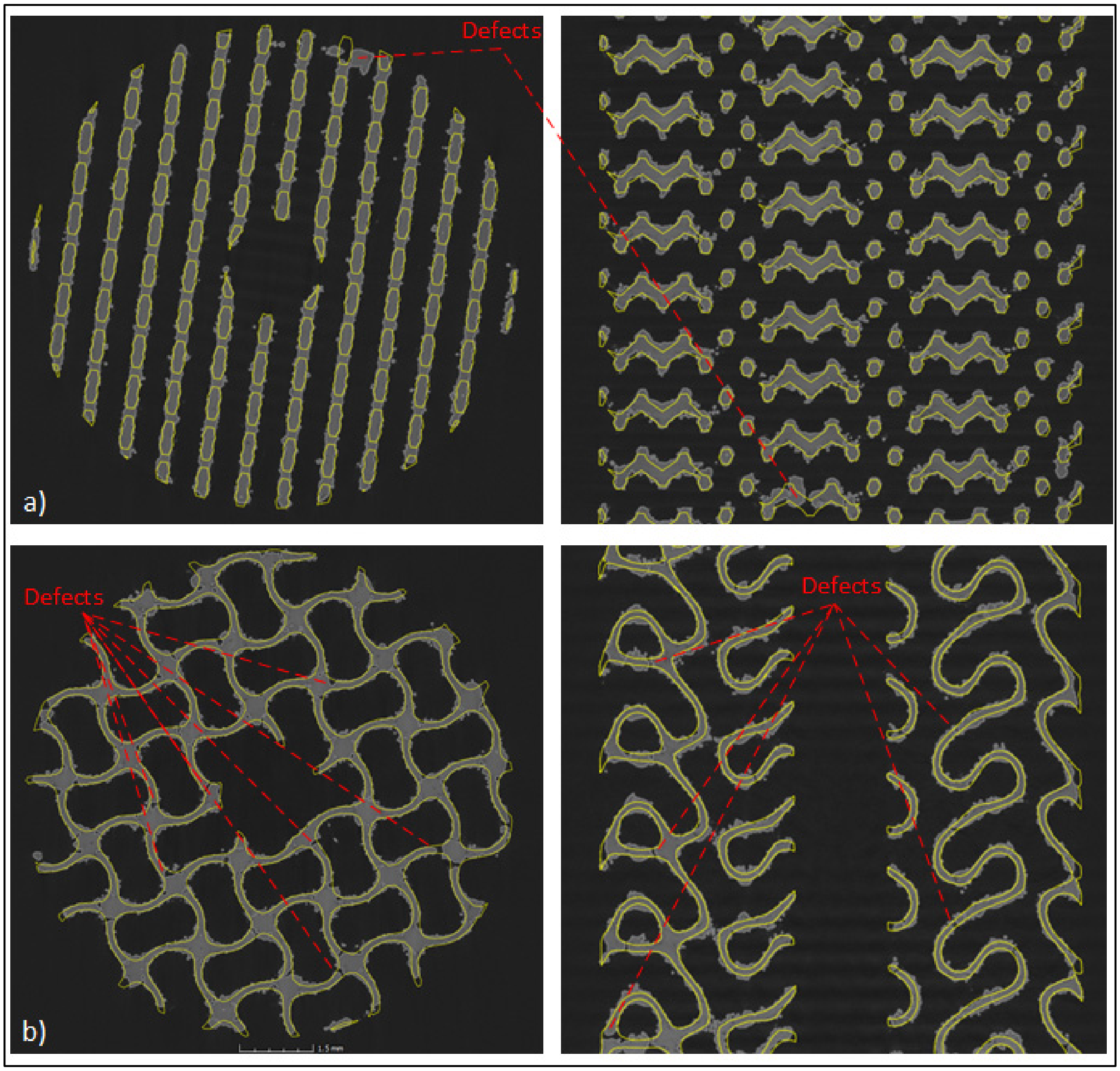

Figure 3.8 Manufacturing-induced defects in the most porous (~80%) diamond (a) and gyroid (b) structures and comparison to the idealised CAD outlined in yellow

3.6.2 Numerical simulations

Numerical models predict quasi-identical mechanical behaviors for both structures in compression and tension at all porosity levels (Figure 3.9). The gyroid structures are expected to have 1.4-2.7 times higher apparent elasticity moduli as well as 1.1-1.7 times higher apparent yield stresses than their diamond equivalents (Tableau 3.2). In torsion, both structures perform identically for the same porosity levels, except for the most porous lattices where the gyroids are 1.4 times stiffer and more resistant than the diamonds (refer to values in Tableau 3.2). Stresses in the gyroid structures are more evenly spread compared to the diamond structures where the matter is subjected to more concentrated stresses (Figure 3.10). At the same global strains, the volume fractions of matter with stresses exceeding the onset of the yield stress (900 MPa) are higher for the gyroid than for the diamond structures, and the more porous the structure, the more pronounced this effect (Tableau 3.2). That means that under the same global displacements, the gyroid structures will contain more plastically, and therefore, irreversibly deformed matter than their diamond equivalents. It is noteworthy that the stress concentrations in the diamond lattices are at the strut junctions, as often cited in the literature (Yu et al., 2020). For the gyroid structures in tension and compression, the maximal stresses are present along helical contours as was also observed by Downing, Jones, Brandt, et Leary (2021). It is also worth noting that some isolated and scattered small regions of the lattice are subjected to stresses exceeding the ultimate tensile stress of Ti6Al4V (970 MPa) and their cumulated volume fraction does not exceed 0.5% of the volume of the entire structure (Figure 3.10). This effect is due to the specimen design process where the lattices were cut using a cylinder, leaving not only floating particles (which are removed) but also areas with extremely thin sections acting as singularities. As verified by additional simulations, where these zones were effectively removed (“killed”), such a small number of highly distorted elements bear a negligible impact on the global behavior of these structures and could therefore be ignored.

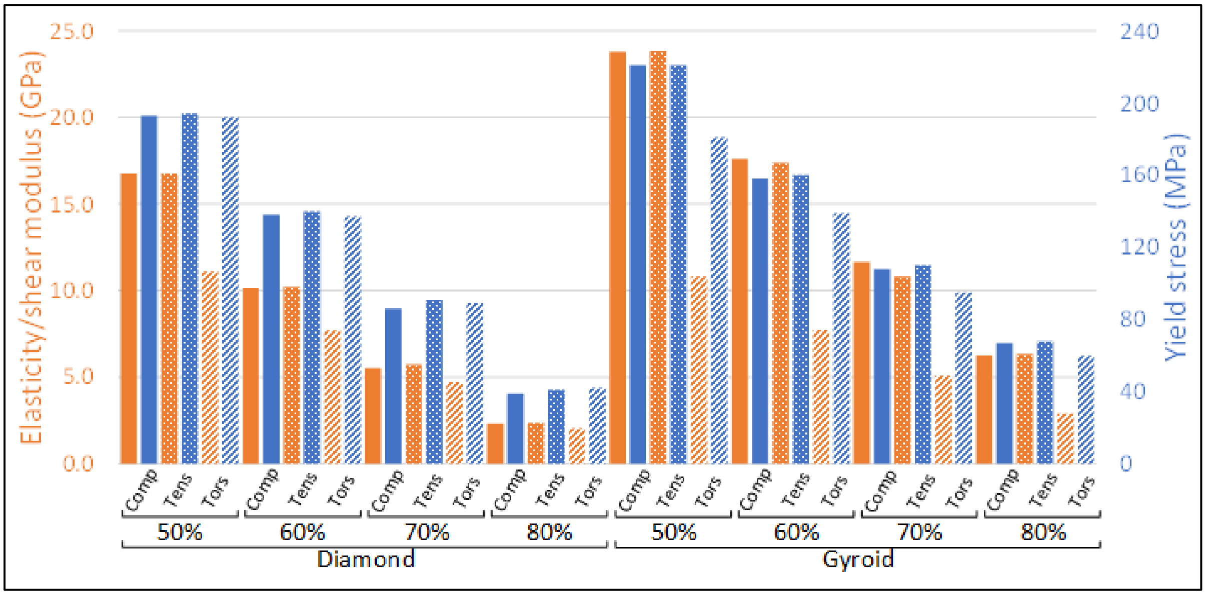

Figure 3.9 Numerically predicted apparent mechanical properties: elasticity/shear moduli and yield stresses

Tableau 3.2 Numerically predicted apparent mechanical properties: elasticity/shear moduli and yield stresses and volume fractions of the lattice structures undergoing plastic deformation (stresses exceed the bulk material yield stress of 900 MPa) at 5% of axial and 4% of torsional global strains

	Compression			Tension			Torsion		
	E (GPa)	S_y (MPa)	Volume fraction %	**E (GPa)**	S_y (MPa)	Volume fraction %	**G (GPa)**	S_{Sy} (MPa)	Volume fraction %
D50	**16.7**	193	46	**16.8**	194	49	**11.1**	192	29
D60	**10.2**	138	41	**10.2**	140	43	**7.7**	137	21
D70	**5.5**	86	24	**5.7**	91	29	**4.7**	89	13
D80	**2.3**	39	6	**2.4**	41	7	**2.0**	42	2
G50	**23.8**	221	57	**23.8**	221	58	**10.8**	181	35
G60	**17.6**	158	49	**17.4**	160	50	**7.7**	139	28
G70	**11.6**	108	42	**10.8**	110	45	**5.1**	95	22
G80	**6.3**	67	36	**6.4**	68	39	**2.9**	60	17

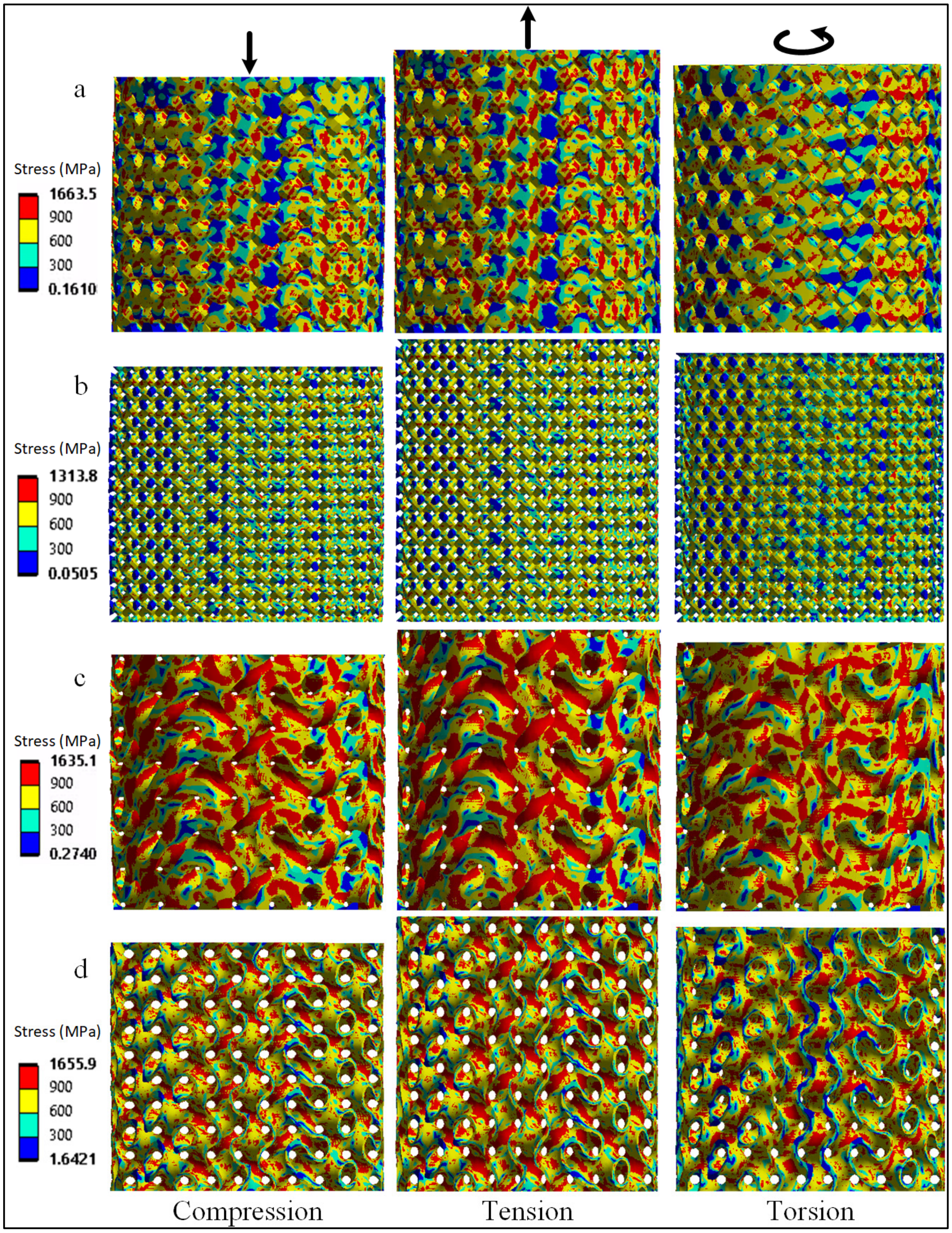

Figure 3.10 Simulated stress distributions in the diamond (a, b) and gyroid (c, d) structures at ~50% (a, c) and ~80% (b, d) porosity levels under global strains of 5% compression, 5% tension and 4% torsion

3.6.3 Experimental validation

Figure 3.11 presents all the experimental (apparent) compression, tension and torsion stress-strain diagrams corresponding to central constant porosity portions of the diamond and gyroid specimens. It is worth noting that for uniaxial loading, i.e., compression and tension, the diamond and gyroid structures with the lowest porosity (~50%) reached the testing machine loading limit, and therefore, the specimens did not fail completely. Nonetheless, the onset of plastic deformation was observed and the yield stress calculated. Overall, the repeatability of the lattice mechanical responses was observed for all three specimens tested in each condition. The loading-unloading cycling strains were not identical for the specimens because the overall displacement and the local strains of the porous sections were not always matched from one specimen to the next caused by the assembly clearances. The average experimental apparent elasticity moduli and yield stresses with their standard deviations can be found in Tableau 3.3.

Scaling relations in the form of a power law were calculated from the experimental values, allowing the prediction of lattice structure properties as functions of the bulk material properties and the lattice porosity (Tableau 3.4). The exponents of the power laws range from approximately 1.6 to 2.3, which are of the same order of magnitude as 2.0 in L.J. Gibson, Ashby, et Harley (2010).

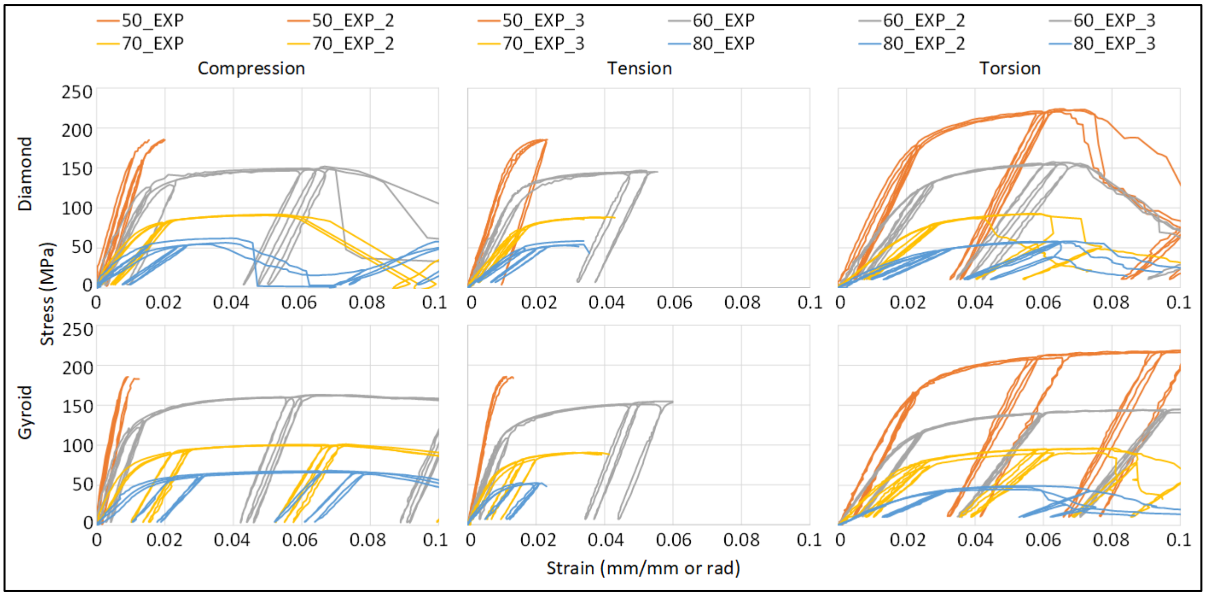

Figure 3.11 Stress-strain diagrams of all the experimental tests of the 50, 60, 70 and 80% porosity diamond and gyroid structures under compression, tension and torsion

Tableau 3.3 Experimentally determined (apparent) mechanical properties of the diamond and gyroid structures under compression, tension and torsion

	Compression		Tension		Torsion	
	E (GPa)	S_y (MPa)	**E (GPa)**	S_y (MPa)	**G (GPa)**	S_{Sy} (MPa)
D50 (51.5*)	**15.0 ±0.05**	173 ±2.1	**13.8 ±0.67**	171 ±2.7	**9.0 ±0.04**	172 ±2.2
D60 (60.4)	**9.3 ±0.56**	122 ±3.4	**9.4 ±0.81**	121 ±2.1	**6.2 ±0.12**	120 ±1.1
D70 (69.1)	**5.1 ±0.08**	75 ±0.9	**5.3 ±0.60**	74 ±0.5	**3.4 ±0.07**	71 ±0.6
D80 (75.9)	**3.1 ±0.25**	48 ±1.9	**3.0 ±0.12**	48 ±3.1	**1.8 ±0.10**	40 ±2.1
G50 (52.2*)	**22.0 ±0.47**	186 ±3.3	**22.4 ±0.65**	182 ±3.1	**8.7 ±0.14**	162 ±0.6
G60 (62.6)	**12.6 ±0.58**	119 ±1.5	**12.0 ±0.17**	118 ±1.9	**5.8 ±0.22**	106 ±1.0
G70 (71.9)	**7.6 ±0.41**	75 ±1.1	**7.6 ±0.17**	72 ±1.0	**3.9 ±0.20**	71 ±1.5
G80 (79.0)	**4.8 ±0.16**	51 ±1.2	**5.2 ±0.11**	45 ±0.6	**1.9 ±0.02**	36 ±2.0

*values in parentheses contained in the left column denote the measured porosity levels

Tableau 3.4 Scaling relations of the diamond (D) and gyroid (G) lattice elasticity moduli (E and G) and yield stresses (S_y and S_{Sy}) for three loading modes and the corresponding R^2 correlation coefficients

	Compression		Tension		Torsion	
D	$E_{app}=$ $E*0.6968*(1-\varphi)^{2.2773}$	R^2.998	$E_{app}=$ $E*0.6304*(1-\varphi)^{2.1911}$	R^2.998	$G_{app}=$ $G*1.1196*(1-\varphi)^{2.2905}$	R^2.997
	$S_{y\_app}=$ $S_y*0.7458*(1-\varphi)^{1.8589}$	R^2.999	$S_{y\_app}=$ $S_y*0.7144*(1-\varphi)^{1.8237}$	R^2.999	$S_{Sy\_app}=$ $S_{Sy}*1.4755*(1-\varphi)^{2.0994}$	R^2.997
G	$E_{app}=$ $E*0.7289*(1-\varphi)^{1.8253}$	R^2.993	$E_{app}=$ $E*0.6802*(1-\varphi)^{1.757}$	R^2.978	$G_{app}=$ $G*0.7910*(1-\varphi)^{1.8162}$	R^2.981
	$S_{y\_app}=$ $S_y*0.6413*(1-\varphi)^{1.5763}$	R^2.996	$S_{y\_app}=$ $S_y*0.6988*(1-\varphi)^{1.6945}$	R^2.999	$S_{Sy\_app}=$ $S_{Sy}*1.1285*(1-\varphi)^{1.7867}$	R^2.989

By comparing the experimental and numerical data, it can be observed that the numerical simulations overestimated the elasticity moduli and yield stresses of all the specimens (by ~25% on average), except for the ~80% porous diamond structures, where the calculations underestimated these values in compression and tension (~21 and ~19%) (Figure 3.12). This latter discrepancy is partially explained by the fact that for the highest-porosity diamond structures, the manufactured porosity was ~5% lower than the designed one, while for the highest-porosity gyroids, this difference was only ~1.5%. Modeling of the diamond structures was globally closer to the experimental results than the gyroids', with the former having an average relative error of 16%, and the latter, of 34% (Figure 3.13). The presence of manufacturing defects, coupled with the uncertainty in the actually obtained porosities, have been noted in the literature as factors that influence the accuracy of the numerical modeling (S. Ma et al., 2020; A Yánez et al., 2018). Surface-sintered particles, as can be seen in Figure 3.14, affect the density measurements, but do not contribute to the structural integrity of the lattice structures, and therefore introduce errors in the numerical-experimental comparison. Finally, only central parts of the specimens were simulated, thus making the numerical boundary conditions not entirely representative of the experimental testing conditions.

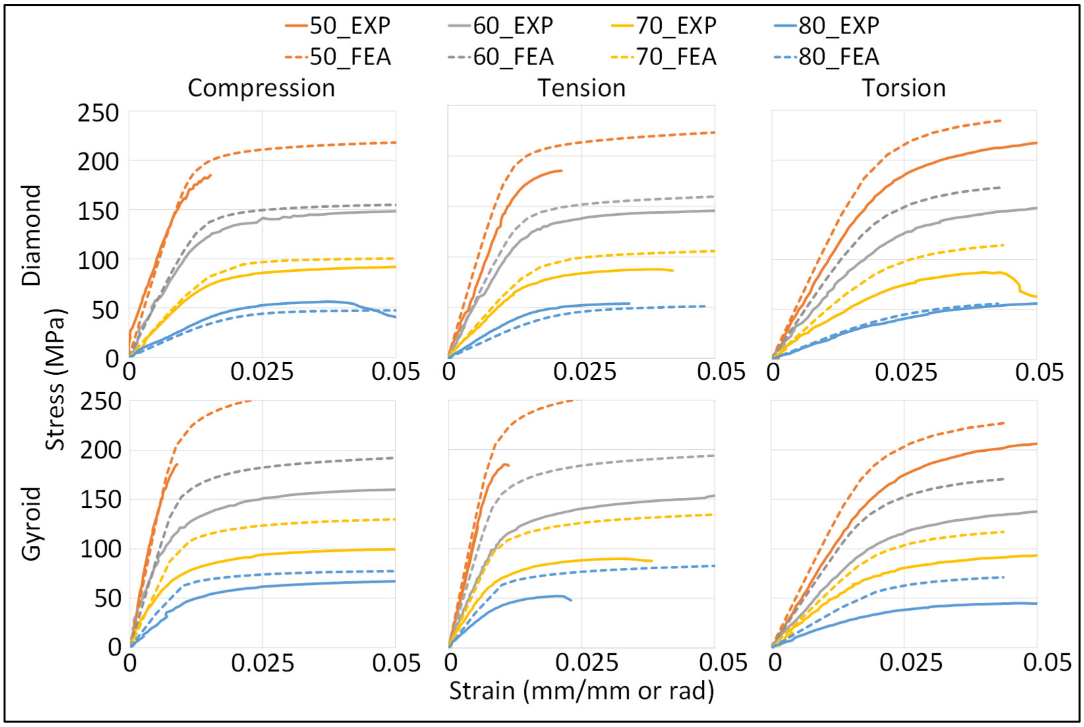

Figure 3.12 Comparison of the experimental and FEA stress-strain diagrams (bold lines-experiment, dotted-calculations)

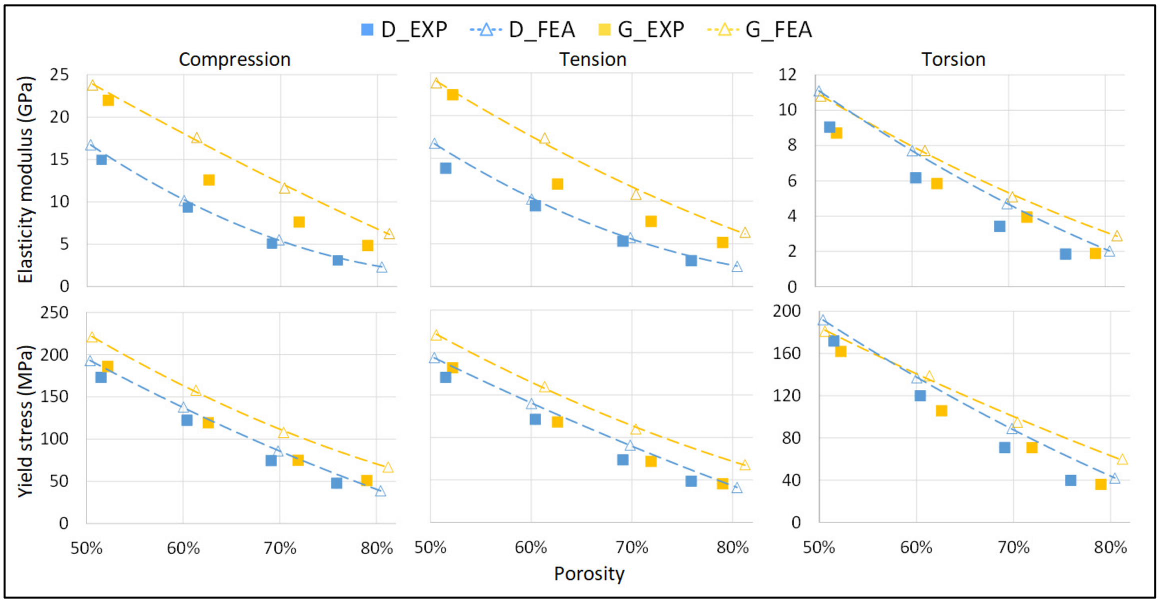

Figure 3.13 Experimental (EXP) and numerical (FEA) moduli of elasticity (E) and yield stresses (Sy) as functions of porosity for diamond (D) and gyroid (G) structures in compression, tension and torsion

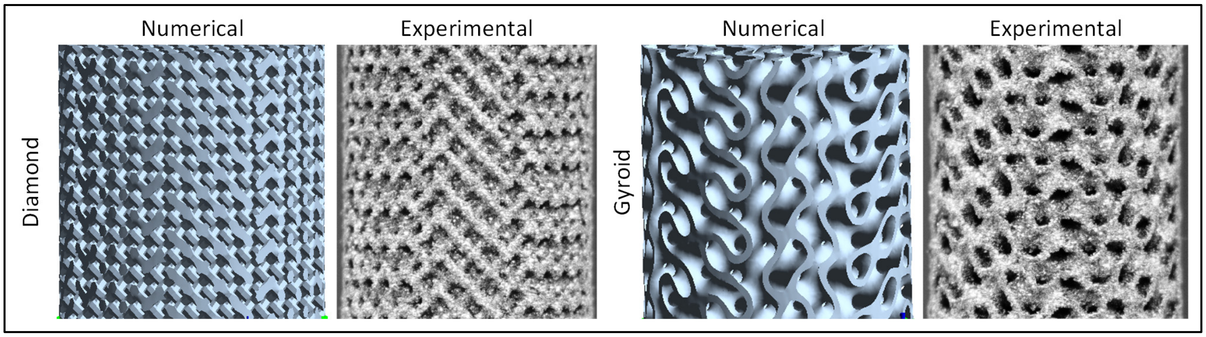

Figure 3.14 Comparison of the numerical and experimental 70% diamond and gyroid structures under 4% tension strain

3.7 Discussion

3.7.1 Manufacturing of lattices

The difference between the results obtained using two porosity measurement methods, weighting (Archimedes) and CT, although small, can be partly attributed to the thresholding used for the CT. Although the applied automatic thresholding is based on the background and material grey value peaks to determine the matter-void interface, the CT-related effects, such as beam hardening and halo artefacts, can skew the grey value distribution, thus altering the surface determination, and ultimately, the structure volume. In addition, CT scans were performed on the mechanical testing specimens, while the Archimedes measurements were performed on the plain cylindrical specimens; this difference in the specimen shape and size might also partly account for variations in the porosity measurements. Nonetheless, the two measurement methods follow the same trend and inform us of deviations between the designed and manufactured structures. At lower porosities, the printed structures follow the CAD more closely, with deviations increasing alongside the porosity. For both the diamond and gyroid structures, the largest deviations occurred at the highest porosity levels, which are at limits of printability of the LPBF system used in this study. As previously stated, given thin cross-sections of some porous structures, the LPBF system only used contour parameters for printing, with the latter regimes employing lower laser power and higher scanning speed, resulting in smaller energy densities delivered to the powder bed as compared to the infill printing strategy. This can explain some manufacturing defects, particularly geometric discontinuities observed in the ~80% gyroid structures, where the contour printing parameters were prevalent.

Similar trends were observed by Kelly et al. (2019), who tried to correct the manufacturing defects (internal voids) by adjusting the printing parameters. While they were successful in reducing these defects, there were still deviations between the manufactured and the designed porosity levels (49 vs. 53.9% and 87 vs. 88.1%). Salem, Carter, Attallah, et Salem (2019) analyzed the influence of laser power and scanning speed on the geometric conformity and internal porosity of a 200 μm strut-thickness Ti6Al4V lattice structure and identified five zones of different manufacturing defects. One parameter set with the lowest tested power (100 W) and one of the lowest tested scanning speeds (1600 mm/s) was identified as the one most closely replicating the CAD and having the least defects. Although the comparison is not straightforward due to the differences in manufacturing systems, this combination of laser power and speed would result in a lower energy density than even the contouring parameters used in the present work. In addition to the geometric conformity, Sing, Wiria, et Yeong (2018) also studied the impact of scanning parameters on the mechanical properties, finding that the strut dimensions are most influenced by the laser power whereas the mechanical properties depend not only on the laser power, but also on the scanning speed and layer thickness. This indicates that the printing parameters of lattice structures must be adapted not only to the lattice type, but also to the porosity level, considering that modifying the printing parameters to obtain targeted geometries might negatively affect the material microstructure, and therefore, the mechanical properties.

3.7.2 Mechanical behavior of lattices

In terms of the mechanical behavior, all the manufactured lattice structures exhibit quasi-reversible properties between compression and tension, in agreement with the numerical predictions. Overall, the gyroid structures are stiffer and as strong as the diamond structures under the compressive and tensile loading modes. Looking at the performance in torsion, both structures have almost identical shear moduli and shear yield stresses for similar porosity levels. According to the maximum distortion energy theory, for the bulk material considered homogenous and isotropic, the generally accepted ratio between the shear (S_{sy}) and axial (S_y) yield stresses is 0.577. This ratio can vary for specific alloys and manufacturing techniques. Some studies analyzed bulk Ti6Al4V alloys produced by additive manufacturing and found S_{sy}/S_y to vary from 0.49 to 0.57 (Suryawanshi, Singh, Msolli, Jhon, & Ramamurty, 2021). Conversely, on average, this ratio for the diamond structures is 0.94 and for the gyroid, it is 0.87. This difference in the mechanical resistance behavior implies that for the simulation of lattice structures using the homogenization approach (Dong et al., 2017), the yield criterion of ductile isotropic materials is no longer adequate and alternative criteria, such as Drucker-Prager for example, must be considered. A similar trend was observed for the compression and torsion stiffness and yield stress by A Yánez et al. (2018). In addition, the equation linking the shear and Young's modulus ($E=2G(1+\nu)$), which is derived from Hooke's law, can also be considered as not applicable to the lattice structure apparent properties. Applying this formula using the diamond structure moduli results in negative Poisson's ratios, indicating an auxetic structure, a phenomenon that is not observed numerically or experimentally. Therefore, when simulating lattice structures using the homogenization strategy (Dong et al., 2017), particular care must be taken when continuous material properties and material behavior are used, given the fact that lattices do not behave as equivalent isotropic materials. While comparison of different lattice types based on the apparent Young's modulus alone remains adequate in cases where only one type of loading is applied to the structure, further analyses are needed to establish a generalized approach to simulate complex elastic behavior of lattice structures.

Although failure occurred in the central portion of all specimens (Figure 3.15), a key difference between the two structures is in their failure mode, which is more abrupt for diamonds and more gradual for gyroids. When comparing the scaling relations obtained in this study (Tableau 3.4) with those of a previously published work (Timercan et al., 2021), the yield stress relations have similar coefficient and exponent values, whereas the modulus of elasticity equations are indeed very different, with the previous study's values being much lower (coefficients of 0.09-0.20 vs 0.67-0.70, and exponents 0.9-1.7 vs 1.8-2.3). This might be explained by the fact that in this work, these values were calculated using unloading branches of the experimental stress-strain, while in the previous work, they were obtained using the loading branches, where the stiffness of the testing assembly alters the specimen apparent behavior. Another explanation is that different AM systems and testing apparatus were used, which could also have influenced the results obtained. Finally, in the previous work, only three levels of porosity were analysed over a smaller range (59%-76%), thus making the fitted power laws less robust and more susceptible to changes if the properties at one of the three levels of porosity fluctuated.

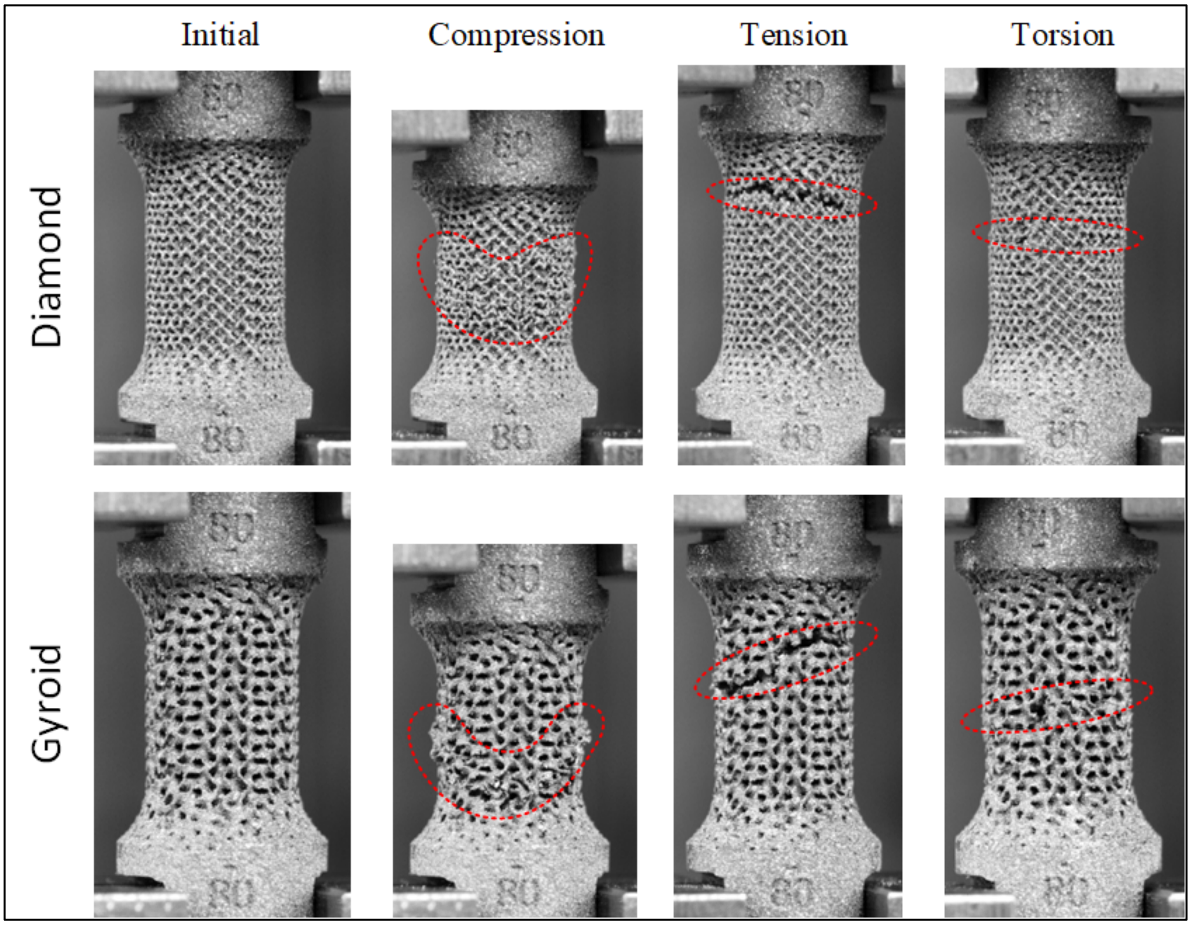

Figure 3.15 Examples of specimen failure of the 80% porous diamond and gyroid structures in compression, tension and torsion. Failure regions are encircled in red

Figure 3.16 brings together the numerically-obtained apparent elastic moduli and yield stresses of the two studied lattice structures in compression, tension and torsion, and compares them to the range of properties of trabecular (Ford & Keaveny, 1996; Galante, Rostoker, & Ray, 1970; Hakim & King, 1979; Kasra & Grynpas, 2007; X. Wang et al., 2016) and cortical bone (Hart et al., 2017; Mirzaali et al., 2016; T. Tang et al., 2015; Turner, Wang, & Burr, 2001; X. Wang et al., 2016; Wolfram & Schwiedrzik, 2016). The scarcity of studies on the mechanical properties of bones under tensile and shear loading, as well as the scatter and degree of anisotropy of the reported data makes the selection of ideal lattice candidates challenging. For a specific application such as intervertebral cages, the lattice structures must outperform the vertebrae during flexion/extension, compression and rotation of the human spine, which have properties close to those of trabecular bone: yield stresses of 2-6 MPa and moduli of elasticity of 0.087-0.791 GPa (El Masri et al., 2012; Singer et al., 1995; Wolfram, Wilke, & Zysset, 2010). It appears that all the structures studied in this work would fulfill the strength requirements for such an application, but would be too stiff to match the properties of the surrounding tissues. On the other hand, for an application where the implantation site is the femur having a yield stress ranging from 41 to 150 MPa and a modulus of elasticity ranging from 6 to 19 GPa (Mirzaali et al., 2016), 60% gyroid structures provide an appropriate combination of stiffness-strength characteristics.

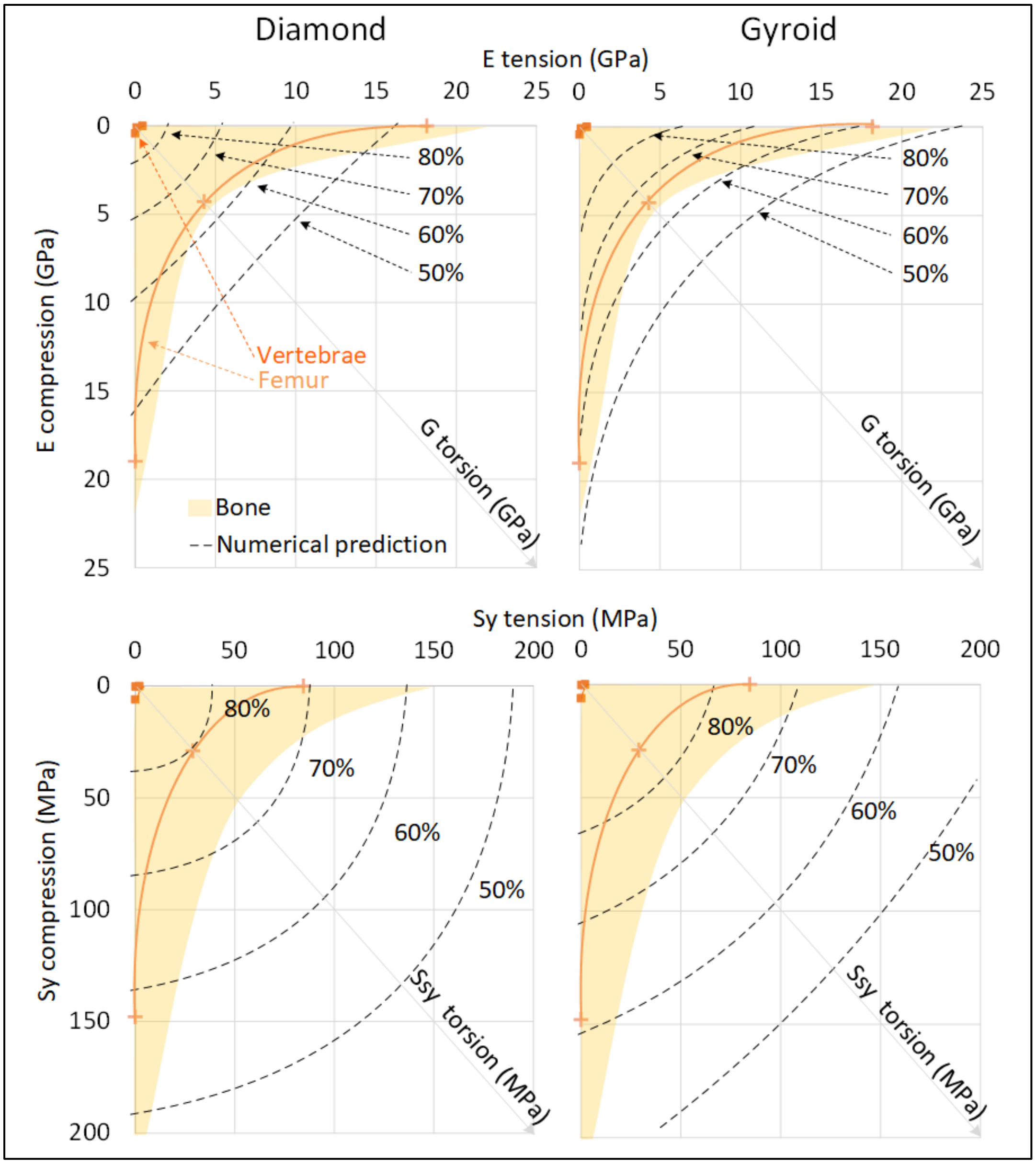

Figure 3.16 Comparison of the numerically-obtained apparent elastic moduli (E and G) and yield stresses (Sy and Ssy) of the diamond and gyroid lattices for compression (vertical axis), tension (horizontal axis), and torsion (diagonal) to the range of properties of bone structures, presented as shaded zones in each diagram. Properties of the vertebrae and the femur for the three loading modes are shown as tangible examples of the potential application requirements

3.8 Conclusions

The main goal of this work was to compare numerically and experimentally 50-80% porosity strut-based diamond and sheet-based gyroid lattice structures for three loading modes: axial compression/tension and torsion.

- Manufactured specimens were within 0-5% of the targeted 50-80% porosity levels, with the highest deviations occurring at the upper bounds of porosity, where the structures approached the manufacturing limits of the AM system. Printing defects were present in the form of internal pores, geometrical discontinuities, structural distortions and surface sintered particles.
- Experimental testing showed quasi-identical behavior of the tested structures in tension and compression with elastic moduli ranging from 3-22 GPa and yield stresses ranging from 48-186 MPa. Torsional results indicate that the lattice structures do not follow the von Mises limitation theory, since the ratio between the shear and axial yield stresses is higher than the traditional 0.577 for isotropic alloys (~0.94 for diamonds and ~0.87 for gyroids).
- Numerical models of all the studied structures were developed for the three loading modes and partially validated by mechanical testing. Simulations overestimated the stiffness and yield stress of the structures by 25% on average. These discrepancies are attributable to the uncertainty in the manufactured density, as well as to the limited representativity of the model boundary conditions.
- All studied lattice structures exhibited adequate resistance for the use in intervertebral cages. Their stiffness (3-22 GPa) was greater than those of the vertebrae (0.087-0.791 GPa), while situated in the stiffness range of cortical bone (7-22 GPa).

3.9 Acknowledgments

The authors would like to acknowledge R. Romanica J. Grignon and S. Plamondon for their technical support with AM system preparation, specimen machining and mechanical testing, respectively. In addition, the authors are thankful to D. Campion for his contribution to the literature review.

3.10 Funding

This work was funded by the Fonds de Recherche du Québec - Nature et Technologies [272262]; the Natural Sciences and Engineering Research Council of Canada [V. Brailovski’s Discovery grant]; and the Fonds de Développement de l’École de technologie supérieure [A. Timercan’s scholarship].

3.11 Data availability

The raw and processed data required to reproduce these findings cannot be shared at this time as the data also forms part of an ongoing study.

CHAPITRE 4

PROCESS OPTIMIZATION OF LASER POWDER BED FUSION OF SUPERELASTIC TI-NI LATTICE STRUCTURES: AN EXPERIMENTAL AND NUMERICAL STUDY

Anatolie Timercan [1], Donatien Campion [1], Patrick Terriault [1] and Vladimir Brailovski [1]

[1] Department of Mechanical Engineering, École de Technologie Supérieure, 1100 Notre-Dame West, Montreal, Quebec, Canada H3C 1K3

Article soumis pour publication dans la revue « Journal of Manufacturing Processes »,
le 2 février 2024

4.1 Avant-propos

Ayant analysé et confirmé l'applicabilité des structures en diamant et gyroide pour l'application visée, la troisième publication porte sur la fabrication additive de ces structures à partir d'un AMF, à savoir le Ti-Ni. Tout d'abord, il est nécessaire d'identifier les paramètres de fabrication optimaux de ce matériau pour l'équipement de FLLP utilisé en produisant et caractérisant des échantillons pleins. Ensuite il est possible de fabriquer les structures architecturées et de les tester mécaniquement, tout en comparant les résultats expérimentaux aux prédictions des simulations numériques.

4.2 Résumé

La fusion laser sur lit de poudre permet la fabrication de géométries complexes et facilite la mise en forme de matériaux difficiles à transformer, tels que les alliages à mémoire de forme équiatomiques de Ti-Ni. Dans cette étude, un modèle numérique a été utilisé pour sélectionner 11 ensembles de paramètres d'impression avec différentes densités d'énergie volumétrique (DEV) et taux de fabrication (TF) afin de produire des échantillons pleins en Ti-50,26%Ni. Les spécimens imprimés ont été étudiés en termes d'intégrité structurelle, de densité, de composition chimique, de températures de transformation et de phases cristallines. À une DEV élevée et un faible TF, une diminution significative de la teneur en

nickel a été observée. Une DEV de 90 J/mm^3 et un TF de 10 cm^3/h ont permis la fabrication d'échantillons avec une densité de 99,94% et une température finale de transformation en austénite Af = 26,3°C. Les mêmes conditions d'impression ont été utilisées pour fabriquer des structures architecturées en diamant et gyroïdes avec un taux de porosité de 60%. Suite à un traitement thermique à 500°C pendant 30 minutes, les structures en diamant ont manifesté des déformations apparentes réversibles plus importantes que leurs équivalents gyroïdes (7% contre 6%), une souplesse plus importante (2.9 contre 3.4 GPa), et des contraintes élastiques similaires (~48 MPa). Une analyse par éléments finis a permis de comparer le taux de matière transformée plastiquement dans les structures lorsque celles-ci sont globalement comprimées à 6%. Seulement ~2% du volume des structures en diamant subissait une déformation plastique, comparativement à ~20% pour leur équivalent gyroïde.

4.3 Abstract

Laser powder bed fusion allows the production of complex geometries and eases the shaping of difficult-to-transform materials, such as near-equiatomic Ti-Ni shape memory alloys. In this study, a numerical model was used to select 11 sets of printing parameters with different volumetric energy densities (VED) and build rates (BR) to produce bulk Ti-50.26at%Ni alloy specimens. The manufactured specimens were studied in terms of their structural integrity, printed density, chemical composition, transformation temperatures and crystalline phases. At high VED and low BR, a significant decrease in the nickel content was observed. VED=90 J/mm^3 and BR=10 cm^3/h yielded a printed density of 99.94% and an austenite finish temperature of Af = 26.3°C. The same printing conditions were used to produce 60% porous diamond and gyroid lattice structures. After heat treatment at 500°C for 30 minutes, the diamond lattices manifested larger apparent recovery strains (7 vs 6%), higher compliance (2.9 vs 3.4 GPa) and similar yield stresses (~48 MPa) compared to their gyroid equivalents. The numerical model predicted that at an equivalent apparent compression strain of 6%, only ~2% volume fraction of the diamond lattice material underwent plastic deformation as compared to ~20% for its gyroid equivalent.

4.4 Introduction

The advent of additive manufacturing has opened the door to numerous new applications and developments in recent years, most notably the manufacture of complex geometries for the aerospace and biomedical fields (Khorasani et al., 2020; Wong & Hernandez, 2012). Particularly of interest in biomedical science is the production of porous implants having mechanical properties close to those of bone (Mahmoud & Elbestawi, 2017; X. Wang et al., 2016; X.-Y. Zhang et al., 2017). In this context, various types of lattice structures are being studied and are providing favorable outcomes (L.-Y. Chen et al., 2021; Kelly et al., 2021). Additive manufacturing has also facilitated the shaping of materials that are difficult and costly to form. One such material is near-equiatomic Ti-Ni shape memory alloy (SMA), also known as Nitinol, a functional metallic material that has been widely used in stents and orthodontics due to its shape memory and superelastic properties (Otsuka & Wayman, 1999). These remarkable properties are attributable to the diffusionless transformation occurring between the two crystallographic phases: high-temperature austenite and low-temperature martensite. This martensitic transformation can be triggered either by inducing a mechanical stress or by changing the temperature. The notoriously low formability of Ti-Ni has been a limiting factor for its wider practical application, since commonly used forming methods such as casting, forging, rolling, drawing, and laser or electrochemical machining, restrain the product geometry to relatively simple shapes (Mwangi et al., 2019). Since additive manufacturing, more specifically laser powder bed fusion (LPBF), allows the production of complex geometries and eases the shaping of difficult-to-transform functional materials, an investigation is warranted into the synergy between benefits offered by LPBF, the design flexibility of porous structures and the functional properties of Ti-Ni.

Multiple attempts to produce Ti-Ni by laser powder bed fusion have been documented in the literature, but with varying degrees of success (Chekotu et al., 2019; Elahinia et al., 2016; Y. Zhang et al., 2021). The main difficulty encountered in this effort appears to be the selection of printing parameters which would allow printing of defect-free parts, while preventing an excessive nickel evaporation from the alloy (Bassani et al., 2023; Biffi, Fiocchi, et al., 2020;

Borisov et al., 2021; Chmielewska et al., 2021; Leon et al., 2023; Mahmoudi et al., 2018). The latter is especially important, since the shape memory and superelastic properties of Ti-Ni are strongly dependent on the chemistry of the material (Brailovski et al., 2003). In a bid to produce low-stiffness structures, Bartolomeu et al. (2020) attempted to manufacture superelastic Ti-Ni lattices, but they were not able to observe in them any superelastic response. Biffi, Bassani, et al. (2020) were more successful, but the superelasticity of their lattice structures was only partial. This was partially due to increased martensitic transformation temperatures caused by the complexity to control the material composition during printing. The above-mentioned difficulties mean that more work must be devoted to the optimization of laser powder bed fusion of superelastic Ti-Ni lattice structures.

With this objective in mind, this study aims to design, manufacture, numerically simulate and experimentally characterize superelastic Ti-Ni lattice structures. To find an optimal manufacturing regime, a series of Ti-Ni specimens will be manufactured using a simulation-driven density process mapping. The printed specimens will be analyzed in terms of their density and chemical composition, and subjected to structural and differential scanning calorimetry analyses. Next, the most promising printing regime will be selected and used to manufacture bulk testing coupons as well as diamond and gyroid lattice structures. The lattice structures will be analyzed in terms of their structural integrity, geometric conformity and mechanical behavior, and the experimental results will be compared to those of the numerical simulations to validate the numerical model and establish a comprehensive basis for the optimal use of these structures.

4.5 Materials and methods

4.5.1 Manufacturing parameter selection

In this study, Ti-Ni 50.26 at% 15-53 µm powder was procured from *Avimetal Powder Metallurgy Technology Co Ltd (Beijing,China)* and loaded into a laser powder bed fusion *TruPrint 1000* system *(Trumpf GmbH, Ditzingen, Germany)* equipped with two 200 W fiber lasers (spot diameter of 55 µm). The powder was also subjected to a particle size analysis using a *LS 13 320 XR* apparatus *(Beckman Coulter, Indianapolis, USA)* (Figure 4.1a) and to scanning electron microscopy (SEM) observations, using a *TM3000* microscope *(Hitachi, Tokyo, Japan)* (Figure 4.1b).

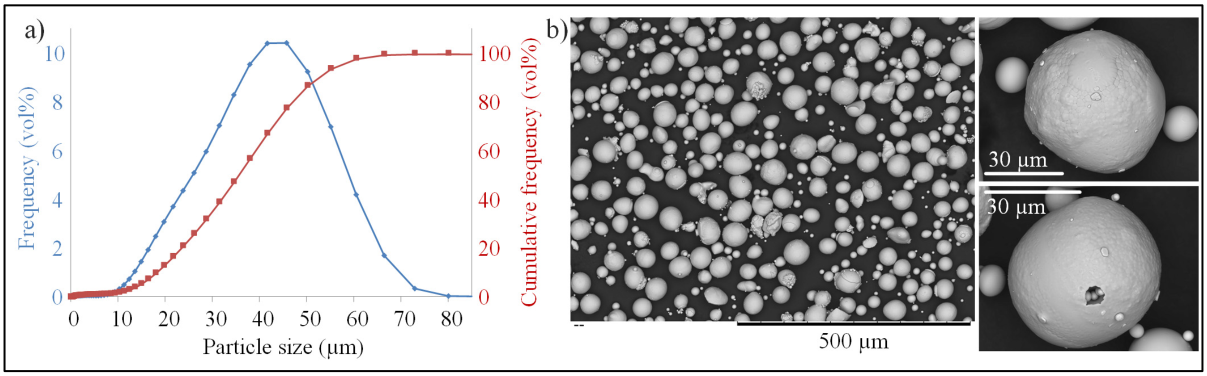

Figure 4.1 (a) Ti-Ni powder particle size distribution and (b) particle morphology observed by SEM

To determine the process parameter sets allowing to print highly dense components, a proprietary numerical algorithm allowing the prediction of the density of a printed material as a function of the volumetric laser energy density (VED=P/vth) and the material build rate (BR=vth) was used; with P [W] being the laser power; v [mm/s], the laser speed; t [mm], the layer thickness and h [mm], the hatch distance (Letenneur et al., 2017). This algorithm is based on the numerical modeling of a melt pool created by moving a Gaussian heat source across the powder bed and targeting the simultaneous satisfaction of three adimensional ratios relating melt pool dimensions to laser scanning parameters: the melt pool width-to-hatch distance ratio, $W/h \in 1.5\text{-}2.5$; the melt pool depth-to-layer thickness ratio, $D/t \in 2\text{-}3.5$, and the melt pool length-to-width ratio, $L/W \leq 4$. The Ti-Ni alloy material properties used in the model are presented in Tableau 4.1.

Tableau 4.1 Material properties of Ti-Ni used for the LPBF process modeling and specimen densities prediction

Tiré de Davis et Committee (1998) et Otsuka et Wayman (1999)

Melting temperature [K]	1573
Thermal conductivity [W/m*K]	18
Specific heat capacity [J/kg*K]	450
Laser absorptivity, %*	45.6
Powder bed density, %	60
*Absorptivity was calculated using the Hagen-Rubens model and an electrical resistivity value of 1*10-6 Ohm*m (Letenneur et al., 2017)	

To build the printed density process map shown in Figure 4.2, the laser power *P* was varied from 60 to 200 W, the laser speed *v*, from 200 to 3000 mm/s and the hatch distance *h*, from 30 to 130 µm. Based on the particle size distribution available, the layer thickness *t* was set to 30 µm. In accordance with the algorithm predictions, a 70 µm hatch distance with VED=70-100 J/mm^3 and BR=3-10 mm^3/h processing parameter ranges predicted a sufficiently large area of the highest printed density. Next, to cover a large portion of the processing map with predicted densities ranging from 97 to 100% with a bid to validate the algorithm, eleven processing parameter sets were selected (Tableau 4.2).

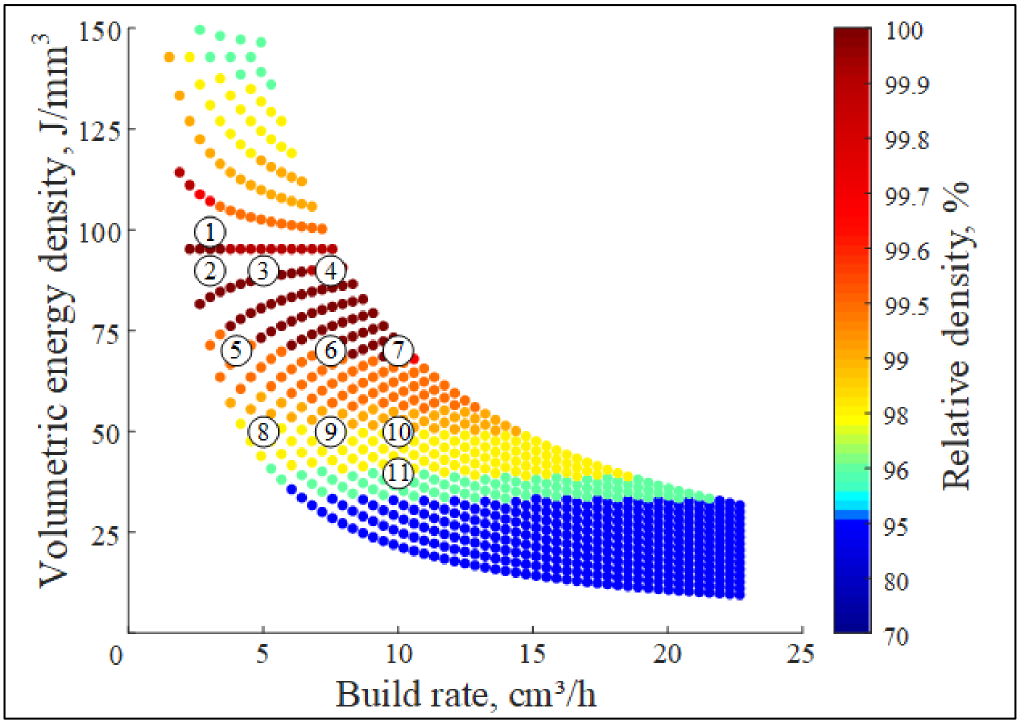

Figure 4.2 Processing map of the predicted material density as a function of VED and BR for 30 µm layer thickness and 70 µm hatch distance; zone encompassed by VED=70-100 J/mm^3 and BR=3-10 cm^3/h corresponds to the highest expected printed density

Tableau 4.2 Printing parameters and predicted densities for 30 µm layer thickness and 70 µm hatch distance

Specimen	Power (W)	Speed (mm/s)	Volumetric energy density (J/mm^3)	Build rate (cm^3/h)	Predicted density (%)
1	83	397	100	3	99.86
2	75	397	90	3	100.00
3	125	661	90	5	99.94
4	188	992	90	7.5	99.85
5	78	529	70	4	99.66
6	146	992	70	7.5	99.86
7	**194**	**1323**	**70**	**10**	**99.87**
8	69	661	50	5	97.73
9	104	992	50	7.5	98.04
10	139	1323	50	10	98.07
11	111	1323	40	10	96.10

4.5.2 Manufacture, preparation, chemical and structural analyses of printed specimens

The first printing iterations were carried out on titanium and steel substrates and resulted in the separation of parts from the build plate, forcing the cancellation of the builds after a few layers. This problem was resolved by using a Ti-Ni build plate. Printing was carried out under argon atmosphere with an O_2 content ≤ 0.01%. Two types of cylindrical specimens were manufactured for each parameter set: 5 mm diameter-10 mm height for DSC and XRD measurements and 10 mm diameter-20 mm height, for density measurements. Furthermore, 60% porous gyroid and diamond lattice structures were manufactured with Parameter set 7, which had a predicted density of 99.87% and the fastest productivity (BR) among the selected parameters. The sheet-based gyroid lattice structure was designed using *nTopology (nTopology, New York, USA)* software with the following parameters: a sheet thickness of 0.305 mm, a cell size of 2.431 mm and a pore size of 0.75 mm. The equivalent porosity strut-based diamond structure was designed using a proprietary *MATLAB (MathWorks, Massachusetts, USA)* algorithm with a strut thickness of 0.455 mm, a cell size of 1.485 mm and a pore size of 0.75 mm. The selection of these lattice configurations was discussed in detail in a previously published study (Timercan, Terriault, & Brailovski, 2023). Finally, a heat treatment at 500 °C for 30 min followed by air cooling was performed on some of the printed specimens to study the effect of removing residual stresses on the printed material properties.

Titanium and nickel compositions of the as-received powder and printed specimens were measured using electron probe microanalysis (EPMA) on a *Cameca SX100 FiveFE* system *(Ametek, Gennevilliers, France)*. An accelerating voltage of 20 kV, a beam current of 20 nA and a beam size of 5 µm were used to analyze 10 points on each specimen. In accordance with the Tuckey's significant difference test results, outlier values were discarded. Porosity analyses on the 5 mm-diameter cylinders and lattice structures were carried out using a *Nikon XTH225 (Tokyo, Japan)* computed tomography (CT) system. Scans were carried out using a 0.25 mm Cu filter and with a 208 kV tube voltage, 60 µA current and 5 µm resolution for the cylinders, and a 210 kV tube voltage, 93 µA current and 12.4 µm resolution, for the lattice structures. The resulting images were treated in *Dragonfly software (Comet Technologies Inc, Montreal, Canada)* and the relative density was calculated by porosity segmentation. To validate the CT scan results, pycnometry density measurements on the 10 mm-diameter specimens were carried out on a *Micromeritics AccuPyc II 1340* apparatus using helium gas with three repetitions of 10 purging cycles.

A phase analysis of the as-received powder, and of the as-built and heat-treated specimens, was carried out on a *Panalytical X'Pert Pro (Malvern Panalytical, Malvern, United Kingdom)* X-ray diffractometer in the 30 to 100° 2θ range, using a copper Kα radiation (λ=0.1506 nm), a step size of 0.0167°, a generator voltage of 45 kV and a tube current of 40 A. Specimens for the XRD analyses were polished to remove the surface oxide layer using 400 grit sandpaper. To remove the background, smoothen the curves and identify the phase peaks, the resulting data were treated using a custom *MATLAB* algorithm. References from the *HighScore* software database *(Malvern Panalytical, Malvern, United Kingdom)* were used to correlate the measured phase peaks with the known austenitic (B2), martensitic (B19') and R-phase peak positions (Krishnan, Manjeri, Clausen, Brown, & Vaidyanathan, 2008; Kudoh, Tokonami, Miyazaki, & Otsuka, 1985; Semenova & Kudryavtsev, 1994; Sitepu, 2003, 2008, 2009). The as-built and heat-treated Parameter set 7 specimens were observed by optical microscope (*Leica DMLM, Leica Microsystems, Wetzlar, Germany*) and subjected to the EBSD analysis using a *Hitachi SU8230* SEM *(Hitachi, Tokyo, Japan)*. For the latter, specimens were mounted in carbon-charged resin, polished using grit 400, 600, 800 and 1200 SiC sandpaper and colloidal silica (24h), and etched using Kroll's reagent (1.9% HF, 4.7% HNO_3 and 93.4% H_2O) for 45 seconds. Finally, the EBSD specimens were subjected to secondary colloidal-silica polishing for 2 hours and ion milling.

4.5.3 Measurement of the transformation temperatures and mechanical testing

The phase transition temperatures of the powder, as-built and heat-treated specimens were measured by differential scanning calorimetry using a *DSC2500* apparatus *(TA Instruments, New Castle, USA)*. Specimens in the shape of discs cut from the 5 mm-diameter cylinders were sanded down in cold water until reaching a mass of 15 to 45 μg and tested in the -85 to 100 °C temperature range at a heating-cooling rate of 5 °C/min under nitrogen cover gas. It is known that Ti-Ni SMA can undergo martensitic transformation via direct austenite-martensite transformation, asymmetric R-phase transformation and symmetric R-phase transformation. Depending on the material condition, multiple phase transformation peaks could therefore be expected: during cooling, an R-phase peak (R) and a martensite peak (M) representing respectively the austenite transformation to R-phase and the R-phase change to martensite. Inversely, during heating, an R-phase peak (R) and an austenite peak (A), representing the transformation of martensite into R-phase and then into austenite. For each peak (p), the transformation start (s) and finish (f) temperatures can be identified as intercepts between the tangents of the baselines and the tangents to the inflection points on the heating and cooling peaks, as per ASTM F2004-17 (ASTM, 2017b) (Figure 4.3a). The characteristic temperature of greatest interest for this study is Af (austenite finish) and it corresponds to the fully austenitic state of the material; above this temperature, Ti-Ni should manifest the superelastic behavior, which is targeted for the biomedical applications of lattice structures.

Mechanical testing was performed on bulk specimens manufactured with Parameter set 7. ASTM E8 dogbone sub-specimens with a 4 mm diameter and a 24 mm length gauge section were tested in tension to assess the mechanical response of the alloy. An *Alliance RF/200* system *(MTS, Eden Prairie, MN, USA)* was used to apply incremental displacements in 0.015 mm/mm steps at a rate of 0.001 mm/mm/s. The load-displacement data can be used to determine the modulus of elasticity (E), the martensite transformation start (σ_{tr} or σ_{AMS}) and finish (σ_{AMF}) stresses, the austenitic transformation start (σ_{MAS}) and finish (σ_{MAF}) stresses, the dislocation yield stress (σ_y), the maximum stress before failure (σ_{max}) and the relative elongation to failure (δ), as shown on the idealized stress-strain diagram of Figure 4.3b. These material properties represent a minimum set of material characteristics required for the finite element analysis (FEA) of superelastic lattice structures.

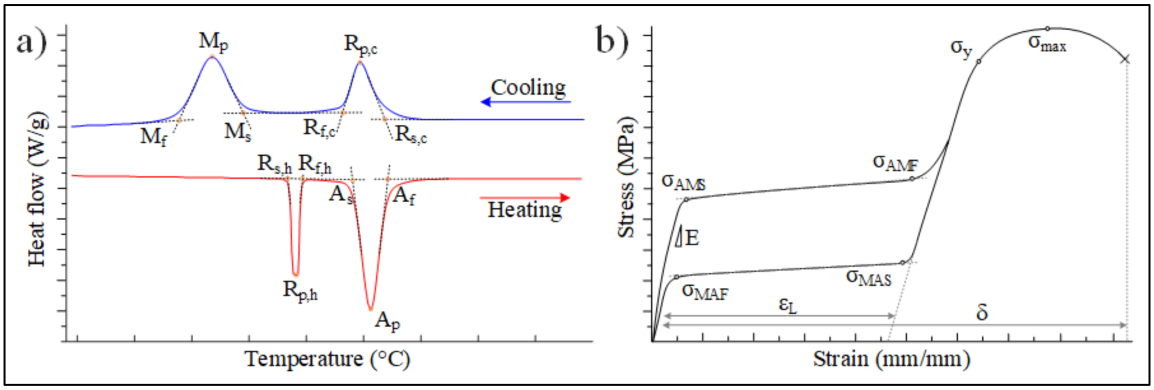

Figure 4.3 Idealized (a) DSC and (b) tensile diagrams of Ti-Ni SMA and corresponding temperature, stress and strain characteristics

4.5.4 Numerical simulations and experimental validation

Numerical simulations were carried out on the idealized CADs of the 60% porous gyroid and diamond lattice specimens using a workstation with two 14 core Intel Xeon E5-2660 CPUs and 256GB of RAM. STLs of the specimens were imported into Ansys Workbench 2021R1 where compression was simulated with large deformation analysis. Following a mesh convergence analysis using a 5% deviation criterion, a layered tetrahedrons method with an element size of 0.1 mm and a layer height of 0.1 mm was used to create the FEA mesh with an average of 2.5 million elements. For the simulation of the structures, a standard Ansys idealized superelastic material law was approximated from the tensile testing results.

The boundary conditions consisted of displacements applied directly to the mesh nodes. The displacements of all bottom surface nodes were set to zero in the axial direction and the bottom nodes along the symmetry planes were blocked laterally to prevent the transverse displacement of the structure. The axial displacements of the top nodes were applied using automatic stepping up to 6% apparent strain, with an average of 20 steps to resolution. The reaction force probe was applied to the blocked displacements and then converted to compression stress using the specimens' apparent cross-section area. The resulting stress-strain data were used to calculate the apparent modulus of elasticity and the apparent yield stress of the structures. In addition to calculating the stress-strain data, the simulations were also used to assess the material volume fractions under different states (elastic, plastic, stress-induced phase transformation). To select the elements in different states and extract their relative volumes, a script was written using the Ansys parametric design language (APDL) commands tool. The numerical model was validated by testing the manufactured lattice structures in compression and comparing the measured apparent stress-strain responses of the specimens to those of the simulations.

4.6 Results

4.6.1 Integrity and density of manufactured specimens

By using a Ti-Ni substrate, all components were manufactured in their entirety, as shown in Figure 4.4. However, all the 10 mm-diameter specimens exhibited cracking, while only some of the 5 mm-diameter specimens showed visible cracks. However, CT scanning showed that most of the 5 mm diameter cylinders also contained cracks (highlighted in yellow on the sideview of Figure 4.5), which were more pronounced and more numerous with a decrease in the VED. While gauge sections of the tensile specimens did not show signs of cracking, the endpieces touching the baseplate contained some cracks and the endpieces away from the baseplate showed signs of oxidation. No cracks were found in the lattice structures and the measured porosities of diamond lattices were 54.4% and those of gyroid lattices were 56.7%, i.e., 5.6% and 3.3% lower than the 60% design target, respectively.

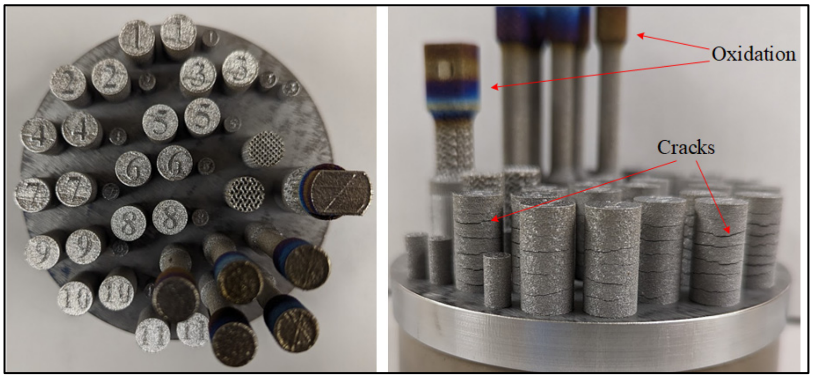

Figure 4.4 Ti-Ni substrate featuring cylindrical specimens (10 and 5 mm diameter), tensile specimens and lattice structures

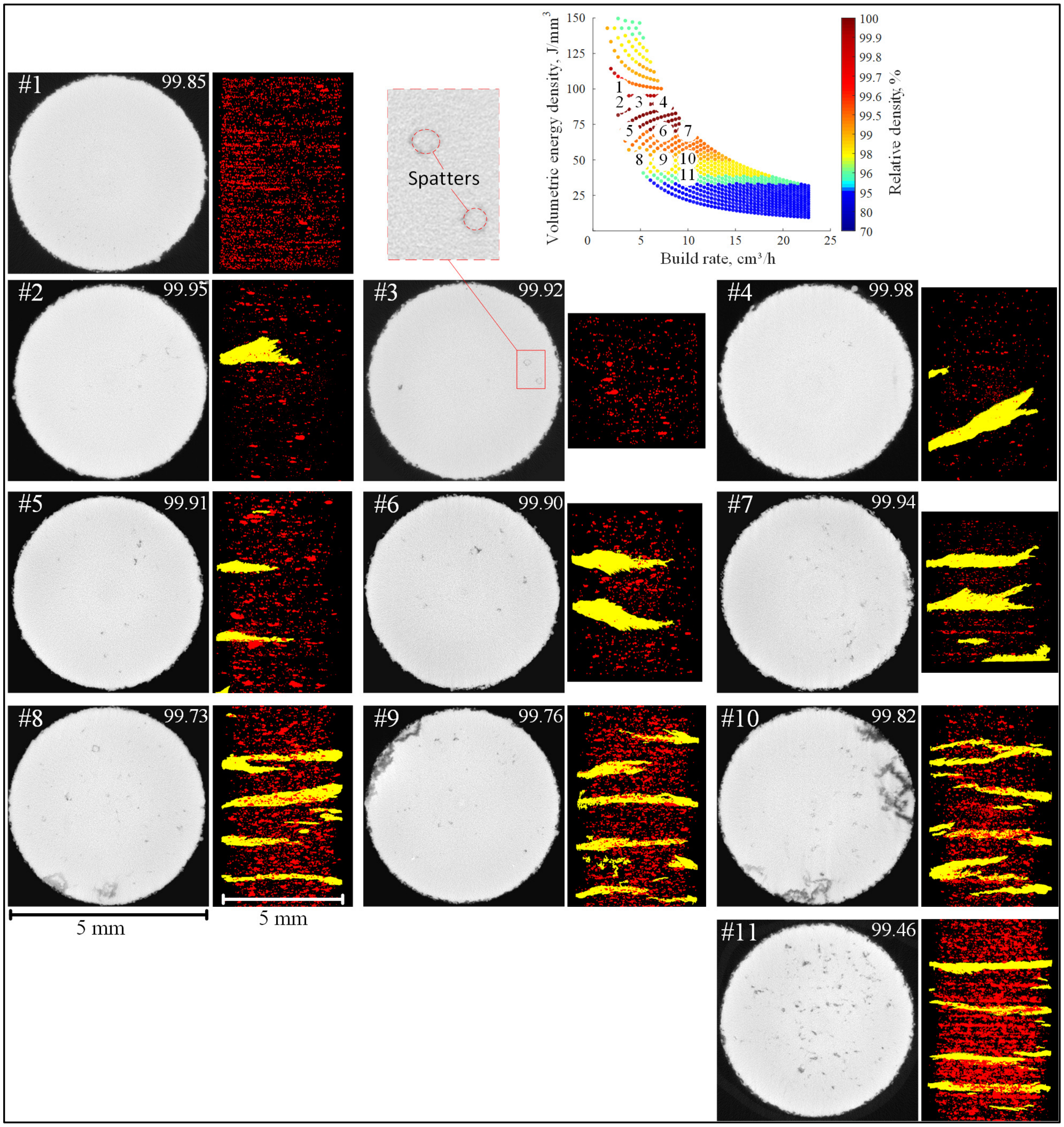

Figure 4.5 CT-scan analysis of the 5 mm diameter specimens printed with the 11 sets of parameters shown as a cross-section image and the sideview of the specimen porosity (red) and cracks (yellow). Images are arranged according to the specimen position on the processing map

Relative density results are presented in Figure 4.6 and in Tableau 4.4 of the Annex. It is noteworthy that the CT-scan and pycnometry measurements did not consider the presence of cracks. During the CT measurements, the cracks were removed in the imaging software, while during the pycnometry measurements, cracks were filled with gas, thus being neglected. Various types of processing-induced pores were detected by the CT measurements, with the largest ones caused by spattering. These spatters, up to 0.25 mm in diameter, or 5 times the size of an average powder particle, were trapped and formed toroidal pores partially filled with unmelted powder particles, as can be observed in Specimens 3, 6 and 8 of Figure 4.5.

All measurements indicated that the relative density of the printed parts was higher than 99%, which significantly diverged from the numerical predictions, which underestimated the printed densities by 1-3%. However, the low VED Parameter sets 8-11 resulted in the lowest densities (≤99.4%), while the high VED Parameter sets 1-7 resulted in the highest densities (≥99.7%), which is qualitatively consistent with the predicted values. Note that when taking into account the standard deviations of density measurements, only the results of pycnometry measurements on specimens printed using Parameter sets 8-11 and 1-7 were statistically different ($P<0.05$). Although specimens printed using Parameter set 1 did not show signs of cracking, they manifested systematic porosity, which was repeated layer-wise, as seen in Figure 4.5. Finally, specimens printed using Parameter set 7 were among the densest, while also providing the fastest build rate. Based on these results, this Parameter set was selected for future printing.

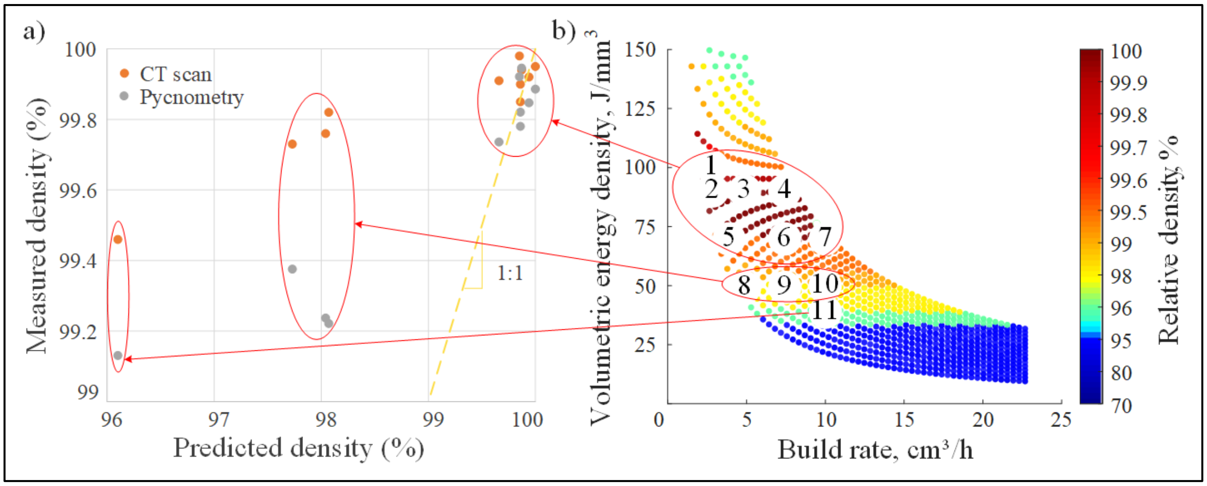

Figure 4.6 (a) Measured relative density compared to the model prediction for each parameter set as related to the (b) processing map

4.6.2 Chemical composition

A chemical analysis of the as-received powder showed that its nickel content was ~50.26 at%. As illustrated in Figure 4.7, all the printed specimens had lower nickel concentrations as compared to the powder, indicating different levels of nickel evaporation during manufacturing. Figure 4.7b shows a best-fit model of the experimental points in the VED-BR design space. It appeared, as a general trend, that the nickel content decreases as the VED increases and the BR decreases. Specimen 1, manufactured with a VED of 100 J/mm^3 and BR of 3 cm^3/h, had the lowest nickel content of 49.83 at% and Specimen 7, manufactured with a VED of 70 J/mm^3 and BR of 10 cm^3/h, had one of the highest nickel contents of 50.16 at%. Specimen 3 appeared to be an outlier, having a nickel content identical to that of the powder. Note however, that considering a relatively high standard deviation of the measurements (±0.15 at%), the observed differences in the chemical compositions are not statistically significant ($P<0.05$). Of note, such a significant scatter in otherwise very precise EPMA measurements could be caused by a high level of chemical heterogeneity in the as-printed specimens.

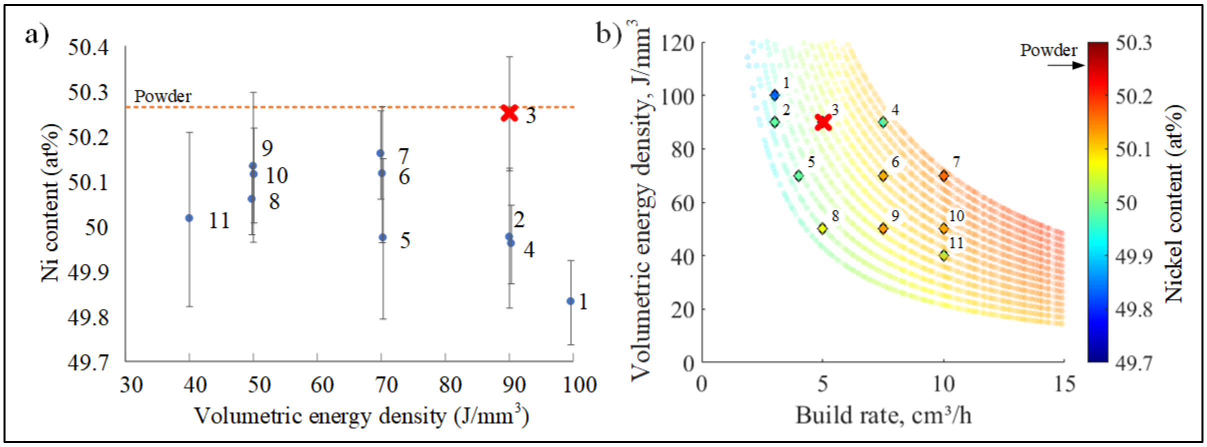

Figure 4.7 Nickel content in the manufactured specimens as (a) a function of the VED and (b) in the BR-VED design space. Specimen 3 is considered an outlier; arrow indicates nickel content in the as-received powder

4.6.3 Phase transition temperatures

It can be seen from the DSC curves (Figure 4.8) that the printing parameters influence phase transformation temperatures. Indeed, these temperatures were lower by 40 to 60°C for the low VED-high BR than for the high VED-low BR specimens. Specimens 1 and 2 were significantly different from the other specimens, and were the only specimens with transformation temperatures higher than those of the as-received powder. The as-built specimens had wide peaks revealing direct austenite-to-martensite transformation during cooling and heating. Following the heat treatment, the transformation peaks became narrower and more pronounced, and the presence of transient R-phase was observed. The appearance of R-phase proved problematic when it came to determining the transition temperatures, since some specimens exhibited asymmetric transformations, and others, symmetric transformations, resulting in an overlap between the R-phase and austenite transformation peaks during heating, as observed for Specimens 1, 2, 6, 7, 9, 10 and 11. The heat treatment increased the phase transition temperatures of all the investigated specimens, except for Specimens 1 and 2, for which the Mf and Af temperatures remained virtually unchanged (Tableau 4.5 in the Annex). Moreover, the differences in Af temperatures of the specimens manufactured using different VED-BR parameter sets was reduced from ~50°C in the as-built conditions to ~12°C, after the heat treatment, with Specimens 4-11 stabilizing at an Af of 26-30°C (Figure 4.9).

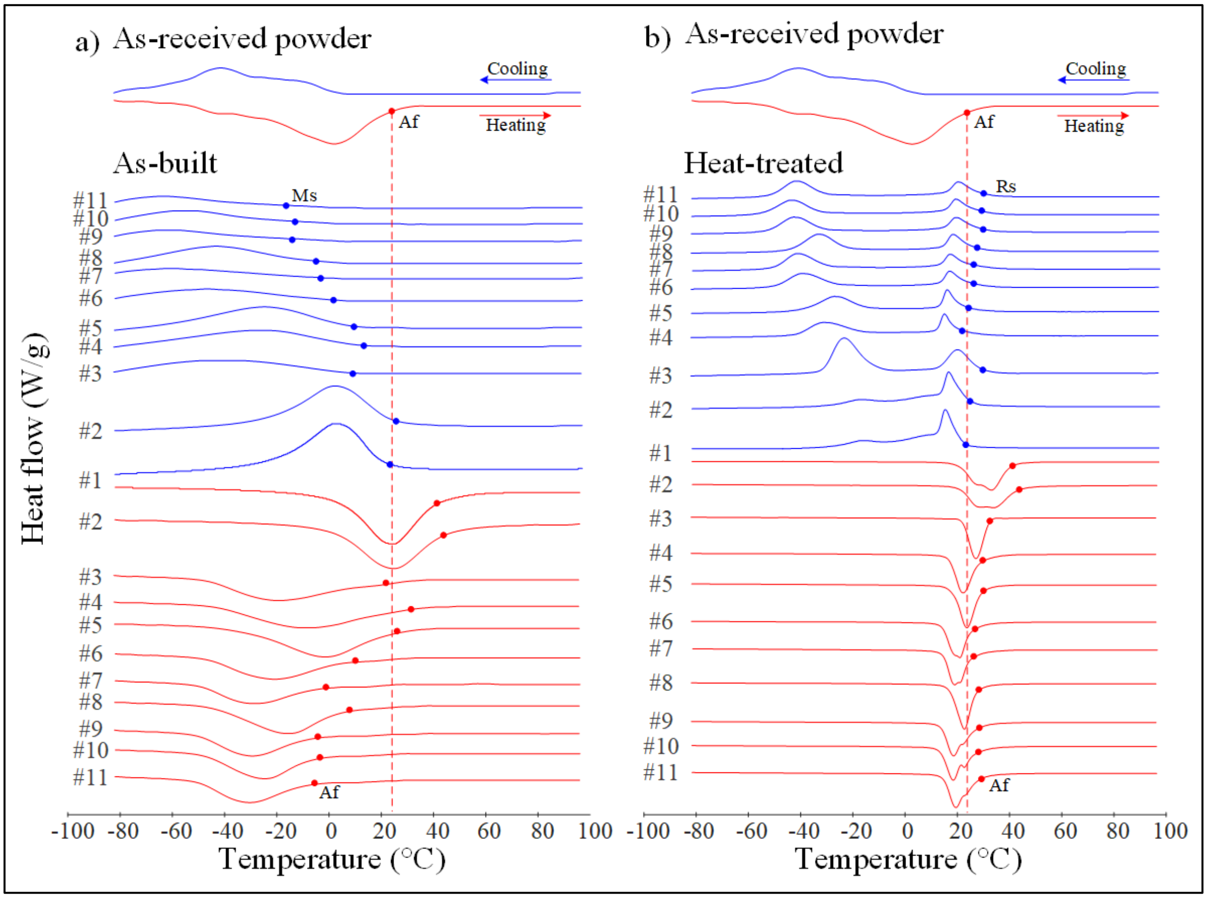

Figure 4.8 DSC results of the as-received powder and printed specimens: (a) as-built and (b) heat-treated

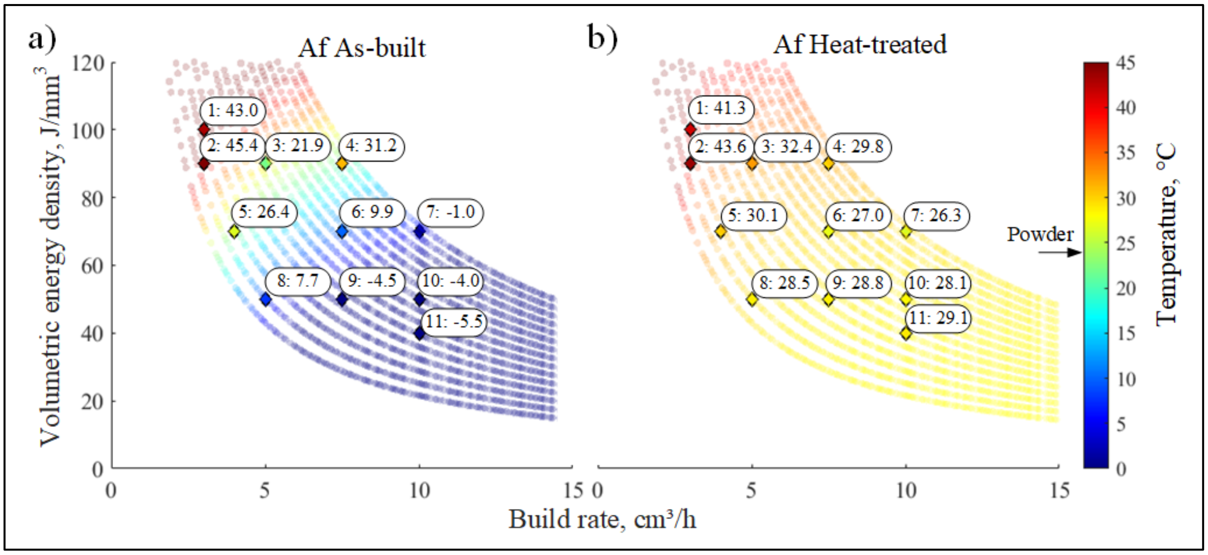

Figure 4.9 Af temperature of the specimens in the (a) as-built and (b) heat-treated conditions in the VED-BR coordinates; arrow indicates Af temperature of the as-received powder

4.6.4 Crystalline phase analysis

Figure 4.10 presents XRD diffractograms with the detected phase peaks encircled. Phases were identified as austenitic (red) (Semenova & Kudryavtsev, 1994; Sitepu, 2009), martensitic (blue) (Kudoh et al., 1985; Sitepu, 2008) or R-phase (green) (Krishnan et al., 2008; Sitepu, 2003). The as-received powder had four main diffraction peaks of the austenite (B2) phase and three minor peaks representing the martensite (B19’) phase. Specimens in the as-built conditions displayed the same austenitic peaks as the powder, their intensities however, being lower. Austenite in the high VED-low BR specimens had a preferential (200) orientation, whereas in the low VED-high BR specimens, the (110) peak was the most intense, similarly to the powder. The martensitic phase increased in intensity and new martensite peak positions appeared in the printed specimens, as compared to the powder. Some B19 peaks were not detected by the software, because they blended in with adjacent peaks (e.g. B19 (022) with B2 (200)).

The heat-treated specimens were different from the as-built specimens in two ways: an increased intensity and shifted angular positions of the martensite peaks as well as the appearance of new peaks indicating the presence of R-phase. The latter was consistent with the DSC results, which indicated that at room temperature, all heat-treated specimens underwent R-phase transformation. An apparently lower martensite content in the as-built specimens as compared to their heat-treated counterparts could be explained by the presence of high residual stresses in the former. Figure 4.11 illustrates the as-built and heat-treated microstructures of the specimen printed with Parameter set 7. Columnar grains typical of the LPBF process were observed in both states. However, it appeared that the as-built specimens were mostly austenitic, whereas after the heat-treatment, fine lamella appeared inside the grains, indicative of an increase in the martensite content also seen in the XRD results. On the top surfaces, grains are aligned along the laser tracks. EBSD analyses showed a preferential (100) grain orientation in the build direction in both the as-built and heat-treated states. In addition, the as-built specimens manifested a larger fraction of non-indexed phases than their heat-treated equivalents because of a higher dislocation density and a higher level of residual stresses in the former.

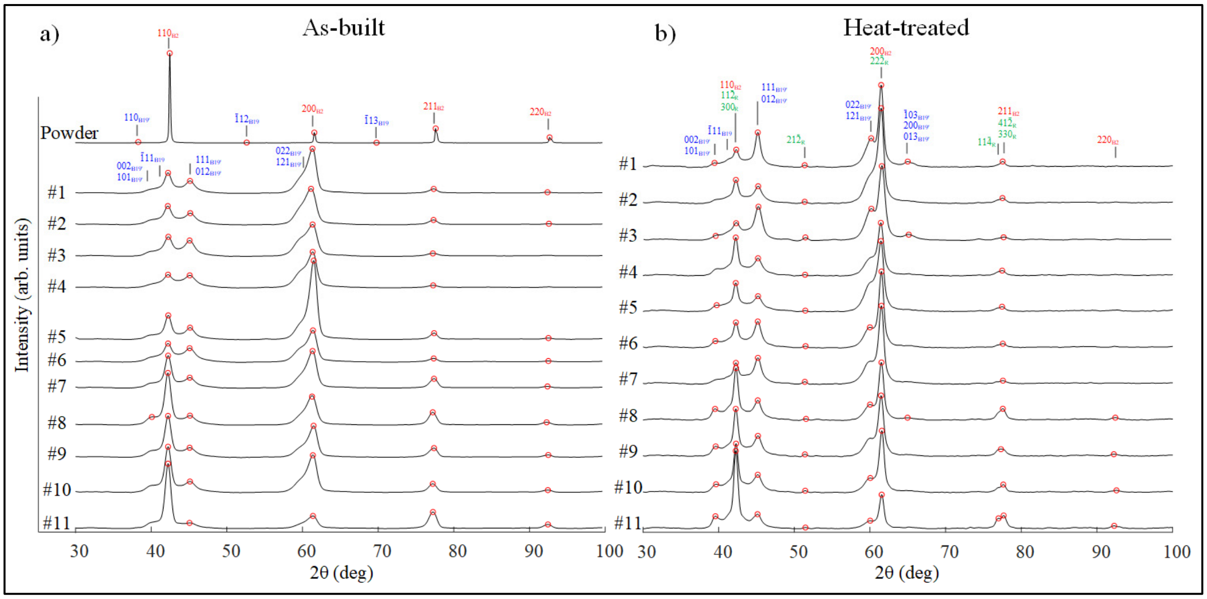

Figure 4.10 X-ray diffractograms of the powder and printed specimens in the (a) as-built condition and (b) after heat treatment; peaks of austenite (red), martensite (blue) and R-phase (green) are identified

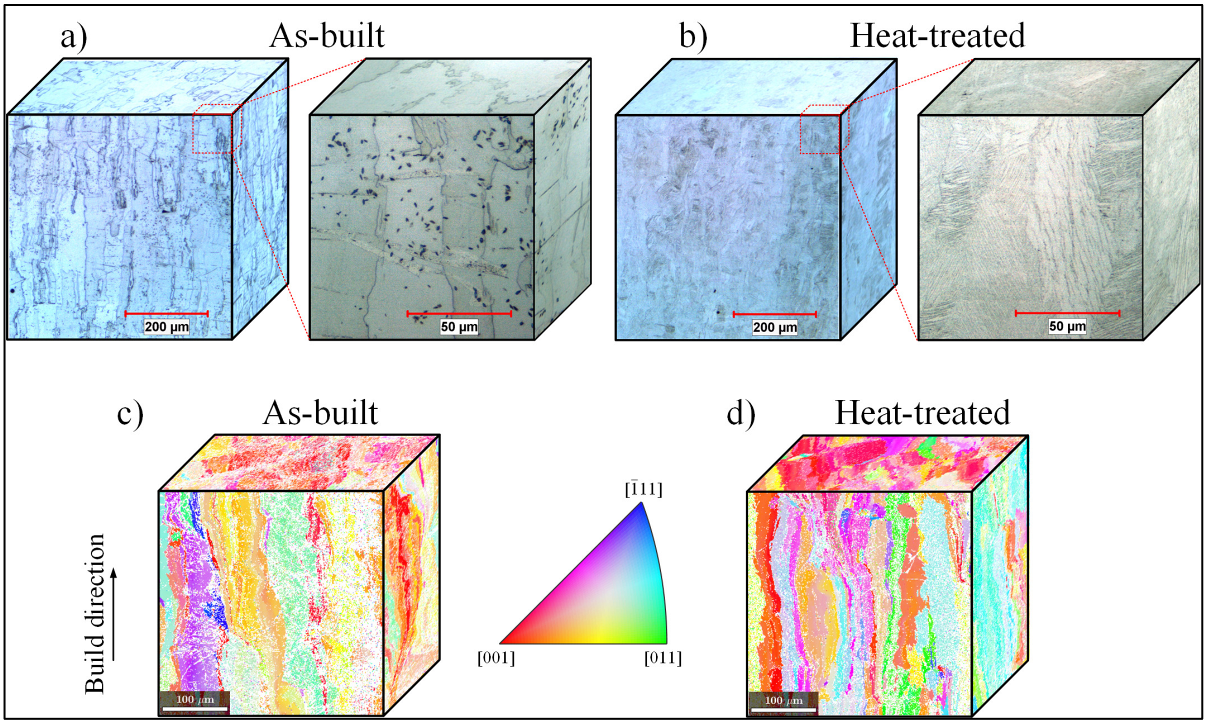

Figure 4.11 Microstructure of the specimen printed using Parameter set 7: (a,b) optical microscopy and (c, d) EBSD in the as-built (a, c) and heat-treated (b, d) conditions

4.6.5 Numerical model and validation

The tensile stress-strain diagrams of bulk specimens printed with Parameter set 7 are shown in Figure 4.12 and the mechanical properties determined from these diagrams are collected in Tableau 4.3. It can be seen that the as-built specimens had a brittle behavior, suffering failure at 1% of strain, whereas the heat-treated specimens failed at 5.5%. For both conditions, the phase transformation yield stress corresponded to ~250 MPa and the modulus of elasticity varied as a function of the specimen state: 22.2 GPa in the as-built condition and 18.7 GPa, in the heat-treated condition. Even though testing of the as-built specimens was performed above their DSC-measured Af temperatures (-1°C), the presence of residual stresses hindered superelasticity. After the heat treatment, the Af temperature increased and the room-temperature microstructure was no longer completely austenitic, thus resulting in a partial superelastic behavior with recoverable strains (elastic and superelastic, $\varepsilon_r = \varepsilon_e + \varepsilon_{se}$) of ~2%. For the FEA of lattice structures, an idealized stress-strain material diagram was approximated from the tensile diagrams of heat-treated specimens (Figure 4.12b), with $E = 18.7$ GPa, $\nu = 0.3$, $\sigma_{AMS} = 250$ MPa, $\sigma_{AMF} = 500$ MPa, $\sigma_{MAS} = 200$ MPa, $\sigma_{MAF} = 0$ MPa and $\varepsilon_L = 0.028$ (Tableau 4.3). The alpha parameter, which reflects the asymmetrical behavior of the material in tension and compression, was assumed to be zero.

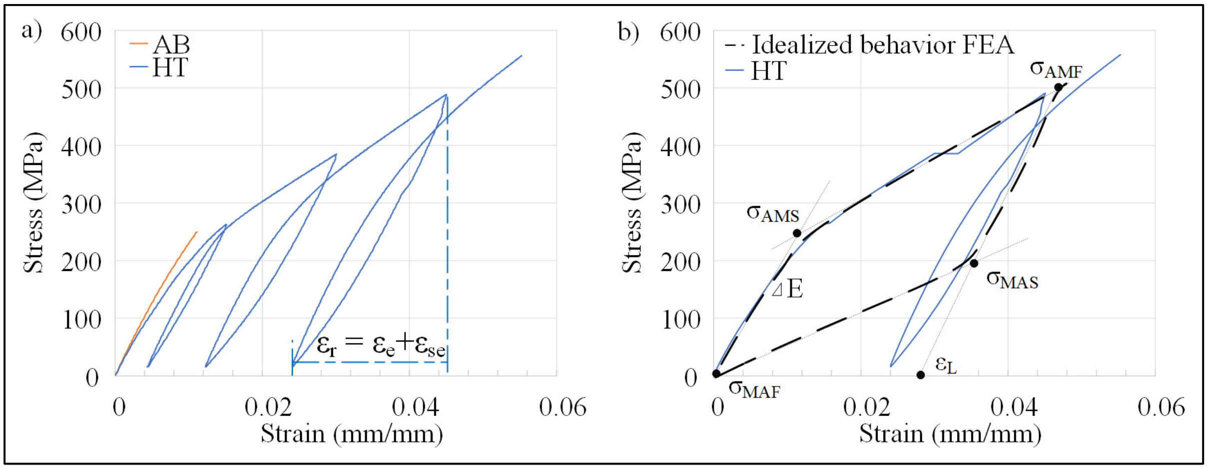

Figure 4.12 Tension stress-strain diagrams of the bulk specimens (Parameter set 7) in the as-built (AB) and heat-treated (HT) conditions with (a) incremental loading and (b) idealized material behavior law for the FEA simulations (dashed curve) based on an averaged stress-strain diagram in the heat-treated state (solid curve)

Tableau 4.3 Mechanical properties of the as-built and heat-treated specimens in tension and idealized stress-strain parameters of the heat-treated specimens used for FEA simulations

		E (GPa)	σ_{AMS} (MPa)	σ_{AMF} (MPa)	σ_{MAS} (MPa)	σ_{MAF} (MPa)	σ_{max} (MPa)	ε (%)
Experimental	As-built	22.2	-	-	-	-	250	1
	Heat-treated	18.7	250	-	-	-	556	5.5
Simulation	Idealized heat-treated	18.7	250	500	200	0	-	2.8

Figure 4.13a compares the stress-strain behavior of the simulated gyroid and diamond lattice structures under compression, the former being significantly stiffer than the latter. The gyroid lattices had an apparent elastic modulus of 2.9 GPa and a yield stress of 48 MPa, whereas their diamond equivalents had an apparent elastic modulus of 1.8 GPa and a yield stress of

41 MPa. The stress distributions in the structures close to their respective apparent yield strains (1.8 and 2.4%, respectively) were almost identical for both lattices, ~75% of the volume of material in the elastic state and ~25% in the superelastic state. However, at an equivalent apparent strain of 6%, ~20% of the gyroid structure underwent plastic deformation, as compared to only ~2% for its diamond equivalent because of the much higher compliance of the latter (Figure 4.13b,c).

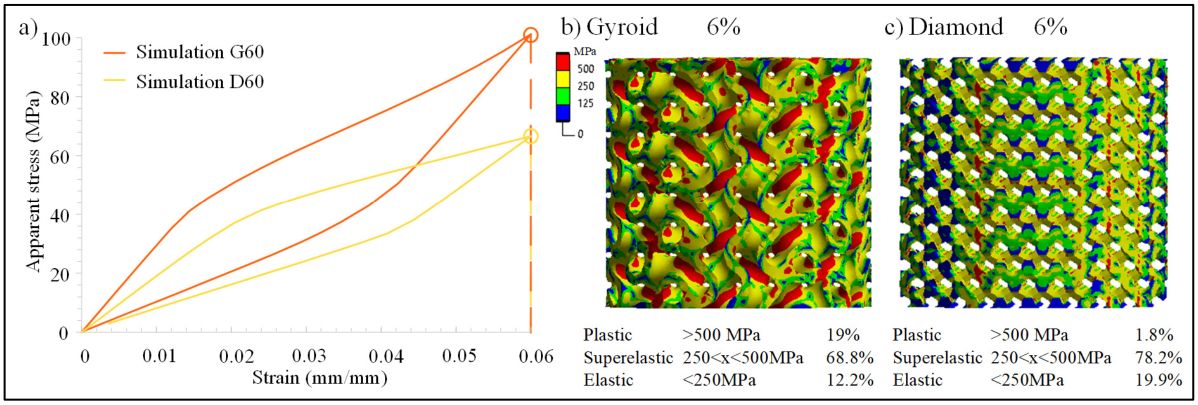

Figure 4.13 (a) Simulated stress-strain curves of the gyroid and diamond lattices, and stress distribution in the (b) gyroid and (c) diamond structures at a common apparent strain of 6% with the material volume fraction in the plastic, superelastic and elastic stress states

Figure 4.14a,b shows the stress-strain diagrams resulting from compression testing of the gyroid and diamond lattices in the as-built and heat-treated conditions. It was observed that, as predicted by the numerical simulations, the gyroids are stiffer than the diamonds both in the as-built (E = 3.5 vs 3.1 GPa) and heat-treated (E = 3.4 vs 2.9 GPa) conditions. Although yield stresses in both structures in the as-built (Sy= ~70 MPa) and heat-treated conditions (Sy = ~48 MPa) are similar, the ultimate stress and compression strain at failure are significantly greater for the gyroids. Similarly to the effect on the bulk material, heat treatment appeared to decrease the yield stress and reduce the compression strain at failure for both types of lattice structure, while increasing their ultimate stresses (Figure 4.14c). Going up to 5% applied strain, the recovered strain ε_r was the same for both tested structures (Figure 4.14d), while beyond that, the diamond lattices outperformed their gyroid counterparts. At ~11% applied strain, the heat-treated diamond lattices exhibited recoverable strains reaching 7.25%, about 1.25% more than their gyroid counterparts. These results are consistent with the numerical simulations, which showed that for the same level of apparent strain, the diamond lattices limit the degree of irreversible (plastic) deformation because of their higher compliance.

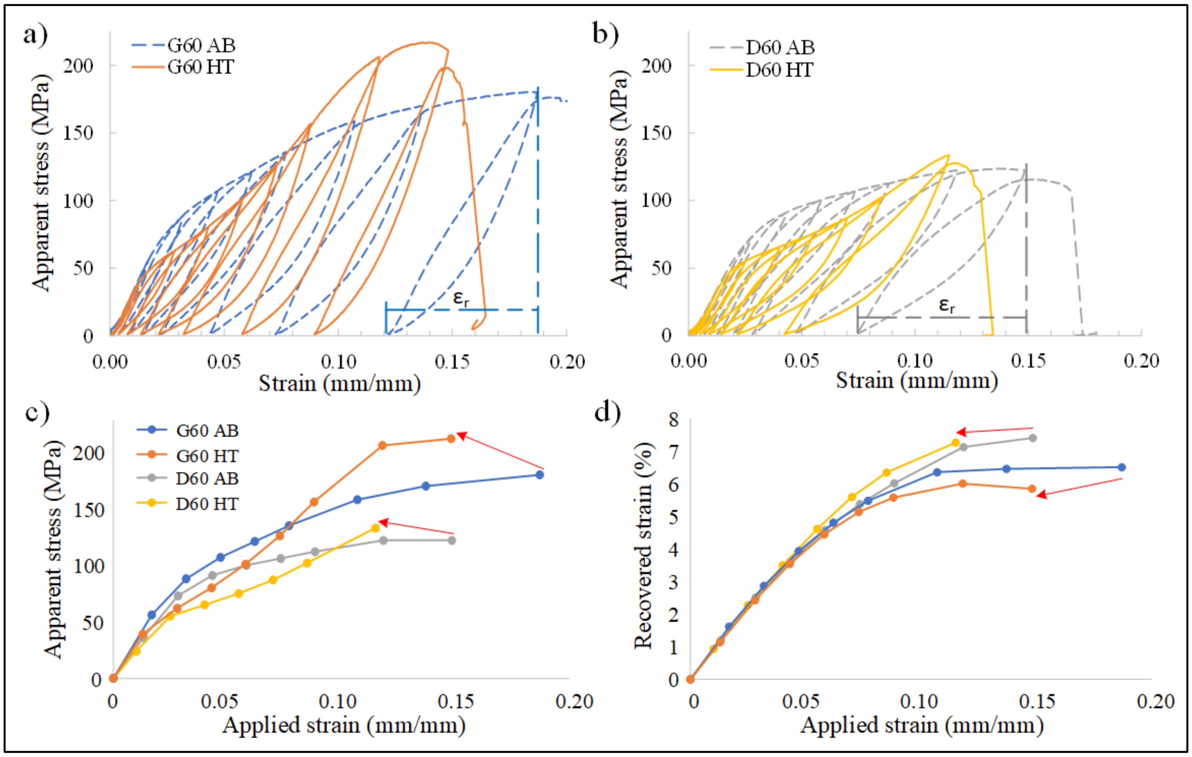

Figure 4.14 Compression behavior of the as-built and heat-treated 60% porous (a) gyroid and (b) diamond lattices. (c) Apparent stress and (d) recovered strain values are plotted against the applied strain of all the tested structures with arrows indicating the effect of the heat treatment on the structures' properties

The simulated and experimental stress-strain diagrams of the lattice structures are compared in Figure 4.15. The simulation of the loading behavior of the gyroid lattices reproduced the experimental behavior almost exactly, whereas in the case of diamonds, the simulation underestimated the experiment both in terms of stress and stiffness. These discrepancies might be attributed to two facts: the manufactured diamond lattices were 2.3% less porous (54.4%) than their gyroid equivalents (56.7%), with their strut junctions significantly blended by the manufacturing process (Figure 4.16). In addition, unlike the experiments, where the superelastic behavior of the material was only partial, the numerical model was built using an idealized superelastic material law.

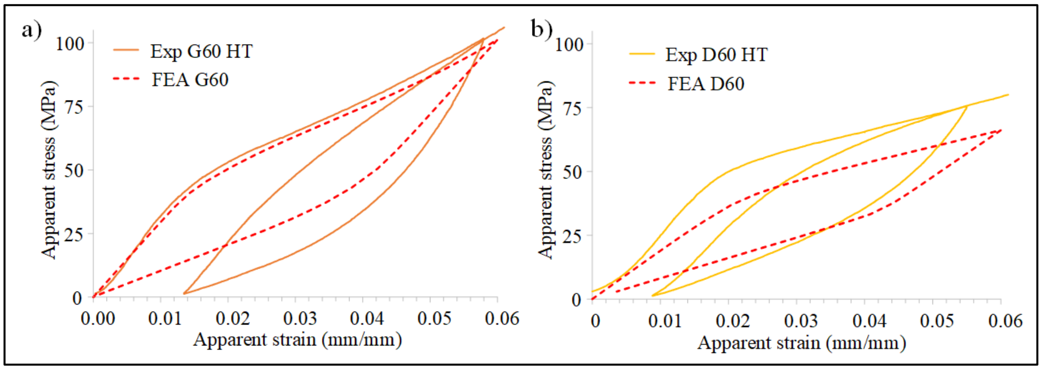

Figure 4.15 Comparison of experimental and simulated stress-strain behavior of 60% porous (a) gyroid and (b) diamond lattices

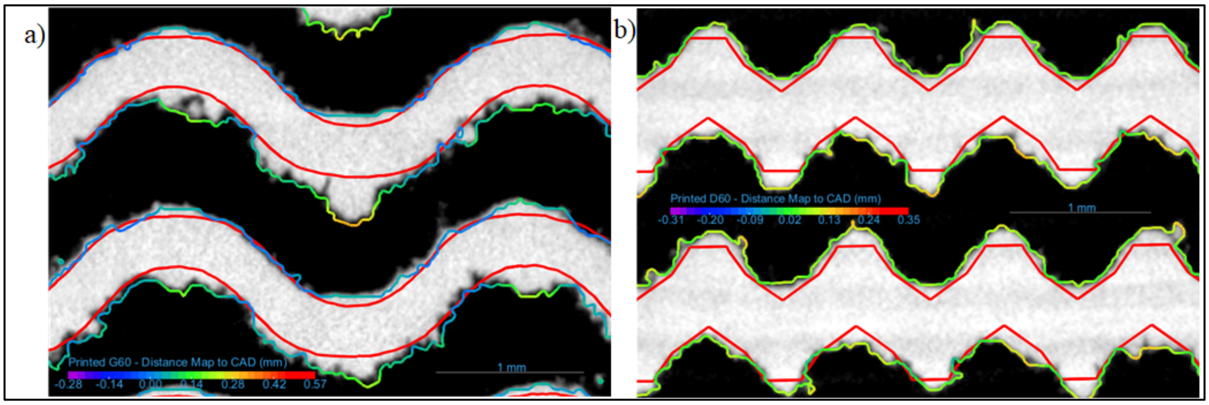
a)
Printed G60 - Distance Map to CAD (mm)
-0.28
-0.14
0.00
0.14
0.28
0.42
0.57
1 mm
b)
Printed D60 - Distance Map to CAD (mm)
-0.31
-0.20
-0.09
0.02
0.13
0.24
0.35
1 mm

Figure 4.16 Geometrical comparison between the designed and manufactured (a) gyroid and (b) diamond lattices. The red outline corresponds to the CAD and the colored outline corresponds to the printed surface, color-coded to the distance between the printed and CAD surfaces

4.7 Discussion

The bulk printed Ti-Ni specimens exhibited macroscopic cracking resulting from large residual stresses caused by significant thermal gradients during laser printing. The specimen size and the VED-BR conditions appeared to influence the size and frequency of cracking: 10 mm diameter cylinders had cracks up to 2 mm thick, whereas in the 5 mm diameter cylinders, the cracks were much finer and could not be detected with the naked eye. The lower the VED and the higher the BR values, the more intensive the cracking. Cracking of bulk specimens has also been reported in the literature (Mahmoudi et al., 2018; Xue et al., 2022; Zhao et al., 2020). Potential solutions to this problem include heating the printing substrate (Qiu et al., 2020; Q. Zhang et al., 2020), applying higher VED and lower BR (at the risk of evaporating too much nickel and altering the functional properties of the alloy) (Fu et al., 2020; Mahmoudi et al., 2018), using specifically-designed support structures to reduce the heat transfer to the build plate and therefore, the thermal gradients (McCue et al., 2019), or using HIP (Ren et al., 2023) and spark plasma sintering (Zhu et al., 2023) to heal the processing-induced microcracks. Lattice structures did not exhibit any cracks or delamination due, in part, to their architecture; being less stiff, the lattice structures accommodated the residual stresses better than their bulk counterparts.

The measured density of solid regions in all the specimens was ≥99.4% (CT) and ≥99.1% (pycnometry). Although each measurement method had its limitations (human-bias of the manual thresholding of the CT analyses and specimen size-dependence of the pycnometry measurements), a similar trend was found between the two. The density prediction model accurately forecasted the area of increased density at BR=3-10 cm^3/h and VED=70-100 J/mm^3 ranges (Figure 4.17a). Discrepancies outside this region might be due to the assumptions made on the material property inputs for the model. In particular, the specific heat capacity and thermal conductivity of Ti-Ni can vary by a factor of 0.5 and 2, respectively, depending on the phase state of the material, i.e., austenitic or martensitic (Davis & Committee, 1998).

At higher VED-lower BR printing conditions, Specimen 1 had numerous small pores distributed layer-wise, similar to the keyhole defects and gas pores caused by over-melting. At lower VED-higher BR conditions, Specimens 8-10 showed larger lack-of-fusion and spatter-related defects (Figure 4.17b). A VED of 70-90 J/mm^3 and BR of 3-10 cm^3/h appeared to yield the highest densities. Similar trends of increased porosity for VEDs under 60 J/mm^3 and over 163 J/mm^3 were observed in the literature by Biffi, Fiocchi, et al. (2020)

and Zamani, Kadkhodaei, Badrossamay, et Foroozmehr (2021). Conversely, Ge et al. (2023) were unable to successfully print specimens with VEDs higher than 75.8 J/mm^3, whereas Saghaian et al. (2021) successfully manufactured specimens with VEDs up to 666 J/mm^3, but failed for specimens with VED lower than 80 J/mm^3. This indicates that the manufacturability of Ti-Ni SMA is highly dependent on the LPBF system and the effective printing conditions, including the temperature of a build plate, the laser spot size and the scanning strategy.

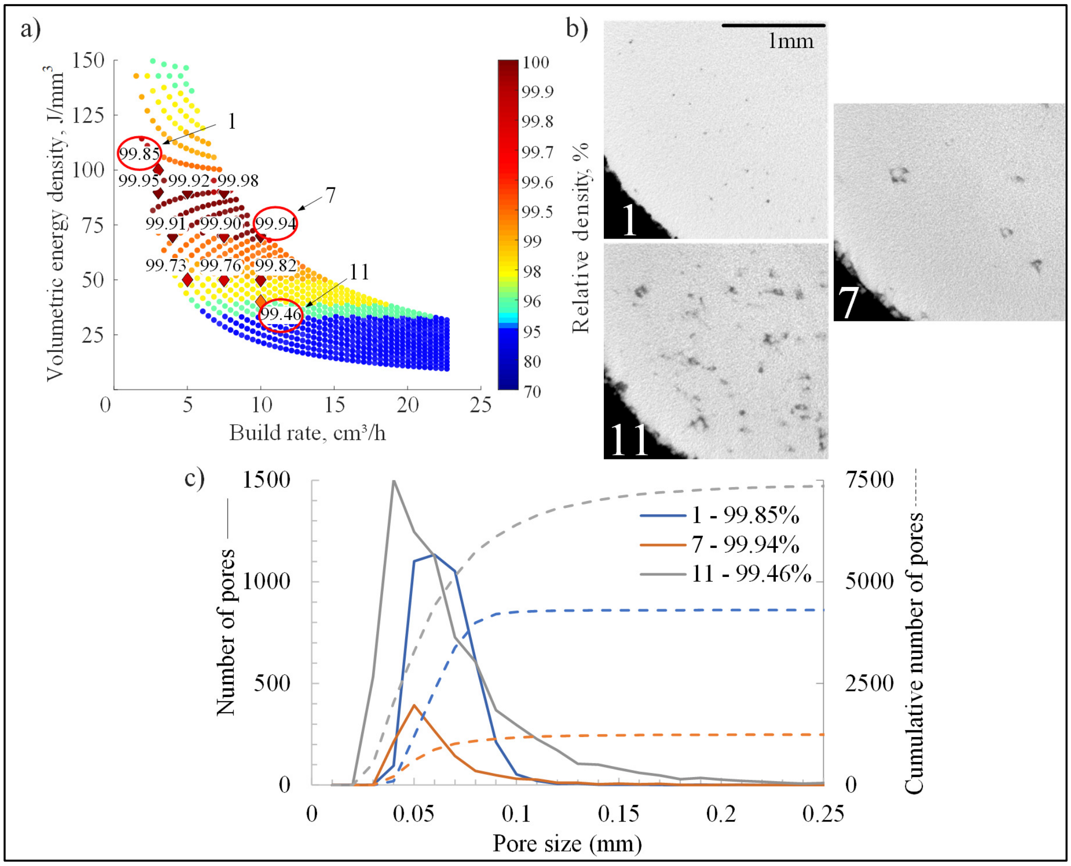

Figure 4.17 (a) Color-coded measured densities superimposed on the model predictions map, (b) typical pore shape for high and low VED specimens and (c) pore size distribution for Specimens 1, 7 and 11

In addition to the structural integrity of printed specimens at the macroscopic and microscopic levels, it is known that printing parameters can affect the chemical composition, which in turn changes the transformation temperatures and alters the functional properties of

Ti-Ni SMA at a given temperature. In agreement with the chemical analysis observations, at higher VEDs, the nickel content was lower than at low VEDs, which has also been reported in the literature (Bassani et al., 2023; Biffi, Fiocchi, et al., 2020; Borisov et al., 2021; Chmielewska et al., 2021; Leon et al., 2023; Mahmoudi et al., 2018). This can be explained by the physical properties of nickel and titanium, particularly the higher boiling point of titanium (3289°C) as compared to nickel (2914°C), and 3-times higher vapor pressure of the latter as compared to the former at the Ti-Ni alloy's melting temperature (Xue et al., 2022). Together, these effects result in an overall higher evaporation of nickel than that of titanium. Nickel-rich powders can be used to mitigate this problem, although it was noted that Ni-rich Ti-Ni feedstock has a higher propensity to in-process macro-cracking due to the formation of Ni-rich precipitates that strengthen the matrix but reduce the material ductility (Xue et al., 2022).

As a result of nickel evaporation, transformation temperatures of the printed parts are expected to increase in respect to those of the powder. As such, higher VEDs and lower BRs lead to increased phase transition temperatures (Bassani et al., 2023; H. Lu et al., 2019; Mahmoudi et al., 2018). In this study, although this trend was observed (Figure 4.9), some as-built specimens manifested lower Af temperatures than the powder (e.g., -5.5°C for Specimen 11 vs 23.7°C for powder). After the heat treatment, Af temperatures of all the specimens increased, but to different extents. For example, intermediate VED-BR Specimens 5-11 demonstrated an increase by 26-29°C, low VED-high BR Specimen 11 by 35°C, while high VED-low BR Specimens 1 and 2 saw almost no changes in their Af temperatures after the heat treatment.

It is well known that the phase transformation temperatures in Ti-Ni SMA are dependant not only on the chemical composition of the alloy (Figure 4.18a,b) but also on the stress state of the matter. Therefore, these variations in the phase transformation temperatures can be explained by high residual stresses generated during printing and by their relaxation during heat treatment. It can be stipulated that when the VED is high and BR low, the specimens contain less residual stresses because the excess energy partially acts as a stress relief throughout the printing process. Biffi, Fiocchi, et al. (2020) and Saedi et al. (2017) similarly observed an increase in the transformation temperatures after heat treatments, which was attributed to the relaxation of residual stresses and to the formation of nickel-rich precipitates Ni_4Ti_3 that depleted nickel from the matrix.

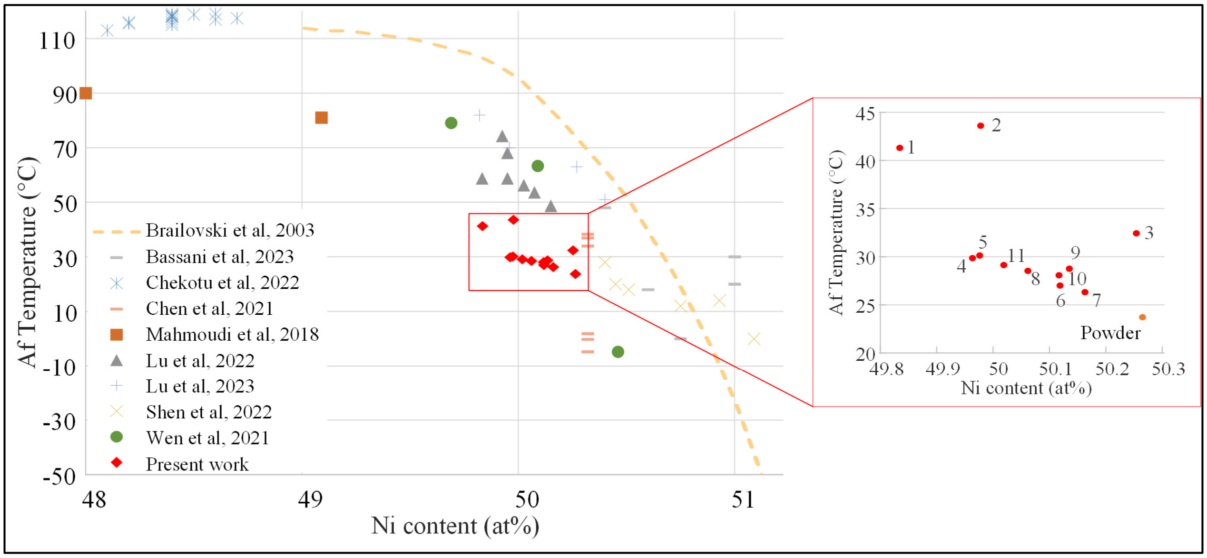

Figure 4.18 Af temperature in relation to the nickel content as presented in the literature and detailed view of the powder and the heat-treated specimens from the present work
Tiré et adapté de Bassani et al. (2023), Brailovski et al. (2003), Chekotu, Goodall, Kinahan, et Brabazon (2022), W. Chen et al. (2021), H. Lu et al. (2022), H. Lu et al. (2023), Mahmoudi et al. (2018), Shen, Li, Guo, Guo, et Fang (2022) et Wen et al. (2021)

The XRD analyses showed that by varying VED delivered to the powder bed, the phase content and crystallographic texture can be modified. Indeed, low VED-high BR specimens were more austenitic and had a signature closer to that of the powder. High VED-low BR specimens displayed more intense martensitic peaks and a preferential (200) austenitic orientation. The same effect was noted in the literature, with higher VED parts exhibiting a preferential (100) crystallographic orientation corresponding to the building direction (Bassani et al., 2023; Biffi, Fiocchi, et al., 2020; Moghaddam et al., 2019; Saedi, Shayesteh Moghaddam, Amerinatanzi, Elahinia, & Karaca, 2018; Xue et al., 2022). It was found that such a texture improves superelasticity in compression, effectively allowing to tailor the mechanical behavior of printed material by adjusting the printing parameters (S. Dadbakhsh, Vrancken, Kruth, Luyten, & Van Humbeeck, 2016; Moghaddam et al., 2019; Saedi et al., 2017). Moreover, the superelastic behavior can also be improved by increasing the heat treatment temperatures and times: Saedi et al. (2017) showed that a 600 °C aging for 1.5h significantly increased the stress recovery of printed Ti-Ni alloy samples.

The results of mechanical testing of the bulk specimens in the as-built state (ultimate tensile stress of 250 MPa and failure strain of 1%) and after the heat-treatment (550 MPa and 5.5%, respectively) are comparable to those reported in the literature (Ge et al., 2023; H. Lu et al., 2022; Ren et al., 2023; Xue et al., 2022). The heat treatment resulted in a partial superelastic behavior of the material, bringing forth the classic “flag”-like aspect of the stress-strain curve reported by Biffi, Fiocchi, et al. (2020) and Elahinia et al. (2016), with an onset martensite transformation stress of ~250 MPa, which is also in the literature range (S. Dadbakhsh et al., 2016; Elahinia et al., 2016; Fu et al., 2020; Shen et al., 2022; Wen et al., 2021).

Numerical simulations of the lattices predicted that the diamond structures are more suited to take advantage of the functional properties of Ti-Ni SMA, and that was confirmed by experimental testing. At the same apparent strain, highly compliant diamond structures had a lower volume fraction of plastically deformed material as compared to their gyroid equivalents. Although a fully superelastic behavior was not observed experimentally, partly due to the difficulty of controlling the material composition during printing, the recoverable strains were increased from ~2% for the bulk to 6-7% for the lattices, and the stiffness was reduced from ~19 GPa for the bulk to 3-4 GPa for the lattices. Similar difficulties in achieving perfect superelasticity in lattices were encountered by H. Lu et al. (2021), Bartolomeu et al. (2020) and Biffi, Bassani, et al. (2020).

Nonetheless, the benefits of using SMAs in the manufacturing of lattice structures can be observed when comparing the experimental behavior of Ti-Ni lattices studied in this work to the behavior of analogous Ti64 structures from a previously published work (Timercan et al., 2023) (Figure 4.19). Indeed, although the Ti-Ni lattices are ~2 times less strong than their Ti64 equivalents, they exhibit ~3-4 times larger recoverable strains, thus offering an extra margin of safety, if loaded above the onset of phase transformation ($\geq\sigma_{AMS}$). When comparing the strength-to-stiffness ratios (Sy/E or σ_{AMS}/E) of the Ti-Ni lattices of this study with those of their Ti-6Al-4V equivalents (Timercan et al., 2023), both with 60% porosity, the former outperform the latter, being closer to the range of properties of trabecular bones (Timercan et al., 2021). Of note, since for the same porosity, the stiffness of Ti-Ni structures is significantly lower than that of their Ti64 equivalents, the stiffness of Ti-Ni lattices can be adjusted to match that of Ti64 lattices by using larger struts/walls with lesser sensitivity to the presence of manufacturing defects (in fact, 60% porous diamond Ti-Ni lattice has the same stiffness as the 80% porous diamond Ti64 lattice).

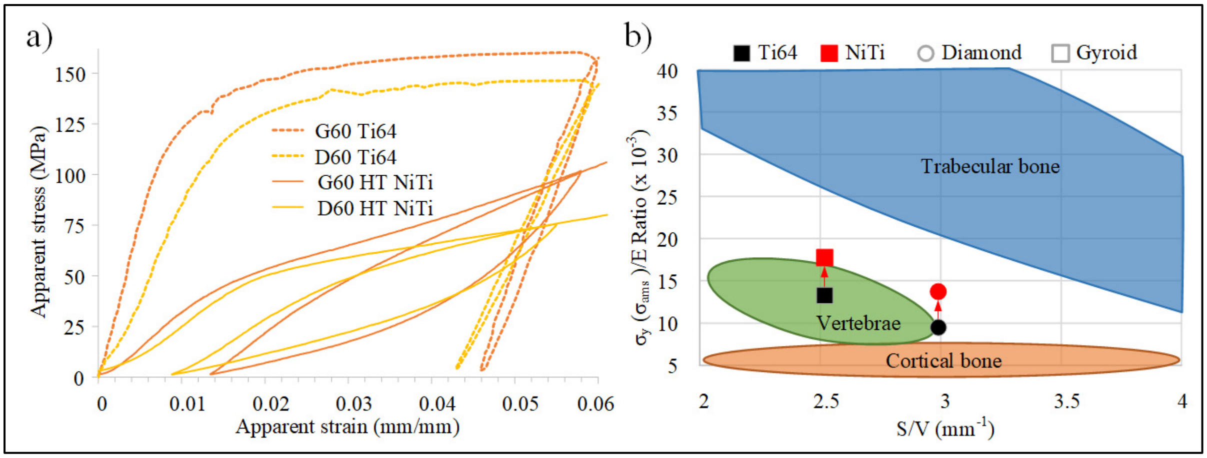

Figure 4.19 Comparison of the (a) experimental stress-strain diagrams of 60% porous Ti64 and Ti-Ni gyroid and diamond lattices and (b) Sy/E ratios of the studied lattices structures and data adapted from a previous study
Tiré et adapté de Timercan et al. (2023)

4.8 Conclusions

Laser powder bed fusion of Ti-50.26 at%Ni powders was carried out with the goal of finding an optimal printing regime to manufacture superelastic lattice structures. Different printing parameters were selected with the use of a numerical algorithm that predicts density of the printed material. The manufactured specimens were characterized in terms of structural integrity, density, chemical composition, phase transformation temperatures and crystalline phases. A parameter set offering the best compromise between printed density (99.94%) and transformation temperatures (Af 26.3°C), while also achieving a relatively high build rate (10 cm^3/h), was selected for mechanical testing and lattice manufacturing. Simultaneously, a numerical FEA model was built to simulate the mechanical behavior of superelastic lattice structures. Using the FEA model, partially validated in the framework of this study, Ti-Ni SMA superelastic lattice structures could be optimized further to better exploit their superelastic potential for particular applications.

The following conclusions can be drawn:

- While the proposed melt pool-based model can be used to select printing parameters yielding high-density specimens, the predicted densities were significantly lower than their measured equivalents. Better predictions can be achieved by considering the temperature-dependent behavior of Ti-Ni powders.
- Higher VEDs and slower BRs resulted in increased Ni evaporation, increased transformation temperatures and increased fraction of martensitic phase. The nickel content, and therefore the transformation temperatures of printed specimens can be tailored by adjusting both the powder composition and the printing parameters.
- As-built parts exhibited large residual stresses which resulted in cracking and affected the mechanical behavior of printed material. Heat treatment was necessary to relieve these stresses and improve superelasticity. A partial superelastic behavior of the printed material at room temperature with a recoverable strain of up to ~2% was achieved using a VED=90 J/mm^3 and BR=10 cm^3/h parameter set and a stress-relief heat treatment at 500°C for 30 min.
- Numerical simulation of the 60% porous Ti-Ni lattice structures offered useful insights into the material stress/strain state during loading. These simulations accurately predicted the apparent yield stress of the gyroid lattices, but underestimated their apparent stiffness by 18%. As far as the diamond lattices are concerned, the model underestimated their apparent yield stress by 25% and stiffness, by 60%.
- At the same apparent strain of 6%, recovery strains of the highly compliant diamond lattices were significantly greater than those of their gyroid equivalents (7.25 vs 6%).

This effect is caused by a significantly lower volume fraction of the material undergoing plastic deformation in the diamond lattices (2%) as compared to their gyroid equivalents (20%).

4.9 Acknowledgments

The authors would like to thank R. Romanica, S-E. Brika, A. Ayatollahi Tafti, M. Saadati, and S. Plamondon for their technical support with AM system preparation, CT-scanning, specimen preparation, SEM and mechanical testing, respectively.

4.10 CRediT author contribution

Anatolie Timercan: Conceptualization, Methodology, Investigation, Visualization, Writing-Original draft preparation. **Donatien Campion**: Conceptualization, Methodology, Data curation. **Patrick Terriault**: Software, Writing-Reviewing and Editing. **Vladimir Brailovski**: Conceptualization, Supervision, Funding acquisition, Visualization, Writing-Reviewing and Editing.

4.11 Funding

This work was funded by the Fonds de Recherche du Québec - Nature et Technologies [272262]; the Natural Sciences and Engineering Research Council of Canada [V. Brailovski's Discovery grant]; and the Fonds de Développement de l'École de technologie supérieure [A. Timercan's scholarship].

4.12 Data availability

The raw and processed data required to reproduce these findings cannot be shared at this time as the data also forms part of an ongoing study.

4.13 Annex A

Tableau 4.4 Density measurements using CT imaging and pycnometry

Specimen	Predicted density (%)	CT scan (%)*	Pycnometry (%)*
1	99.86	99.85 ± 0.2	99.78 ± 0.06
2	100.00	99.95 ± 0.2	99.89 ± 0.09
3	99.94	99.92 ± 0.2	99.85 ± 0.08
4	99.85	99.98 ± 0.2	99.92 ± 0.11
5	99.66	99.91 ± 0.2	99.74 ± 0.05
6	99.86	99.90 ± 0.2	99.82 ± 0.04
7	99.87	99.94 ± 0.2	99.95 ± 0.10
8	97.73	99.73 ± 0.2	99.38 ± 0.06
9	98.04	99.76 ± 0.2	99.24 ± 0.07
10	98.07	99.82 ± 0.2	99.22 ± 0.09
11	96.10	99.46 ± 0.2	99.13 ± 0.07

*standard deviation values are not always symmetrical, since the density has an upper limit of 100%

Tableau 4.5 Phase transition temperatures (°C) of the as-received powder (AR) and printed specimens (as-built and heat-treated)

		Mf	Ms	As	Af	Mf	Ms	Rf	Rs	As	Af
	AR powder	-57.6	3.7	-33.9	23.7	-57.6	3.7			-33.9	23.7
		As-built				Heat treated					
Specimen	1	-19.7	22.0	1.4	43.0	-27.1	-3.0	11.5	23.0	19.9	41.3
	2	-23.6	25.7	-1.3	45.4	-29.7	-3.3	10.0	24.9	19.3	43.6
	3	-77.9	8.7	-45.7	21.9	-32.0	-11.6	12.7	29.8	22.0	32.4
	4	-60.0	12.9	-42.3	31.2	-42.4	-15.6	10.6	22.2	15.9	29.8
	5	-50.1	9.3	-33.4	26.4	-40.0	-14.9	11.5	24.1	16.9	30.1
	6	-80.9	1.6	-50.2	9.9	-51.1	-25.5	11.6	26.4	13.2	27.0
	7	-80.1	-3.9	-50.8	-1.0	-51.6	-30.0	10.5	26.3	12.8	26.3
	8	-73.7	-5.5	-44.4	7.7	-44.5	-22.0	12.7	27.6	16.0	28.5
	9	-81.0	-14.6	-51.7	-4.5	-53.6	-30.5	13.1	30.0	12.6	28.8
	10	-80.6	-13.9	-51.0	-4.0	-55.4	-32.3	13.3	29.1	12.0	28.1
	11	-81.2	-17.1	-50.7	-5.5	-52.4	-29.7	14.3	30.1	13.1	29.1

CONCLUSION GÉNÉRALE

La fabrication additive a ouvert la porte à de nombreuses nouvelles applications et à l’utilisation de matériaux qui étaient trop couteux à mettre en forme par les moyens traditionnels. Dans cet ordre d’idée, ce projet de recherche avait pour but la fabrication de structures architecturées en alliages à mémoire de forme pour application dans les cages intervertébrales. La combinaison des avantages offerts par structures architecturées comme la porosité interconnectée et la réduction de la rigidité en conservant un rapport S_y/E adéquat, et des propriétés fonctionnelles offerts par le Ti-Ni, permettrait d’envisager une amélioration des performances des cages en termes d’intégration osseuse et de transfert de charges. Afin de développer la méthodologie de travail et d’établir un cas de référence comparatif, les premiers travaux ont été réalisés sur un alliage classique de Ti-6Al-4V.

En un premier lieu, une étude a été menée pour définir les requis fonctionnels des cages intervertébrales et deux structures architecturées ont été sélectionnées avec divers niveaux de porosité. Les résultats ont indiqué que les propriétés géométriques, mécaniques et de perméabilité fluidique des structures en diamant et des gyroides imprimés étaient dans la plage des valeurs des spécifications identifiées. Les deux structures avaient un comportement similaire, la seule grande différence étant leur mode de défaillance qui était plus abrupte pour les diamants que pour le gyroides. La rigidité des deux structures (1.9-4.8 GPa) était bien inférieure à celle du matériau dense utilisé pour leur fabrication (environ 100 GPa), tandis que leur résistance mécanique (52-160 MPa) était supérieure à celle des vertèbres (3-6 MPa), réduisant ainsi les risques de défaillance de l’os et de l'implant.

Dans un deuxième temps, les propriétés mécaniques de ces structures sous différents modes de chargement, à savoir la compression, la tension et la torsion, ont été étudiées numériquement et expérimentalement. Malgré une surestimation des simulations numériques d’environ 25% des résultats expérimentaux, il fut possible de conclure que les propriétés en tension et en compression des structures cellulaires étaient quasi-identiques. Toutefois, en analysant les propriétés en torsion, il fut remarqué que celles-ci ne respectent pas les théories conventionnelles de résistance des matériaux. En effet, le ratio S_{sy}/S_y était de 0.94 pour les diamants et de 0.87 pour les gyroides comparé à 0.577 pour les matériaux denses isotropes. Ceci impliquait que lors de la simulation de structures architecturées par la méthode d'homogénéisation, des modèles de matériau spécifiques devraient être utilisés pour fidèlement reproduire leur comportement. Malgré cela, toutes les structures étudiées ont démontré des propriétés mécaniques adéquates pour utilisation dans les cages intervertébrales pour les trois types de chargement.

En troisième lieu, la fabrication additive d'un AMF de Ti-50.26 at%Ni a été réalisée, permettant la production de structures architecturées partiellement superélastiques à température ambiante. Pour y arriver, divers ensembles de paramètres d'impression ont été utilisés pour fabriquer des spécimens denses qui par la suite ont été analysés en termes d'intégrité, densité, composition chimique, températures de transformation de phases et microstructure. Malgré des difficultés de contrôle de la composition chimique du matériau imprimé, un ensemble de paramètres offrant un meilleur compromis entre la densité (99.94%) et la température de transformation austénitique (Af 26.3°C) fut utilisé pour la fabrication des structures architecturées ayant une porosité de 60%. Ces structures avaient des rigidités de 3-4 GPa et contraintes de début de transformation martensitique de 48 MPa ainsi que des déformations réversibles de l'ordre de 6-7%. Les résultats pointent à une meilleure utilisation des propriétés fonctionnelles des AMF par les structures en diamant comparé aux structures gyroides. Les structures poreuses en Ti-Ni avec une porosité de 60% offrent la même souplesse et résistance que les structures poreuses en Ti64 avec une porosité de 80%, mais un retour élastique 3-4 fois plus élevé. Comme leur porosité est moins élevée, les structures en Ti-Ni présentent un risque d'apparition des défauts de fabrication plus faible, et donc, potentiellement, une plus grande résistance en fatigue. Le modèle numérique développé et partiellement validé dans le cadre de cette étude pourrait servir à optimiser les structures architecturées pour tirer meilleur profit des propriétés fonctionnelles des AMF.

Les contributions principales de cette thèse peuvent être résumées comme suit :

- Comparaison des structures architecturées en diamant à base de membrures et gyroide surfacique, imitant les différentes structures osseuses présentes dans le corps humain, fabriquées en un alliage classique de Ti-6Al-4V, et ce, pour différents modes de chargement.
- Développement et validation partielle de modèles numériques permettant la simulation du comportement des structures architecturées avec un potentiel d'exploration de diverses configurations de formes de structures cellulaires et de propriétés de matériau.
- Développement des paramètres de fabrication du Ti-Ni et caractérisation des spécimens imprimés en termes de propriétés géométriques, mécaniques, microstructurales et fonctionnelles.
- Comparaison des structures architecturées fabriquées en alliage superélastique de TiNi avec l'alliage traditionnel de Ti-6Al-4V, pour une application spécifique qui est pour les cages intervertébrales.

RECOMMANDATIONS

En prenant du recul, plusieurs pistes d’exploration sont identifiées n’ayant pas été adressées dans le cadre de ces travaux.

Fabrication et caractérisation de cages intervertébrales en Ti-6Al-4V et Ti-Ni

La comparaison des performances d’une cage pleine et poreuse en alliage de titane conventionnel, ainsi qu’une cage poreuse en AMF doit être effectuée. Les tests doivent suivre les normes ASTM F2077 et F2267, développées pour la comparaison des cages intervertébrales. Ceci permettrait de quantifier l’amélioration des performances des cages poreuses et en AMF par rapport aux cages traditionnelles.

Analyse des propriétés en fatigue des structures architecturées pour les différents modes de chargement

Malgré le nombre de publications traitant de la vie en fatigue des structures cellulaires, la panoplie de types de structures et la variation d’un très grand nombre de paramètres, comme l’équipement utilisé, le régime d’impression, la taille et le niveau de porosité des structures, les post-traitements, etc., rendent difficile la prédiction des propriétés en fatigue de ces meta-matériaux. Étant donné un manque de théorie adéquate pour prédire la vie en fatigue des structures architecturées, une plus grande base de données empiriques est nécessaire pour bâtir des modèles prédictifs.

Post-traitement et finition des structures architecturées

Une des problématiques de la FA est un mauvais fini de surface des composants, en partie dû à la nature incrémentale de fabrication (effet escalier engendré par l’empilement des couches) et d’autre part en raison des particules de poudre attachées en surface par frittage. Cette problématique affecte davantage les structures architecturées en raison de leurs surfaces spécifiques importantes. La concordance géométrique et le niveau de porosité en sont aussi affectés. De plus, pour les applications biomédicales, le risque de détachement des particules frittées en surface est particulièrement problématique pour des raisons de toxicité dans le corps. Il est alors nécessaire de développer des méthodes de finition surfacique permettant de se délaisser de ces problématiques. L'électro-polissage et le polissage chimique sont deux solutions potentielles méritant d'être explorées.

Améliorer la fabrication additive du Ti-Ni

Puisque le matériau dense n'a pas pu être fabriqué sans fissuration, il est nécessaire de mettre des efforts pour optimiser sa fabrication. Pour cela, il est envisageable d'utiliser un plateau de fabrication chauffant permettant de réduire les contraintes résiduelles dans le matériau. Ceci n'est pas possible sur l'imprimante Trumpf utilisée dans cette étude, mais faisable sur l'imprimante EOS M280. Toutefois, cela impliquerait l'ajustement des paramètres d'impression pour cette imprimante.

Optimiser le traitement thermique pour le Ti-Ni produit par FA

Étant donné que la superélasticité observée du Ti-Ni imprimé n'était que partielle, il est possible que les propriétés fonctionnelles de ce matériau pourraient être améliorées en effectuant certains traitements thermiques. En effet, certaines études explorent divers traitements thermiques de vieillissement pour réduire avec succès les températures de transformation du Ti-Ni .

Optimiser la cellule unitaire pour mieux tirer avantage des propriétés fonctionnelles

En utilisant le modèle numérique, l'optimisation topologique d'une cellule unitaire serait possible permettant une meilleure distribution des contraintes dans le matériau et un meilleur changement de phase pour mieux exploiter la superélasticité.

LISTE DE RÉFÉRENCES BIBLIOGRAPHIQUES

Abbushi, A., Čabraja, M., Thomale, U.-W., Woiciechowsky, C., & Kroppenstedt, S. N. (2009). The influence of cage positioning and cage type on cage migration and fusion rates in patients with monosegmental posterior lumbar interbody fusion and posterior fixation. *European Spine Journal, 18*(11), 1621.

Abou-Ali, A. M., Al-Ketan, O., Lee, D.-W., Rowshan, R., & Al-Rub, R. K. A. (2020). Mechanical behavior of polymeric selective laser sintered ligament and sheet based lattices of triply periodic minimal surface architectures. *Materials & Design, 196*, 109100.

Aharinejad, S., Bertagnoli, R., Wicke, K., Firbas, W., & Schneider, B. (1990). Morphometric analysis of vertebrae and intervertebral discs as a basis of disc replacement. *American journal of anatomy, 189*(1), 69-76.

Aihara, H., Zider, J., Fanton, G., & Duerig, T. (2019). Combustion Synthesis Porous Nitinol for Biomedical Applications. *International Journal of Biomaterials, 2019*.

Al-Ketan, O., Lee, D.-W., Rowshan, R., & Al-Rub, R. K. A. (2020). Functionally graded and multi-morphology sheet TPMS lattices: Design, manufacturing, and mechanical properties. *J Mech Behav Biomed Mater, 102*, 103520.

Al-Ketan, O., Rowshan, R., & Abu Al-Rub, R. K. (2018). Topology-mechanical property relationship of 3D printed strut, skeletal, and sheet based periodic metallic cellular materials. *Additive Manufacturing, 19*, 167-183. doi: 10.1016/j.addma.2017.12.006

Ali, D., & Sen, S. (2017). Finite element analysis of mechanical behavior, permeability and fluid induced wall shear stress of high porosity scaffolds with gyroid and lattice-based architectures. *J Mech Behav Biomed Mater, 75*, 262-270.

Almeida, H. A., & Bártolo, P. J. (2013). Topological optimisation of scaffolds for tissue engineering. *Procedia Engineering, 59*, 298-306.

Ashby, M. (2005). The properties of foams and lattices. *Philosophical Transactions of the Royal Society A: Mathematical, Physical and Engineering Sciences, 364*(1838), 15-30.

Assad, M., Chernyshov, A., Jarzem, P., Leroux, M., Coillard, C., Charette, S., & Rivard, C. (2003b). Porous titanium-nickel for intervertebral fusion in a sheep model: Part 2. Surface analysis and nickel release assessment. *Journal of Biomedical Materials Research Part B: Applied Biomaterials: An Official Journal of The Society for Biomaterials, The Japanese Society for Biomaterials, and The Australian Society for Biomaterials and the Korean Society for Biomaterials, 64*(2), 121-129.

Assad, M., Jarzem, P., Leroux, M. A., Coillard, C., Chernyshov, A. V., Charette, S., & Rivard, C. H. (2003a). Porous titanium-nickel for intervertebral fusion in a sheep model: Part 1. Histomorphometric and radiological analysis1. *Journal of Biomedical Materials Research Part B: Applied Biomaterials: An Official Journal of The Society for Biomaterials, The Japanese Society for Biomaterials, and The Australian Society for Biomaterials and the Korean Society for Biomaterials, 64*(2), 107-120.

ASTM. (2017a). *B963-17 Standard Test Methods for Oil Content, Oil-Impregnation Efficiency, and Surface-Connected Porosity of Sintered Powder Metallurgy (PM) Products Using Archimedes' Principle*.

ASTM. (2017b). *F2004-17 Standard Test Method for Transformation Temperature of Nickel-Titanium Alloys by Thermal Analysis*.

ASTM. (2018). *F2450-18 Standard Guide for Assessing Microstructure of Polymeric Scaffolds for Use in Tissue-Engineered Medical Products*.

ASTM. (2021). E143-20 Standard Test Method for Shear Modulus at Room Temperature.

Barber, H., Kelly, C. N., Nelson, K., & Gall, K. (2021). Compressive anisotropy of sheet and strut based porous Ti–6Al–4V scaffolds. *J Mech Behav Biomed Mater, 115*, 104243.

Baroud, G., Falk, R., Crookshank, M., Sponagel, S., & Steffen, T. (2004). Experimental and theoretical investigation of directional permeability of human vertebral cancellous bone for cement infiltration. *Journal of biomechanics, 37*(2), 189-196.

Bartolomeu, F., Costa, M., Alves, N., Miranda, G., & Silva, F. (2020). Engineering the elastic modulus of NiTi cellular structures fabricated by selective laser melting. *J Mech Behav Biomed Mater*, 103891.

Bassani, P., Fiocchi, J., Tuissi, A., & Biffi, C. A. (2023). Investigation of the Effect of Laser Fluence on Microstructure and Martensitic Transformation for Realizing Functionally Graded NiTi Shape Memory Alloy via Laser Powder Bed Fusion. *Applied Sciences, 13*(2), 882.

Belytschko, T., Kulak, R., Schultz, A., & Galante, J. (1974). Finite element stress analysis of an intervertebral disc. *Journal of biomechanics, 7*(3), 277-285.

Biffi, C. A., Bassani, P., Fiocchi, J., & Tuissi, A. (2020). Microstructural and mechanical response of NiTi lattice 3D structure produced by selective laser melting. *Metals, 10*(6), 814.

Biffi, C. A., Fiocchi, J., Valenza, F., Bassani, P., & Tuissi, A. (2020). Selective Laser Melting of NiTi Shape Memory Alloy: Processability, Microstructure, and Superelasticity. *Shape Memory and Superelasticity*, 1-12.

Bobbert, F., Lietaert, K., Eftekhari, A. A., Pouran, B., Ahmadi, S., Weinans, H., & Zadpoor, A. (2017). Additively manufactured metallic porous biomaterials based on minimal surfaces: A unique combination of topological, mechanical, and mass transport properties. *Acta Biomaterialia, 53*, 572-584.

Borisov, E., Starikov, K., Popovich, A., & Tihonovskaya, T. (2021). Investigation of the possibility of tailoring the chemical com-position of the NiTi alloy by selective laser melting. *Metals, 11*(9), 1470.

Bormann, T., de Wild, M., Beckmann, F., & Müller, B. (2013). *Assessing the morphology of selective laser melted NiTi-scaffolds for a three-dimensional quantification of the one-way shape memory effect* présentée à Behavior and Mechanics of Multifunctional Materials and Composites 2013. doi: 10.1117/12.2012245

Brailovski, V., Prokoshkin, S., Terriault, P., & Trochu, F. (2003). *Shape memory alloys: fundamentals, modeling and applications*. École de technologie supérieure.

Brika, S. E., Letenneur, M., Dion, C. A., & Brailovski, V. (2020). Influence of particle morphology and size distribution on the powder flowability and laser powder bed fusion manufacturability of Ti-6Al-4V alloy. *Additive Manufacturing, 31*, 100929.

Buehler, W. J., Gilfrich, J., & Wiley, R. (1963). Effect of low-temperature phase changes on the mechanical properties of alloys near composition TiNi. *Journal of applied physics, 34*(5), 1475-1477.

Caiazzo, F., Alfieri, V., & Bujazha, B. D. (2021). Additive manufacturing of biomorphic scaffolds for bone tissue engineering. *The International Journal of Advanced Manufacturing Technology*, 1-15.

Castro, A., Pires, T., Santos, J., Gouveia, B., & Fernandes, P. (2019). Permeability versus Design in TPMS Scaffolds. *Materials, 12*(8), 1313.

Challis, V. J., Roberts, A. P., Grotowski, J. F., Zhang, L. C., & Sercombe, T. B. (2010). Prototypes for bone implant scaffolds designed via topology optimization and manufactured by solid freeform fabrication. *Advanced Engineering Materials, 12*(11), 1106-1110.

Chang, L., & Read, T. (1951). Plastic deformation and diffusionless phase changes in metals—the gold-cadmium beta phase. *JOM, 3*(1), 47-52.

Chekotu, J. C., Goodall, R., Kinahan, D., & Brabazon, D. (2022). Control of Ni-Ti phase structure, solid-state transformation temperatures and enthalpies via control of L-PBF process parameters. *Materials & Design, 218*, 110715.

Chekotu, J. C., Groarke, R., O'Toole, K., & Brabazon, D. (2019). Advances in Selective Laser Melting of Nitinol Shape Memory Alloy Part Production. *Materials, 12*(5), 809.

Chen, L.-Y., Liang, S.-X., Liu, Y., & Zhang, L.-C. (2021). Additive manufacturing of metallic lattice structures: Unconstrained design, accurate fabrication, fascinated performances, and challenges. *Materials Science and Engineering: R: Reports, 146*, 100648.

Chen, W., Yang, Q., Huang, S., Huang, S., Kruzic, J. J., & Li, X. (2021). Laser power modulated microstructure evolution, phase transformation and mechanical properties in NiTi fabricated by laser powder bed fusion. *Journal of Alloys and Compounds, 861*, 157959.

Chen, Y., Wang, X., Lu, X., Yang, L., Yang, H., Yuan, W., & Chen, D. (2013). Comparison of titanium and polyetheretherketone (PEEK) cages in the surgical treatment of multilevel cervical spondylotic myelopathy: a prospective, randomized, control study with over 7-year follow-up. *European Spine Journal, 22*(7), 1539-1546.

Chmielewska, A., Wysocki, B., Buhagiar, J., Michalski, B., Adamczyk-Cieślak, B., Gloc, M., & Święszkowski, W. (2021). In situ alloying of NiTi: Influence of Laser Powder Bed Fusion (LBPF) scanning strategy on chemical composition. *Materials Today Communications*, 103007.

Chung, S. S., Lee, K. J., Kwon, Y. B., & Kang, K. C. (2017). Characteristics and efficacy of a new 3-dimensional printed mesh structure titanium alloy spacer for posterior lumbar interbody fusion. *Orthopedics, 40*(5), e880-e885.

Cioranescu, D., & Paulin, J. S. J. (1979). Homogenization in open sets with holes. *Journal of mathematical analysis and applications, 71*(2), 590-607.

Coelho, P. G., Hollister, S. J., Flanagan, C. L., & Fernandes, P. R. (2015). Bioresorbable scaffolds for bone tissue engineering: optimal design, fabrication, mechanical testing and scale-size effects analysis. *Medical engineering & physics, 37*(3), 287-296.

Dadbakhsh, S., Speirs, M., Kruth, J.-P., & Van Humbeeck, J. (2015). Influence of SLM on shape memory and compression behaviour of NiTi scaffolds. *CIRP Annals, 64*(1), 209-212. doi: 10.1016/j.cirp.2015.04.039

Dadbakhsh, S., Vrancken, B., Kruth, J. P., Luyten, J., & Van Humbeeck, J. (2016). Texture and anisotropy in selective laser melting of NiTi alloy. *Materials Science and Engineering: A, 650*, 225-232. doi: 10.1016/j.msea.2015.10.032

Davis, J. R. (2003). *Handbook of Materials for Medical Devices*. ASM International. Repéré à https://books.google.ca/books?id=JEJRAAAAMAAJ

Davis, J. R., & Committee, A. I. H. (1998). *Metals Handbook Desk Edition 2nd Edition*. Taylor & Francis. Repéré à https://books.google.ca/books?id=IpEnvBtSfPQC

Deshpande, V., Ashby, M., & Fleck, N. (2001). Foam topology: bending versus stretching dominated architectures. *Acta Materialia, 49*(6), 1035-1040.

Dong, G., Tang, Y., & Zhao, Y. F. (2017). A survey of modeling of lattice structures fabricated by additive manufacturing. *Journal of Mechanical Design, 139*(10), 100906.

Downing, D., Jones, A., Brandt, M., & Leary, M. (2021). Increased efficiency gyroid structures by tailored material distribution. *Materials & Design, 197*, 109096.

Du Plessis, A., Yadroitsava, I., Yadroitsev, I., le Roux, S., & Blaine, D. (2018). Numerical comparison of lattice unit cell designs for medical implants by additive manufacturing. *Virtual and Physical Prototyping, 13*(4), 266-281.

Dumas, M. (2016). *Modélisation et simulation du comportement d'une tige fémorale poreuse* (École de technologie supérieure).

Dumas, M., Terriault, P., & Brailovski, V. (2017). Modelling and characterization of a porosity graded lattice structure for additively manufactured biomaterials. *Materials & Design, 121*, 383-392.

El Masri, F., Sapin de Brosses, E., Rhissassi, K., Skalli, W., & Mitton, D. (2012). Apparent Young's modulus of vertebral cortico-cancellous bone specimens. *Computer methods in biomechanics and biomedical engineering, 15*(1), 23-28.

Elahinia, M., Shayesteh Moghaddam, N., Taheri Andani, M., Amerinatanzi, A., Bimber, B. A., & Hamilton, R. F. (2016). Fabrication of NiTi through additive manufacturing: A review. *Progress in Materials Science, 83*, 630-663. doi: 10.1016/j.pmatsci.2016.08.001

Estermann, S.-J., & Scheiner, S. (2018). Multiscale modeling provides differentiated insights to fluid flow-driven stimulation of bone cellular activities. *Frontiers in Physics, 6*, 76.

Evans, A. G., Hutchinson, J., & Ashby, M. (1998). Multifunctionality of cellular metal systems. *Progress in Materials Science, 43*(3), 171-221.

Food and Drug Administration. (2007). *Class II Special Controls Guidance Document*.

Ford, C. M., & Keaveny, T. M. (1996). The dependence of shear failure properties of trabecular bone on apparent density and trabecular orientation. *Journal of biomechanics, 29*(10), 1309-1317.

Friis, E., Arnold, P., & Goel, V. (2017). Mechanical testing of cervical, thoracolumbar, and lumbar spine implants. Dans *Mechanical Testing of Orthopaedic Implants* (pp. 161-180). Elsevier.

Fu, J., Hu, Z., Song, X., Zhai, W., Long, Y., Li, H., & Fu, M. (2020). Micro selective laser melting of NiTi shape memory alloy: Defects, microstructures and thermal/mechanical properties. *Optics & Laser Technology, 131*, 106374.

Galante, J., Rostoker, W., & Ray, R. (1970). Physical properties of trabecular bone. *Calcified tissue research, 5*(1), 236-246.

Ge, J., Yuan, B., Chen, H., Pan, J., Liu, Q., Yan, M., . . . Zhang, L. (2023). Anisotropy in microstructural features and tensile performance of laser powder bed fusion NiTi alloys. *Journal of Materials Research and Technology, 24*, 8656-8668.

Gibson, L. J. (2005). Biomechanics of cellular solids. *Journal of biomechanics, 38*(3), 377-399.

Gibson, L. J., & Ashby, M. F. (1999). *Cellular solids: structure and properties*. Cambridge university press.

Gibson, L. J., Ashby, M. F., & Harley, B. A. (2010). *Cellular Materials in Nature and Medicine*. Cambridge University Press. Repéré à https://books.google.ca/books?id=AKxiS4AKpyEC

Gorgin Karaji, Z., Speirs, M., Dadbakhsh, S., Kruth, J. P., Weinans, H., Zadpoor, A. A., & Amin Yavari, S. (2017). Additively Manufactured and Surface Biofunctionalized Porous Nitinol. *ACS Appl Mater Interfaces, 9*(2), 1293-1304. doi: 10.1021/acsami.6b14026. Repéré à https://www.ncbi.nlm.nih.gov/pubmed/28001358

Habijan, T., Haberland, C., Meier, H., Frenzel, J., Wittsiepe, J., Wuwer, C., . . . Koller, M. (2013). The biocompatibility of dense and porous Nickel-Titanium produced by selective laser melting. *Mater Sci Eng C Mater Biol Appl, 33*(1), 419-426. doi: 10.1016/j.msec.2012.09.008. Repéré à https://www.ncbi.nlm.nih.gov/pubmed/25428090

Hakim, N. S., & King, A. I. (1979). A three dimensional finite element dynamic response analysis of a vertebra with experimental verification. *Journal of biomechanics, 12*(4), 277-292.

Han, C., Li, Y., Wang, Q., Wen, S., Wei, Q., Yan, C., . . . Shi, Y. (2018). Continuous functionally graded porous titanium scaffolds manufactured by selective laser melting for bone implants. *J Mech Behav Biomed Mater, 80*, 119-127.

Hara, D., Nakashima, Y., Sato, T., Hirata, M., Kanazawa, M., Kohno, Y., . . . Nakao, Y. (2016). Bone bonding strength of diamond-structured porous titanium-alloy implants manufactured using the electron beam-melting technique. *Materials Science and Engineering: C, 59*, 1047-1052.

Hart, N. H., Nimphius, S., Rantalainen, T., Ireland, A., Siafarikas, A., & Newton, R. (2017). Mechanical basis of bone strength: influence of bone material, bone structure and muscle action. *Journal of musculoskeletal & neuronal interactions, 17*(3), 114.

Hassanizadeh, S. M., & Gray, W. G. (1987). High velocity flow in porous media. *Transport in porous media, 2*(6), 521-531.

Head, W. C., Bauk, D. J., & Emerson, J. R. (1995). Titanium as the material of choice for cementless femoral components in total hip arthroplasty. *Clinical orthopaedics and related research,* (311), 85-90.

ISO13314. (2011). *Mechanical testing of metals — Ductility testing — Compression test for porous and cellular metals*.

Issariyapat, A., Kariya, S., Alhazaa, A., Umeda, J., & Kondoh, K. (2021). Additive Manufacturing and Characterization of High Strength Ti-Zr Gyroid Scaffolds Using Pre-Mixed Ti-ZrH2 Powders. *JOM*, 1-11.

Jetté, B., Brailovski, V., Dumas, M., Simoneau, C., & Terriault, P. (2018). Femoral stem incorporating a diamond cubic lattice structure: Design, manufacture and testing. *J Mech Behav Biomed Mater, 77*, 58-72.

Kasra, M., & Grynpas, M. D. (2007). On shear properties of trabecular bone under torsional loading: effects of bone marrow and strain rate. *Journal of biomechanics, 40*(13), 2898-2903.

Kelly, C. N., Francovich, J., Julmi, S., Safranski, D., Guldberg, R. E., Maier, H. J., & Gall, K. (2019). Fatigue Behavior of As-Built Selective Laser Melted Titanium Scaffolds with Sheet-based Gyroid Microarchitecture for Bone Tissue Engineering. *Acta Biomaterialia*.

Kelly, C. N., Wang, T., Crowley, J., Wills, D., Pelletier, M. H., Westrick, E. R., . . . Walsh, W. R. (2021). High-strength, porous additively manufactured implants with optimized mechanical osseointegration. *Biomaterials*, 121206.

Khoo, Z. X., Liu, Y., An, J., Chua, C. K., Shen, Y. F., & Kuo, C. N. (2018). A Review of Selective Laser Melted NiTi Shape Memory Alloy. *Materials (Basel), 11*(4). doi: 10.3390/ma11040519. Repéré à https://www.ncbi.nlm.nih.gov/pubmed/29596320

Khorasani, A., Gibson, I., Veetil, J. K., & Ghasemi, A. H. (2020). A review of technological improvements in laser-based powder bed fusion of metal printers. *International Journal of Advanced Manufacturing Technology*.

Kienapfel, H., Sprey, C., Wilke, A., & Griss, P. (1999). Implant fixation by bone ingrowth. *The Journal of arthroplasty, 14*(3), 355-368.

Kreitcberg, A., Brailovski, V., & Prokoshkin, S. (2018). New biocompatible near-beta Ti-Zr-Nb alloy processed by laser powder bed fusion: Process optimization. *Journal of Materials Processing Technology, 252*, 821-829.

Krishnan, V., Manjeri, R. M., Clausen, B., Brown, D., & Vaidyanathan, R. (2008). Analysis of neutron diffraction spectra acquired in situ during mechanical loading of shape memory NiTiFe at low temperatures. *Materials Science and Engineering: A, 481*, 3-10.

Kuang, X., Roach, D. J., Wu, J., Hamel, C. M., Ding, Z., Wang, T., . . . Qi, H. J. (2018). Advances in 4D Printing: Materials and Applications. *Advanced Functional Materials*, 1805290.

Kudoh, Y., Tokonami, M., Miyazaki, S., & Otsuka, K. (1985). Crystal structure of the martensite in Ti-49.2 at.% Ni alloy analyzed by the single crystal X-ray diffraction method. *Acta Metallurgica, 33*(11), 2049-2056.

La Rosa, G., Clienti, C., & Mineo, R. (2018). Experimental tests on new titanium alloy interbody cervical cages. *Procedia Structural Integrity, 13*, 373-378.

Lee, A. Y., An, J., & Chua, C. K. (2017). Two-Way 4D Printing: A Review on the Reversibility of 3D-Printed Shape Memory Materials. *Engineering, 3*(5), 663-674. doi: 10.1016/j.eng.2017.05.014

Leon, E. S., Singamneni, S., Guraya, T., & Chen, Z. (2023). Effect of laser power in laser powder bed fusion on Ni content and structure of Nitinol. *Materials Today: Proceedings*.

Lerebours, C., Thomas, C., Clement, J., Buenzli, P., & Pivonka, P. (2015). The relationship between porosity and specific surface in human cortical bone is subject specific. *Bone, 72*, 109-117.

Letenneur, M., Brailovski, V., Kreitcberg, A., Paserin, V., & Bailon-Poujol, I. (2017). Laser powder bed fusion of water-atomized iron-based powders: process optimization. *Journal of Manufacturing and Materials Processing, 1*(2), 23.

Lin, C. Y., Kikuchi, N., & Hollister, S. J. (2004). A novel method for biomaterial scaffold internal architecture design to match bone elastic properties with desired porosity. *Journal of biomechanics, 37*(5), 623-636.

Lindahl, O. (1976). Mechanical properties of dried defatted spongy bone. *Acta Orthopaedica Scandinavica, 47*(1), 11-19.

Liu, F., Mao, Z., Zhang, P., Zhang, D. Z., Jiang, J., & Ma, Z. (2018). Functionally graded porous scaffolds in multiple patterns: New design method, physical and mechanical properties. *Materials & Design, 160*, 849-860.

Lu, C., Zhang, C., Wen, P., & Chen, F. (2021). Mechanical Behavior of Al-Si10-Mg Gyroid Surface with Variable Topological Parameters Fabricated via Laser Powder Bed Fusion. *Journal of Materials Research and Technology*.

Lu, H., Ma, H., Cai, W., Luo, X., Qu, S., Wang, J., . . . Yang, C. (2022). Altered phase transformation behaviors and enhanced bending shape memory property of NiTi shape memory alloy via selective laser melting. *Journal of Materials Processing Technology, 303*, 117546.

Lu, H., Ma, H., Luo, X., Wang, Y., Wang, J., Lupoi, R., . . . Yang, C. (2021). Microstructure, shape memory properties, and in vitro biocompatibility of porous NiTi scaffolds fabricated via selective laser melting. *Journal of Materials Research and Technology*.

Lu, H., Ma, H., Yang, Y., Cai, W., Luo, X., Yan, A., . . . Yang, C. (2023). Tailoring phase transformation behavior, microstructure, and superelasticity of NiTi shape memory alloys by specific change of laser power in selective laser melting. *Materials Science and Engineering: A, 864*, 144576.

Lu, H., Yang, C., Luo, X., Ma, H., Song, B., Li, Y., & Zhang, L. (2019). Ultrahigh-performance TiNi shape memory alloy by 4D printing. *Materials Science and Engineering: A, 763*, 138166.

Luxner, M. H., Stampfl, J., & Pettermann, H. E. (2005). Finite element modeling concepts and linear analyses of 3D regular open cell structures. *Journal of Materials Science, 40*(22), 5859-5866.

Ma, J., Franco, B., Tapia, G., Karayagiz, K., Johnson, L., Liu, J., . . . Elwany, A. (2017). Spatial Control of Functional Response in 4D-Printed Active Metallic Structures. *Sci Rep, 7*, 46707. doi: 10.1038/srep46707. Repéré à https://www.ncbi.nlm.nih.gov/pubmed/28429796

Ma, S., Tang, Q., Han, X., Feng, Q., Song, J., Setchi, R., . . . Engstrøm, D. S. (2020). Manufacturability, mechanical properties, mass-transport properties and biocompatibility of TPMS scaffolds fabricated by selective laser melting. *Materials & Design*, 109034.

Mahmoud, D., & Elbestawi, M. (2017). Lattice structures and functionally graded materials applications in additive manufacturing of orthopedic implants: A review. *Journal of Manufacturing and Materials Processing, 1*(2), 13.

Mahmoudi, M., Tapia, G., Franco, B., Ma, J., Arroyave, R., Karaman, I., & Elwany, A. (2018). On the printability and transformation behavior of nickel-titanium shape memory alloys fabricated using laser powder-bed fusion additive manufacturing. *Journal of Manufacturing Processes, 35*, 672-680. doi: 10.1016/j.jmapro.2018.08.037

Maitrejean, G., Terriault, P., Devis Capilla, D., & Brailovski, V. (2014). Unit Cell Analysis of the Superelastic Behavior of Open-Cell Tetrakaidecahedral Shape Memory Alloy Foam under Quasi-Static Loading. *Smart Materials Research, 2014*, 11. doi: 10.1155/2014/870649. Repéré à http://dx.doi.org/10.1155/2014/870649

Martin, R. B. (1984). Porosity and specific surface of bone. *Critical reviews in biomedical engineering, 10*(3), 179-222.

Maskery, I., & Ashcroft, I. (2020). The deformation and elastic anisotropy of a new gyroid-based honeycomb made by laser sintering. *Additive Manufacturing, 36*, 101548.

MatWeb. (2019). Polyetheretherketone material properties (unreinforced). Repéré le 01 september à http://www.matweb.com/search/DataSheet.aspx?MatGUID=2164cacabcde4391a596640d553b2ebe&ckck=1

McCue, I., Peitsch, C., Montalbano, T., Lennon, A., Sopcisak, J., Trexler, M. M., & Storck, S. (2019). Scalable laser powder bed fusion processing of nitinol shape memory alloy. *MRS Communications*, 1-7. doi: https://doi.org/10.1557/mrc.2019.134

Mirzaali, M. J., Schwiedrzik, J. J., Thaiwichai, S., Best, J. P., Michler, J., Zysset, P. K., & Wolfram, U. (2016). Mechanical properties of cortical bone and their relationships with age, gender, composition and microindentation properties in the elderly. *Bone, 93*, 196-211. Repéré à https://www.sciencedirect.com/science/article/pii/S8756328215004196?via%3Dihub

Mitchell, A., Lafont, U., Hołyńska, M., & Semprimoschnig, C. (2018). Additive Manufacturing-A Review of 4D Printing and Future Applications. *Additive Manufacturing*.

Mobbs, R. J., Parr, W. C., Choy, W. J., McEvoy, A., Walsh, W. R., & Phan, K. (2019). Anterior Lumbar Interbody Fusion Using a Personalized Approach: Is Custom the Future of Implants for Anterior Lumbar Interbody Fusion Surgery? *World neurosurgery*.

Moghaddam, N. S., Saedi, S., Amerinatanzi, A., Hinojos, A., Ramazani, A., Kundin, J., . . . Elahinia, M. (2019). Achieving superelasticity in additively manufactured NiTi in compression without post-process heat treatment. *Sci Rep, 9*(1), 41.

Momeni, F., M.Mehdi Hassani.N, S., Liu, X., & Ni, J. (2017). A review of 4D printing. *Materials & Design, 122*, 42-79. doi: 10.1016/j.matdes.2017.02.068

Moore, K. L., Dalley, A. F., & Agur, A. M. R. (2013). *Clinically Oriented Anatomy*. Wolters Kluwer Health/Lippincott Williams & Wilkins. Repéré à https://books.google.ca/books?id=-Le5bc5F0sYC

Murphy, K., Gorber, S. K. C., Spence, S. T., & McIntosh, C. N. (2006). *Health state descriptions for Canadians: Musculoskeletal*. Statistics Canada.

Murr, L. (2020). Metallurgy principles applied to powder bed fusion 3D printing/additive manufacturing of personalized and optimized metal and alloy biomedical implants: an overview. *Journal of Materials Research and Technology, 9*(1), 1087-1103.

Mwangi, J. W., Nguyen, L. T., Bui, V. D., Berger, T., Zeidler, H., & Schubert, A. (2019). Nitinol manufacturing and micromachining: a review of processes and their suitability in processing medical-grade nitinol. *Journal of Manufacturing Processes, 38*, 355-369.

Nauman, E. A., Fong, K., & Keaveny, T. (1999). Dependence of intertrabecular permeability on flow direction and anatomic site. *Annals of biomedical engineering, 27*(4), 517-524.

Nelson, K., Kelly, C. N., & Gall, K. (2022). Effect of stress state on the mechanical behavior of 3D printed porous Ti6Al4V scaffolds produced by laser powder bed fusion. *Materials Science and Engineering: B, 286*, 116013.

Nemoto, O., Asazuma, T., Yato, Y., Imabayashi, H., Yasuoka, H., & Fujikawa, A. (2014). Comparison of fusion rates following transforaminal lumbar interbody fusion using polyetheretherketone cages or titanium cages with transpedicular instrumentation. *European Spine Journal, 23*(10), 2150-2155.

Nicholson, P., Cheng, X., Lowet, G., Boonen, S., Davie, M., Dequeker, J., & Van der Perre, G. (1997). Structural and material mechanical properties of human vertebral cancellous bone. *Medical engineering & physics, 19*(8), 729-737.

Obadimu, S. O., & Kourousis, K. I. (2021). Compressive Behaviour of Additively Manufactured Lattice Structures: A Review. *Aerospace, 8*(8), 207.

Otsuka, K., & Wayman, C. M. (1999). *Shape Memory Materials*. Cambridge University Press. Repéré à https://books.google.ca/books?id=DvItE9XUlN8C

Panjabi, M. M., Goel, V., Oxland, T., Takata, K., Duranceau, J., Krag, M., & Price, M. (1992). Human lumbar vertebrae. Quantitative three-dimensional anatomy. *Spine, 17*(3), 299-306.

Park, M.-K., Kim, K.-T., Bang, W.-S., Cho, D.-C., Sung, J.-K., Lee, Y.-S., . . . Lee, W.-K. (2019). Risk factors for cage migration and cage retropulsion following transforaminal lumbar interbody fusion. *The Spine Journal, 19*(3), 437-447.

Peck, J. H., Kavlock, K. D., Showalter, B. L., Ferrell, B. M., Peck, D. G., & Dmitriev, A. E. (2018). Mechanical performance of lumbar intervertebral body fusion devices: An analysis of data submitted to the Food and Drug Administration. *Journal of biomechanics, 78*, 87-93.

Peck, J. H., Sing, D. C., Nagaraja, S., Peck, D. G., Lotz, J. C., & Dmitriev, A. E. (2017). Mechanical performance of cervical intervertebral body fusion devices: A systematic analysis of data submitted to the Food and Drug Administration. *Journal of biomechanics, 54*, 26-32.

Pivonka, P., Buenzli, P. R., Scheiner, S., Hellmich, C., & Dunstan, C. R. (2013). The influence of bone surface availability in bone remodelling—a mathematical model including coupled geometrical and biomechanical regulations of bone cells. *Engineering Structures, 47*, 134-147.

Pooni, J., Hukins, D., Harris, P., Hilton, R., & Davies, K. (1986). Comparison of the structure of human intervertebral discs in the cervical, thoracic and lumbar regions of the spine. *Surgical and radiologic anatomy, 8*(3), 175-182.

Ptochos, E., & Labeas, G. (2012). Elastic modulus and Poisson's ratio determination of micro-lattice cellular structures by analytical, numerical and homogenisation methods. *Journal of Sandwich Structures & Materials, 14*(5), 597-626.

Qiu, P., Gao, P., Wang, S., Li, Z., Yang, Y., Zhang, Q., . . . Hao, S. (2020). Study on corrosion behavior of the selective laser melted NiTi alloy with superior tensile property and shape memory effect. *Corrosion Science*, 108891.

Ravari, M. K., Esfahani, S. N., Andani, M. T., Kadkhodaei, M., Ghaei, A., Karaca, H., & Elahinia, M. (2016). On the effects of geometry, defects, and material asymmetry on the mechanical response of shape memory alloy cellular lattice structures. *Smart Materials and Structures, 25*(2), 025008.

Ravari, M. K., Kadkhodaei, M., Badrossamay, M., & Rezaei, R. (2014). Numerical investigation on mechanical properties of cellular lattice structures fabricated by fused deposition modeling. *International Journal of Mechanical Sciences, 88*, 154-161.

Ren, D., Zhang, L., Liu, Y., Ji, H., Li, S., Jin, W., & Lei, J. (2023). Effect of hot isostatic pressing on the mechanical and corrosive properties of Ti-Ni alloy fabricated by selective laser melting. *Journal of Materials Research and Technology*.

Ritzel, H., Amling, M., Pösl, M., Hahn, M., & Delling, G. (1997). The thickness of human vertebral cortical bone and its changes in aging and osteoporosis: A histomorphometric analysis of the complete spinal column from thirty-seven autopsy specimens. *Journal of Bone and Mineral Research, 12*(1), 89-95.

Saedi, S., Shayesteh Moghaddam, N., Amerinatanzi, A., Elahinia, M., & Karaca, H. E. (2018). On the effects of selective laser melting process parameters on microstructure and thermomechanical response of Ni-rich NiTi. *Acta Materialia, 144*, 552-560. doi: 10.1016/j.actamat.2017.10.072

Saedi, S., Turabi, A. S., Andani, M. T., Moghaddam, N. S., Elahinia, M., & Karaca, H. E. (2017). Texture, aging, and superelasticity of selective laser melting fabricated Ni-rich NiTi alloys. *Materials Science and Engineering: A, 686*, 1-10.

Saghaian, S. E., Nematollahi, M., Toker, G., Hinojos, A., Moghaddam, N. S., Saedi, S., . . . Elahinia, M. (2021). Effect of hatch spacing and laser power on microstructure, texture, and thermomechanical properties of laser powder bed fusion (L-PBF) additively manufactured NiTi. *Optics & Laser Technology*, 107680.

Salem, H., Carter, L., Attallah, M., & Salem, H. (2019). Influence of processing parameters on internal porosity and types of defects formed in Ti6Al4V lattice structure fabricated by selective laser melting. *Materials Science and Engineering: A, 767*, 138387.

Scherbakov, V., & Shishkovsky, I. V. (2018). *4D manufacturing of intermetallic SMA fabricated by SLM process* présentée à Laser 3D Manufacturing V. doi: 10.1117/12.2288176

Scoles, P. V., Linton, A. E., Latimer, B., Levy, M. E., & Digiovanni, B. (1988). Vertebral body and posterior element morphology: the normal spine in middle life. *Spine, 13*(10), 1082-1086.

Semenova, E. L., & Kudryavtsev, Y. V. (1994). Structural phase transformation and shape memory effect in ZrRh and ZrIr. *Journal of Alloys and Compounds, 203*, 165-168.

Shen, F., Li, H., Guo, H., Guo, N., & Fang, X. (2022). Effect of energy density on the superelastic property of Ni-rich NiTi alloy fabricated by laser powder bed fusion. *Materials Science and Engineering: A, 854*, 143874.

Simoneau, C., Brailovski, V., & Terriault, P. (2016). Design, manufacture and tensile properties of stochastic porous metallic structures. *Mechanics of Materials, 94*, 26-37.

Sing, S. L., Wiria, F. E., & Yeong, W. Y. (2018). Selective laser melting of lattice structures: A statistical approach to manufacturability and mechanical behavior. *Robotics and Computer-Integrated Manufacturing, 49*, 170-180.

Singer, K., Edmondston, S., Day, R., Breidahl, P., & Price, R. (1995). Prediction of thoracic and lumbar vertebral body compressive strength: correlations with bone mineral density and vertebral region. *Bone, 17*(2), 167-174.

Sitepu, H. (2003). Use of synchrotron diffraction data for describing crystal structure and crystallographic phase analysis of R-phase NiTi shape memory alloy. *Textures and Microstructures, 35*(3-4), 185-195.

Sitepu, H. (2008). In situ structural and texture analyses of monoclinic phase for polycrystalline Ni-rich Ti49. 86Ni50. 14 alloy from neutron diffraction data. *Powder Diffraction, 23*(1), 35-40.

Sitepu, H. (2009). Texture and structural refinement using neutron diffraction data from molybdite (MoO3) and calcite (CaCO3) powders and a Ni-rich Ni50. 7Ti49. 30 alloy. *Powder Diffraction, 24*(4), 315-326.

Siu, T. L., Rogers, J. M., Lin, K., Thompson, R., & Owbridge, M. (2018). Custom-Made Titanium 3-Dimensional Printed Interbody Cages for Treatment of Osteoporotic Fracture–Related Spinal Deformity. *World neurosurgery, 111*, 1-5.

Sobieski, W., & Trykozko, A. (2014). Darcy's and Forchheimer's laws in practice. Part 1. The experiment. *Technical Sciences/University of Warmia and Mazury in Olsztyn*.

Soro, N., Attar, H., Wu, X., & Dargusch, M. S. (2019). Investigation of the structure and mechanical properties of additively manufactured Ti-6Al-4V biomedical scaffolds designed with a Schwartz primitive unit-cell. *Materials Science and Engineering: A, 745*, 195-202.

Soro, N., Saintier, N., Merzeau, J., Veidt, M., & Dargusch, M. S. (2021). Quasi-static and fatigue properties of graded Ti–6Al–4V lattices produced by Laser Powder Bed Fusion (LPBF). *Additive Manufacturing, 37*, 101653.

Soul, H., Terriault, P., & Brailovski, V. (2018). The static and fatigue behavior of AlSiMg alloy plain, notched, and diamond lattice specimens fabricated by laser powder bed fusion. *Journal of Manufacturing and Materials Processing, 2*(2), 25.

Speirs, M., Van Hooreweder, B., Van Humbeeck, J., & Kruth, J.-P. (2017). Fatigue behaviour of NiTi shape memory alloy scaffolds produced by SLM, a unit cell design comparison. *J Mech Behav Biomed Mater, 70*, 53-59.

Spetzger, U., Frasca, M., & König, S. A. (2016). Surgical planning, manufacturing and implantation of an individualized cervical fusion titanium cage using patient-specific data. *European Spine Journal, 25*(7), 2239-2246.

Sukop, M. C., Huang, H., Alvarez, P. F., Variano, E. A., & Cunningham, K. J. (2013). Evaluation of permeability and non-Darcy flow in vuggy macroporous limestone aquifer samples with lattice Boltzmann methods. *Water Resources Research, 49*(1), 216-230.

Suryawanshi, J., Singh, G., Msolli, S., Jhon, M. H., & Ramamurty, U. (2021). Tension-compression asymmetry and shear strength of titanium alloys. *Acta Materialia, 221*, 117392.

Syahrom, A., Kadir, M. R. A., Harun, M. N., & Öchsner, A. (2015). Permeability study of cancellous bone and its idealised structures. *Medical engineering & physics, 37*(1), 77-86.

Tang, J., Luo, J., Huang, Y., Sun, J., Zhu, Z., Xu, J., . . . Yan, M. (2020). Immunological response triggered by metallic 3D printing powders. *Additive Manufacturing, 35*, 101392.

Tang, T., Ebacher, V., Cripton, P., Guy, P., McKay, H., & Wang, R. (2015). Shear deformation and fracture of human cortical bone. *Bone, 71*, 25-35.

Tang, Y., & Zhao, Y. F. (2016). A survey of the design methods for additive manufacturing to improve functional performance. *Rapid Prototyping Journal, 22*(3), 569-590.

Taniguchi, N., Fujibayashi, S., Takemoto, M., Sasaki, K., Otsuki, B., Nakamura, T., . . . Matsuda, S. (2016). Effect of pore size on bone ingrowth into porous titanium implants fabricated by additive manufacturing: an in vivo experiment. *Materials Science and Engineering: C, 59*, 690-701.

Terriault, P., & Brailovski, V. (2017). Influence of boundary conditions on the simulation of a diamond-type lattice structure: A preliminary study. *Advances in Materials Science and Engineering, 2017*.

Timercan, A., Sheremetyev, V., & Brailovski, V. (2021). Mechanical properties and fluid permeability of gyroid and diamond lattice structures for intervertebral devices: functional requirements and comparative analysis. *Sci Technol Adv Mater, 22*(1), 285-300.

Timercan, A., Terriault, P., & Brailovski, V. (2023). Axial tension/compression and torsional loading of diamond and gyroid lattice structures for biomedical implants: simulation and experiment. *Materials & Design*, 111585.

Turner, C., Wang, T., & Burr, D. (2001). Shear strength and fatigue properties of human cortical bone determined from pure shear tests. *Calcified tissue international, 69*(6).

Van Humbeeck, J. (2018). Additive Manufacturing of Shape Memory Alloys. *Shape Memory and Superelasticity, 4*(2), 309-312. doi: 10.1007/s40830-018-0174-z

Wang, X., Xu, S., Zhou, S., Xu, W., Leary, M., Choong, P., . . . Xie, Y. M. (2016). Topological design and additive manufacturing of porous metals for bone scaffolds and orthopaedic implants: A review. *Biomaterials, 83*, 127-141. doi: 10.1016/j.biomaterials.2016.01.012. Repéré à https://www.ncbi.nlm.nih.gov/pubmed/26773669

Wang, Y., Ren, X., Chen, Z., Jiang, Y., Cao, X., Fang, S., . . . Fang, D. (2020). Numerical and experimental studies on compressive behavior of Gyroid lattice cylindrical shells. *Materials & Design, 186*, 108340.

Weinert, K., & Petzoldt, V. (2004). Machining of NiTi based shape memory alloys. *Materials Science and Engineering: A, 378*(1-2), 180-184.

Wen, S., Liu, Y., Zhou, Y., Zhao, A., Yan, C., & Shi, Y. (2021). Effect of Ni content on the transformation behavior and mechanical property of NiTi shape memory alloys fabricated by laser powder bed fusion. *Optics & Laser Technology, 134*, 106653.

Williams, A. L., Gornet, M. F., & Burkus, J. K. (2005). CT evaluation of lumbar interbody fusion: current concepts. *American Journal of Neuroradiology, 26*(8), 2057-2066.

Wolfram, U., & Schwiedrzik, J. (2016). Post-yield and failure properties of cortical bone. *BoneKEy reports, 5*.

Wolfram, U., Wilke, H.-J., & Zysset, P. K. (2010). Valid µ finite element models of vertebral trabecular bone can be obtained using tissue properties measured with nanoindentation under wet conditions. *Journal of biomechanics, 43*(9), 1731-1737.

Wong, K. V., & Hernandez, A. (2012). A review of additive manufacturing. *ISRN Mechanical Engineering, 2012*.

Xu, P., & Yu, B. (2008). Developing a new form of permeability and Kozeny–Carman constant for homogeneous porous media by means of fractal geometry. *Advances in water resources, 31*(1), 74-81.

Xue, L., Atli, K., Zhang, C., Hite, N., Srivastava, A., Leff, A., . . . Arroyave, R. (2022). Laser Powder Bed Fusion of Defect-Free NiTi Shape Memory Alloy Parts with Superior Tensile Superelasticity. *Acta Materialia*, 117781.

Yánez, A., Cuadrado, A., Martel, O., Afonso, H., & Monopoli, D. (2018). Gyroid porous titanium structures: a versatile solution to be used as scaffolds in bone defect reconstruction. *Materials & Design, 140*, 21-29.

Yánez, A., Fiorucci, M. P., Cuadrado, A., Martel, O., & Monopoli, D. (2020). Surface roughness effects on the fatigue behaviour of gyroid cellular structures obtained by additive manufacturing. *International Journal of Fatigue, 138*, 105702.

Yang, L., Ferrucci, M., Mertens, R., Dewulf, W., Yan, C., Shi, Y., & Yang, S. (2020). An investigation into the effect of gradients on the manufacturing fidelity of triply periodic minimal surface structures with graded density fabricated by selective laser melting. *Journal of Materials Processing Technology, 275*, 116367.

Yu, G., Li, Z., Li, S., Zhang, Q., Hua, Y., Liu, H., . . . Wang, X. (2020). The select of internal architecture for porous Ti alloy scaffold: A compromise between mechanical properties and permeability. *Materials & Design*, 108754.

Zadpoor, A. A. (2019). Additively manufactured porous metallic biomaterials. *Journal of Materials Chemistry B, 7*(26), 4088-4117.

Zamani, M., Kadkhodaei, M., Badrossamay, M., & Foroozmehr, E. (2021). Adjustment of the scan track spacing and linear input energy to fabricate dense, pseudoelastic Nitinol shape memory alloy parts by selective laser melting. *Journal of Intelligent Material Systems and Structures*, 1045389X211063948.

Zhang, L., Feih, S., Daynes, S., Chang, S., Wang, M. Y., Wei, J., & Lu, W. F. (2018). Energy absorption characteristics of metallic triply periodic minimal surface sheet structures under compressive loading. *Additive Manufacturing, 23*, 505-515.

Zhang, Q., Hao, S., Liu, Y., Xiong, Z., Guo, W., Yang, Y., . . . Zhang, Z. (2020). The microstructure of a selective laser melting (SLM)-fabricated NiTi shape memory alloy with superior tensile property and shape memory recoverability. *Applied Materials Today, 19*, 100547.

Zhang, X.-Y., Fang, G., & Zhou, J. (2017). Additively manufactured scaffolds for bone tissue engineering and the prediction of their mechanical behavior: A review. *Materials, 10*(1), 50.

Zhang, X.-Y., Yan, X.-C., Fang, G., & Liu, M. (2020). Biomechanical influence of structural variation strategies on functionally graded scaffolds constructed with triply periodic minimal surface. *Additive Manufacturing, 32*, 101015.

Zhang, Y., Attarilar, S., Wang, L., Lu, W., Yang, J., & Fu, Y. (2021). A Review on Design and Mechanical Properties of Additively Manufactured NiTi Implants for Orthopedic Applications. *International Journal of Bioprinting, 7*(2).

Zhao, C., Liang, H., Luo, S., Yang, J., & Wang, Z. (2020). The effect of energy input on reaction, phase transition and shape memory effect of NiTi alloy by selective laser melting. *Journal of Alloys and Compounds, 817*, 153288.

Zhou, H., Zhao, M., Ma, Z., Zhang, D. Z., & Fu, G. (2020). Sheet and network based functionally graded lattice structures manufactured by selective laser melting: Design, mechanical properties, and simulation. *International Journal of Mechanical Sciences*, 105480.

Zhu, J.-N., Ding, Z., Borisov, E., Yao, X., Brouwer, J. C., Popovich, A., . . . Popovich, V. (2023). Healing cracks in additively manufactured NiTi shape memory alloys. *Virtual and Physical Prototyping, 18*(1), e2246437.